NASA
CR
2914
V.1
c.1

NASA Contractor Report 2914

Two-Dimensional Wind Tunnel Test of an Oscillating Rotor Airfoil

Volume I

LOAN COPY: RETURN TO
AFWL TECHNICAL LIBRARY
KIRTLAND AFB, N. M.

L. U. Dadone

CONTRACT NAS1-13795
DECEMBER 1977

NASA

TECH LIBRARY KAFB, NM
0061744

NASA Contractor Report 2914

Two-Dimensional Wind Tunnel Test of an Oscillating Rotor Airfoil

Volume I

L. U. Dadone
Boeing Vertol Company
Philadelphia, Pennsylvania

Prepared for
Langley Research Center
under Contract NAS1-13795

NASA
National Aeronautics
and Space Administration

**Scientific and Technical
Information Office**

1977

TWO-DIMENSIONAL WIND TUNNEL TEST OF AN OSCILLATING ROTOR AIRFOIL

(VOLUME I)

by

L. U. Dadone
Boeing Vertol Company

SUMMARY

An experimental investigation was conducted to determine the quasi-steady and unsteady characteristics of the NLR 7223-62 airfoil, an advanced section designed for helicopter-rotor applications. The data was obtained with an airfoil model equipped with 17 differential transducers and mounted in the variable-density test section of a blow-down wind tunnel. The test equipment and procedures were similar to other oscillating airfoil tests previously conducted in the same facility.

Quasi-steady pressure data were acquired at Mach numbers between M = 0.2 and 0.9 with porous floor and ceiling (4.9% porosity). Drag data were acquired at a limited number of conditions with a wake-traversing probe. Static and oscillatory tests were then run with solid floor and ceiling at Mach numbers between M = 0.2 and M = 0.7.

The oscillatory test was run at frequencies from 23 Hz to approximately 90 Hz, with amplitudes of oscillation ranging from 2.5° to 10.0°. The test results are presented in two volumes. The first volume documents the test procedure and discusses some of the key results. The second volume is a data report, and it contains tabulations of all static and oscillatory data.

INTRODUCTION

Quasi-steady data are not adequate in describing the flow phenomena which take place on helicopter rotor blades in forward flight. Typically, quasi-steady data will lead to the underprediction of the onset in retreating blade stall because of the presence of a stall-delay mechanism associated with variations in local blade incidence. Such variations are a function of the combined effects of rotor downwash, blade flapping, rotor controls and blade deflections. The evaluation of the rotor flow environment presents a number of difficulties among which the assessment of unsteady aerodynamic effects has a prominent place[1,2,3].

The unsteady flow phenomena of interest in the understanding of retreating blade stall take place at Mach numbers between 0.3 and 0.5. At such Mach numbers, the compressibility effects associated with operation at high lift are significant, while the theoretical understanding of such effects is incomplete. As a result, two-dimensional wind tunnel tests are necessary to provide the data base necessary for an empirical approximation of dynamic stall.

Although many oscillating airfoil tests have been conducted since the 1950's, mostly on the NACA 0012 airfoil (see literature survey in reference 4), the combined effect of compressibility and oscillating motions over a range of conditions of interest for helicopters has been quantified experimentally for the first time in reference 4. Subsequent tests in the same facility are reported in references 5 and 6.

The airfoils in references 4, 5 and 6 are modifications of standard NACA 5-digit sections. Since 1966/1967, when these tests were run, helicopter airfoil design has been pursued utilizing advances in design methodology acquired from fixed wing experience. A partial survey and compilation of data on the new rotor airfoil sections is presented in reference 7. One of the most successful concepts for fixed-wing application has been that of "peaky" airfoils, having blunt leading edges with carefully designed contours to delay the onset of compressibility effects and to minimize drag rise at transonic speeds. Although "peaky" airfoils are generally designed for operation at low lift levels, the concept has been extended to airfoils for helicopter-rotor applications[8], including criteria to limit the sectional pitching moments and to increase the maximum lift capability.

The NLR 7223-62 (or NLR-1) has been designed by theoretical and empirical means following the guidelines set forth in reference 8. Besides a "peaky" leading edge contour to optimize high-speed performance, the NLR 7223-62 has inverse camber built into the trailing edge to reduce sectional pitching moments[9].

Since the unsteady aerodynamic performance of airfoils cannot be predicted theoretically, a wind tunnel test has been conducted to obtain both quasi-steady and oscillatory data. The data from the present test can be used (a) to assess the potential applications of the new airfoil, and (b) to include the unsteady characteristics of "peaky" sections into the guidelines for the design of improved advanced rotor airfoils.

The present test program was conducted under the technical cognizance of Mr. C. E. K. Morris, Jr., of the NASA Langley Research Center.

The author wishes to acknowledge the assistance of the wind tunnel, flight test, and computer services groups. Particularly

valuable throughout the complex data reduction procedure was the assistance of Mr. R. K. Mann.

LIST OF SYMBOLS

a - speed of sound, m/s

b - airfoil semichord, m

c - airfoil chord, m

$C(k)$ - Theodorsen's complex function for unsteady flow, $(A(k) + jB(k))$

C_d - airfoil drag coefficient, (drag force/unit span)/$q_\infty c$

C_{d_o} - drag coefficient at $C_\ell = 0.0$

C_ℓ - airfoil lift coefficient, (lift force/unit span)/$q_\infty c$

$C_{\ell_{MAX}}$ - maximum magnitude of lift coefficient

C_m - airfoils pitching-moment coefficient, (pitching moment/unit span)/$q_\infty c^2$

C_{m_o} - pitching-moment coefficient at $C_\ell = 0.0$

C_n - airfoil normal-force coefficient, (normal force/unit span)/$q_\infty c$

$C_{n_{MAX}}$ - maximum magnitude of normal-force coefficient

$C_{n_{max}}$ - maximum magnitude of normal-force coefficient attained in oscillation cycle

C_p - pressure coefficient, $(P - P_s)/\frac{1}{2}\rho V^2$

f_D - drive frequency of airfoil motion in pitch, Hertz

H - tunnel test-section height, m

k - reduced frequency, $\pi fc/V$

M - Mach number

M_{DD} - drag-divergence Mach number, defined by $dC_d/dM = 0.1$ at constant angle of attack

n - number of harmonic

P - local pressure, N/m^2 (psia)

P_S - tunnel test-section static pressure, N/m^2 (psia)

P_T - tunnel test-section total pressure, N/m^2 (psia)

q - dynamic pressure, defined as $\frac{1}{2}\rho V^2$, N/m^2

Rn - Reynolds number based on airfoil chord

t - airfoil thickness, m

T_T - tunnel test-section total temperature, K

V - tunnel velocity, m/s

x - airfoil chordwise location, measured from the leading edge, positive rearward, m

x_m - airfoil chordwise location of the pitching moment reference center, measured from the leading edge, m

x_p - airfoil chordwise location of the pitch axis, measured from the leading edge, m

y - airfoil surface location measured perpendicular to the chordline, positive upward, m

α - instantaneous airfoil angle of attack, deg

α_{STALL} - angle of attack corresponding to $C_{\ell_{MAX}}$ or $C_{n_{MAX}}$, deg

$\dot{\alpha}$ - first differential of α with respect to time, deg/sec

α_o - mean angle of attack during oscillation cycle, deg

γ - stall delay function (gamma function)

$\Delta\alpha$ - amplitude of pitching motion, deg

ΔC_p - differential pressure coefficient, $\Delta P/\frac{1}{2}\rho V^2$

ΔP - differential pressure, N/m^2 (psi)

θ - pitching-motion reference angle, deg

$\dot{\theta}$ - first differential of θ with respect to time, deg/sec

ρ - density of air, kg/m^3 ($slug/ft^3$)

1/rev, 2/rev - one per revolution, two per revolution, etc., corresponding to ratio of airfoil drive frequency to equivalent rotor drive frequency

MODEL AND TEST EQUIPMENT

Model

The characteristics of the airfoil model and of the instrumentation are summarized in Table I. Airfoil coordinates are presented in Table II. The coordinates are the same as given in the airfoil design documentation, reference 9, except that the shape is truncated at 99% of the original chord. Figure 1 shows the model prior to installation in the test section.

Differential transducers were installed in the model to measure the net pressure across the airfoil at seventeen (17) chordwise stations as listed in Table I. Of the seventeen transducers, twelve were mounted directly inside the airfoil model, while three leading edge and two trailing edge transducers were installed inside detachable elements. All transducers were secured with a ketone-soluble structural foam which permitted the replacement of failed units.

Wind Tunnel

The test was conducted in the two-dimensional subsonic insert of the Boeing Supersonic Wind Tunnel (BSWT) in Seattle, Wash. A layout of the two-dimensional insert is shown in figure 2. The test section of the two-dimensional insert is 0.914m (36 in.) high and 0.305m (12 in.) wide at the airfoil model. The porosity of the floor and ceiling of the test section can be varied. A porosity of 4.9% was used during most of the quasi-steady test runs. Solid floor and ceiling were employed for the oscillatory tests and for the corresponding quasi-steady baseline runs. The Boeing Supersonic Wind Tunnel is of the blow-down type and it can be operated at total pressures ranging approximately from 170,000 N/m^2 (25 psi) to 520,000 N/m^2 (75 psi). Automatic Mach number control is provided to compensate for the drop in supply pressure during a run.

Airfoil Drive Mechanism

The drive mechanism was the same as used in the forced pitch oscillation tests of references 4, 5, and 6. The mechanism is illustrated in figure 3; it consists of an arm, rigidly mounted on one side of the airfoil, connected to an eccentrically mounted cam/follower arrangement on a fly-wheel driven by a hydraulic motor. To minimize the velocity fluctuations within each cycle, the fly-wheel inertia has been maximized within the space available on the subsonic test rig. The cam/follower arrangement and the fly-wheel provide an angle of attack variation which is nearly sinusoidal, as documented by the harmonic

coefficients obtained from the measured angle of attack records in the data report (Volume II of this document). The roller in the cam/follower system had to be replaced periodically during the test because of wear.

Data Acquisition and Reduction System

A portion of the quasi-steady data and all the drag data were processed on-line through the computer facility available at the test site. The quasi-steady data in presence of solid floor and ceiling and the oscillatory data were recorded on magnetic tape and reduced off-site. Appendix A describes in some detail the data acquisition and reduction path. The procedure is also outlined in figure 4.

TEST PROCEDURE

Static Test

The static, or quasi-steady, portion of the test was conducted in several separate phases, each of which will be briefly discussed in the following sections. The separation into phases is because of different test section configuration and instrumentation requirements.

Oil Flow Visualization. Flow visualization over the entire surface of the airfoil model was required to verify the adequacy of the seal between the walls of the test section and the edges of the model. To achieve this, the entire surface of the airfoil was covered with an oil suspension of a fluorescent compound. The tunnel was then run at the desired test condition long enough to establish a steady flow pattern (a few seconds); next the results were recorded with photographs. The flow-visualization tests provided sufficient qualitative evidence to assist in the definition of adequate end seals.

The fluorescent compound was applied after the surface of the model was covered with tape to prevent the oil from reaching and damaging the transducers. However, the oil penetration caused the tape to lift in spots and caused some degradation in the overall quality of the visualization results. It is important to note, however, that features of the flow presented during dynamic stall have an overriding effect over side-wall induced separation.[10]

Typical oil flow patterns are shown in figures 5 and 6.

Drag Measurements. Drag was determined by measuring the momentum loss in the wake with a traversing static and total pressure probe. The wake probe assembly is shown in figure 7. Wake-drag measurements were carried out under the following conditions:

Traversing Rate: 3.81 cm/sec (1.5 in./sec)

Sampling Rate: 11 samples/cm (29 samples/in.)

Filters: f_{c_o} = 32 Hz (frequency cutoff)

The traversing limits were adjusted for the longest wake in a set.

Repeatability of individual drag measurements was usually better than 1.5%. Some scatter in drag measurements is normal due to the unsteady nature of the wake.

Pressure Measurements. The measurement of differential pressures across the airfoil model was made while the model was pitched continuously from low to high angles of attack at a rate not exceeding 1.5°/sec. Two separate runs were generally required to cover the full angle-of-attack range from small negative lift levels to and through stall. Tests were conducted at Mach numbers up to M = 0.9 with a floor and ceiling porosity of 4.9%. This porosity was also used in earlier quasi-steady tests.

Since the oscillatory tests were run with solid floor and ceiling, a quasi-steady baseline was obtained for such test section configuration at Mach numbers up to M = 0.7. The testing procedure was the same as that used for the runs with porous floor and ceiling.

Oscillatory Test

Forced Pitch Oscillation. The oscillatory tests were conducted over a range of Mach numbers from M = 0.2 to M = 0.7. The airfoil drive frequency, based on the equivalent full-scale reduced frequency k, was in multiples of 23 Hz, except for a number of selected conditions. The nominal amplitudes of oscillation available were: 2.5°, 5.0°, 7.5°, and 10°. A substantial portion of the data was obtained with the 5.0° amplitude. At each Mach number, drive frequency, and amplitude combination, the mean angle of attack was varied through a pitch-and-pause sequence at 2.5° increments. At each angle of attack, the model was oscillated for a duration of 1 to 3 seconds, depending on frequency, to ensure the minimum number of required cycles of stabilized data. No drag data was acquired for the oscillatory runs.

Acceleration Tares. At the end of the test, acceleration tare measurements under zero wind condition were made to determine if some of the transducers were sensitive to the motions of the model. These measurements were carried out at nominal drive frequencies of 23, 46, 54, and 60 Hertz after taping over the

pressure orifices to eliminate whatever contribution to the measured loads could be due to airloads. The results of this test are tabulated in Volume II of this report.

The acceleration effects were found to be quite small. Most of the transducers registered some loads at approximately 185 Hz (8th harmonic of a 1/rev, 4th harmonic for 2/rev, but no clear trend for 3/rev). The magnitude of the measured acceleration tares ranged from less than 0.05 psi to 0.16 psi in the worst cases. Such loads are negligible. Since the oscillatory tests were run at high total pressures, the acceleration tares would be most significant at Mach numbers below M = 0.3. Inspection of the test data shows that pressure fluctuations, when present, appeared most often at low mean angles of attack, and that as the mean incidence was increased such fluctuations vanished.

Acoustic-Resonance Check. After the transducers were installed into the model and connected to the surface pressure orifices, each pressure orifice was tested to determine the acoustic resonance frequency of the tubing and transducer cavity. The results of the resonance tests are presented in Volume II. The lowest measured resonance frequency was approximately 2400 Hz, well in excess of the minimum 1000 Hz requirement.

TEST CONDITIONS

The static test conditions are summarized in Table III. The oscillatory conditions are in Table IV. A more detailed summary is shown in Volume II together with listings of pressures and integrated loads.

During the present tests, data for approximately four hundred (400) oscillatory test conditions have been acquired and processed through the complete data-reduction path. The test conditions were all within the following range of values:

- Mach number, M $0.2 \leq M \leq 0.7$
- Drive frequency, f_D 23 Hz to 90 Hz
- Mean angle of attack, α_o $0° \leq \alpha \leq 20.0°$
- Amplitude of oscillation, $\Delta\alpha$ $2.5° \leq \Delta\alpha \leq 10.0°$ (nominal)
- Tunnel total pressure, P_T $1.7 \times 10^5 N/m^2 \leq P_T \leq 5.2 \times 10^6 N/m^2$

For each test condition, twenty cycles of data were processed and averaged. As the data sampling rate during the analog to digital conversion varied with drive frequency, the total number of data samples ranged from approximately 47,000 points per test condition at 23 Hz to 20,000 points at 69 Hz.

PRESENTATION OF RESULTS

	Figure No.
Quasi-Steady Data	
Oil flow visualization photographs	5,6
Lift, drag and pitching-moment coefficients in presence of 4.9% floor and ceiling porosity	8
Lift and pitching-moment coefficients in presence of solid floor and ceiling (0%, porosity)	9
Effect of floor and ceiling porosity	10
Comparison with predicted characteristics	11
Comparison with other airfoils	12
Effect of Reynolds number variation	13
Oscillatory Data	
Effect of mean angle of attack, αo	14 to 23
Effect of Mach number, M	24 to 34
Effect of drive frequency, f_D	35 to 43
Effect of oscillatory amplitude, $\Delta\alpha$	44 to 48
Effect of Reynolds number, Rn	49 to 53
Comparison of maximum normal-force boundaries	54 to 56
Aerodynamic damping	57 to 60
Gamma functions	61 to 62

Volume II of this report lists all the oscillatory data in the form of harmonic coefficients up to the ninth harmonic. The plots of both pressures and integrated data have been generated on an automatic plotter with data reconstituted from harmonics. Only a limited number of plots are included in the report to illustrate the most significant trends in the data.

Some key parameters and coefficients used in discussing the oscillatory data are reviewed in Appendix B.

DISCUSSION OF RESULTS

Quasi-Steady Data

The normal-force, drag, and pitching-moment data acquired in presence of porous floor and ceiling in the test section are shown in figure 8. The data at Mach numbers below M = 0.5 were acquired before one of the trailing edge pressure transducers was replaced. The deletion of the pressure information from such transducers caused a small error in the integrated normal-force and pitching-moment values. The normal-force and pitching-moment coefficients affected by the omission of pressure data are shown with a dashed line. The data acquired in presence of solid floor and ceiling in the test section are shown in figure 9. All transducers operated normally during this phase of the test.

Figure 10 compares normal-force and pitching-moment data to illustrate the effect of porosity at M = 0.4 and M = 0.7. At the lower Mach number the porosity causes a small reduction in the angle of zero lift ($\Delta\alpha \approx 0.2°$) and a reduction in lift-curve slope, which results in a change in stall angle. The maximum normal force and the stall character were not affected. The difference in pitching-moment levels at M = 0.4 is mostly attributable to the deletion of a trailing-edge pressure, which prevented the measurement of some of the nose-up compensation designed into the trailing edge of the NLR 7223-62 airfoil. The data at M = 0.7 show no change in the angle for zero lift and virtually no change in the zero-lift pitching moment as a function of porosity/ this is a consequence of the fact that all transducers were operating normally.

The changes in lift-curve slope, pitching-moment slope, and stall characteristics are small but more significant than for the lower Mach number case. Operation at Mach numbers above M = 0.7 with solid floor and ceiling in the BSWT test section is not recommended. Quasi-steady data with a solid floor and ceiling was acquired to establish the baseline for the oscillatory data.

A listing of the static data, presented in Volume II, includes: the flow conditions, the angle of attack, differential pressure coefficients for each transducer, integrated loads and, in a limited number of cases, drag coefficients from wake momentum loss measurements.

Review of Quasi-Steady Data

Comparison with Predicted Performance. The measured maximum lift boundary agrees with the predictions[9] at Mach numbers below M = 0.4. Above M = 0.4, the lifting capability of the NLR 7223-62 was lower than expected by approximately

$\Delta C_{\ell_{MAX}} = 0.15$, which indicates that the airfoil did not take advantage of the beneficial shock/boundary-layer interaction effects described in reference 8. The maximum lift boundaries from test and theory are compared in figure 11.

The drag levels measured in this test were generally higher than predicted, as illustrated in figure 11. The turbulence in the test section has been measured at levels below 0.5% for Mach numbers between 0.3 and 0.5, but the drag of any section tested in this facility has been consistently conservative, particularly so for sections with the potential for extensive laminar boundary layer, such as the NASA 64A-series airfoils reported in reference 7. The difference between the drag measured in BSWT and in other test facilities can be as much as $\Delta C_d = 0.0015$.

Finally, the measured zero-lift pitching moment of the NLR 7223-62 at low speeds was $C_{m_o} = -0.02$. The potential flow value is $C_{m_o} = -0.01$. This is due in part to the fact that viscous effects reduce the effectiveness of the lower surface curvature as a pitching moment compensation device, but part of the discrepancy could be reduced by increasing the number of pressure pickups in the trailing edge region.

Comparison with Other Rotor Airfoils. Table V and figure 12 compare the aerodynamic characteristics of the NLR 7223-62 with other helicopter airfoils tested in the same wind-tunnel facility. The NLR section compared favorably with other airfoil sections at Mach numbers above M = 0.6: its excellent Mach number penetration (i.e., high drag divergence Mach number boundary) would make it a good rotor-tip section, in conjunction with an inboard airfoil with additional thickness to increase the maximum lift capability at M = 0.4.

Reynolds Number Effects. Figure 13 shows data at M = 0.4 and M = 0.6 taken at the extremes of the total pressure capability of the wind tunnel: $P_T = 1.7 \times 10^5$ N/m^2 to 5.2×10^5 N/m^2 (25 psi to 75 psi). The change in Reynolds number associated with such total pressure excursion, $Rn = 2.3 \times 10^6$ to 7.1×10^6 at M = 0.4, and $Rn = 3.1 \times 10^6$ to 9.1×10^6 at M = 0.6, caused:

1) A change in stall character and stall angle for both normal force and pitching moment at M = 0.4, with negligible reduction in the maximum normal-force coefficient.

2) A reduction in the maximum normal force from $C_{n_{MAX}} = 1.0$ to 0.94 with decreasing Reynolds number, but no significant change in stall character, at M = 0.6.

3) No systematic changes in lift-curve slope. (An 8.3% increase at M = 0.4 vs 5.7% decrease at M = 0.6 for the Reynolds number excursions in figure 13).

Oscillatory Data

Since the overall effect of variations in angle of attack, Mach number, frequency and amplitude of oscillation are well understood (references 4 and 5), such effects will be only briefly reviewed as necessary. The discussion will be focused on the characteristics of the NLR 7223-62 with emphasis on the dynamic stall effects at M = 0.4, since the flow phenomena at M = 0.4 are particularly significant in understanding retreating blade stall on helicopter rotors in forward flight. A direct comparison with other airfoil sections will be made on the basis of aerodynamic damping and maximum normal-force characteristics.

Mean Angle-of-Attack Variation. The test conditions selected illustrate the development of dynamic stall with increasing incidence range from M = 0.4 to 0.7, with nominal amplitude of oscillation $\Delta\alpha = 5.0°$. The data in figures 14 through 23 cover the dynamic stall effects related to the 1/rev rotor mode, equivalent to a drive frequency of 23.0 Hz for the 0.162m model chord.

In the hysteresis loop plots, an asterisk marks the nominal start of the cycle of oscillation, corresponding to $\theta = 0.0°$. At $\theta = 0.0°$ the net angle of attack is close to the mean value α_o, and $\partial\alpha/\partial t$ is at its largest positive value.

Normal-force and pitching-moment hysteresis loops over a representative mean angle-of-attack range at Mach numbers from M = 0.4 to 0.7 are shown in figures 14, 16, 18 and 20. The hysteresis loops at M = 0.4 are overlaid in figure 23.

At all Mach numbers, the NLR data show that the pitching-moment stall angles are lower than the lift-stall angles. This is generally true with any airfoil for both static and dynamic conditions. Figures 14 through 20 show that as the mean angle of attack is increased from levels for which no separation is present to conditions displaying dynamic stall, the normal-force loop reverses in direction and the recovery from stall takes place at levels below the unstalled values.

As already observed in the quasi-steady data, figures 8c and 9b, the pitching moment coefficients of the NLR 7223-62 display a nose-up shift before stall. This shift is present both during dynamic stall and during recovery from stall, and it appears to give rise to more positive damping on the NLR airfoil than on conventional sections such as the V0012 or the V23010-1.58 (figure 60).

The mechanism of stall is shown in more detail in the differential pressure time histories. When dynamic stall is present, most of the pressures display an abrupt reduction while the

angle of attack is still increasing (positive α) for $270° < \theta < 90°$. Over the other half of the cycle the angle of attack is decreasing (negative $\dot{\alpha}$) and this is always associated with a reduction in lift and a drop in surface pressure levels. An exception to this is possible if stall occurs with $\alpha > 0$ and the flow reattaches when the incidence is again sufficiently low, but before reaching the minimum angle-of-attack condition (at $\theta = 270°$). In this case some of the pressure coefficients can grow to high levels while α is negative and before the incidence reaches the minimum value in the cycle without giving rise to a multiple stall event. This can be observed on transducers 1 through 4 in figures 17a and 17c. The phenomenon becomes considerably less pronounced at Mach numbers above $M = 0.5$ when compressibility effects start to dominate the flow. Some signs of secondary stall can be observed in figures 15d and 17b at $\theta \approx 90°$.

The propagation of stall from the leading edge to the trailing edge becomes less clear at higher Mach numbers, $M > 0.5$. Although the event is no less discrete, the differential pressure instrumentation hides the true magnitude of the upper surface pressures; this gives the impression that the pressure peak first moves forward and then back again towards the trailing edge (e.g., figure 19b). At higher Mach numbers, the separation turns from "velocity gradient induced" to "shock induced" as a local supersonic region builds up near the leading edge. Figures 21a through 21d illustrate this phenomenon. Figure 22 shows selected chordwise pressure distributions to help in visualizing how pressures collapse downstream of the shock. A larger number of transducers would be necessary to define more clearly the recompression boundary.

One last point of interest is the occasional appearance of pressure fluctuations with a high (7th to 8th) harmonic content. These fluctuations, when present, are strongest near the trailing edge. The best example within the set of conditions discussed in this section is in figures 16b and 17b, Test Point 12035.4, for $M = 0.5$ and $\alpha_0 = 7.5°$. The effect of such fluctuations is particularly visible in the pitching moment hysteresis loop of figure 16b and in the pressure time histories of figure 17b. At angles of attack preceding and following this condition, fluctuations of this kind were not detected, which probably eliminates an elastic response of the model, as it will be discussed later. In figure 17b higher harmonic fluctuations are also present on transducer 5 ($x/c = 0.074$) over a part of the cycle, possibly indicating the presence of a small separated region near the leading edge. Wind-off acceleration tares were obtained at the end of the test, but they had a negligible effect when applied to the data (Volume II).

Mach Number Variation. Compressibility effects on the dynamic stall characteristics of the NLR airfoil are illustrated in

figures 24 through 34 for a drive frequency of 23.0 Hz and at 5.0° and 10.0° nominal amplitudes of oscillation. Overlays of the pressures measured by the 0.01c transducer (ΔCp1) are shown in figures 26, 29 and 34. Normal-force and pitching-moment hysteresis loops are overlaid in figure 33.

Figures 24, 27 and 30 illustrate the progressive reduction in stall angle and the changes in normal-force and pitching-moment stall hysteresis associated with increasing compressibility effects for freestream Mach numbers ranging from M = 0.2 to M = 0.7. At M = 0.3, figures 27 and 30 for the 5.0° and 10.0° pitch amplitudes, normal force and pitching-moment stall take place almost simultaneously at α_{max}, ($\theta \simeq 90°$, and $\dot{\alpha} \simeq 0$). The pressure time histories in figures 28b and 31b show that such stall events start at the leading edge at approximately $\theta = 60°$, and that the wave associated with separation reaches the trailing edge at $\theta \simeq 120°$ when $\dot{\alpha}$ is already negative. With increasing Mach number, the collapse in leading edge pressures occurs at lower angles of attack and earlier in the cycle, and the pressure wave reaches the trailing edge while $\dot{\alpha}$ is still positive. This earlier occurrence of the stall is also due to the decrease in reduced frequency associated with the increased Mach number, since the drive frequency in this particular set of conditions was kept constant.

At M = 0.6 and M = 0.7 some of the transducers over the front half of the airfoil display an abrupt loss in pressure associated with the appearance of a recompression shock. This has already been shown in figures 21 and 22. Figure 22 displays this in the more familiar form of chordwise pressure distributions at different positions during a cycle of oscillation. The collapse in the pressures is generally more pronounced aft of 0.05c and it does not extend beyond 0.30c to 0.40c for the conditions shown in figures 25, 28 and 31 (e,f). However, an evaluation of the onset of stall (whether shock or boundary layer induced) and stall progression from the leading edge is hampered by the measurement technique employed in this test. Since the pressure data were obtained by measuring the difference between upper and lower surface pressures, it is not possible to separate the pressure level on each surface and thus correlate the conditions for stall through local Mach number considerations.

Pressure Fluctuations. The pressure time histories and pitching-moment hysteresis plots in figures 16 through 28 show higher harmonic fluctuations occurring, apparently at random, throughout the test. Some acceleration sensitivity beyond the measured levels cannot be ruled out since the acceleration tares were acquired in a wind-off condition only, thus not allowing for air induced airfoil motions. However, since the tare values measured were quite small, it is unlikely that any significant fluctuations could be attributed to small airfoil motions in response to the airloads. The most probable cause of the

pressure fluctuations measured in this test is from the vorticity shed as a consequence of cyclic changes in circulation. It is quite probable that a wake system with a harmonic content higher than the first or second harmonic could be established due to:

1) The size of the separated region at the trailing edge of the model (a Strouhal number effect).

2) Pressure waves due to the collapse in leading edge pressures during stall, propagating from the leading edge to the trailing edge.

Since separation phenomena are strongly three-dimensional, it is unclear what role, if any, the span-to-chord ratio of the model has in the establishment of higher harmonic vorticity in the wake, and it is equally unclear whether such higher harmonics would be present in the wake along a helicopter rotor blade in flight.

Drive Frequency Variation. There are two main effects associated with drive frequency changes when all other conditions are kept constant. One is a progressive delay in the occurrence of dynamic stall, and the other is an increase in load excursions, both illustrated in the overlay of normal-force and pitching moment hysteresis loops in figures 37 and 40a (5.0° and 10.0° pitch amplitudes, respectively). Individual hysteresis loops are presented in figures 35 and 38. The corresponding pressure time history plots are shown in figures 36 and 39. Figure 40b shows selected pressure distributions at stall overlaid at constant values of the reference angle, θ, to illustrate the effect of drive-frequency variation on chordwise loading.

A complete history of the pressure distributions at $\Delta\theta = 20°$ intervals for the 23.0 Hz, 46.0 Hz and 70.0 Hz drive frequencies is presented in figures 41, 42 and 43. It should be noted that the trailing edge transducer, ΔCp 17, failed during the 70.0 Hz test run.

Pitch Amplitude Variation. The trends observed in conjunction with amplitude changes are similar to those observed for frequency changes, at least to the extent that the delay in dynamic stall is a function of the increase in the rate of change in angle of attack, $\dot{\alpha}$. Figures 44 and 45 show the effect of amplitude variation at $M = 0.4$ and 23.0 Hz. Figures 46 and 47 show data taken at $M = 0.4$ and 70.0 Hz. The conditions were matched on the basis of the maximum angle of attack reached during oscillation. This maximum angle is 15.0° for both frequencies.

Figure 44 shows that the growth in pitching moments after stall is a function of pitch amplitude, so that the larger angle of attack excursions result in more severe nose-down pitching

moment. The recovery from stall is followed by a pitching moment shift in the nose-up (positive) direction which overshoots the quasi-steady level by an amount which also increases with increasing amplitude.

At the higher frequency, shown in figure 46, the pitching moment level after stall is not a function of amplitude, although the nose-up excursions after recovery grow with increasing $\Delta\alpha$. The 70.0 Hz data experience more substantial stall delay effects than the 23 Hz data, which explains why the after-stall excursions in pitching moments were reduced with increasing frequency in a constant α_{MAX} comparison. The hysteresis loops for the two frequencies are overlaid in figure 48. The details of the stall development can be observed in the pressure time histories in figures 45 and 47.

Reynolds Number Effects. Reynolds number excursions in the subsonic test section of BSWT are achieved by varying the tunnel total pressure. The range in Reynolds number is from 2.4×10^6 to 7.0×10^6 at M = 0.4, and from 3.1×10^6 to 9.0×10^6 at M = 0.6, with the 0.162m model chord. The Reynolds number variation within the range of present data is not sufficient to show large effects; however, the data display variations in the character of stall which will be valuable in understanding scale effects in unsteady flow, since the assessment of such effects is crucial in the interpretation of model rotor data. At present, the correlation between model and full scale data is carried out from trends between wind tunnel and flight test data, without an insight into the details of the rotor flow environment. Typically, model rotors vary in size from 1/5 to 1/10 of full scale, while the data from this test ranges within a factor of three from the lowest to the highest Reynolds number value at constant Mach number.

Typical trends in dynamic stall variation with Reynolds number at M = 0.4 and M = 0.6 are shown in figures 49 through 53. The single major effect to be observed is in the stall behavior of the pitching moment at M = 0.4. Figure 49 shows that by increasing the Reynolds number from 2.4×10^6 to 7.0×10^6 for 1/rev pitch oscillations at M = 0.4, the dynamic stall angle for the pitching moment increases from 12.0° to 12.5°. The static stall angle, however, changes from 9.0° to 11.5° over the same Reynolds number range, indicating that more significant dynamic stall-delay effects take place at the lower Reynolds numbers. Similar, although less pronounced effects, can be observed for the normal force. This effect is a clue to the difficulty in correlating model and full scale rotor data since, until now, dynamic stall-delay effects were assumed to be independent of Reynolds number.

Fluctuations during stall recovery are also reduced with increasing Reynolds number. The pressure time histories in

figures 50a through 50d display significant differences only at the lowest Reynolds number (figure 50a). In this case, the pressures collapse abruptly downstream of the 0.03c station. At the higher Reynolds numbers, the collapse in leading edge pressures is followed by a more gradual pressure loss along the airfoil, which indicates that at Rn = 2.3 x 10^6 the flow was more severely separated, as confirmed by the pitching moment hysteresis loop in figure 49a. Similar but less abrupt variations can be observed in figures 51 and 52 for M = 0.6. The pressure distributions in figure 53 provide additional insight downstream of the 0.03c station for the M = 0.6, Rn = 3.1 x 10^6 condition.

Maximum Normal-Force Boundaries. The maximum normal force coefficient attainable during forced pitch oscillation is a measure of the potential benefits an airfoil can gain from unsteady aerodynamic effects over its quasi-steady performance level. As it is the case for steady flow, the maximum normal-force boundary of an airfoil in forced pitch oscillation is strongly influenced by compressibility, which reduces the large stall delay effects observed at Mach numbers below M = 0.4.

Figure 54 summarizes the maximum attainable normal force coefficients of the NLR 7223-62 airfoil for all the oscillatory conditions with 5.0° amplitude of oscillation. Figures 55 and 56 compare the maximum normal-force boundaries of the NLR airfoil with the boundaries of other sections tested in the same oscillatory rig, and reported in references 4 and 5.

Unsteady flow effects do not cause a comparatively large increase in the normal-force boundary of the NLR airfoil. At M = 0.4 and at low frequencies, figure 55, the NLR section appears not to benefit of dynamic stall delay as much as the V0012 and V23010-1.58 airfoils, but its lifting capability improves at higher frequencies. At M = 0.6, figure 56, the NLR section takes advantage of its favorable transonic characteristics and it displays significant stall delay at all frequencies, showing a definite improvement over the V0012 and V23010-1.58. Such improvement, however, does not occur at a condition useful on existing rotor systems. Stall delay effects are important only at Mach numbers between M = 0.3 and M = 0.5.

Aerodynamic Damping. Aerodynamic damping values have been nondimensionalized by the theoretical damping, as described in Appendix B. Figures 57, 58 and 59 summarize the major effects of Mach number, drive frequency and amplitude of oscillation on the damping characteristics of the NLR 7223-62 airfoil. Figure 60 compares the NLR section to other airfoils tested in the same facility at M = 0.4 with pitch amplitude $\Delta\alpha$ = 5.0°.

Figure 57 shows the effect of compressibility on the aerodynamic damping of the NLR airfoil. As observed during the oscillatroy tests of references 4 and 5, an increase in Mach number from low to high subsonic levels causes the aerodynamic damping to grow positive. At Mach numbers below 0.4 negative damping during oscillation is consistently associated with the tendency of a section to stall statically from the leading edge. Quasi-steady thin airfoil stall and trailing edge stall are associated with positively damped oscillatory conditions at the lower (reduced) frequencies of interest on helicopter main rotors. As shown in figure 9a, the NLR 7223-62 displays leading edge stall at M = 0.2 and progressively more gentle stall characteristics at higher Mach numbers, which is in qualitative agreement with the aerodynamic damping trends of figure 57.

As illustrated in figure 58, increasing the drive frequency caused a shift of the damping of the NLR airfoil section to negative values. Increasing amplitude had little effect, figure 59.

In figure 60, the NLR 7223-62 is compared to other rotor airfoils from references 4 and 5. This shows that at M = 0.4 and at a frequency of oscillation corresponding to the 1/rev rotor regime the thin airfoils (t/c = 0.06) are strongly positively damped, while the thick sections (t/c = 0.10 and 0.12) are negatively damped. The NLR airfoil, which is 8.6% thick, falls somewhere in the middle, and the fact that its damping stays positive throughout the angle of attack range is a favorable consideration in comparing it to other helicopter rotor sections.

Gamma Functions. One way to correlate the dynamic stall characteristics of several airfoils is to use the "gamma function" approach of reference 1. This parameter is a relationship between the angle for stall of either normal force or pitching moment and the rate of change in angle of attack at the time stall takes place. Figure 61 shows how static and dynamic stall angles can be plotted against a $\sqrt{b\dot{\alpha}/V}$ parameter. The rate of change of the stall angle with such parameter has been called "gamma function". The quantity γ is different for the normal force and the pitching moment and it decreases in magnitude with increasing Mach number. "γ" functions for the NLR 7223-62 airfoil and other sections are shown in figure 62.

CONCLUSIONS AND RECOMMENDATIONS

1) The NLR 7223-62 airfoil has excellent high speed characteristics as evidenced by a zero-lift drag divergence Mach number $M_{DD_O} = 0.85$, but it does not have a high lift capability at Mach numbers between M = 0.3 and M = 0.5.

2) No unusual dynamic stall delay effects have been observed at Mach numbers below M = 0.6. However, the stall delay parameter for lift at M = 0.7 appears to be large compared to the level of other airfoils tested in the same facility.

3) The quarter-chord pitching moment data show a nose-up trend at positive lift levels due to an unusually forward aerodynamic center position ($x/c_{a.c.} = 0.235$ at $M < 0.3$). Such shift is due to the lower surface trailing edge shape.

4) At M = 0.4, the NLR 7223-62 airfoil displays gradual-stall characteristics in quasi-steady flow and positive damping for 1/rev and 2/rev oscillations at pitch amplitudes ranging from 2.5° to 10.0°.

5) The drag data in this test did not verify the predicted levels because of the turbulence level in the test section.

6) At a Mach number of 0.4, decreases in Reynolds number produce significant decreases in the static-stall angle of attack for pitching moment. The dynamic stall loops however, for both pitching moment and normal force coefficients appear to be relatively unaffected by Reynolds number variation. It is recommended that scale effects on stall delay be reviewed in detail with all the data available in Volume II of this report, and that such stall delay trends be applied to whatever airfoil data would be necessary to carry out model/full scale rotor correlation studies. It would be also useful to conduct a model-rotor test employing the NLR 7223-62 to correlate with the flight test data being acquired at NASA/Langley.

7) It is also recommended that normal force, pitching moment and pressure data from this test be examined a) to understand the detailed mechanism of dynamic stall over the Mach number range from M = 0.2 to M = 0.7 and, b) to define

a more accurate stall delay representation method for use in conjunction with rotor performance prediction analyses. This should be approached by means of a diagnostic computer analysis to sample the data for each oscillating test condition of interest and make a systematic record of single/multiple stall events, chordwise stall progression, and other parameters of interest.

TABLE I. SUMMARY OF MODEL CHARACTERISTICS

Airfoil Section	NLR 7223-62 (or NLR-1)
Model Span	0.3048m (12 inches, nominal)
Model Scale	1/4.23, based on a 0.686m (2.25 ft) full-scale blade chord
Model Chord	0.162m (6.38 in.)
Thickness Ratio	8.6 percent
Construction	Machined from Maraging Steel
Transducers:	
Type	Kulite Model No. 63-11967, Differential
Number Installed	17
Location in Percent Chord	1.01, 1.99, 3.0, 4.91, 7.37, 9.91, 14.93, 19.99, 24.97, 29.98, 39.91, 50.07, 60.05, 70.09, 80.02, 89.96, 96.91
Pressure Range	$\pm$ 5.17x10^5 N/m^2 ($\pm$ 75 psi) from 1 to 5 percent chord
	$\pm$ 3.45x10^5 N/m^2 ($\pm$ 50 psi) from 7.5 to 97 percent chord
Minimum Natural Frequency as Installed	2,800 Hz

NLR 7223-62

TABLE II. NOMINAL AIRFOIL CONTOUR COORDINATES

X/C	Y/C	X/C	Y/C	X/C	Y/C	X/C	Y/C
0.0	0.0	0.28701	0.05465	0.0	0.0	0.31696	-0.03043
0.00125	0.00617	0.30211	0.05486	0.00054	-0.00251	0.34904	-0.03083
0.00416	0.01023	0.31722	0.05501	0.00118	-0.00363	0.38098	-0.03107
0.00978	0.01508	0.33421	0.05512	0.00265	-0.00520	0.41307	-0.03115
0.01748	0.02005	0.34814	0.05516	0.00450	-0.00641	0.44726	-0.03106
0.02729	0.02515	0.36513	0.05514	0.00730	-0.00765	0.48125	-0.03078
0.03956	0.03017	0.38024	0.05508	0.00992	-0.00860	0.51389	-0.03030
0.04498	0.03207	0.39533	0.05497	0.01334	-0.00964	0.54720	-0.02959
0.05219	0.03435	0.41232	0.05478	0.01749	-0.01072	0.58067	-0.02861
0.05969	0.03648	0.42929	0.05455	0.02181	-0.01170	0.61492	-0.02754
0.06728	0.03842	0.44628	0.05425	0.02769	-0.01286	0.64771	-0.02638
0.07672	0.04057	0.46137	0.05394	0.03500	-0.01411	0.67813	-0.02512
0.08617	0.04243	0.47976	0.05351	0.03938	-0.01477	0.70940	-0.02375
0.08977	0.04307	0.49485	0.05310	0.04638	-0.01573	0.74105	-0.02238
0.09217	0.04346	0.51353	0.05254	0.05274	-0.01654	0.76943	-0.02097
0.09337	0.04365	0.53239	0.05189	0.06154	-0.01754	0.79937	-0.01947
0.09457	0.04384	0.54748	0.05133	0.06978	-0.01840	0.82514	-0.01805
0.09577	0.04401	0.56635	0.05055	0.07732	-0.01913	0.85298	-0.01653
0.09766	0.04428	0.58091	0.04991	0.08778	-0.02008	0.87654	-0.01505
0.09955	0.04453	0.59600	0.04919	0.09531	-0.02072	0.90896	-0.01250
0.10145	0.04476	0.61263	0.04833	0.10662	-0.02162	0.94070	-0.00885
0.10522	0.04521	0.62960	0.04740	0.11645	-0.02234	0.97353	-0.00352
0.10901	0.04563	0.64741	0.04635	0.12776	-0.02313	0.98677	-0.00135
0.11493	0.04624	0.66250	0.04539	0.13908	-0.02387	0.99	-0.00092
0.11871	0.04662	0.67758	0.04438	0.15039	-0.02455		
0.12628	0.04730	0.71085	0.04192	0.16170	-0.02520		
0.13619	0.04815	0.73974	0.03909	0.17490	-0.02589		
0.14943	0.04915	0.76970	0.03505	0.18864	-0.02656		
0.16266	0.05004	0.79864	0.03053	0.20185	-0.02714		
0.17401	0.05074	0.82615	0.02614	0.21505	-0.02768		
0.18724	0.05146	0.85176	0.02196	0.22825	-0.02817		
0.20093	0.05212	0.87705	0.01772	0.24145	-0.02862		
0.21605	0.05275	0.90954	0.01262	0.25655	-0.02908		
0.22738	0.05317	0.94056	0.00820	0.27168	-0.02949		
0.24162	0.05363	0.97405	0.00345	0.28678	-0.02985		
0.25673	0.05404	0.98674	0.00161				
0.27184	0.05438	0.99	0.00113				

Note: Model Truncated at c = 0.99

TABLE III. SUMMARY OF STATIC TEST CONDITIONS

Test: BSWT 567 Airfoil: NLR 7223-62

Floor and Ceiling With 4.9-Percent Porosity

M	Total Pressure (pascals x 10^{-3})							
	170	210	340	440	450	470	490	520
0.20		X		X				
0.30					X			
0.40						X		
0.50							X	
0.60	X		X					O
0.70								O
0.75								O
0.80								O
0.85								X
0.90	X		X					X

Solid Floor and Ceiling (Baseline for Oscillatory Data)

M	Total Pressure (pascals x 10^{-3})						
	170	340	440	450	470	490	520
0.20			X				
0.30				X			
0.40	X	X			X		X
0.50						X	
0.60	X	X					X
0.70							X

X Pressure Data
O Pressure and Drag Data

TABLE IV. SUMMARY OF OSCILLATORY CONDITIONS

$\Delta\alpha = 5^{o}$

Mach No.	Nominal Frequency (Hz)								
	23	46	69	92	40	50	52	53	54
0.2	X	X	X		X				
0.3	X	X	X						
0.4	X	X	X	X		X	X	X	X
0.5	X	X	X						
0.6	X	X	X						
0.7	X								

$\Delta\alpha = 2.5^{o}$

Mach No.	Nom Freq (Hz)		
	23	46	69
0.2	X		
0.3	X	X	X
0.4	X	X	X
0.5	X	X	X
0.6	X	X	X
0.7	X	X	X

$\Delta\alpha = 7.5^{o}$

Mach No.	Nom Freq (Hz)			
	23	46	69	40
0.2	X			X
0.3	X			
0.4	X	X		
0.5	X	X		
0.6	X			
0.7	X			

$\Delta\alpha = 10.0^{\circ}$

Mach No.	Nom Freq (Hz)			
	23	46	69	40
0.2	X			X
0.3	X			
0.4	X	X	X	
0.5	X			
0.6	X			
0.7	X			

Test: BSWT 567
Airfoil: NLR 7223-62

TABLE V - COMPARISON OF TWO-DIMENSIONAL AIRFOIL DATA

AIRFOIL	t/c	$C_{\ell_{MAX}}$ at			M_{DD} at $C_\ell=0$	C_d @ $C_\ell=0.6$ M-0.6	C_{m_o}
		M=0.3	M=0.4	M=0.5			
NLR 7223-62	0.086	1.27	1.10	1.08	0.85	0.008	-0.02
NACA 64A(4.5)08 (a = 0.8 mod)	0.080	----	1.23	1.15	0.752	0.007	-0.095
V(1.9)3009-1.25	0.09	1.315	1.225	1.12	0.815	0.0084	-0.012
VR-8 (0° Tab)	0.08	1.06	1.04	1.06	0.811	0.007	-0.011
VR-7 (0° Tab)	0.12	1.63	1.51	1.65	0.742	0.0081	-0.025
V23010-1.58 (0° Tab)	0.102	1.66	1.46	1.22	0.79	0.0108	-0.009

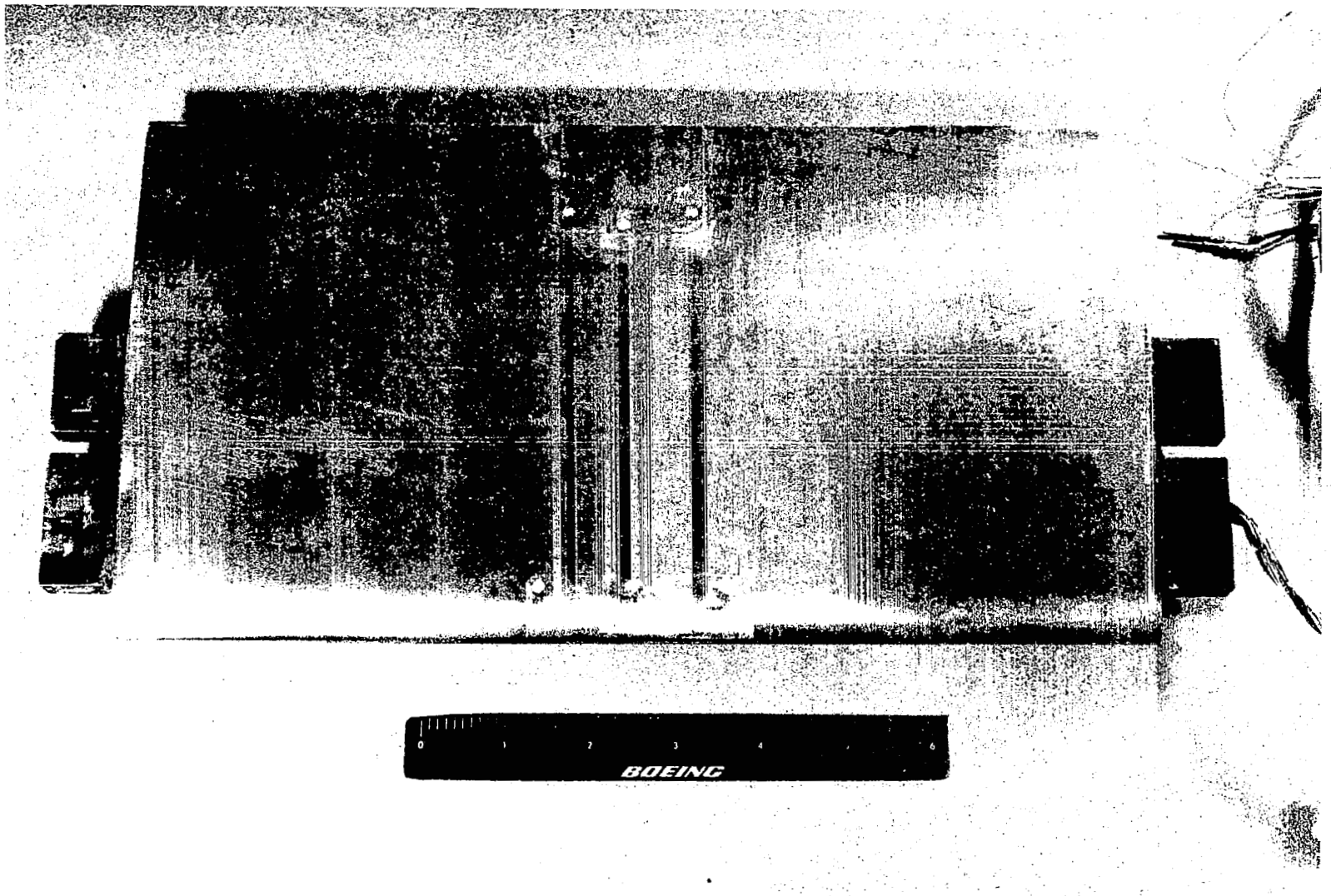

Figure 1. Airfoil model prior to installation in the test section.

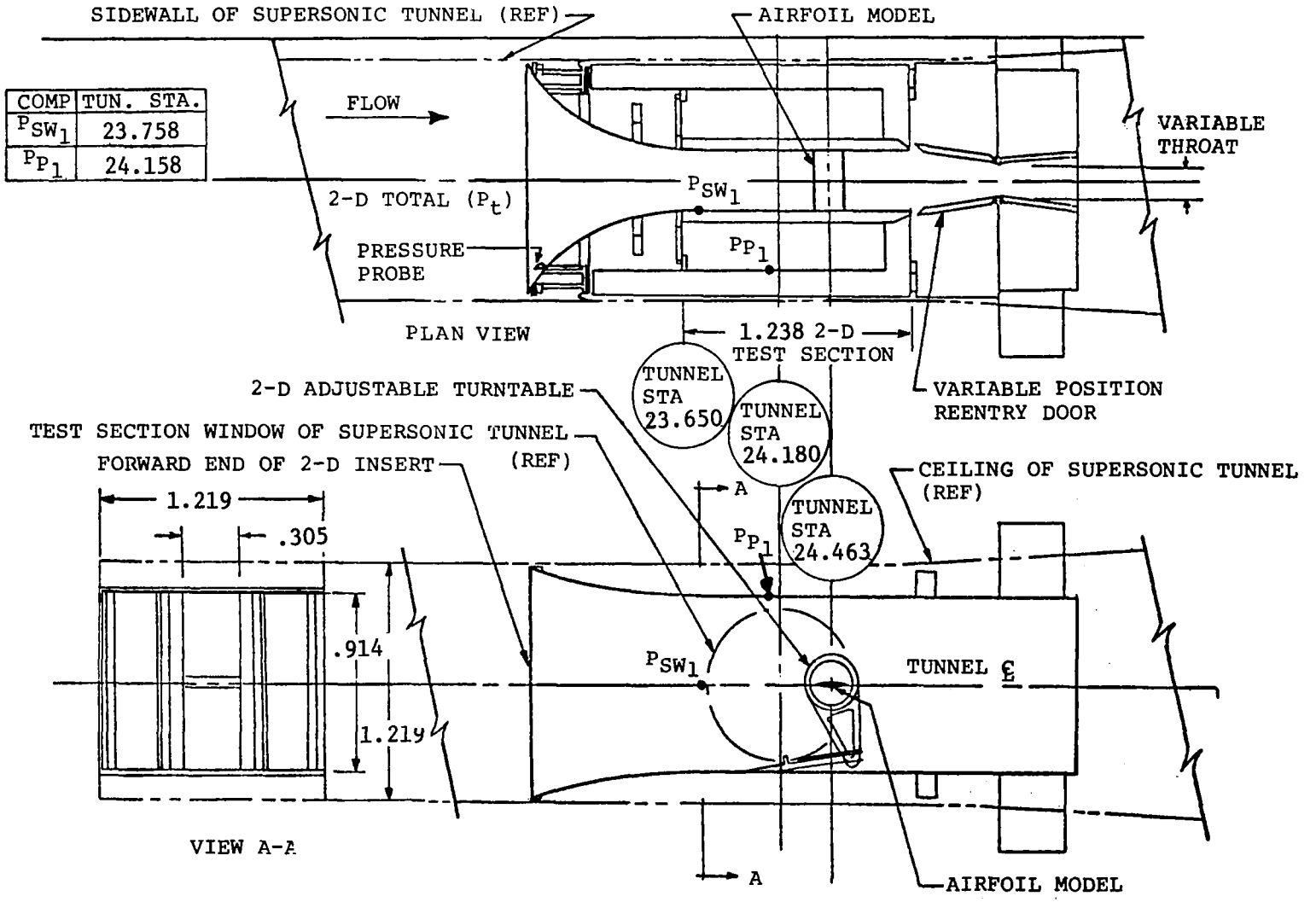

Figure 2. General arrangement for testing two-dimensional airfoils in the Boeing supersonic wind tunnel.

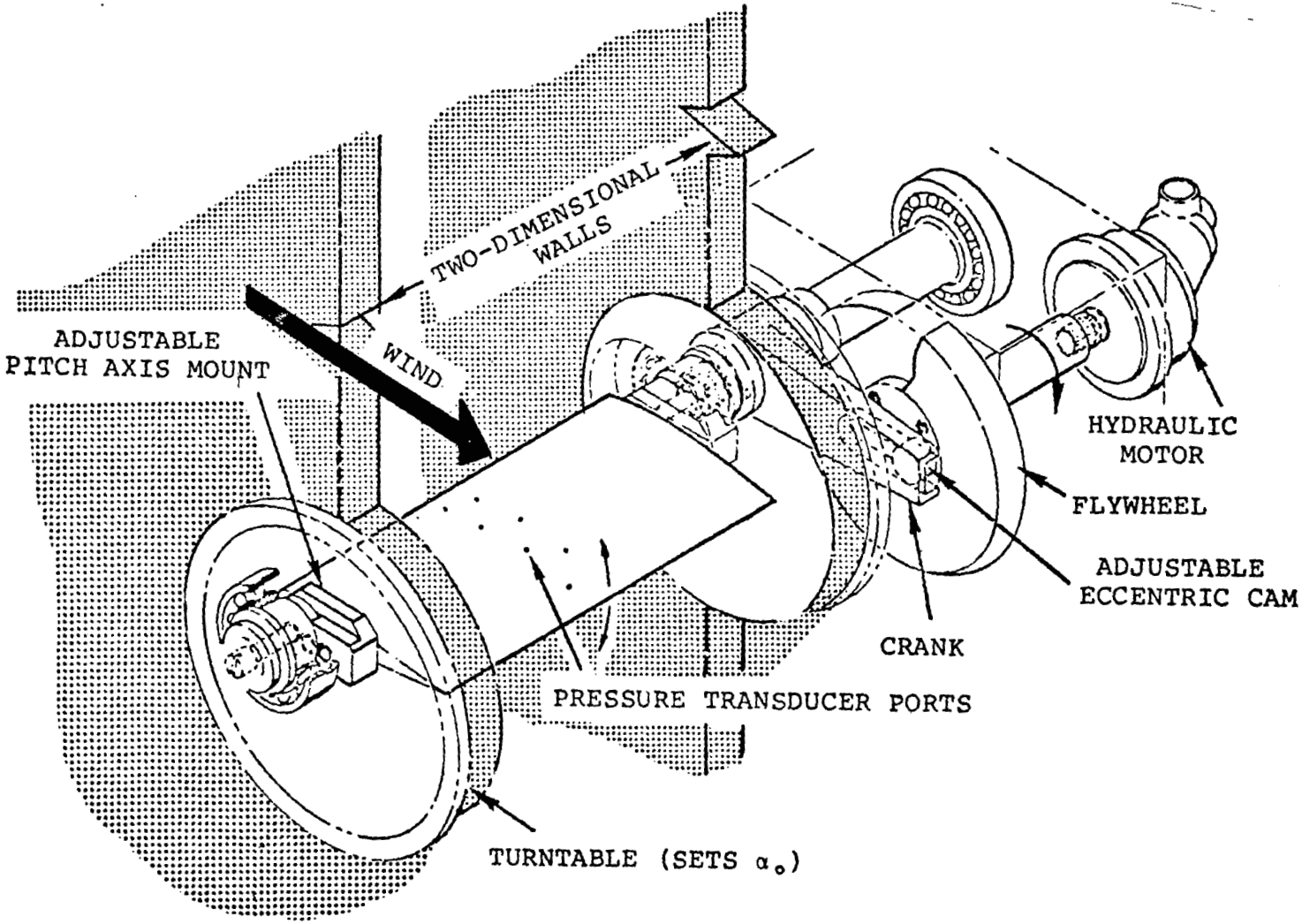

Figure 3. Pitch oscillation mechanism.

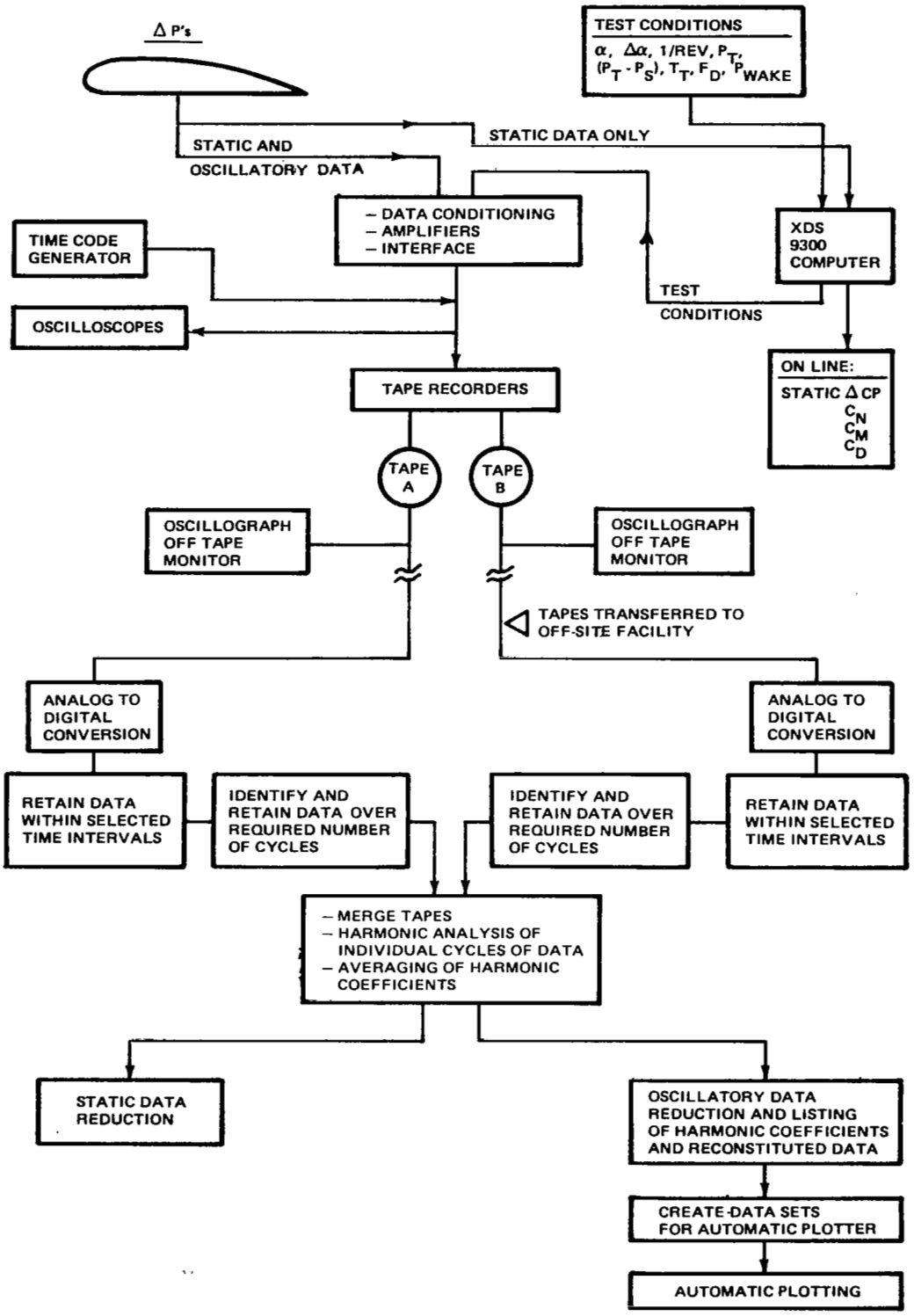

Figure 4. Data acquisition and reduction system.

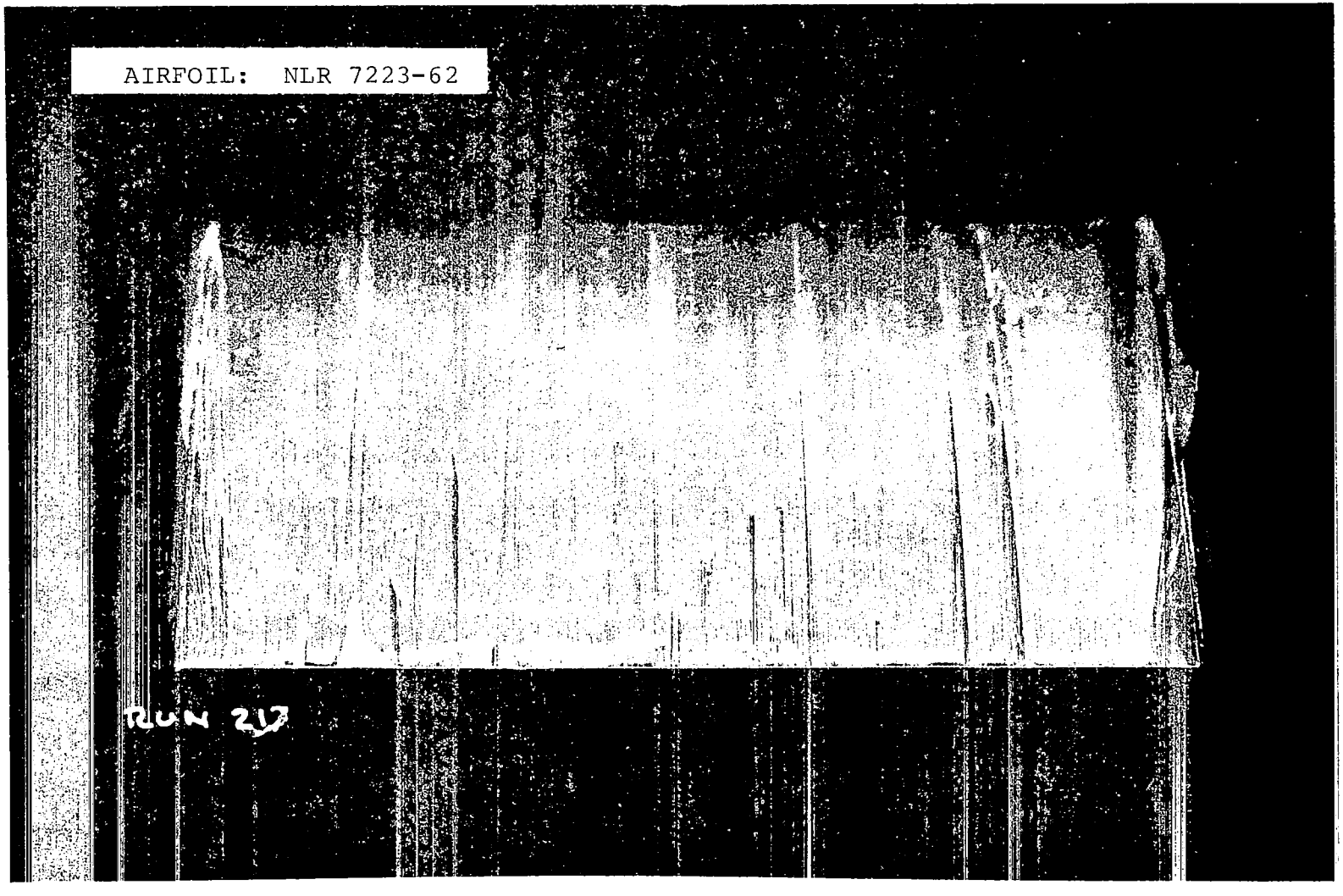

Figure 5. Oil flow visualization at M = 0.4, α = 6°. Upper surface.

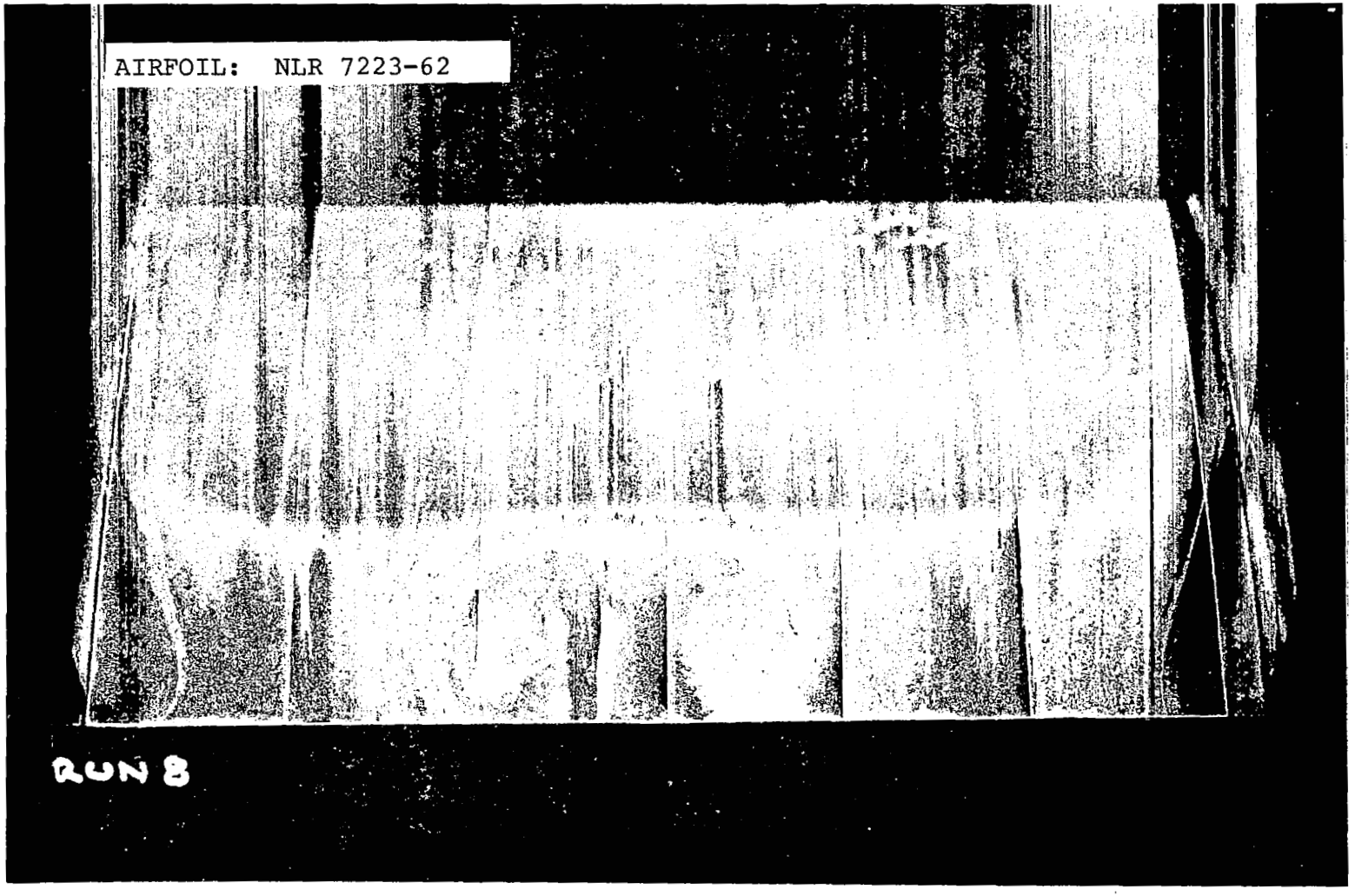

Figure 6. Oil flow visualization at M = 0.8, α = 2°. Upper surface.

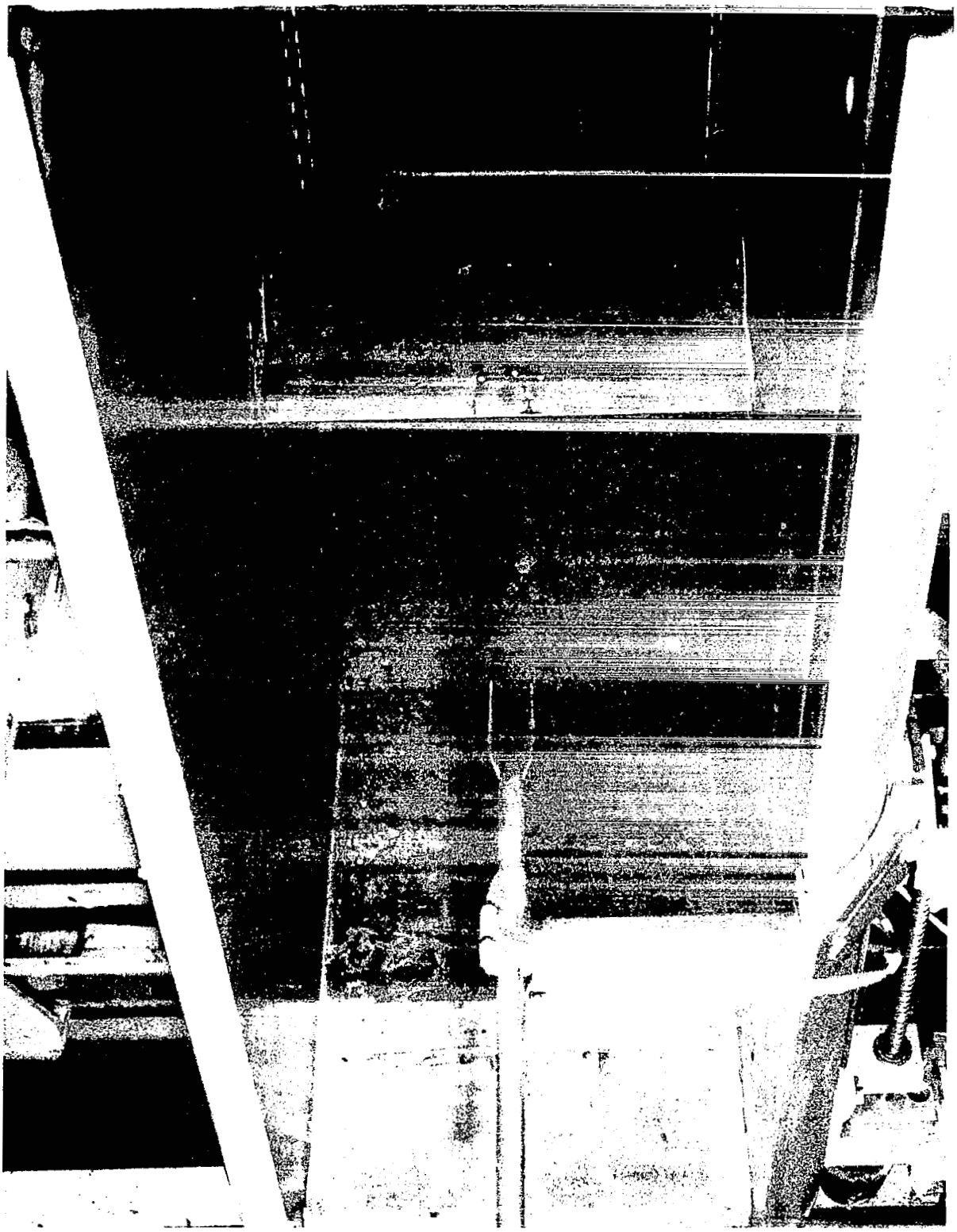

Figure 7. Installation of traversing wake probe for drag measurements.

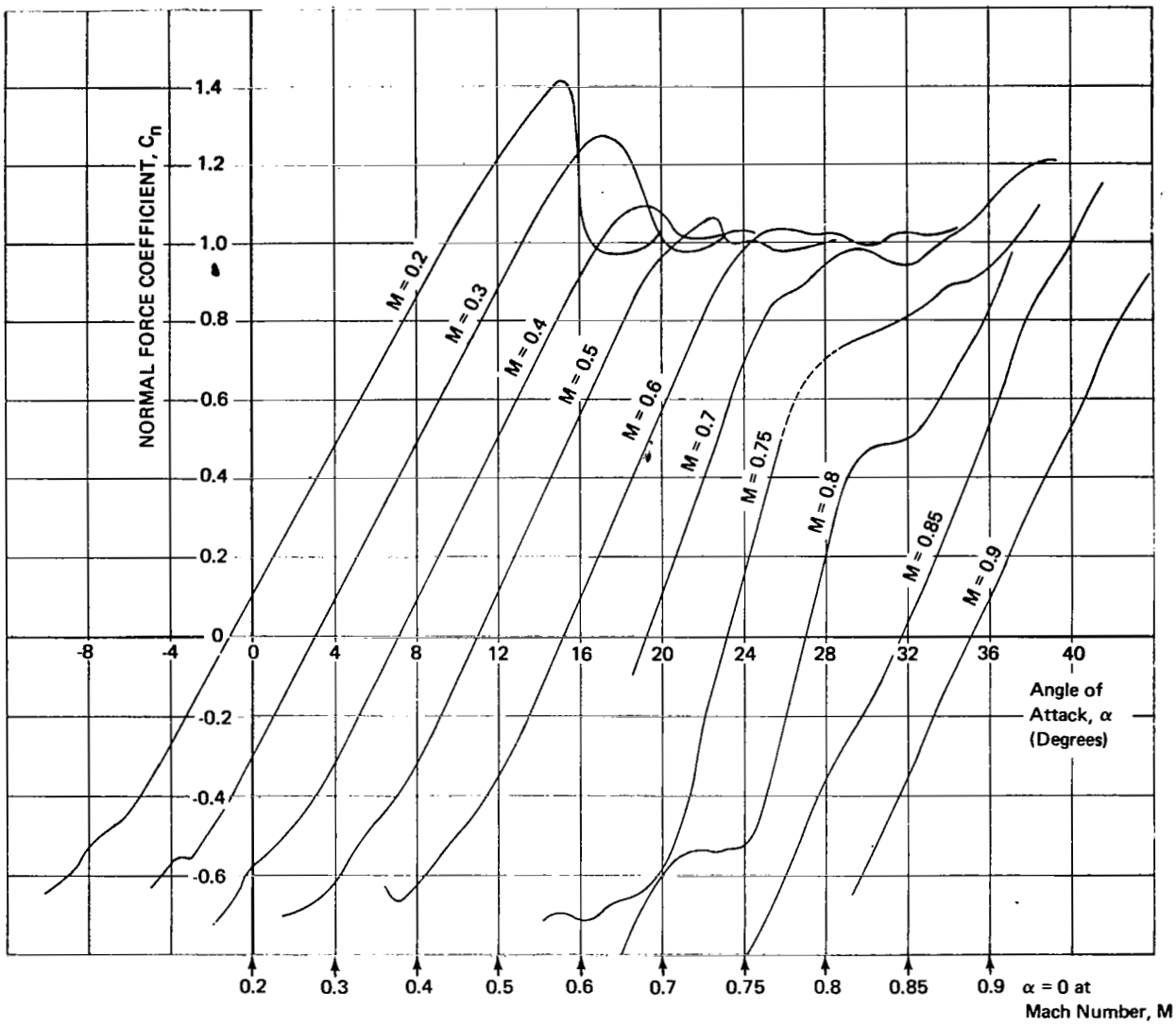

M	0.2	0.3	0.4	0.5	0.6	0.7	0.75	0.8	0.85	0.9
Re x 10^{-6}	3.2	4.8	6.4	7.9	9.4	10.0	10.0	11.0	11.0	11.0

(a) Normal force coefficient

Figure 8. Aerodynamic characteristics of the NLR 7223-62 airfoil with 4.9% test section porosity.

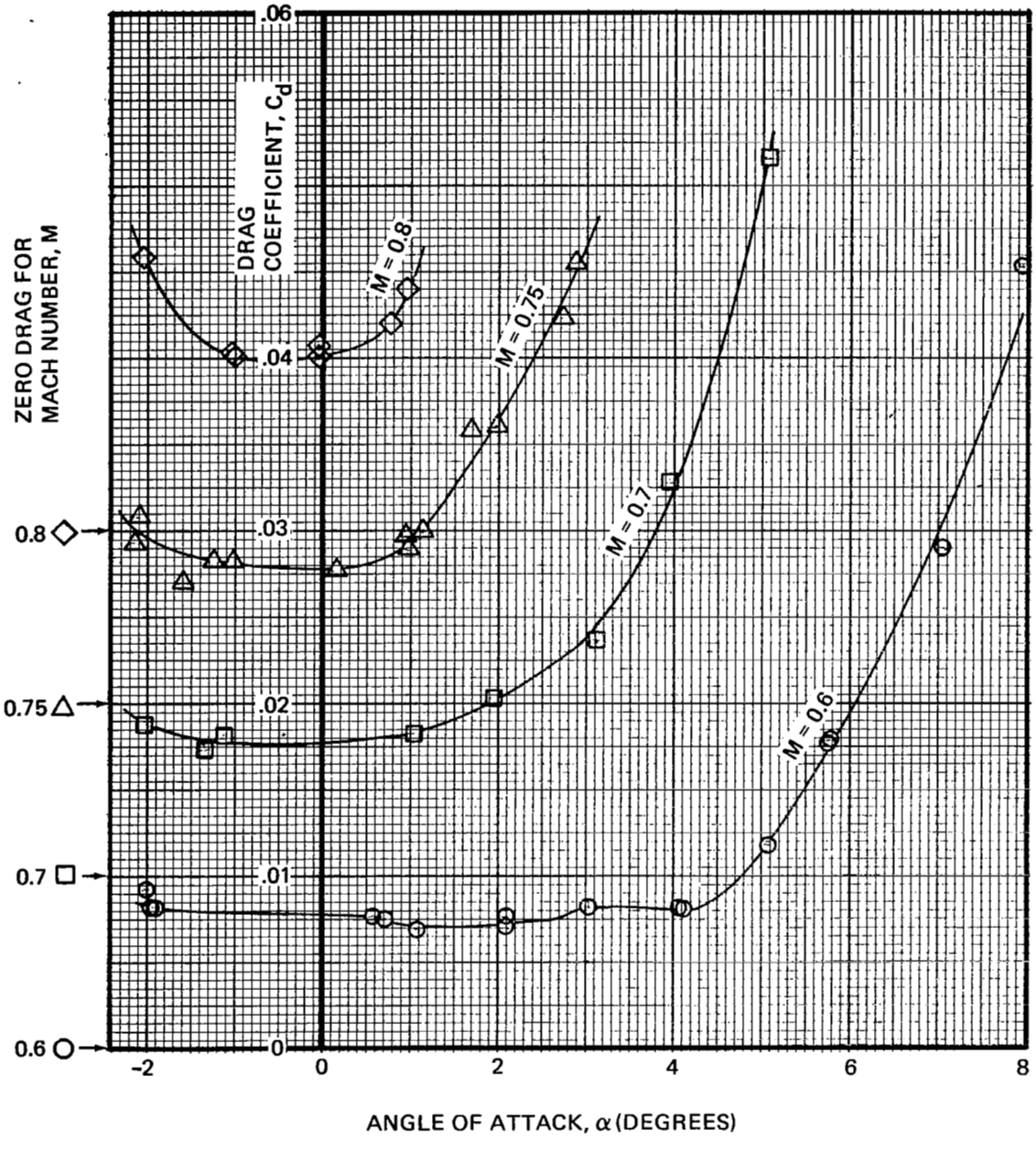

(b) Drag coefficient

Figure 8. Continued

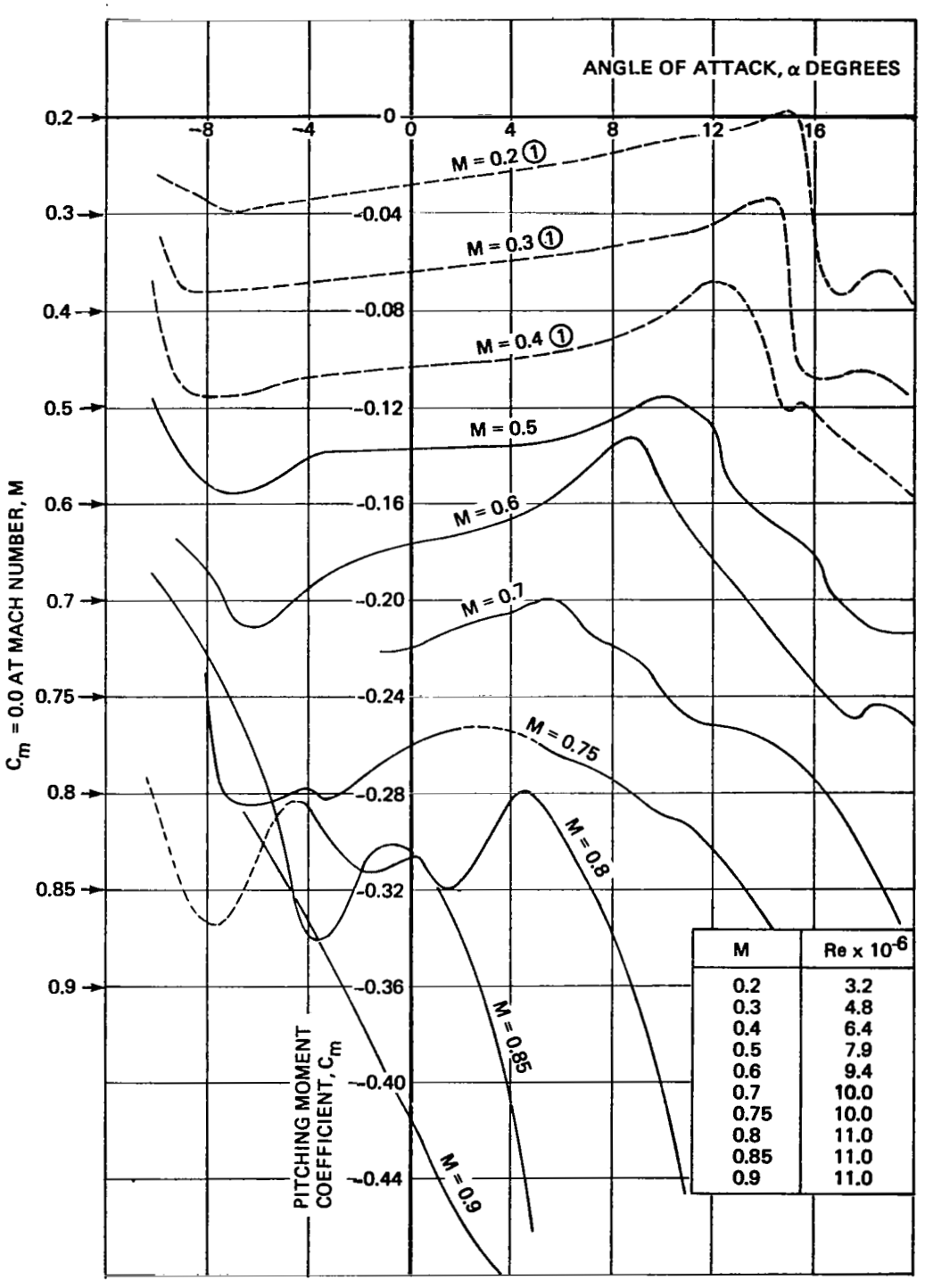

NOTE: 1 INCORRECT C_M LEVEL BECAUSE OF INCOMPLETE INTEGRATION DUE TO T.E. TRANSDUCER MALFUNCTION

(c) Pitching moment coefficient

Figure 8. Concluded

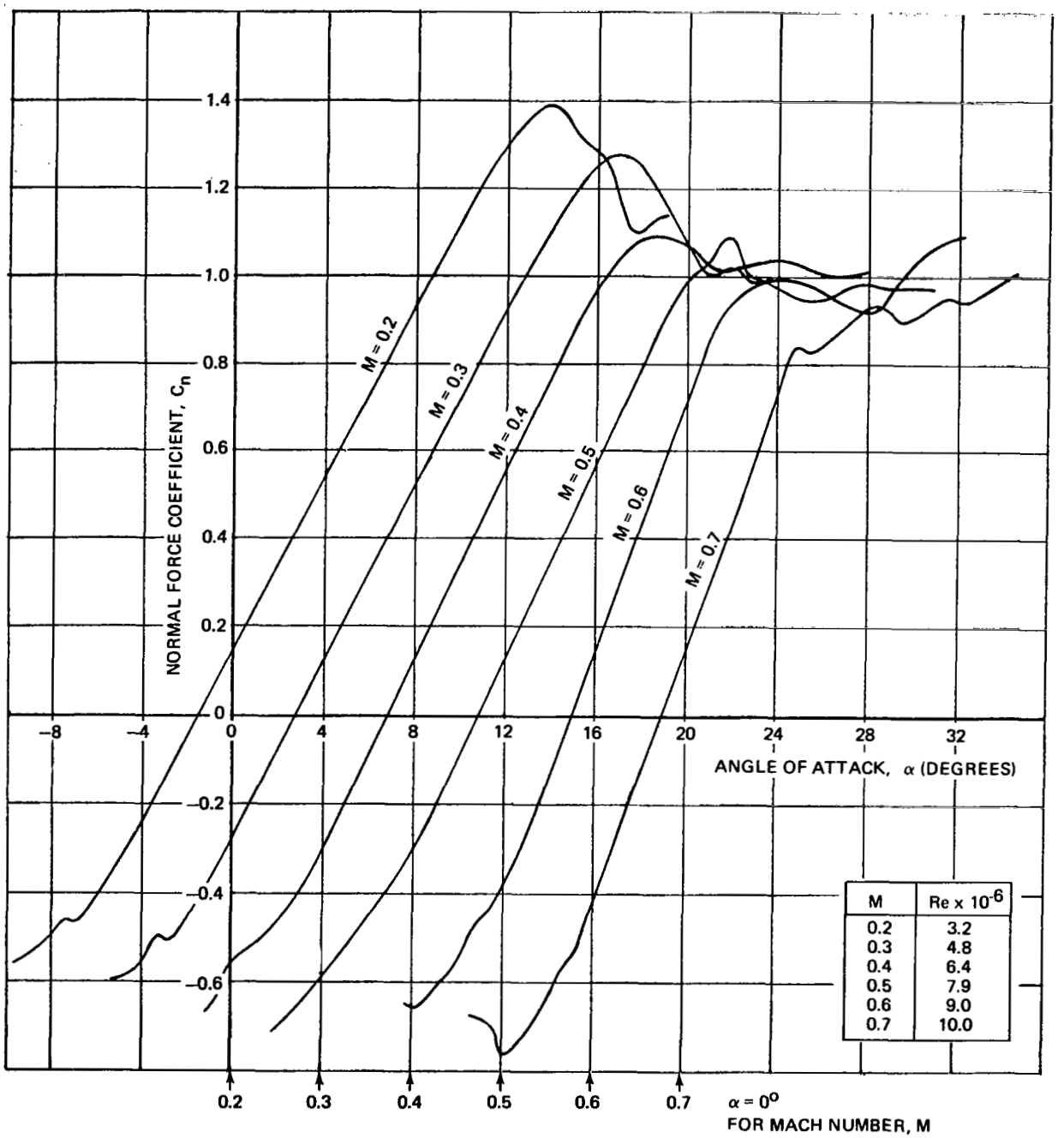

(a) Normal force coefficient

Figure 9. Aerodynamic characteristics of the NLR 7223-62 airfoil in test section with solid floor and ceiling. Base line for oscillatory data.

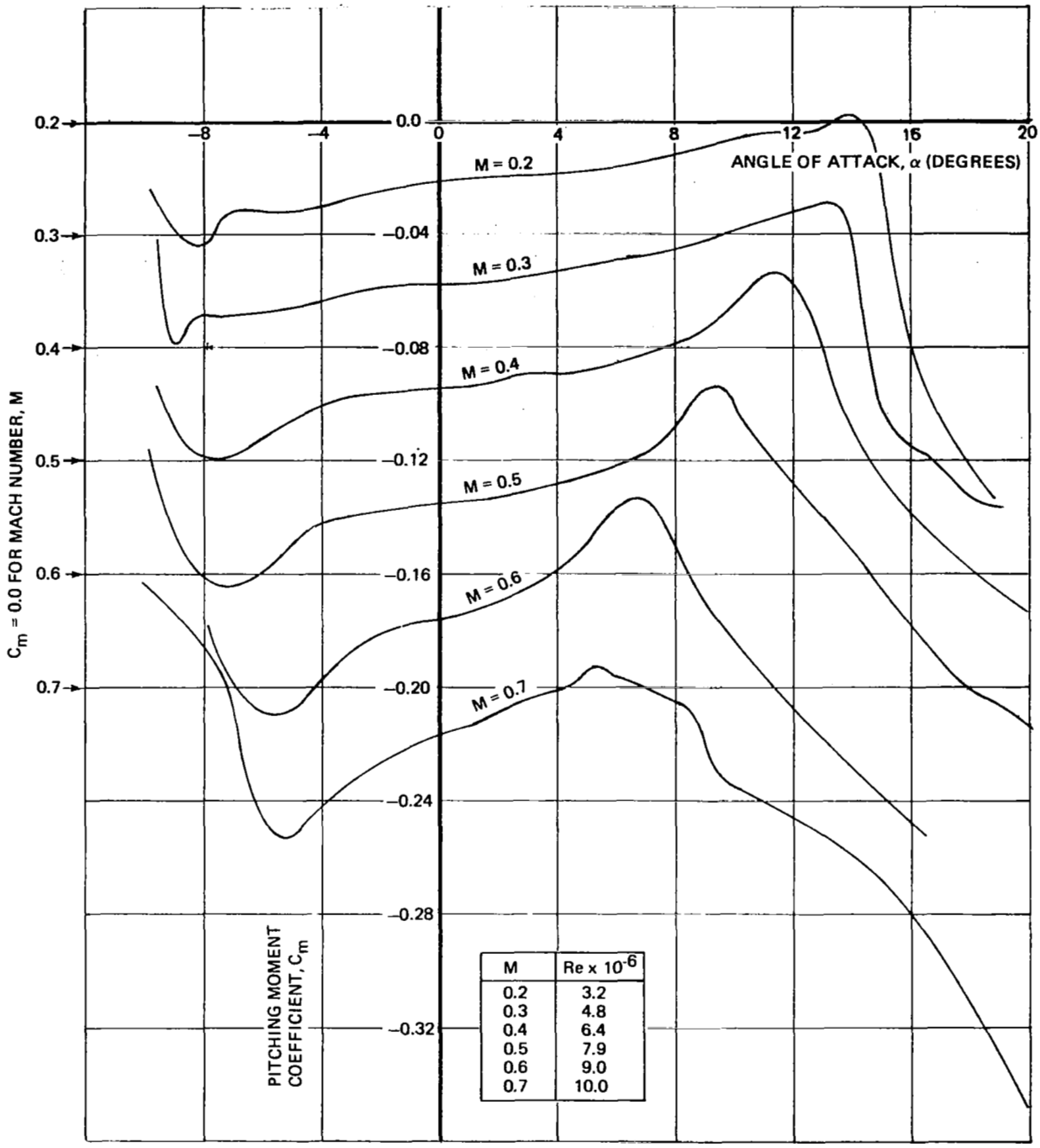

(b) Pitching moment coefficient

Figure 9. Concluded

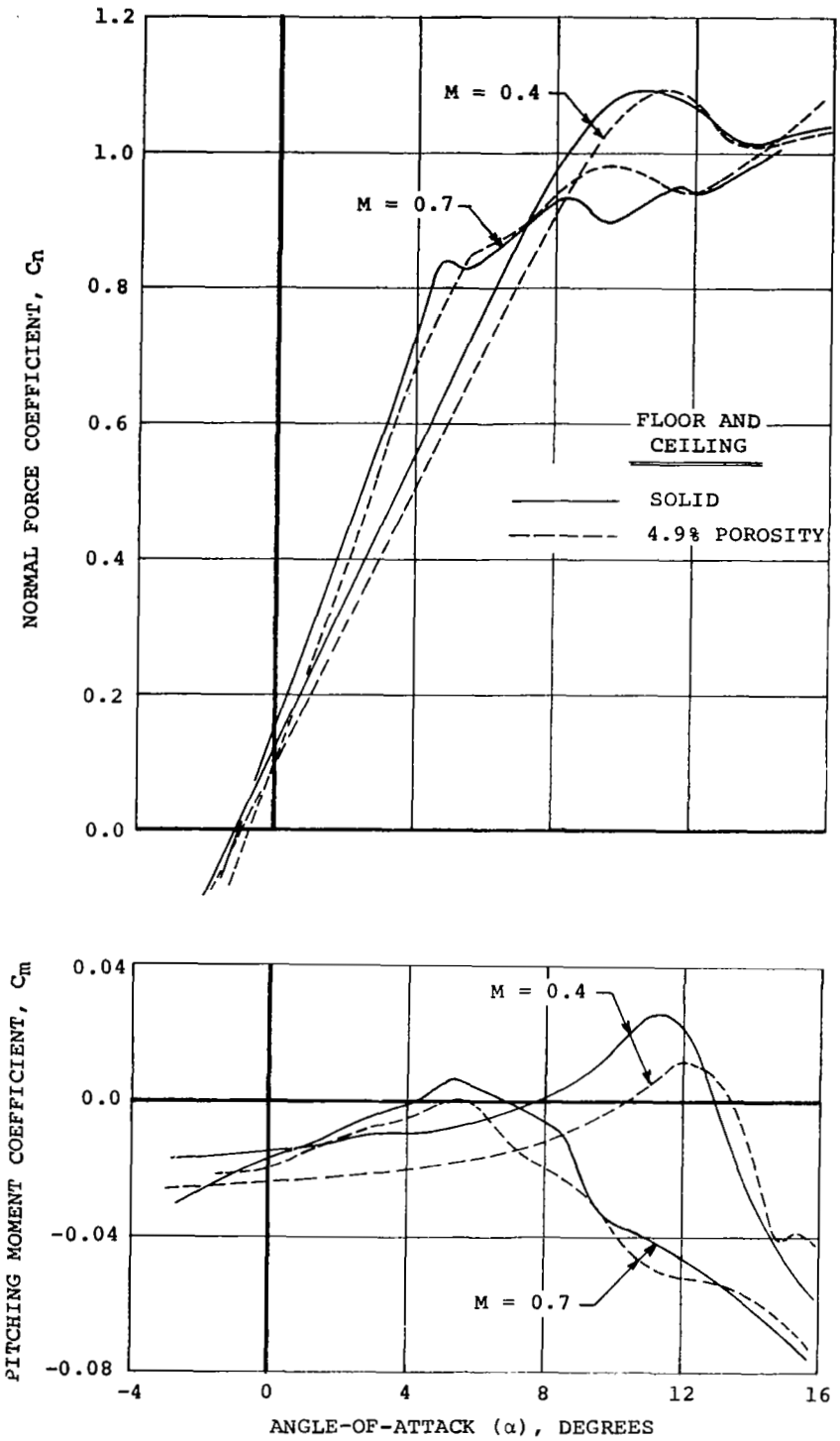

Figure 10. Effect of floor and ceiling porosity.

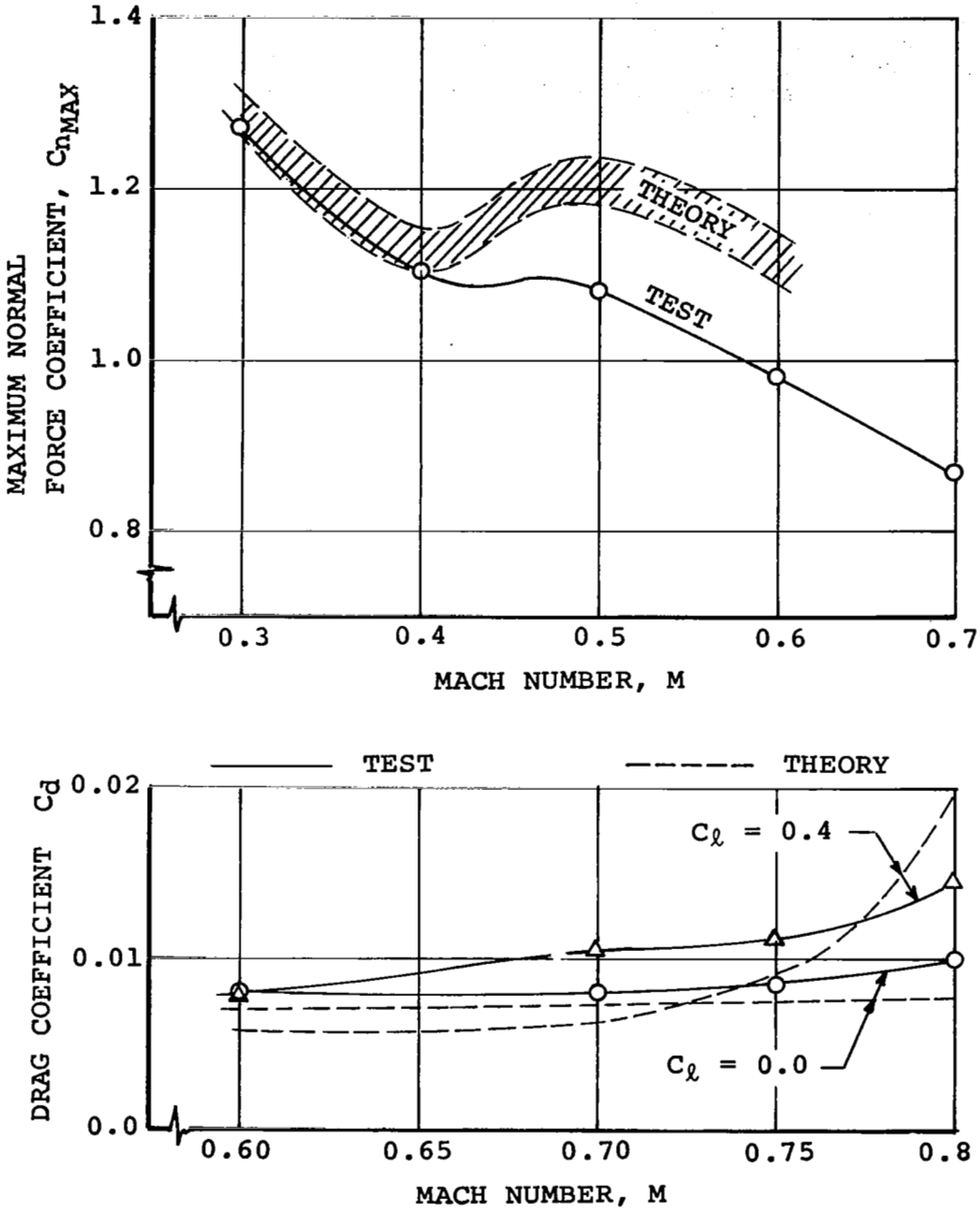

Figure 11. Comparison with predicted sectional characteristics.

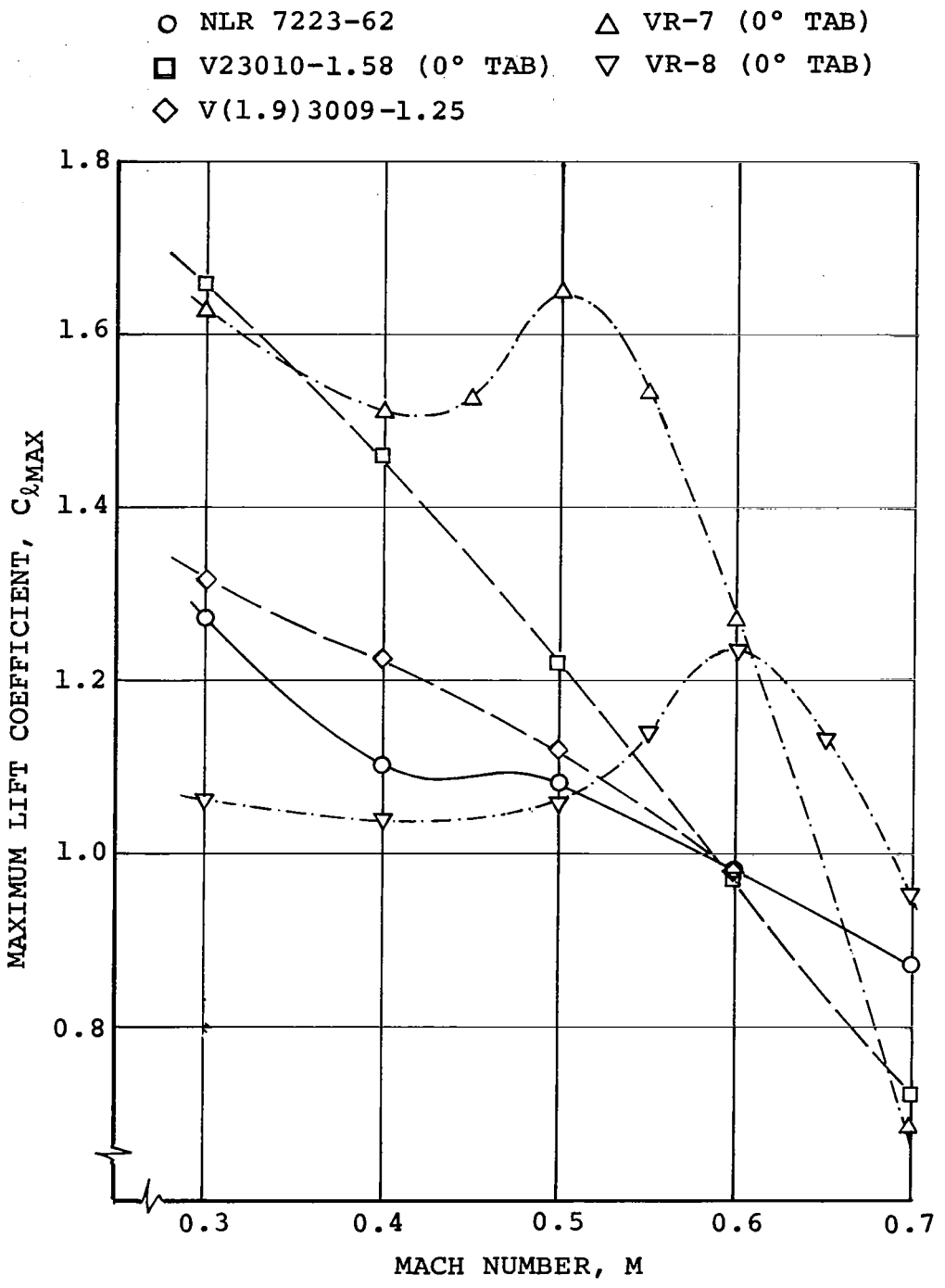

Figure 12. Comparison with other airfoil sections.

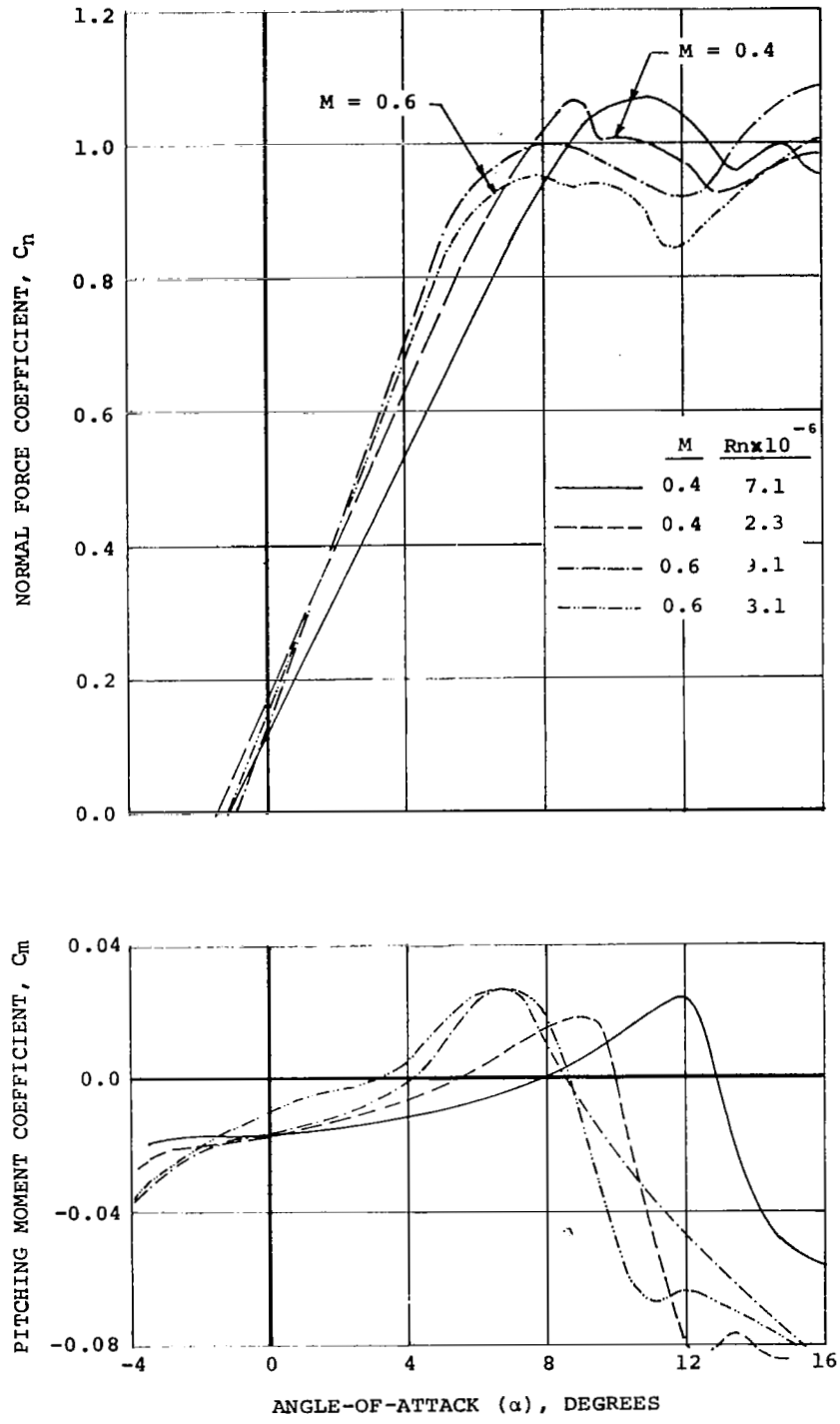

Figure 13. Effect of Reynolds number variation on the normal-force and pitching-moment characteristics of the NLR 7223-62 airfoil.

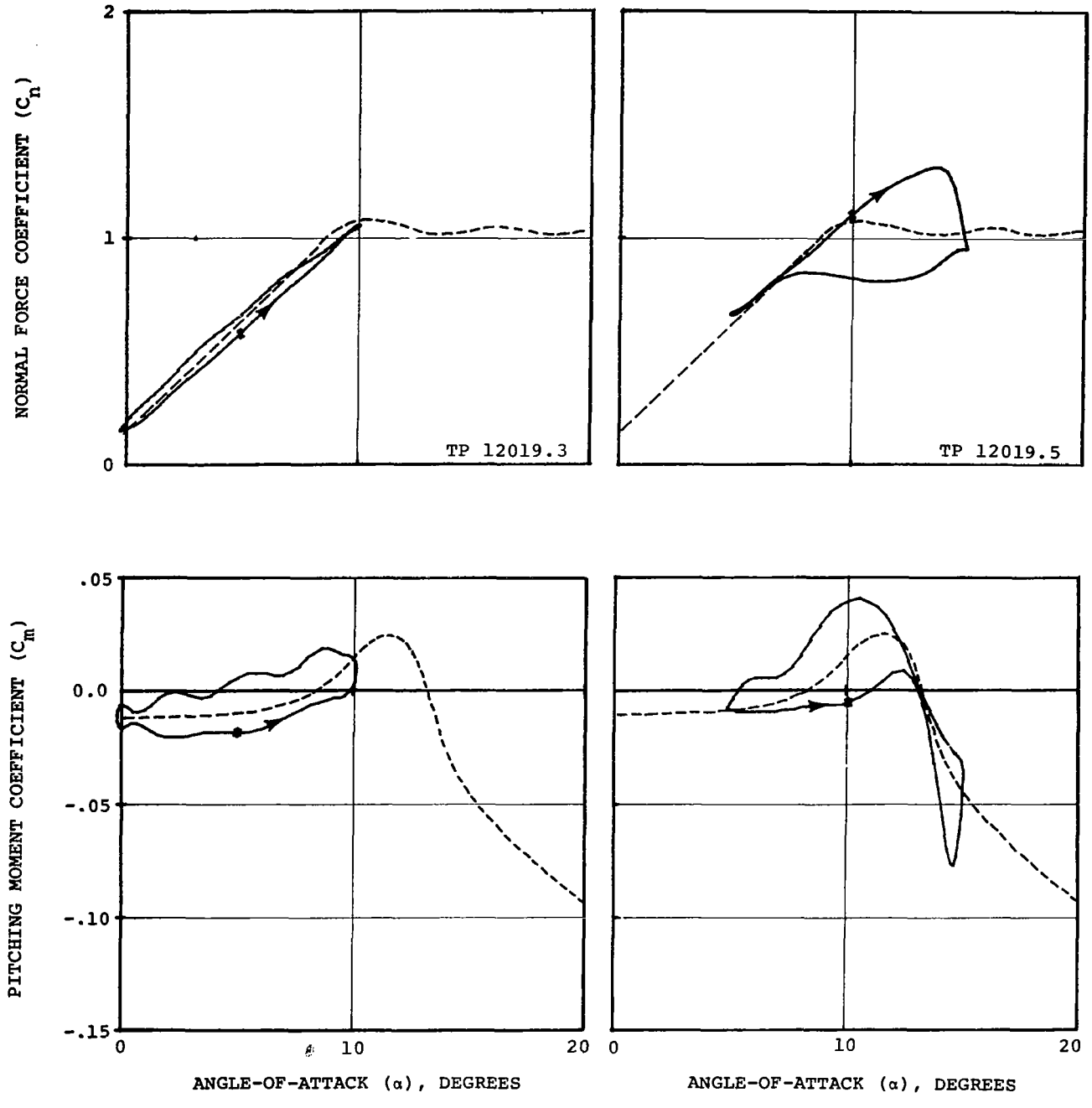

(a) $\alpha_o = 5.0^o$

(b) $\alpha_o = 10.0^o$

Figure 14. Effect of mean angle-of-attack variation on the dynamic stall characteristics of the normal-force and pitching-moment coefficients of the NLR 7223-62 airfoil. Nominal conditions: M = 0.4, Rn = 6.4 x 10^6, f_D = 23.0 Hz, $\Delta\alpha$ = 5.0°.

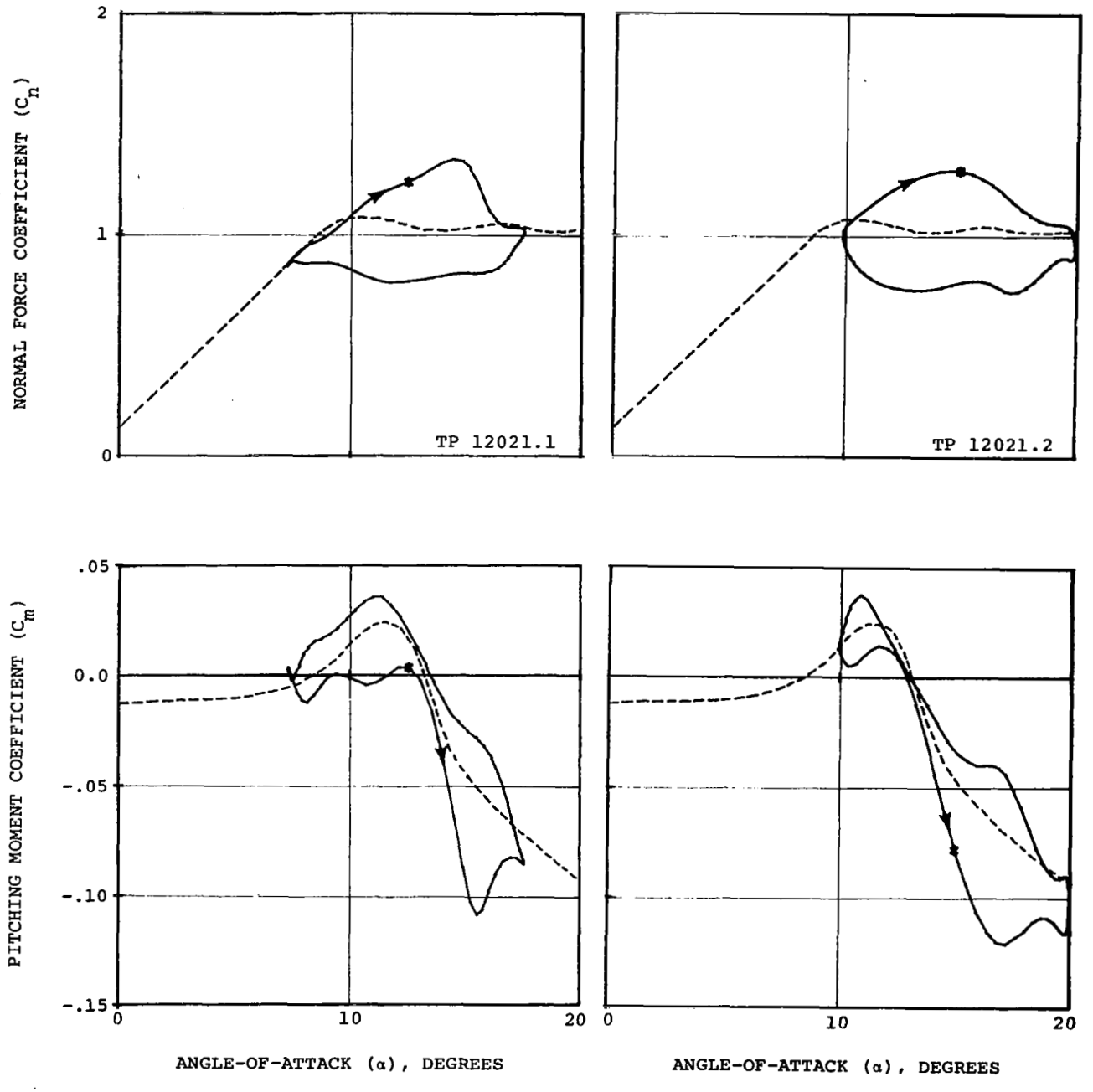

(c) α_o = 12.5°

(d) α_o = 15.0°

Figure 14. Concluded

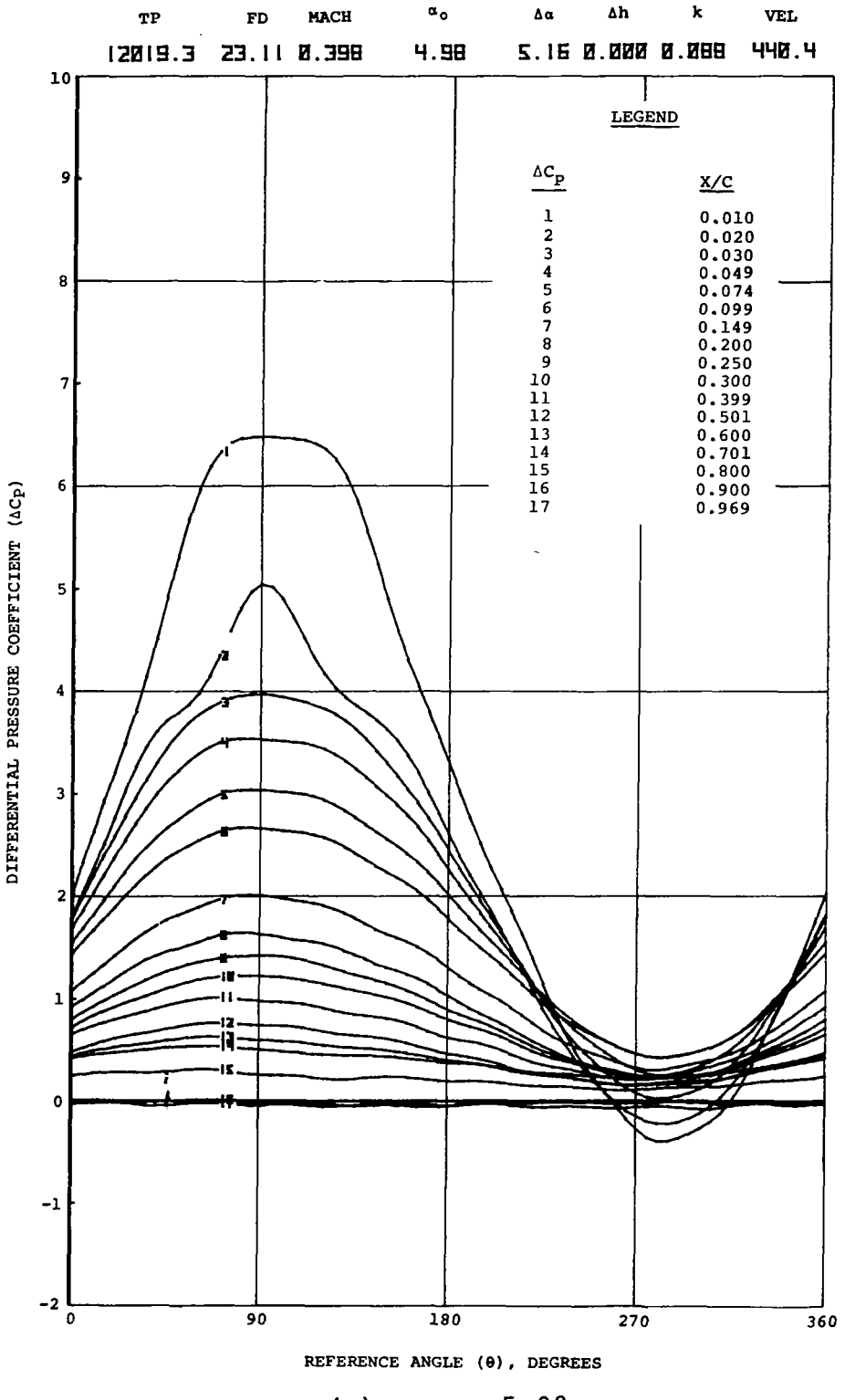

(a) $\alpha_o = 5.0°$

Figure 15. Effect of mean angle-of-attack variation on the local differential pressures over the NLR 7223-62 airfoil. Nominal conditions: M = 0.4, Rn = 6.4 x 10^6, f_D = 23.0 Hz, $\Delta\alpha$ = 5.0°.

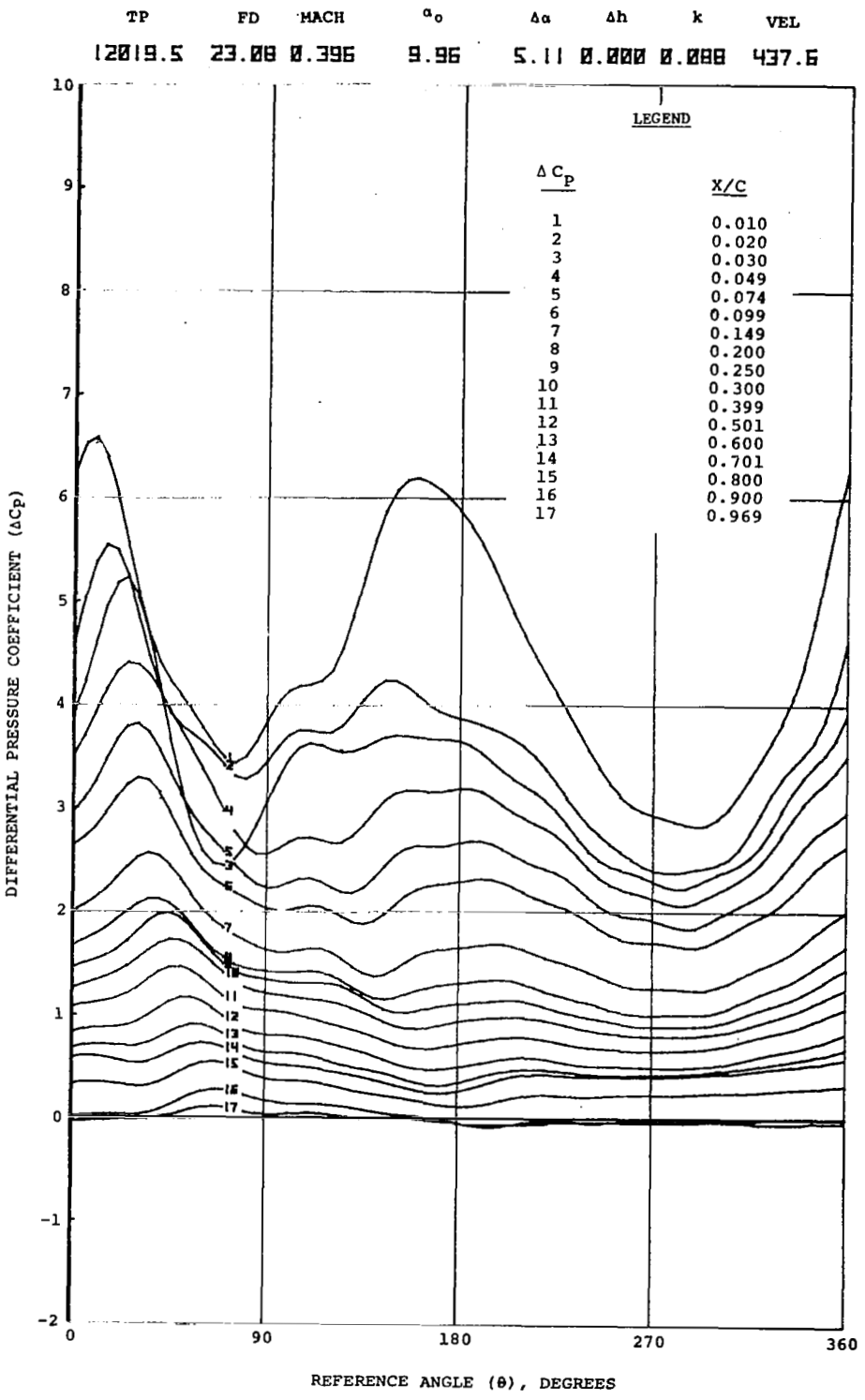

(b) $\alpha_o = 10.0°$

Figure 15. Continued

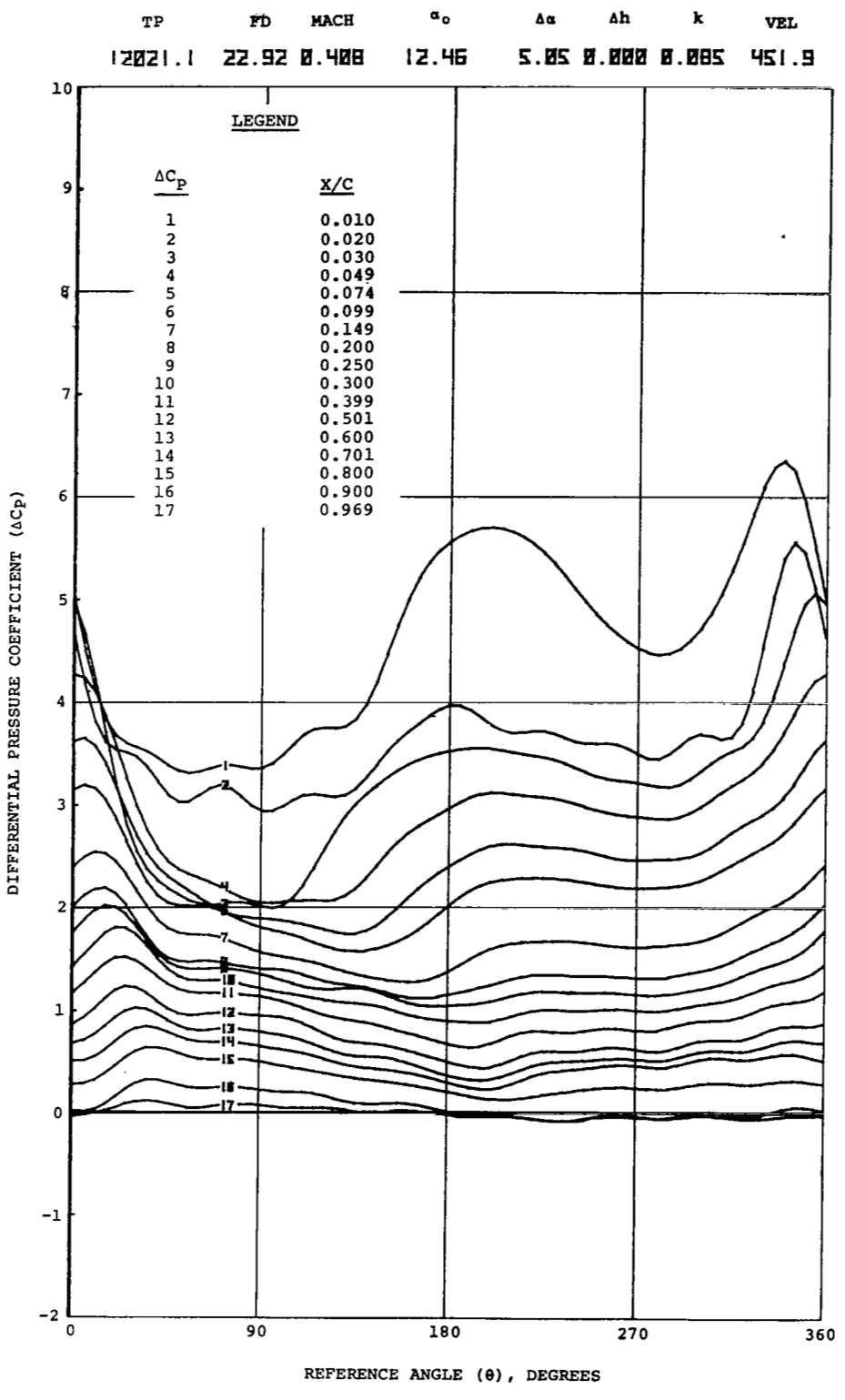

(c) α_o = 12.5°

Figure 15. Continued

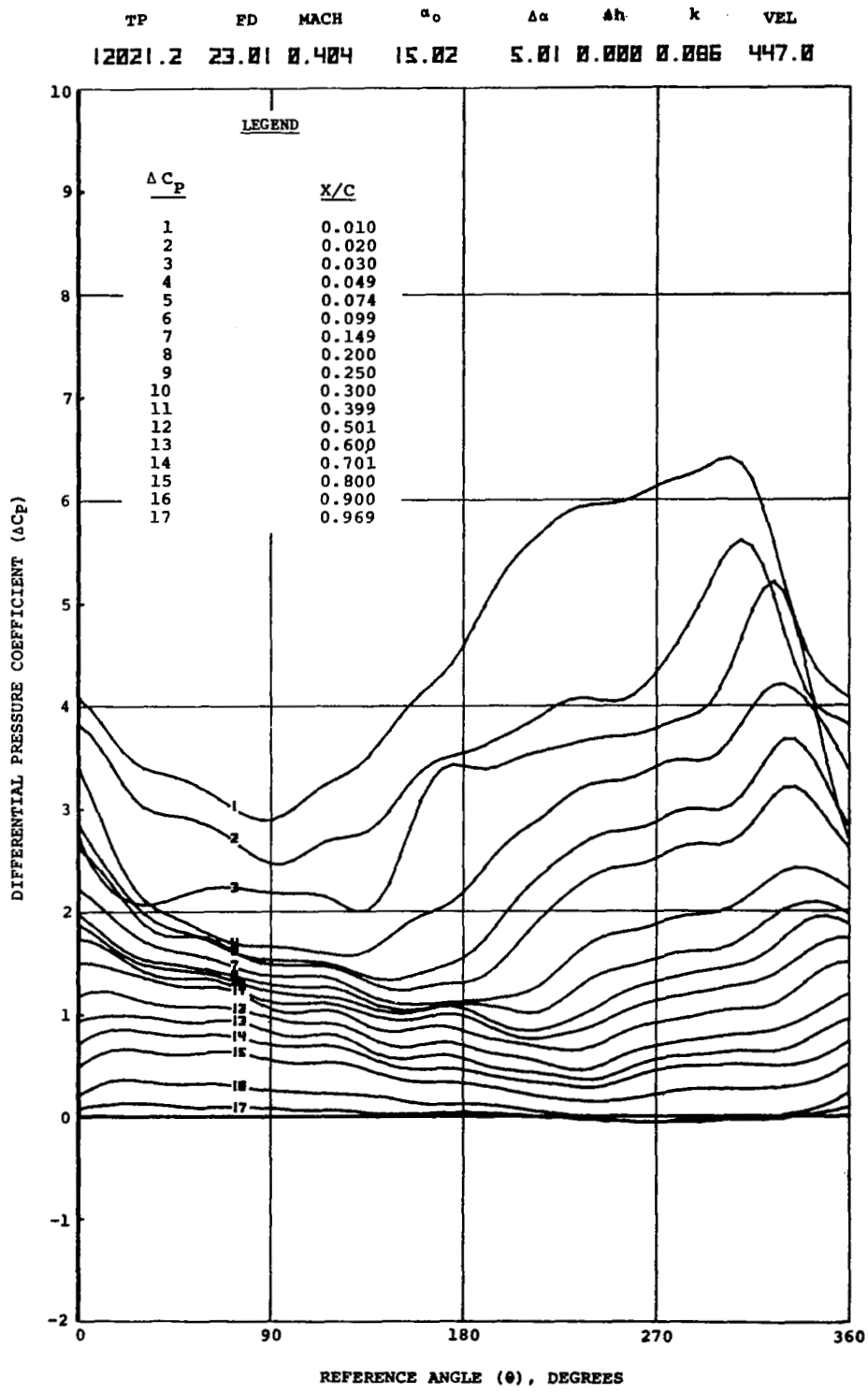

(d) α_o = 15.0°

Figure 15. Concluded

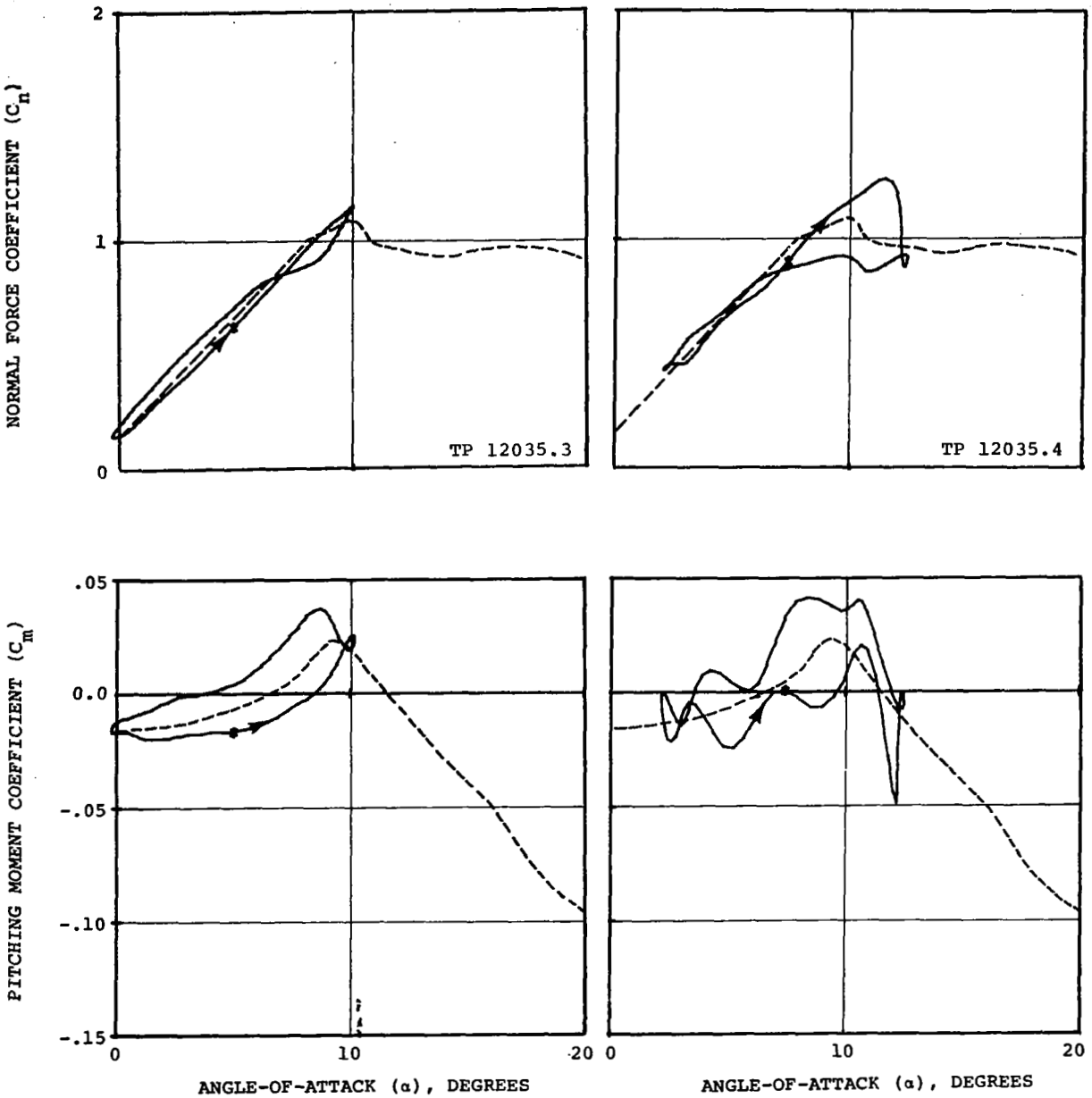

(a) $\alpha_o = 5.0^o$ (b) $\alpha_o = 7.5^o$

Figure 16. Effect of mean angle-of-attack variation on the dynamic stall characteristics of the normal-force and pitching-moment coefficients of the NLR 7223-62 airfoil. Nominal conditions: M = 0.5, Rn = 7.9 x 10^6, f_D = 23.0 Hz, $\Delta\alpha$ = 5.0°.

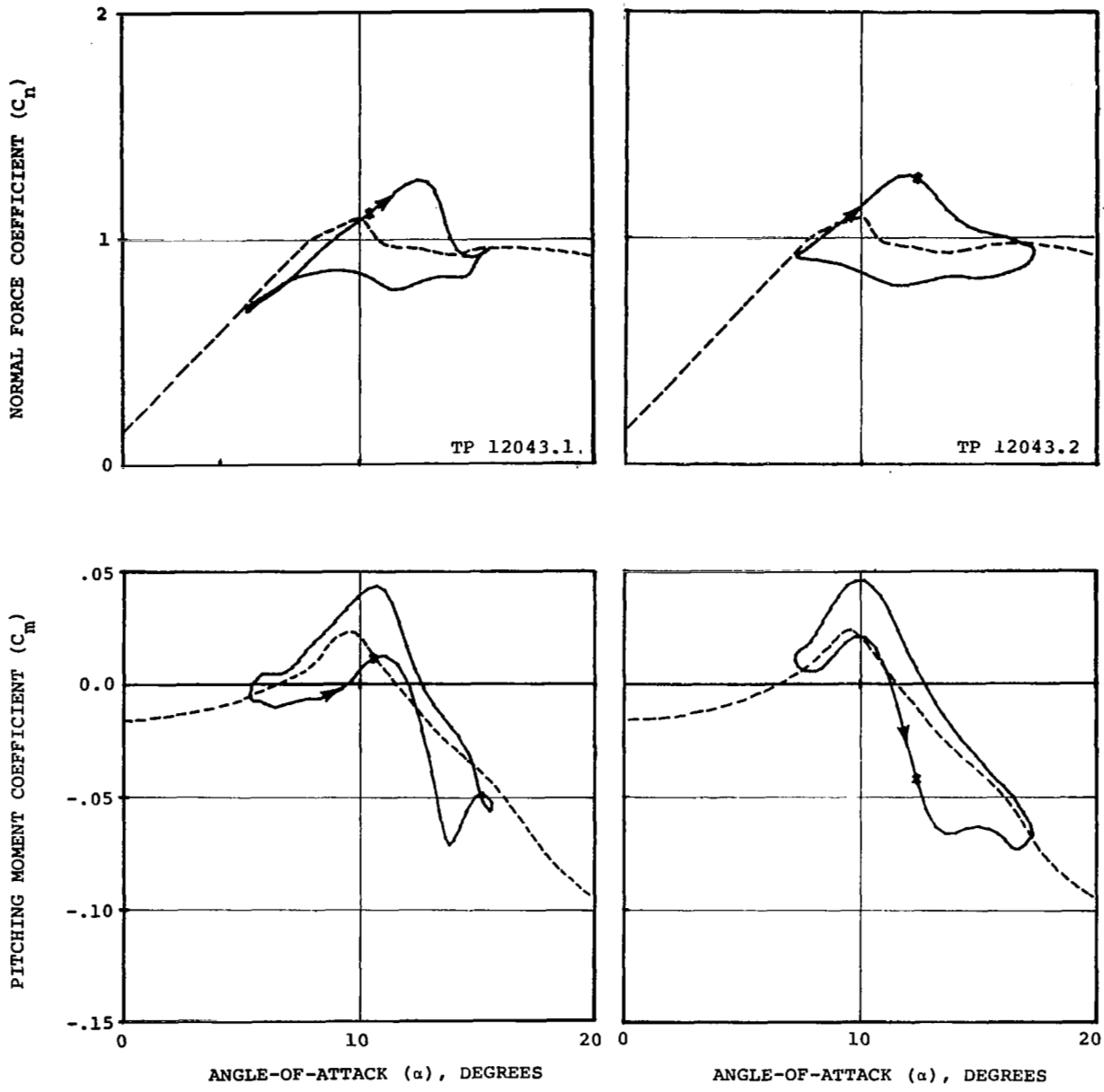

(c) $\alpha_o = 10.0^o$ (d) $\alpha_o = 12.5^o$

Figure 16. Concluded

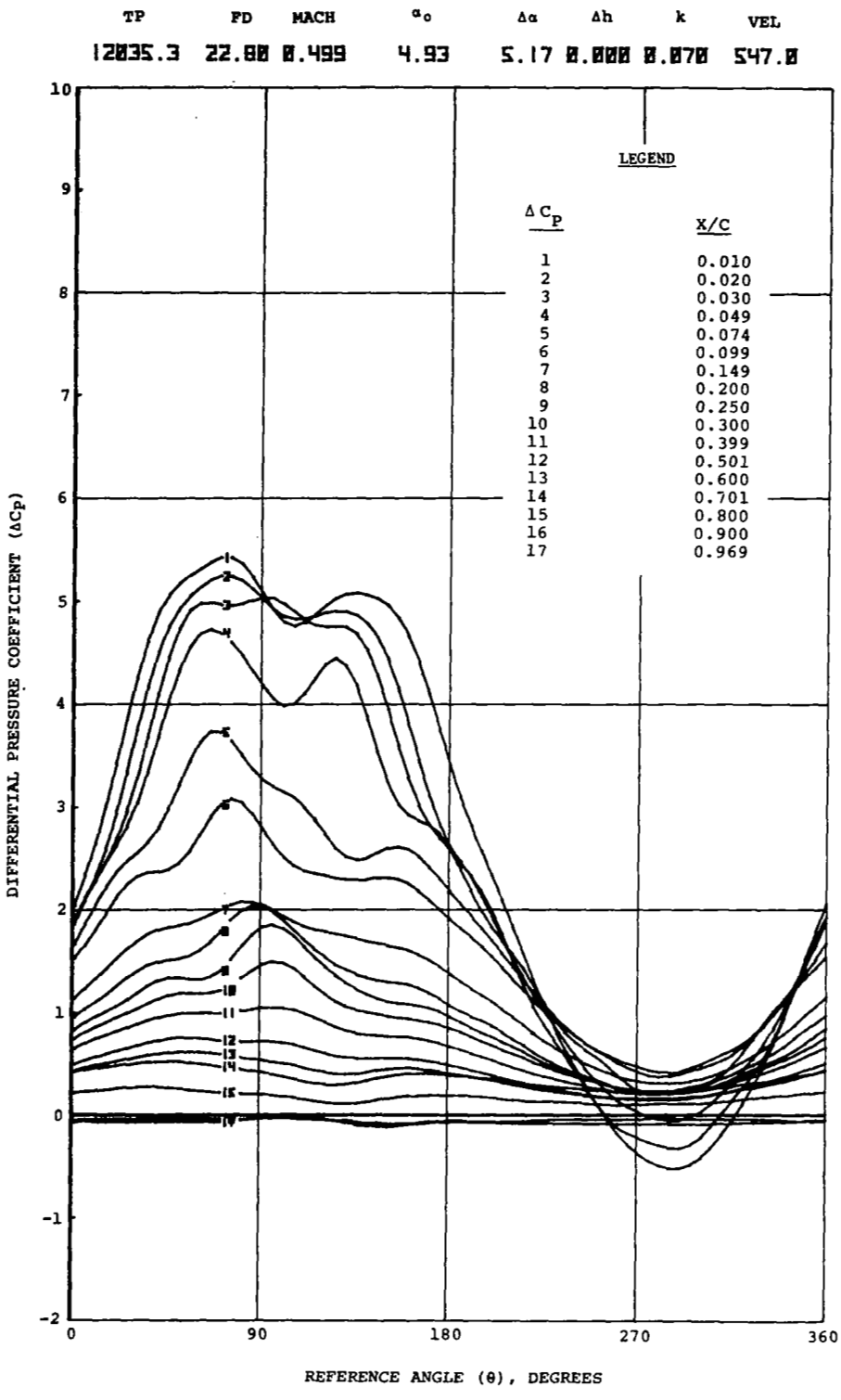

(a) α_o = 5.0°

Figure 17. Effect of mean angle-of-attack variation on the local differential pressures over the NLR 7223-62 airfoil. Nominal conditions: M = 0.5, Rn = 7.9 x 10^6, f_D = 23.0 Hz, $\Delta\alpha$ = 5.0°

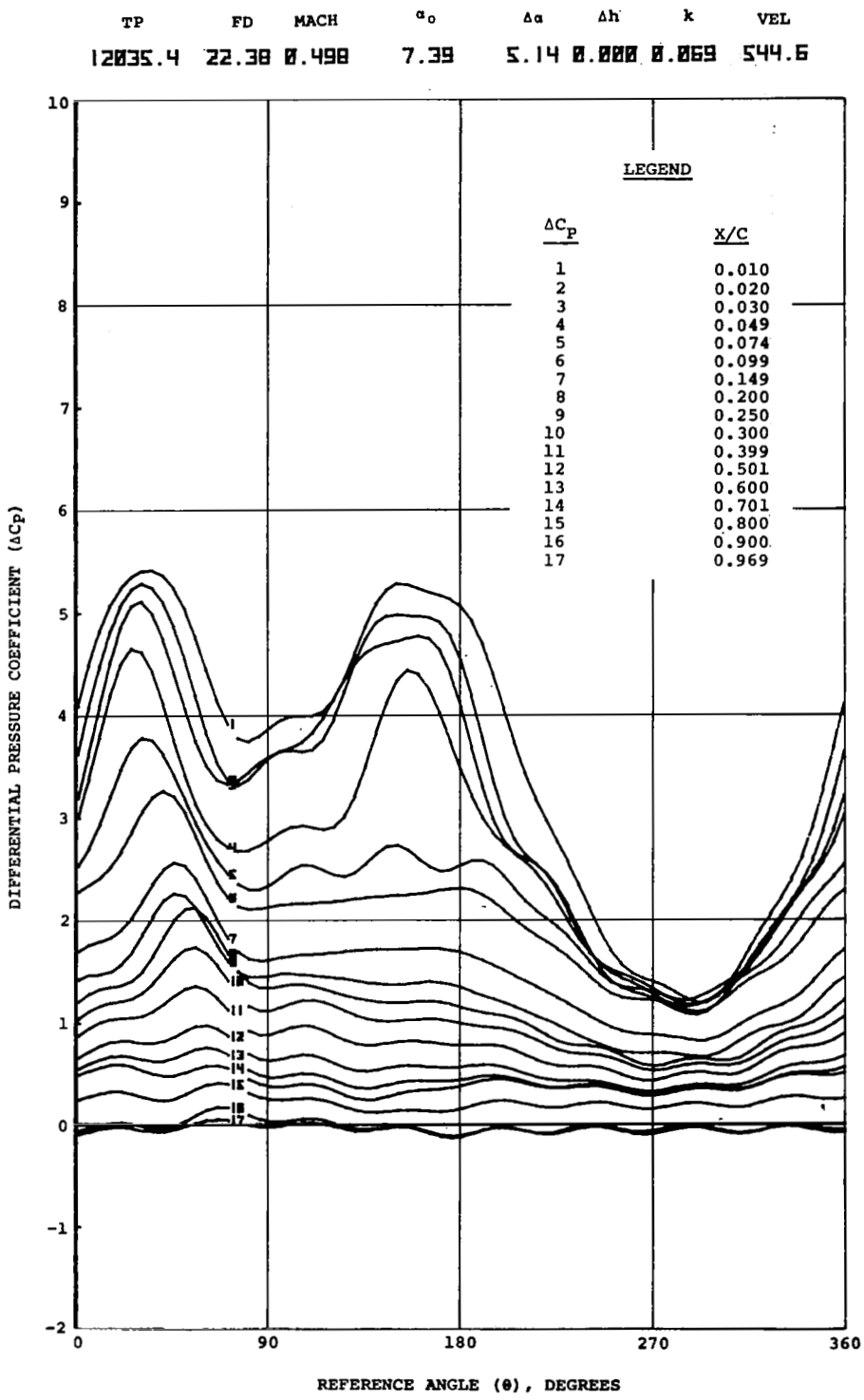

(b) $\alpha_o = 7.5°$

Figure 17. Continued

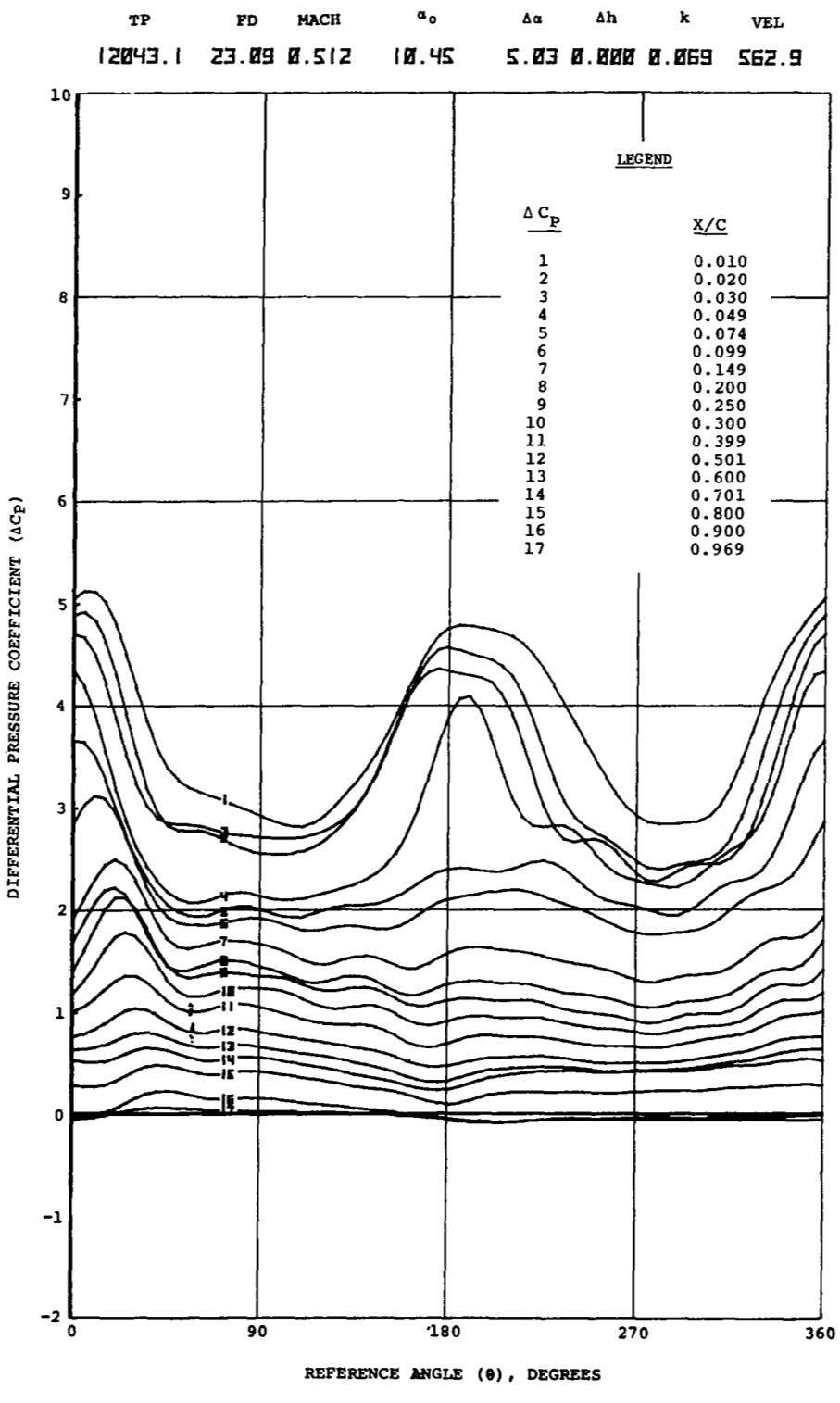

(c) α_o = 10.0°

Figure 17. Continued

TP	FD	MACH	α_o	$\Delta\alpha$	Δh	k	VEL
12043.2	23.07	0.508	12.31	4.97	0.000	0.069	557.7

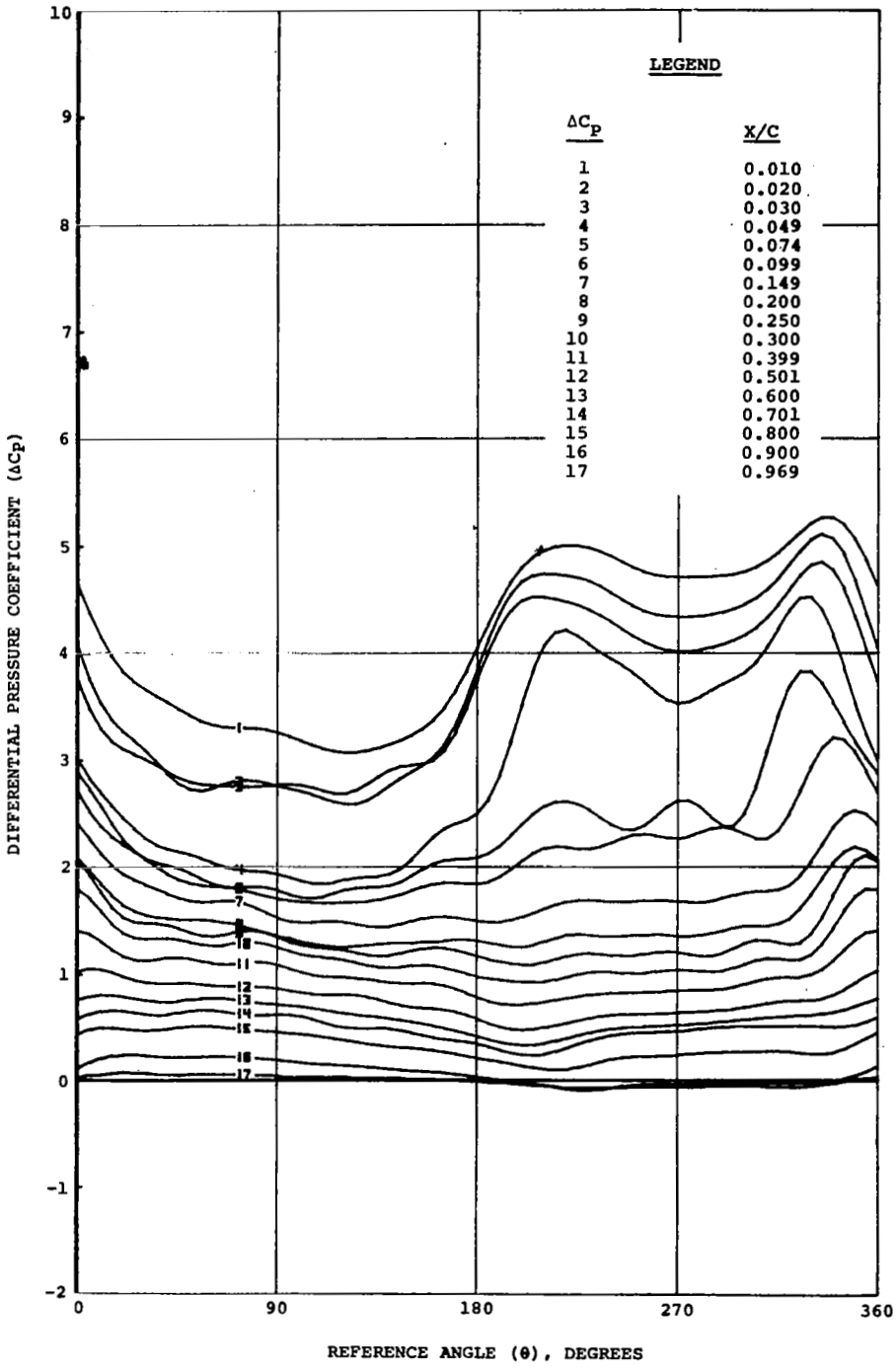

(d) $\alpha_o = 12.5°$

Figure 17. Concluded

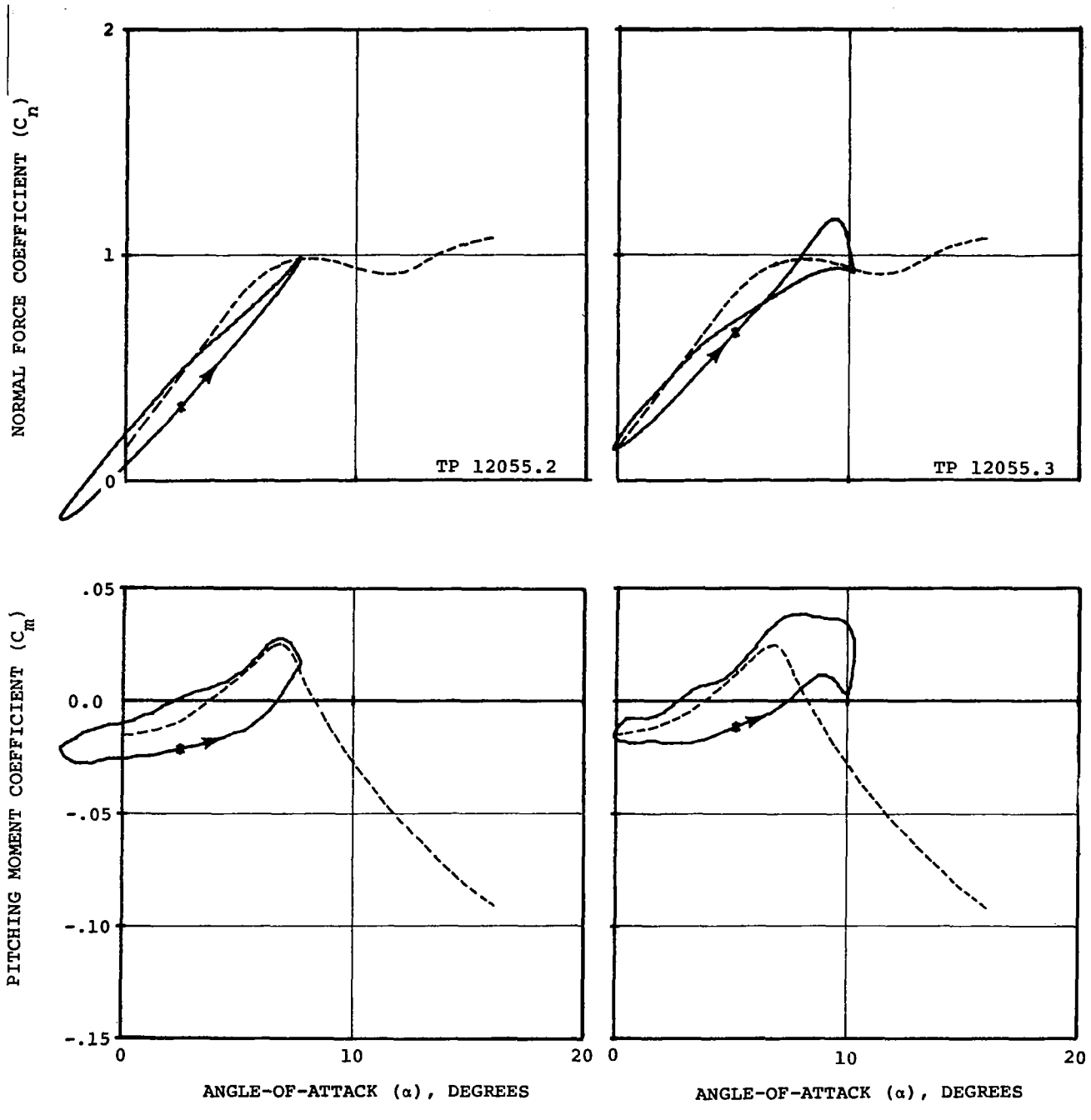

(a) $\alpha_o = 2.5°$ (b) $\alpha_o = 5.0°$

Figure 18. Effect of mean angle-of-attack variation on the dynamic stall characteristics of the normal-force and pitching-moment coefficients of the NLR 7223-62 airfoil. Nominal conditions: M = 0.6, Rn = 9.5 x 10^6, f_D = 23.0 Hz, $\Delta\alpha$ = 5.0°.

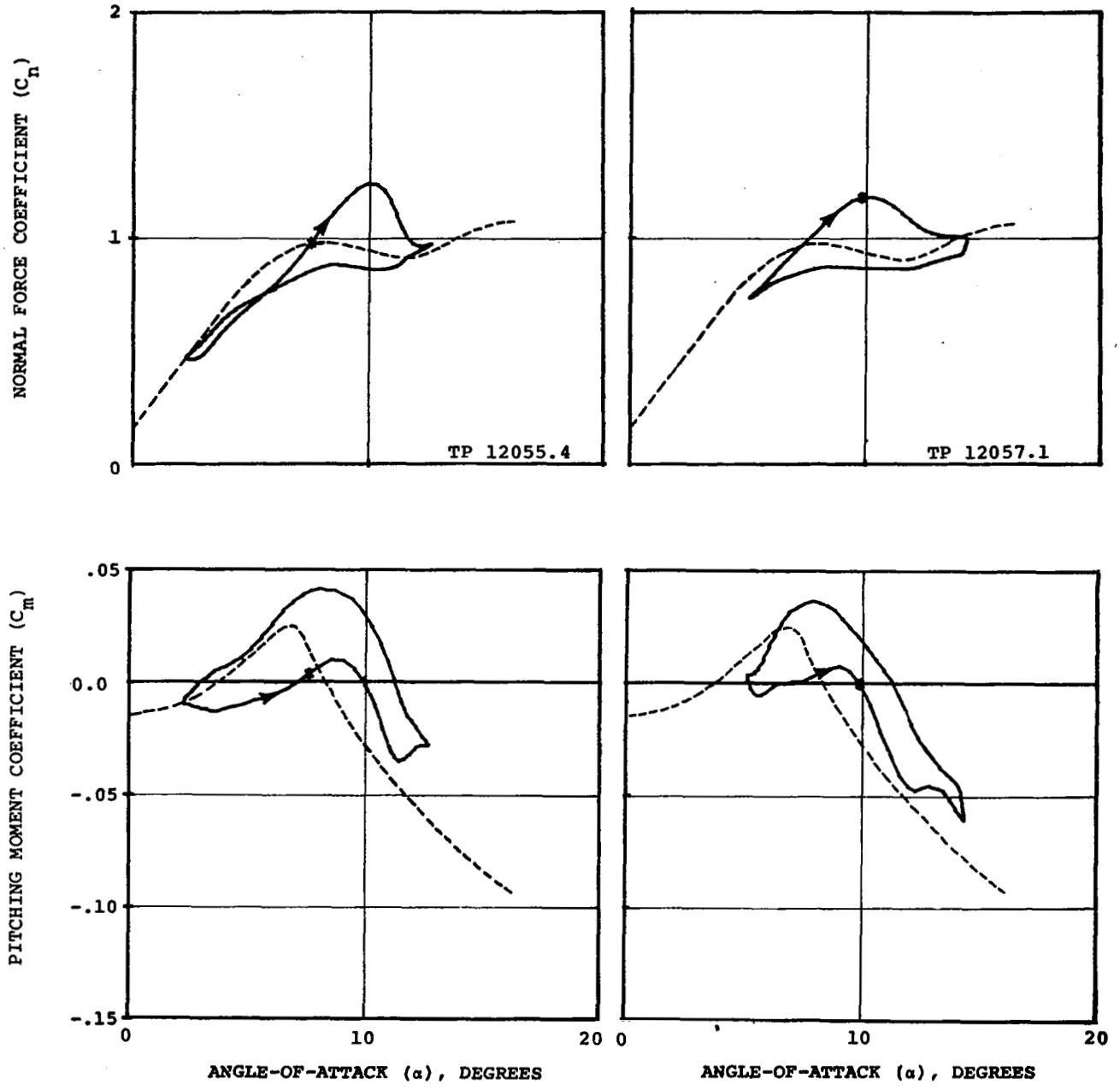

(c) α_o = 7.5°

(d) α_o = 10.0°

Figure 18. Concluded

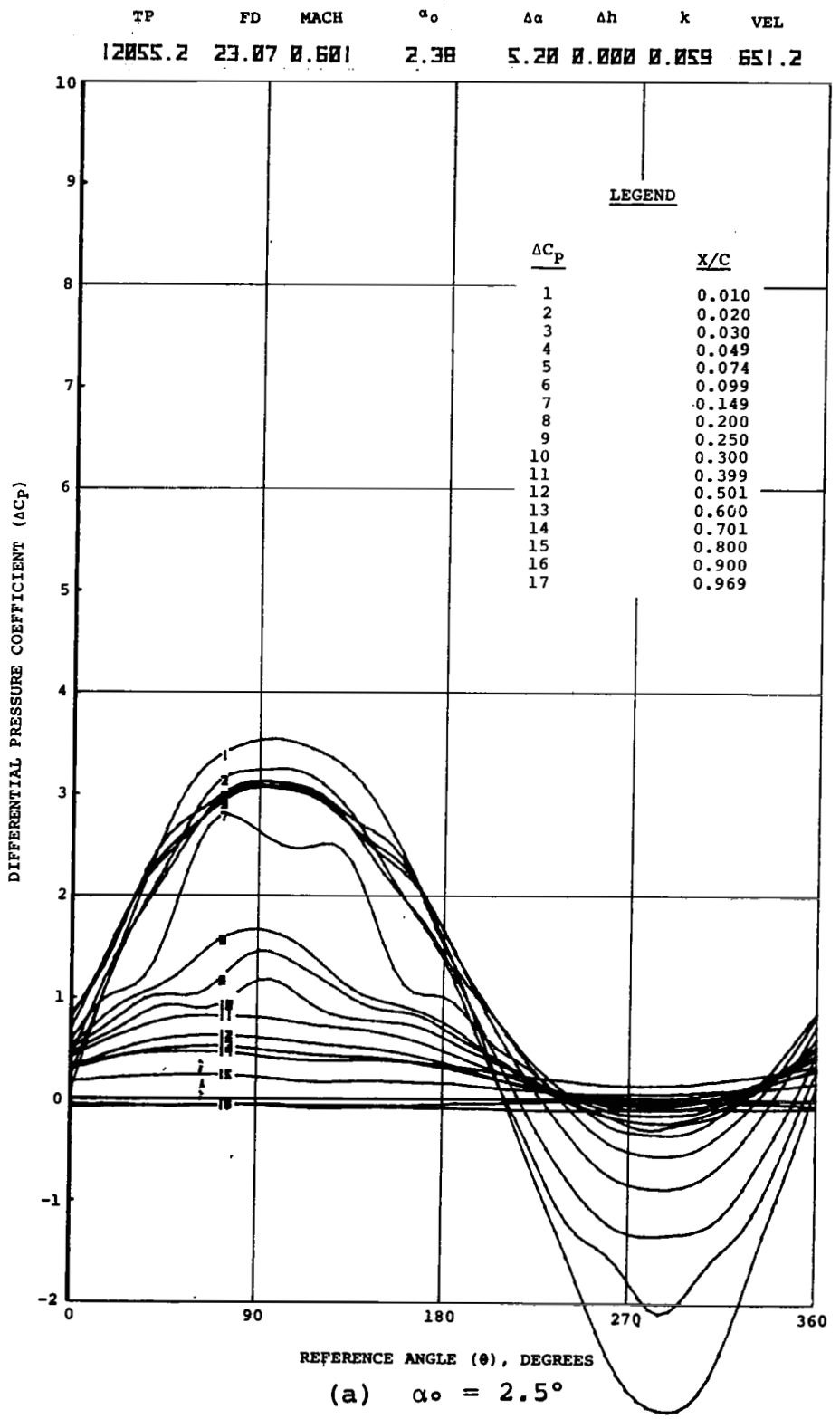

(a) α_o = 2.5°

Figure 19. Effect of mean angle-of-attack variation on the local differential pressures over the NLR 7223-62 airfoil. Nominal conditions: M = 0.6, Rn = 9.5 x 10^6, f_D = 23.0 Hz, $\Delta\alpha$ = 5.0°

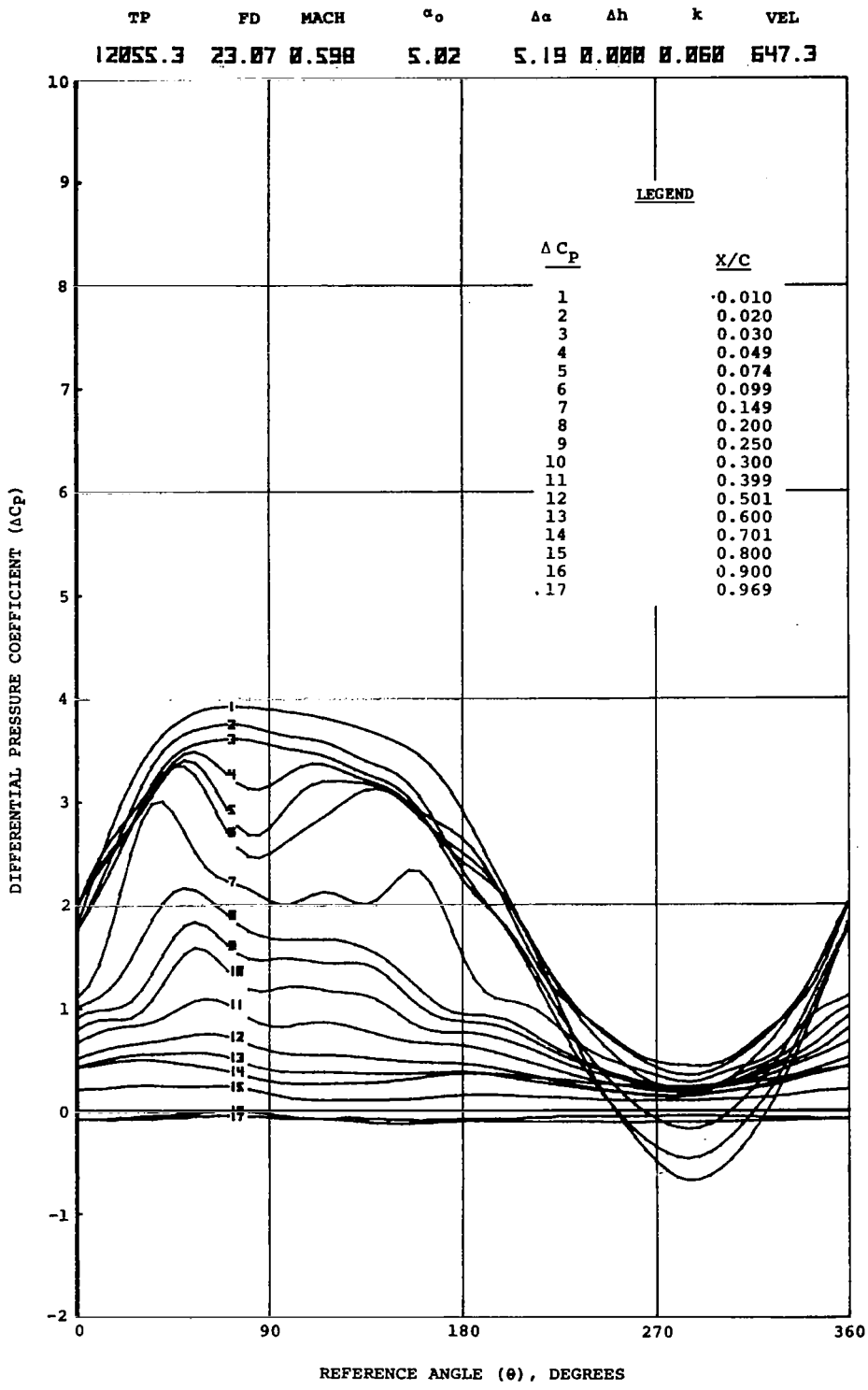

(b) $\alpha_o = 5.0°$

Figure 19. Continued

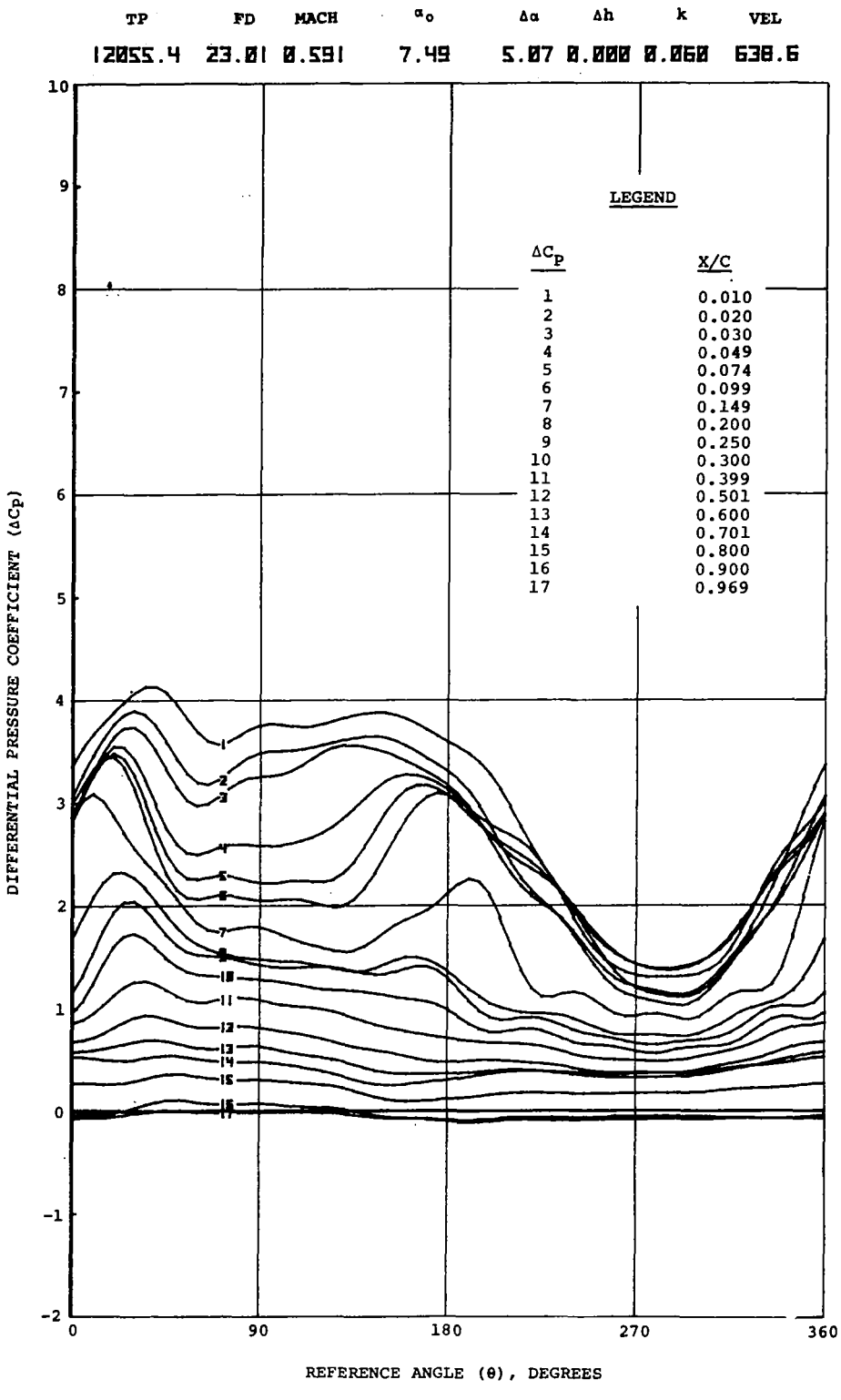

(c) $\alpha_o = 7.5°$

Figure 19. Continued

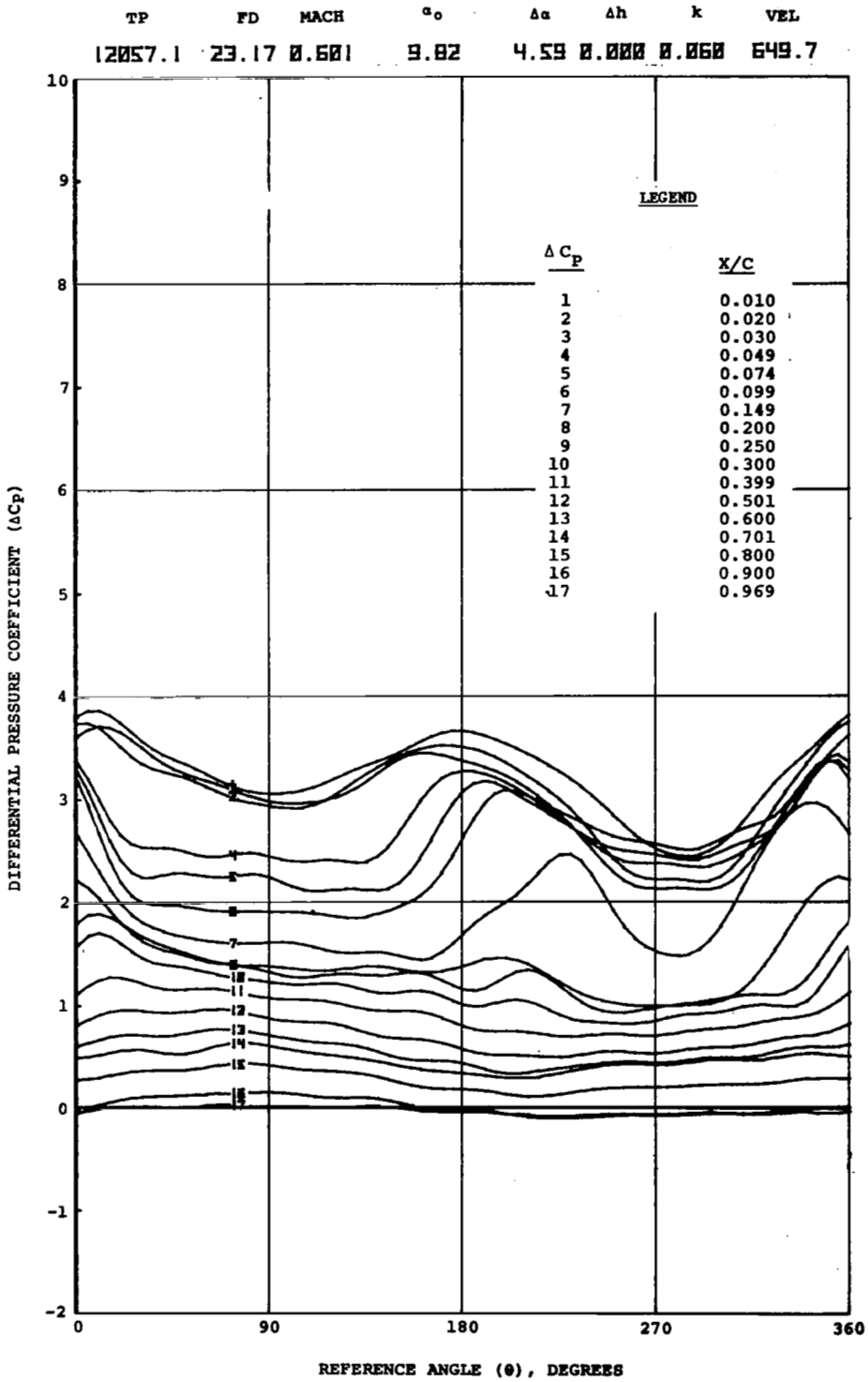

(d) α_o = 10.0°

Figure 19. Concluded

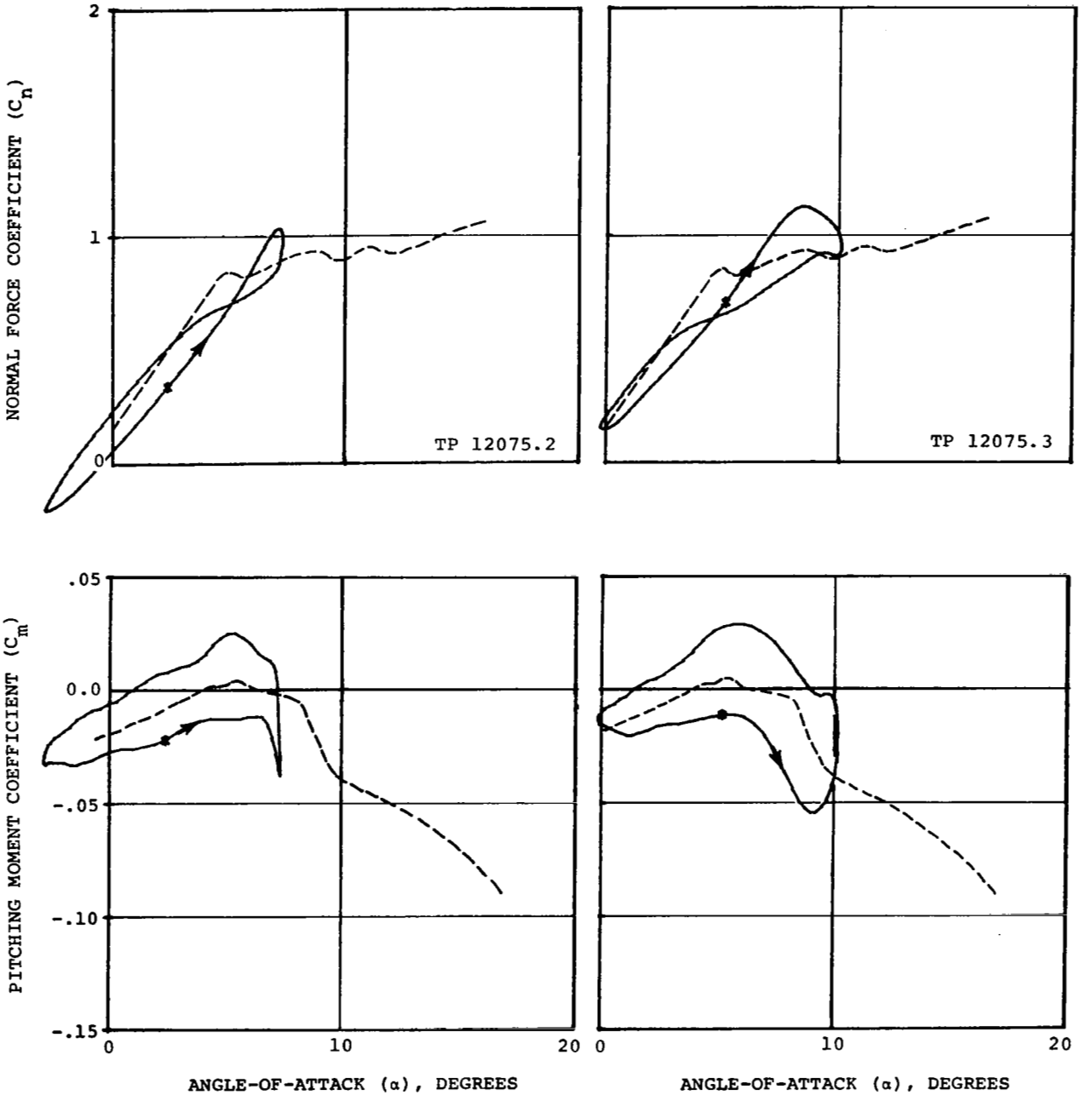

(a) $\alpha_o = 2.5°$ (b) $\alpha_o = 5.0°$

Figure 20. Effect of mean angle-of-attack variation on the dynamic stall characteristics of the normal-force and pitching-moment coefficients of the NLR 7223-62 airfoil. Nominal conditions: M = 0.7, Rn = 10 x 10^6, f_D = 23.0 Hz, $\Delta\alpha$ = 5.0°

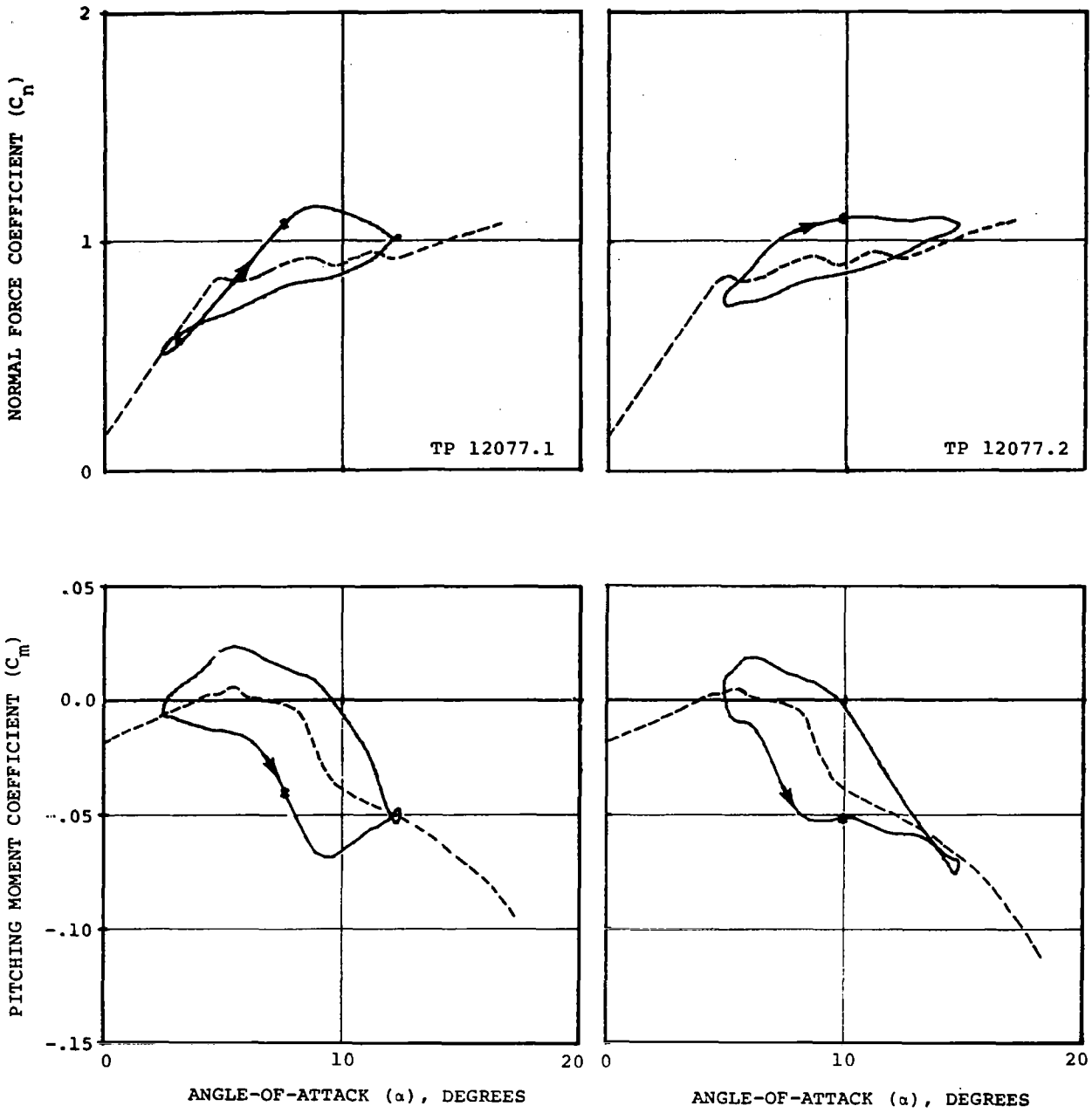

(c) α_o = 7.5°

(d) α_o = 10.0°

Figure 20. Concluded

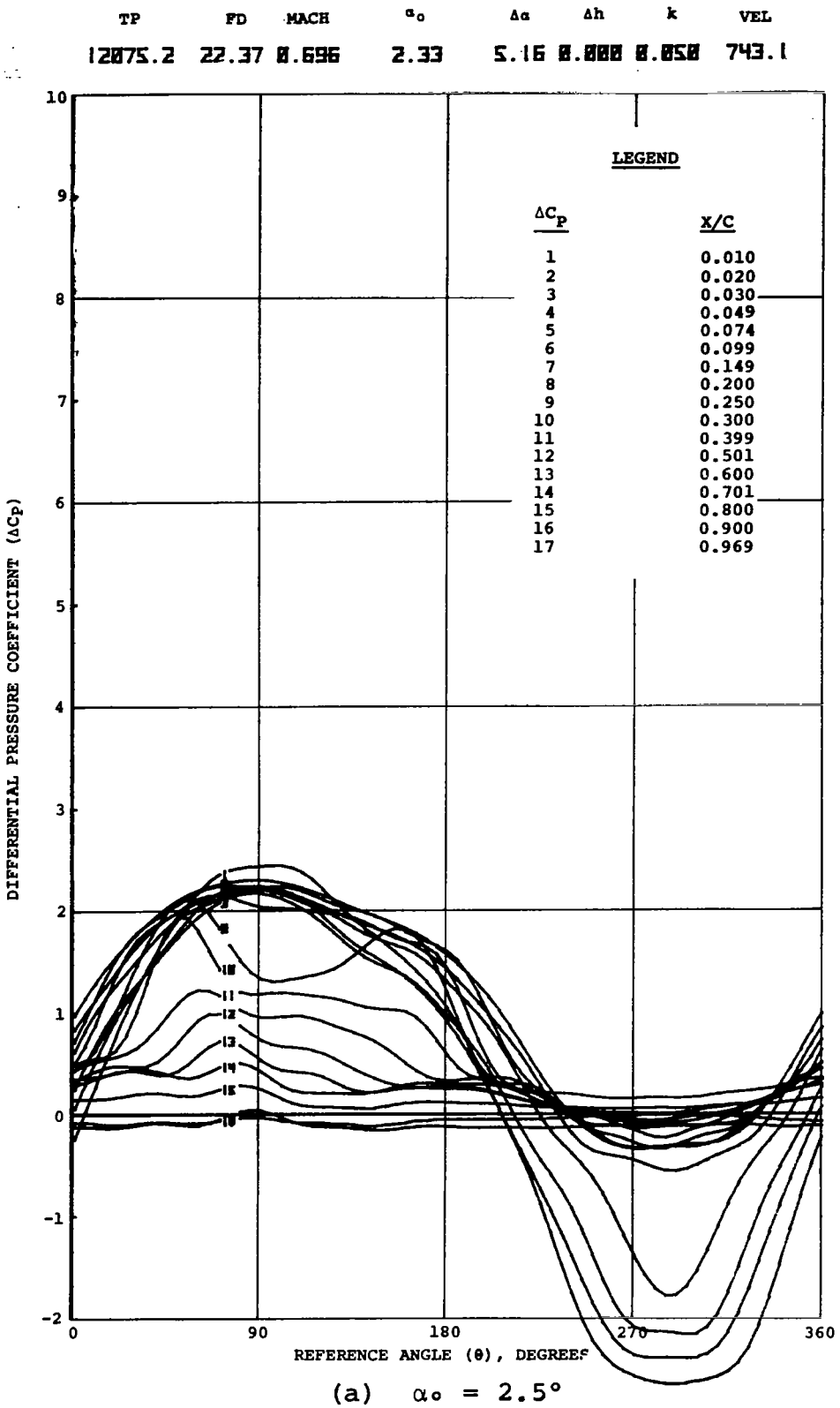

(a) α_o = 2.5°

Figure 21. Effect of mean angle-of-attack variation on the local differential pressures over the NLR 7223-62 airfoil. Nominal conditions: M = 0.7, Rn = 10 x 10^6, f_D = 23.0 Hz, $\Delta\alpha$ = 5.0°

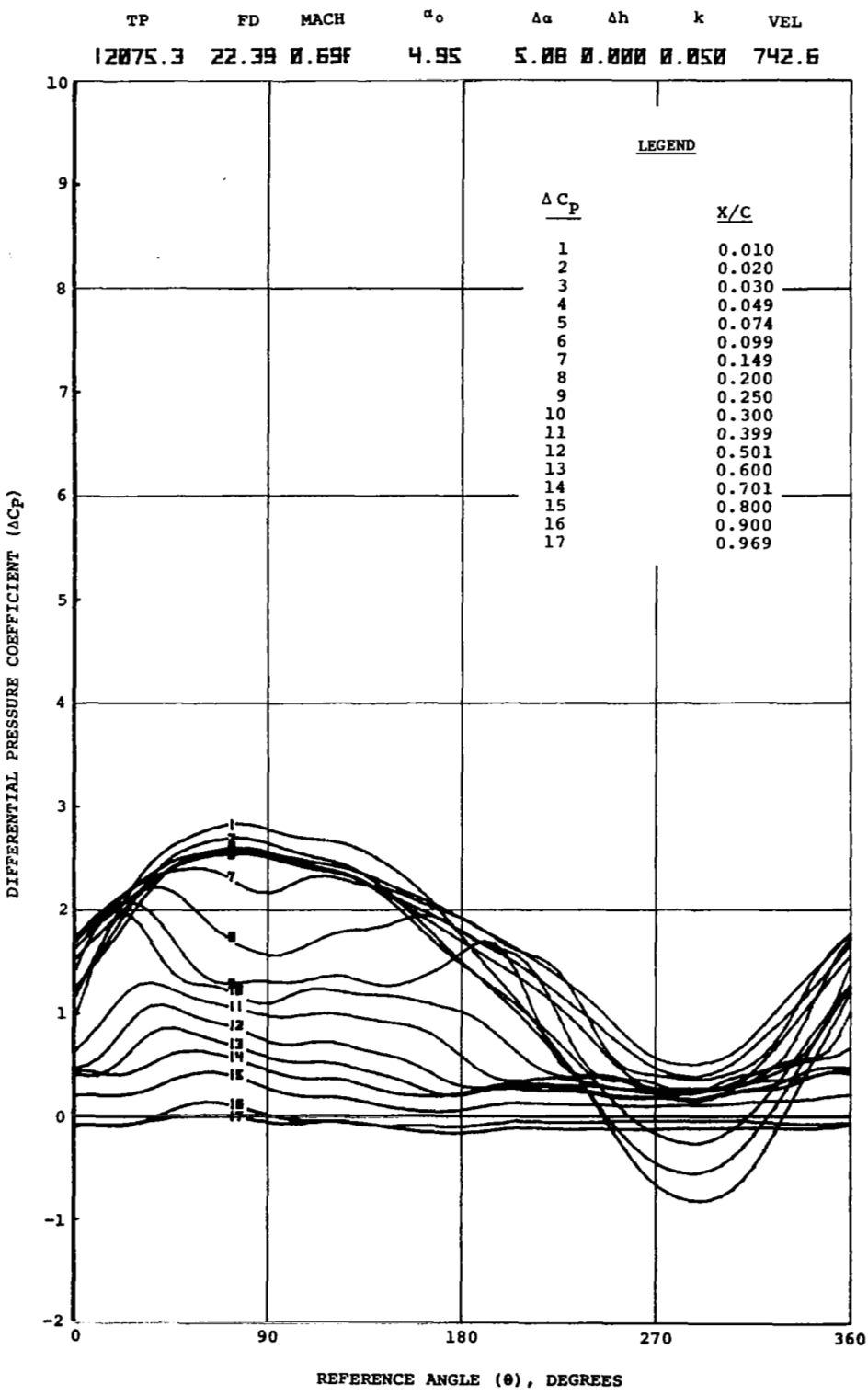

(b) $\alpha_o = 5.0°$

Figure 21. Continued

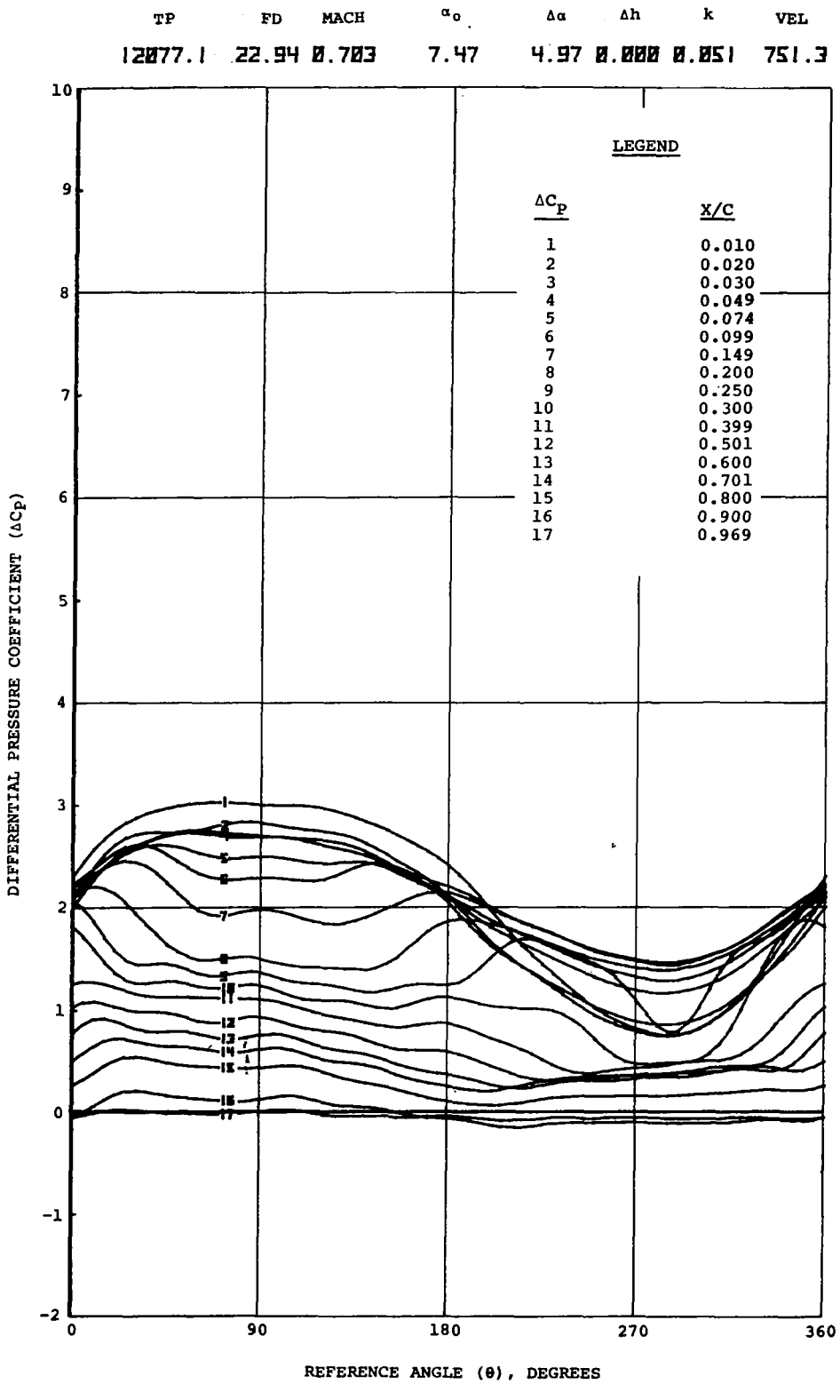

(c) $\alpha_o = 7.5°$

Figure 21. Continued

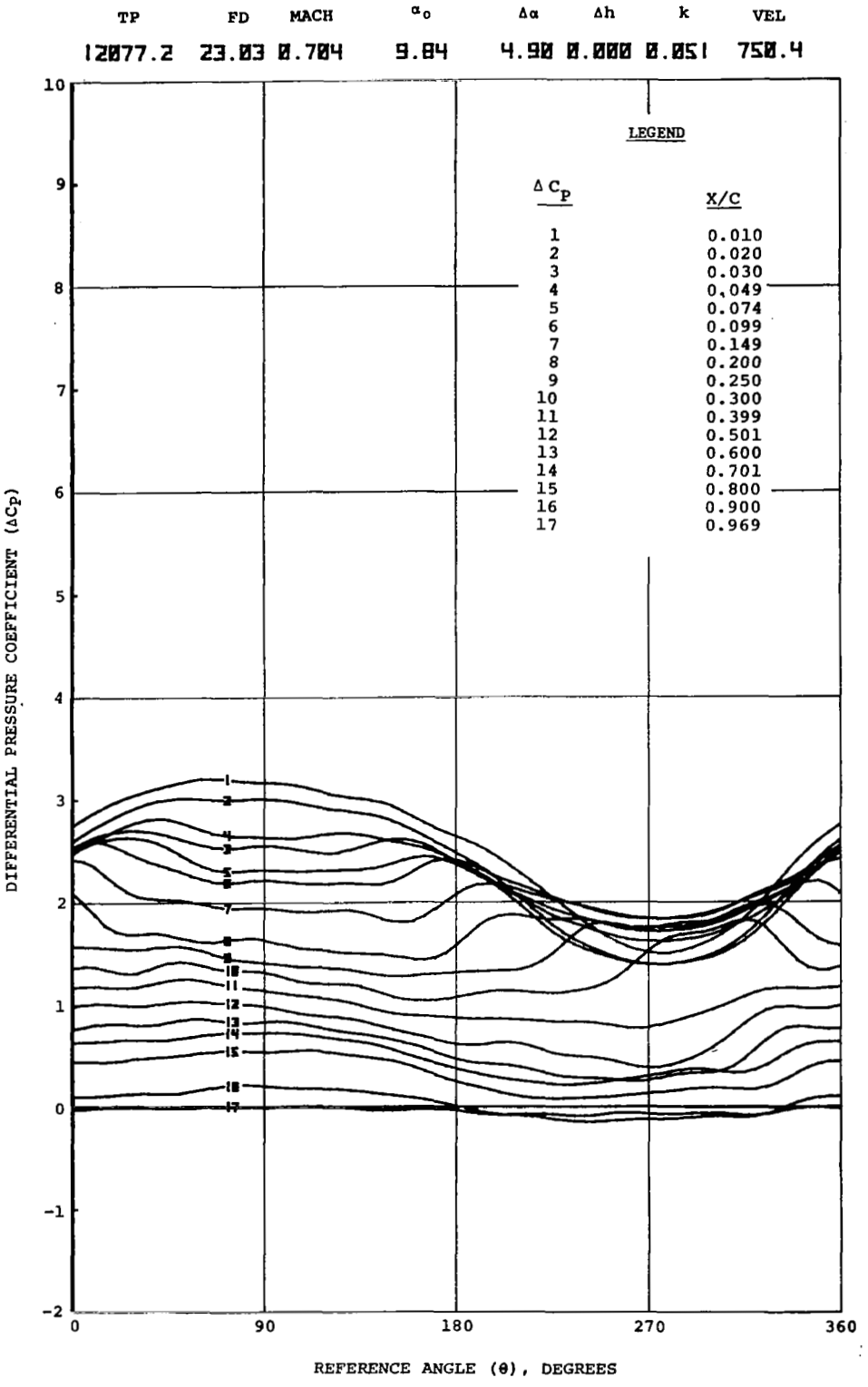

(d) $\alpha_o = 10.0°$

Figure 21. Continued

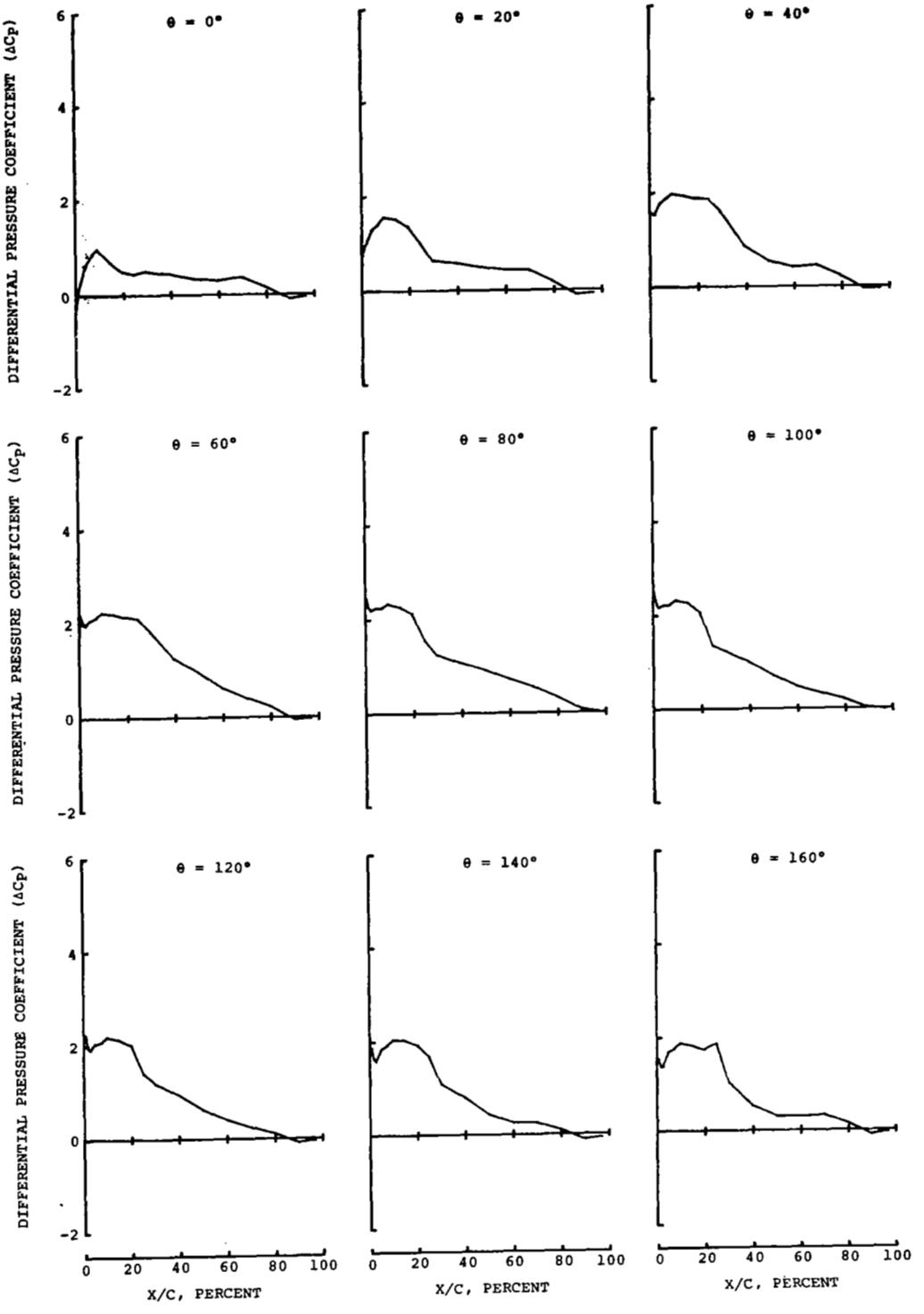

Figure 22. Differential pressure distributions over the NLR 7223-62 airfoil. Nominal conditions: M = 0.7, Rn = 10 x 10^6, f_D = 23.0 Hz, $\Delta\alpha$ = 5.0°, α_o = 2.5° (T.P. 12075.2).

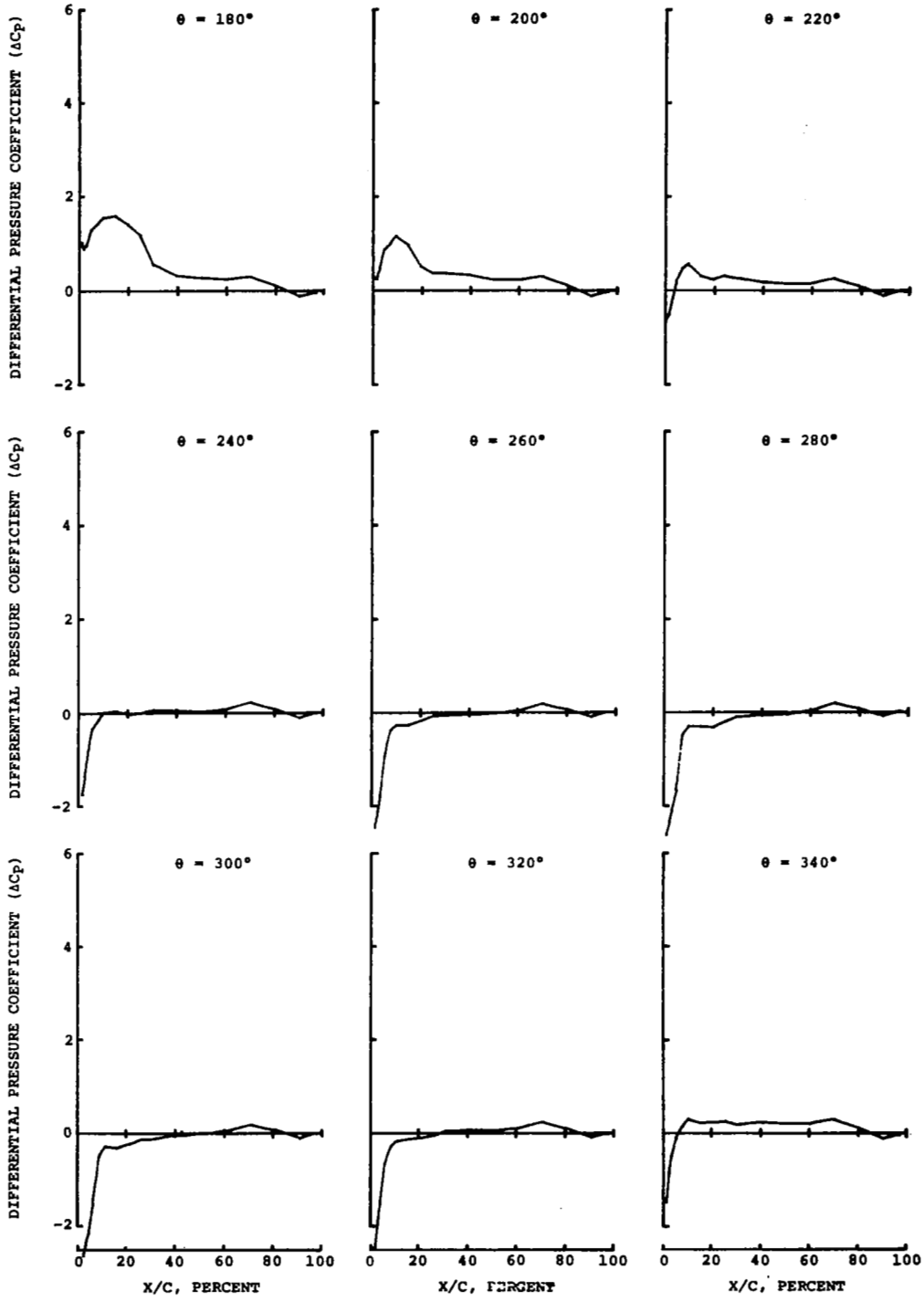

Figure 22. Concluded

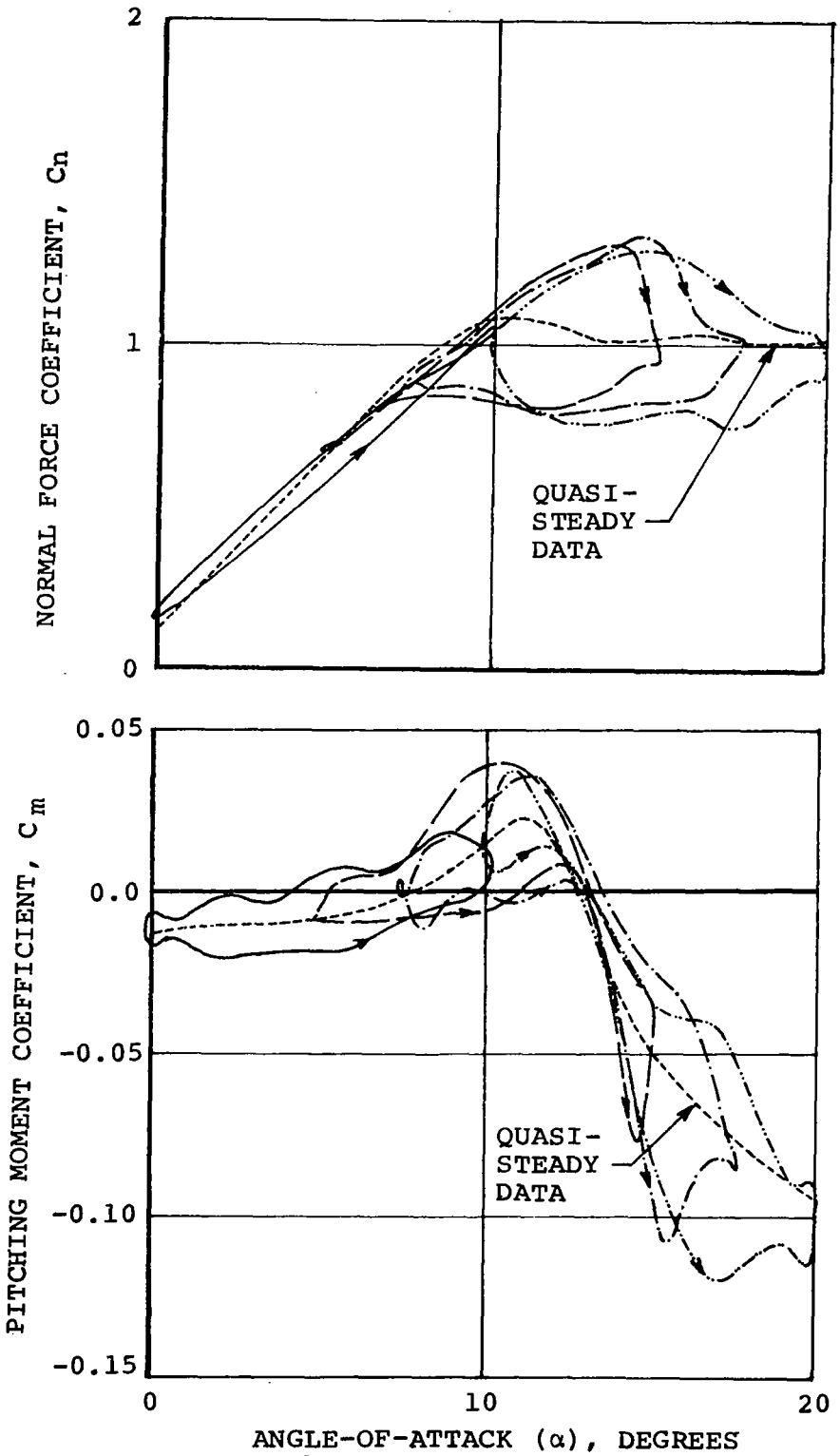

Figure 23. Overlay of normal-force and pitching moment loops of the NLR 7223-62 airfoil to illustrate the effect of mean angle-of-attack variation. Nominal conditions: M=0.4, Rn=6.4x10^6, f_D=23.0 Hz, $\Delta\alpha$=5.0, α_o=5.0° to 15.0°.

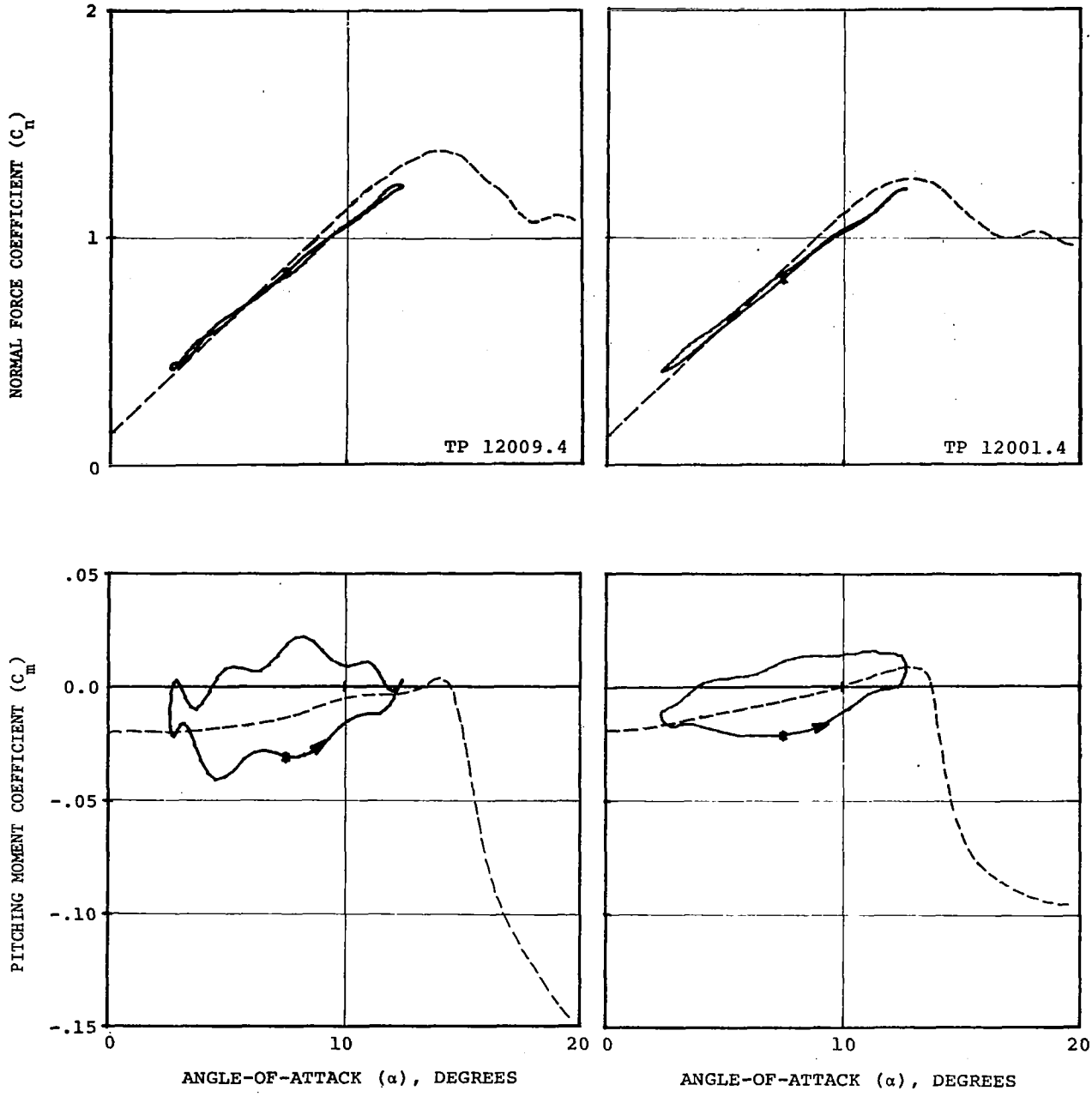

(a) M = 0.2 (b) M = 0.3

Figure 24. Effect of Mach-number variation on the dynamic-stall characteristics of the normal-force and pitching-moment coefficients of the NLR 7223-62 airfoil. Nominal conditions: f_D = 23.0 Hz, α_o = 7.5°, $\Delta\alpha$ = 5.0°.

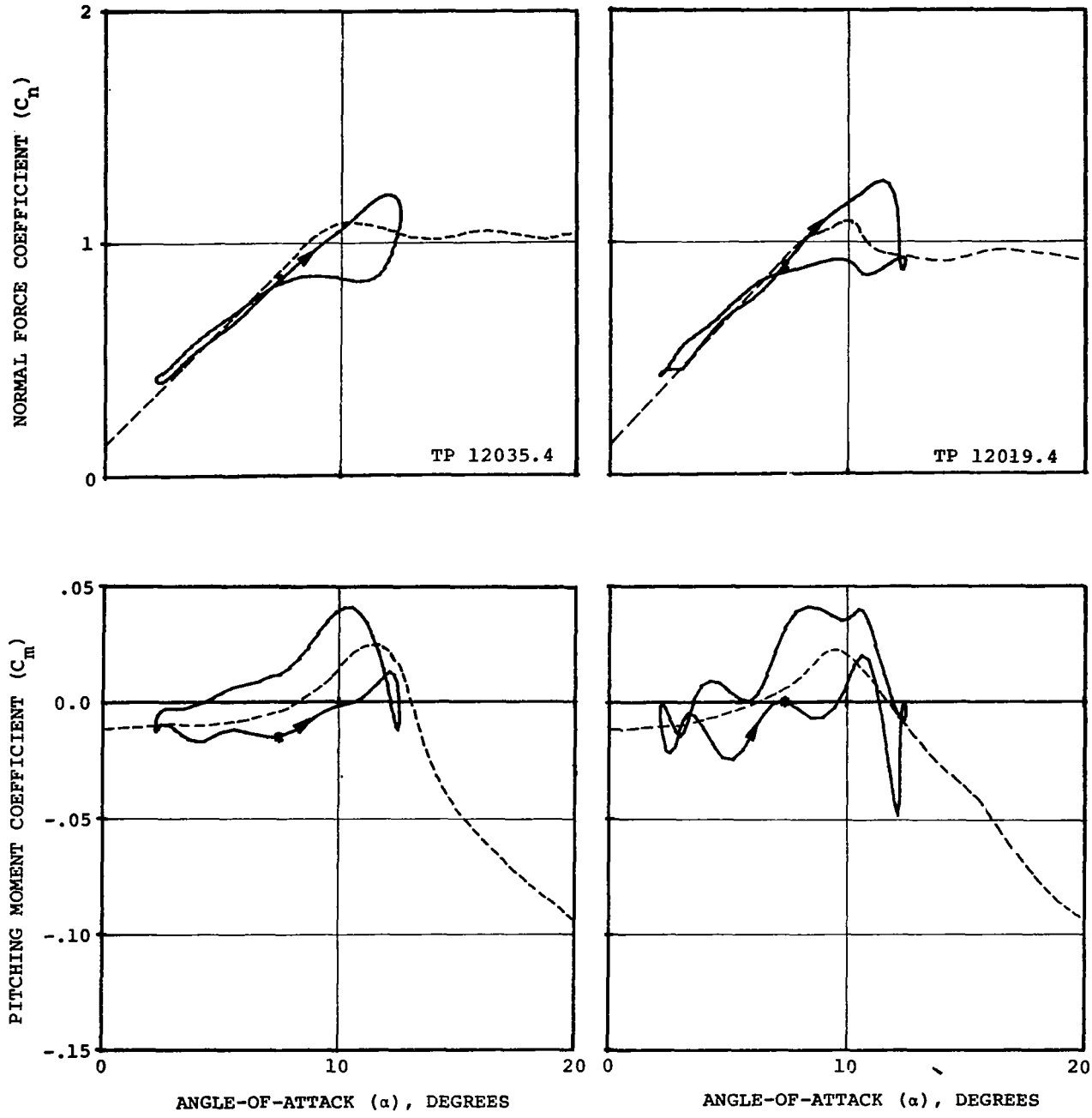

(c) M = 0.4

(d) M = 0.5

Figure 24. Continued

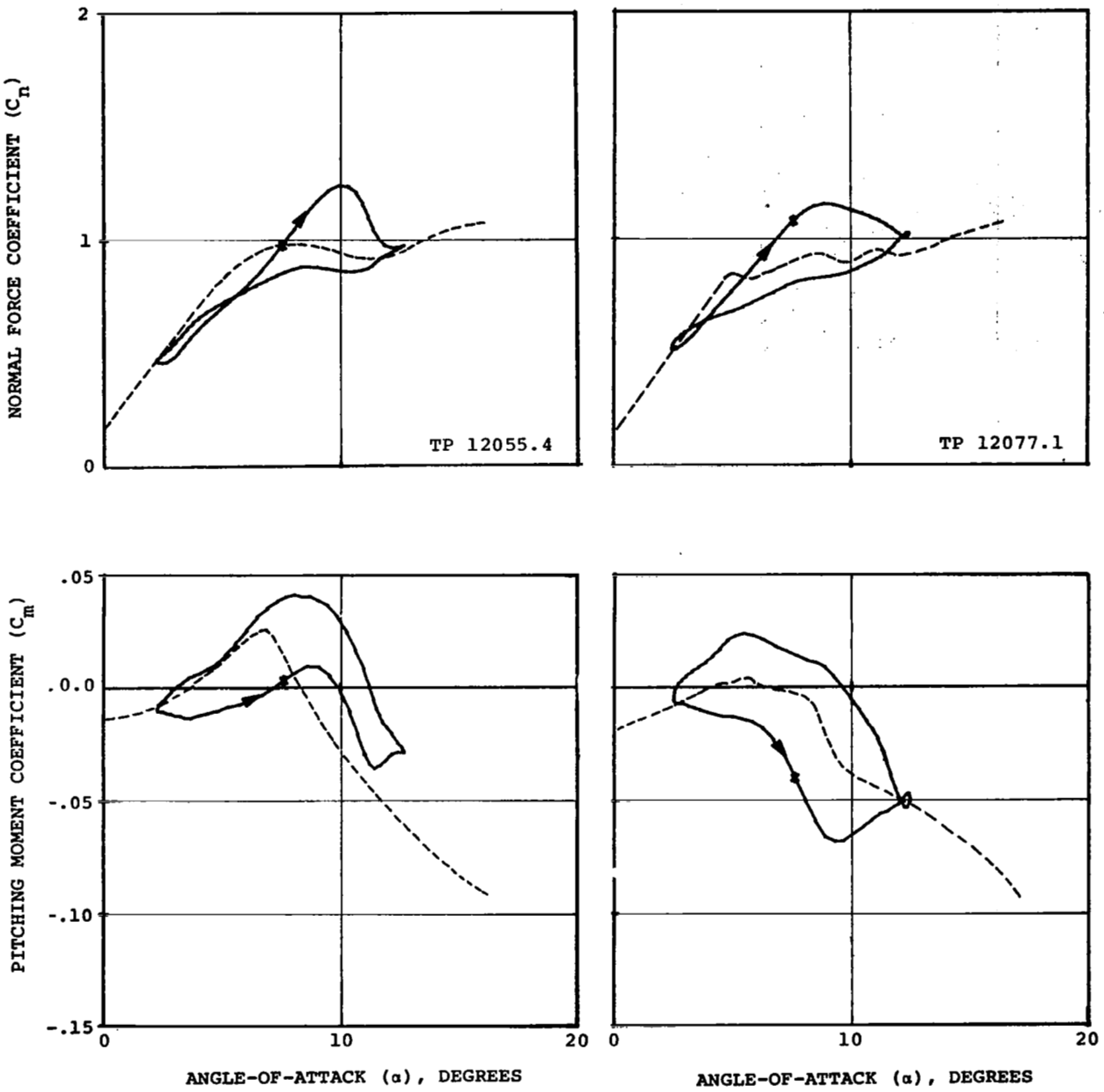

(e) M = 0.6

(f) M = 0.7

Figure 24. Concluded

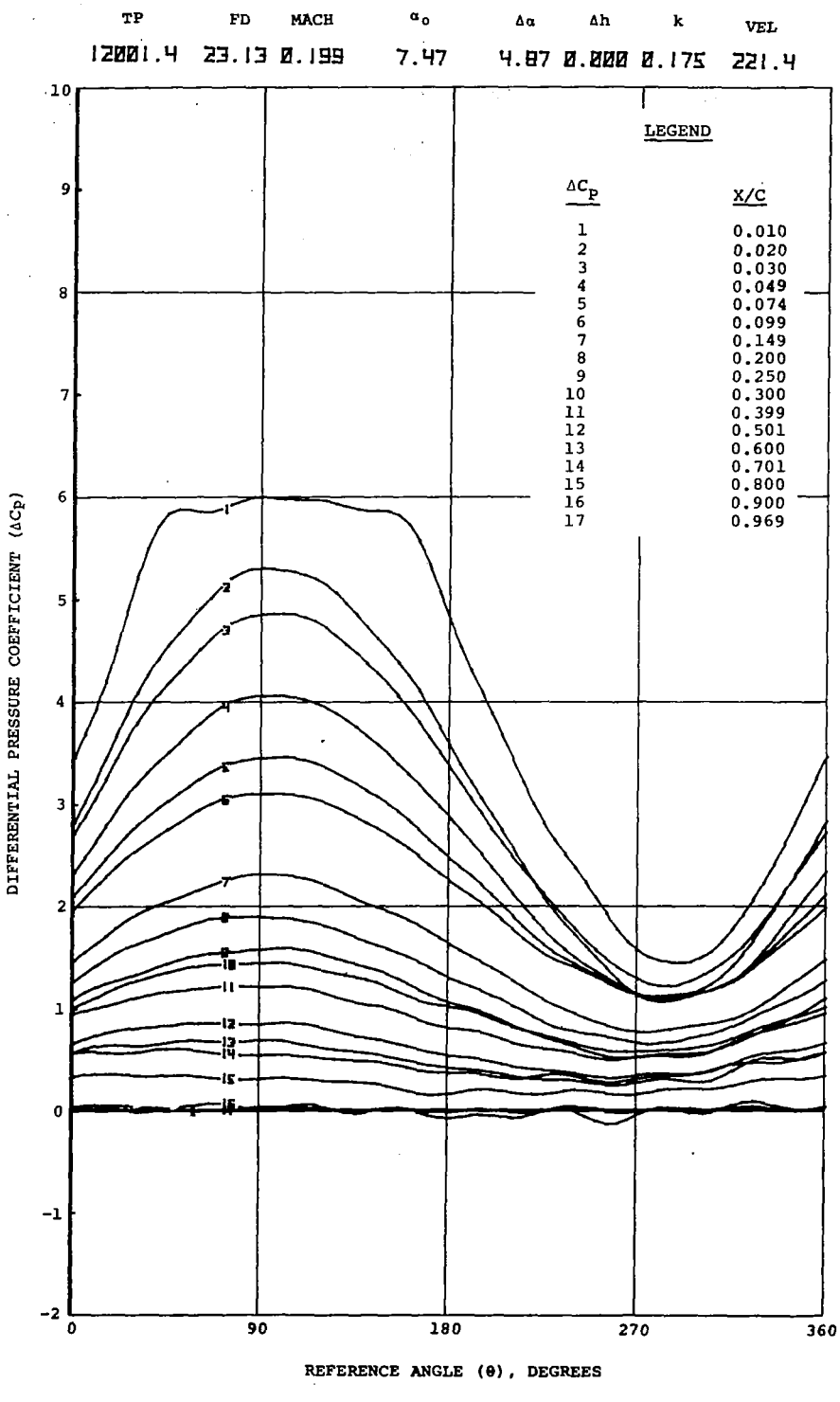

(a) M = 0.2

Figure 25. Effect of Mach number variation on the local differential pressures over the NLR 7223-62 airfoil. Nominal conditions: f_D = 23.0 Hz, α_o = 7.5°, $\Delta\alpha$ = 5.0°.

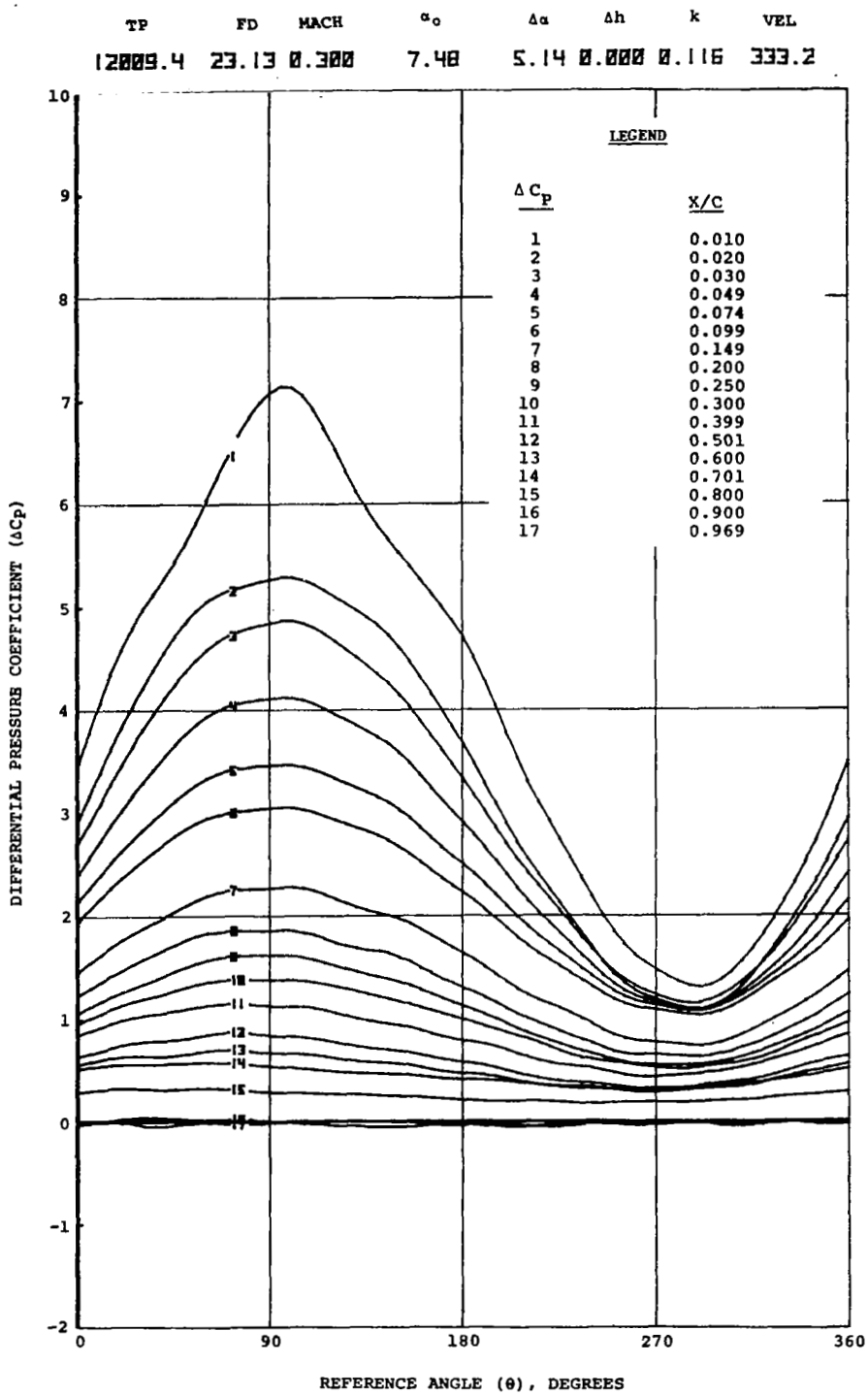

(b) M = 0.3

Figure 25. Continued

TP	FD	MACH	α_o	$\Delta\alpha$	Δh	k	VEL
12019.4	23.15	0.398	7.48	5.16	0.000	0.000	439.6

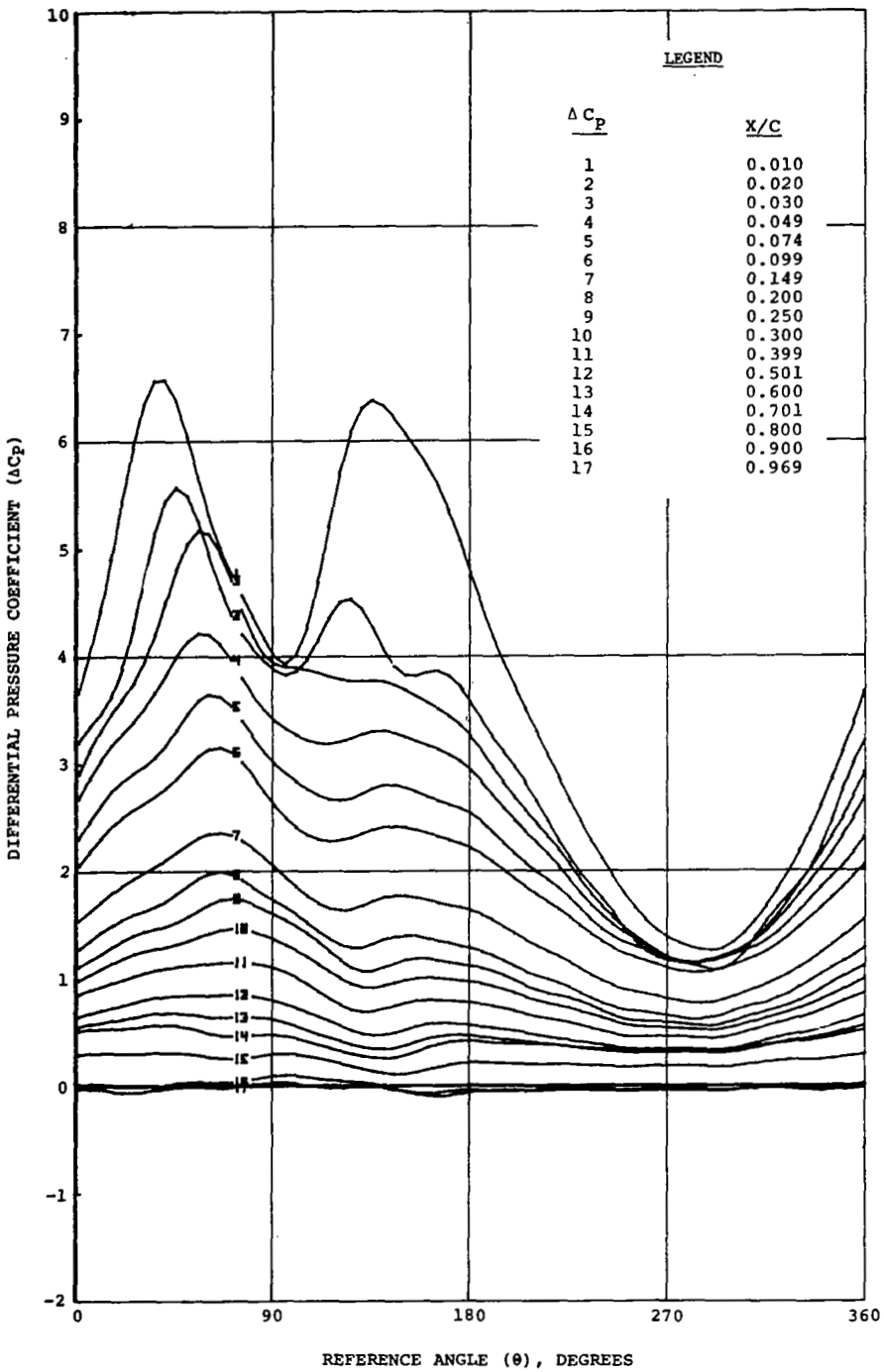

(c) M = 0.4

Figure 25. Continued

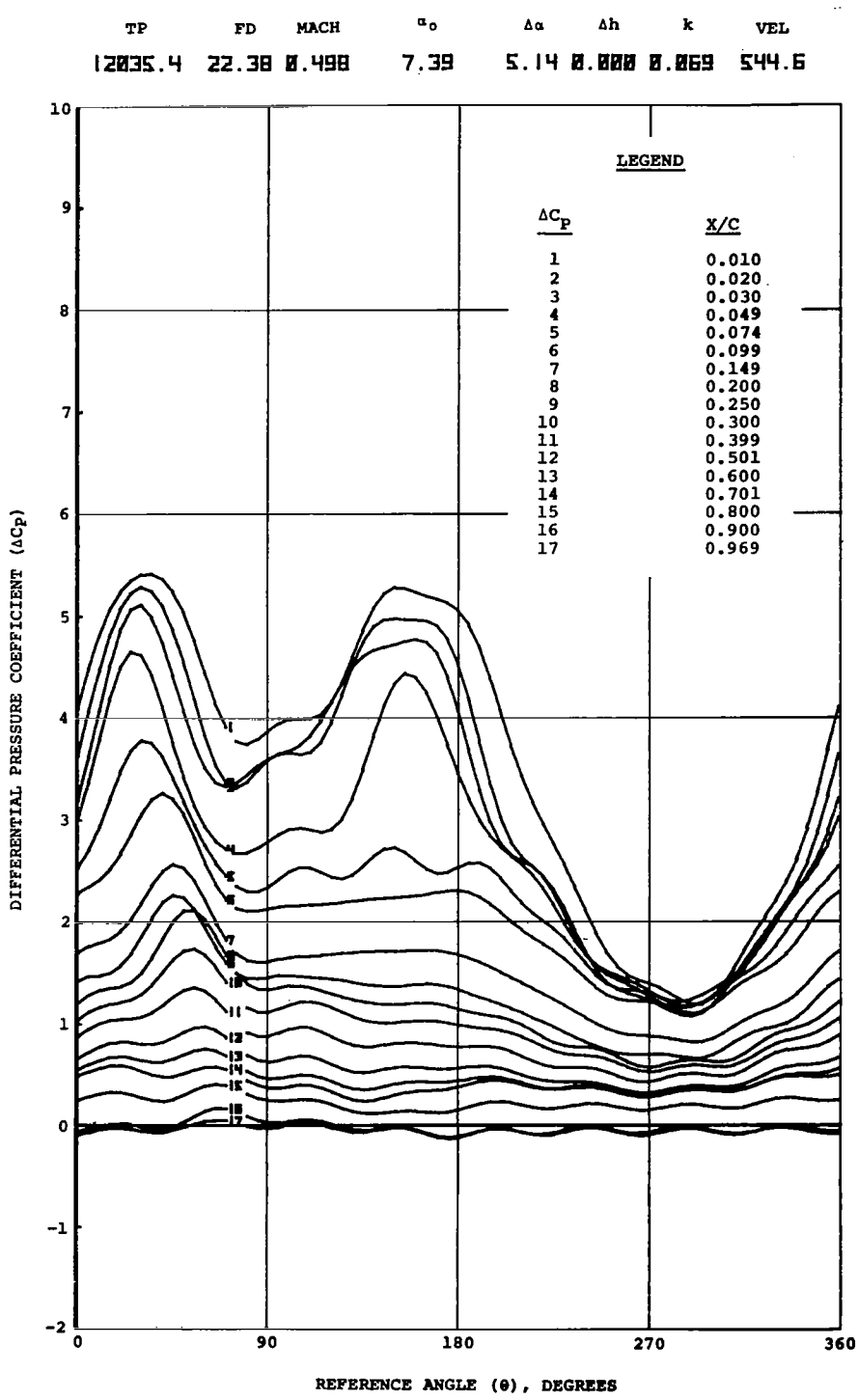

(d) M = 0.5

Figure 25. Continued

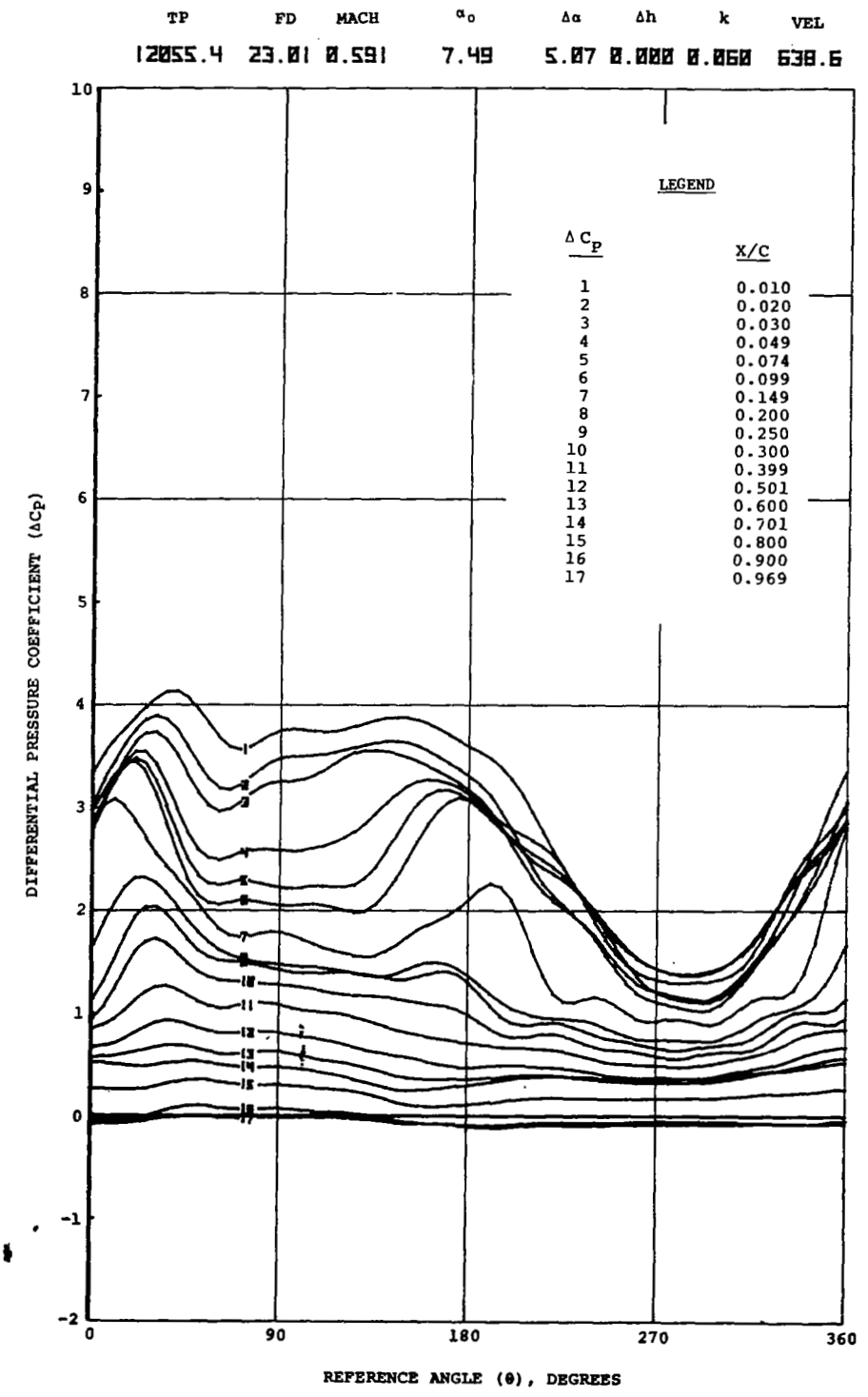

(e) M = 0.6

Figure 25. Continued

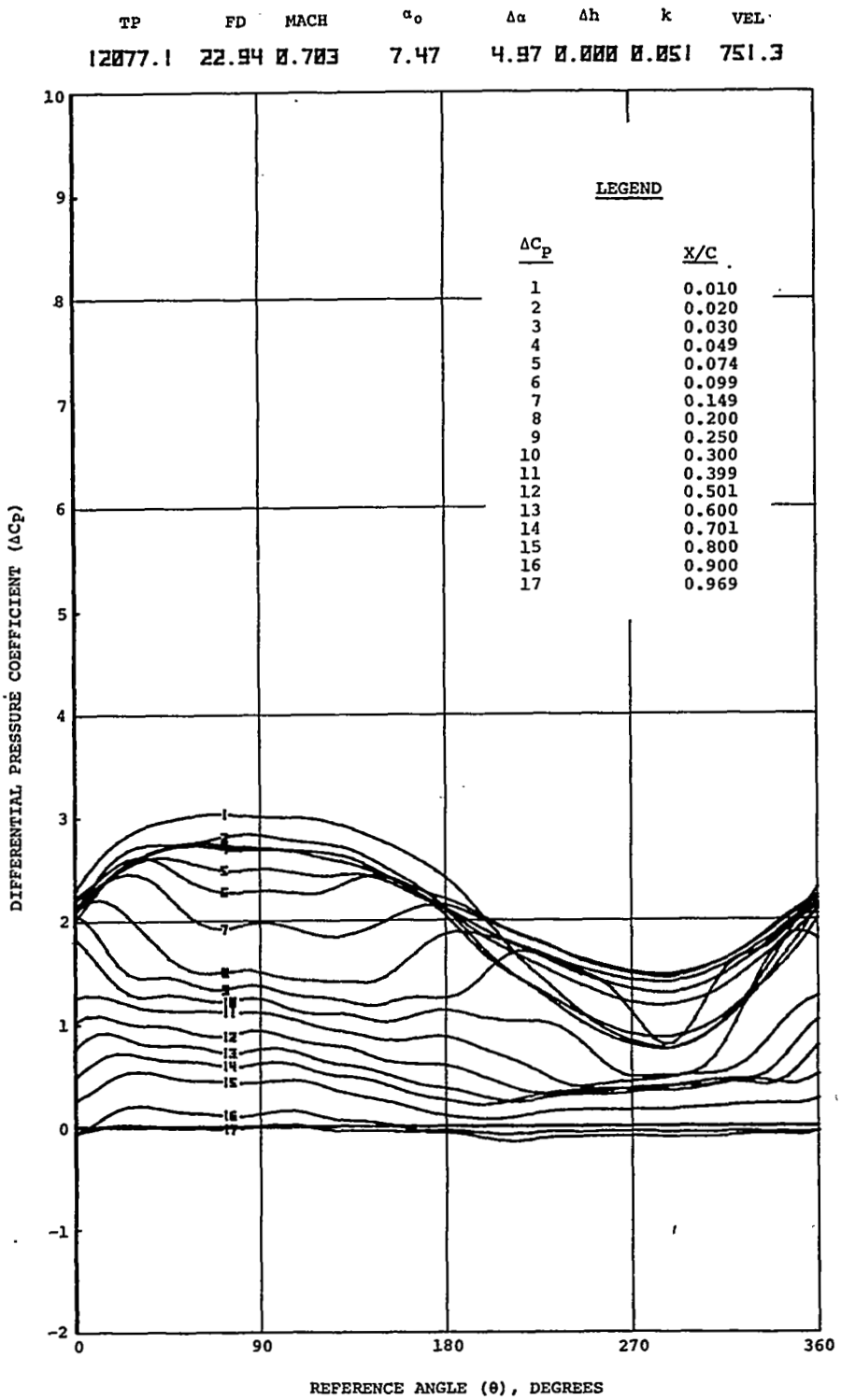

(f) M = 0.7

Figure 25. Concluded

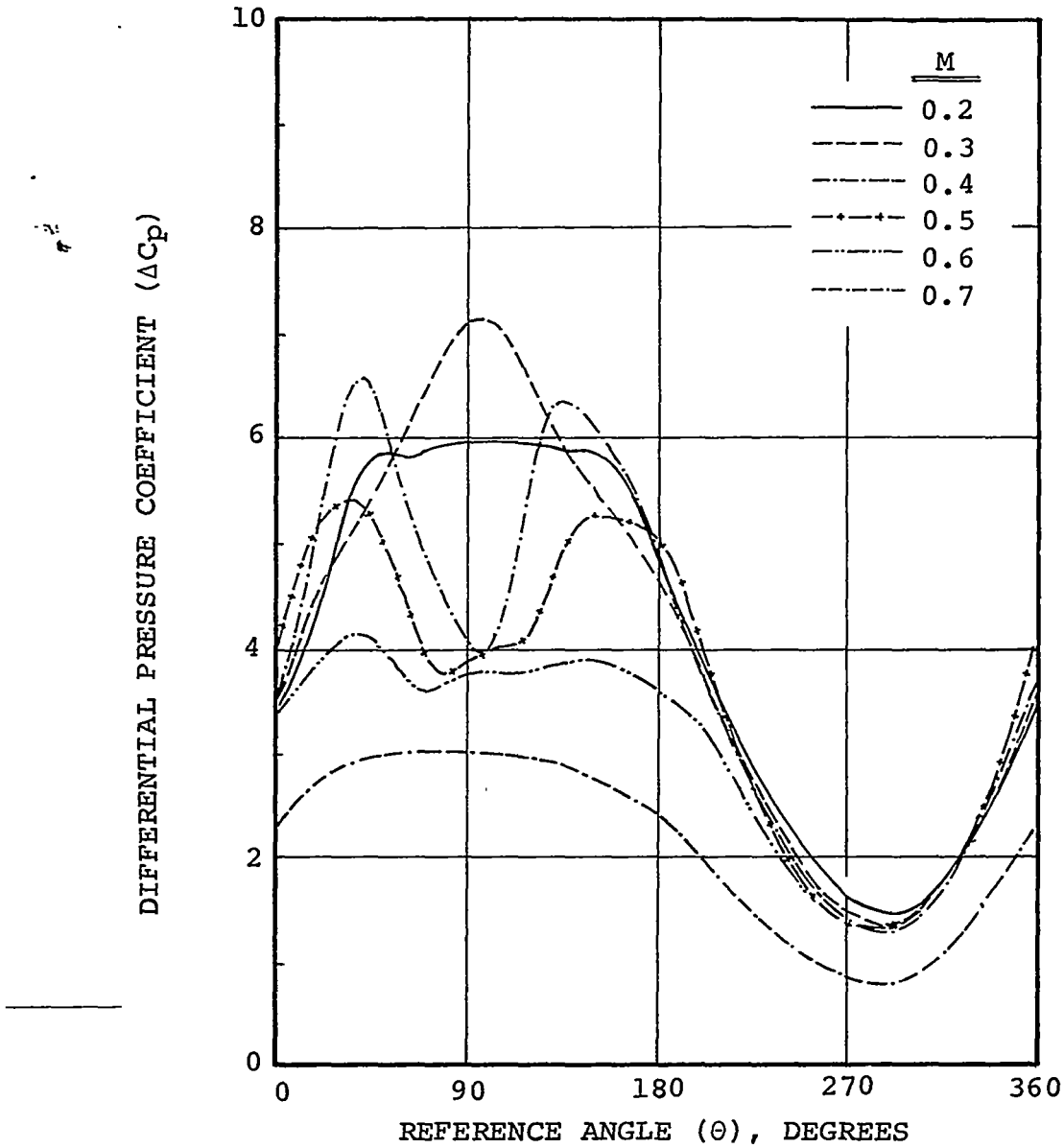

Figure 26. Effect of Mach number variation on the differential pressure at the 1% chord station of the NLR 7223-62 airfoil. Nominal conditions: α_o=7.5°, $\Delta\alpha$=5.0°, f_D=23 Hz, M=0.2 to 0.7.

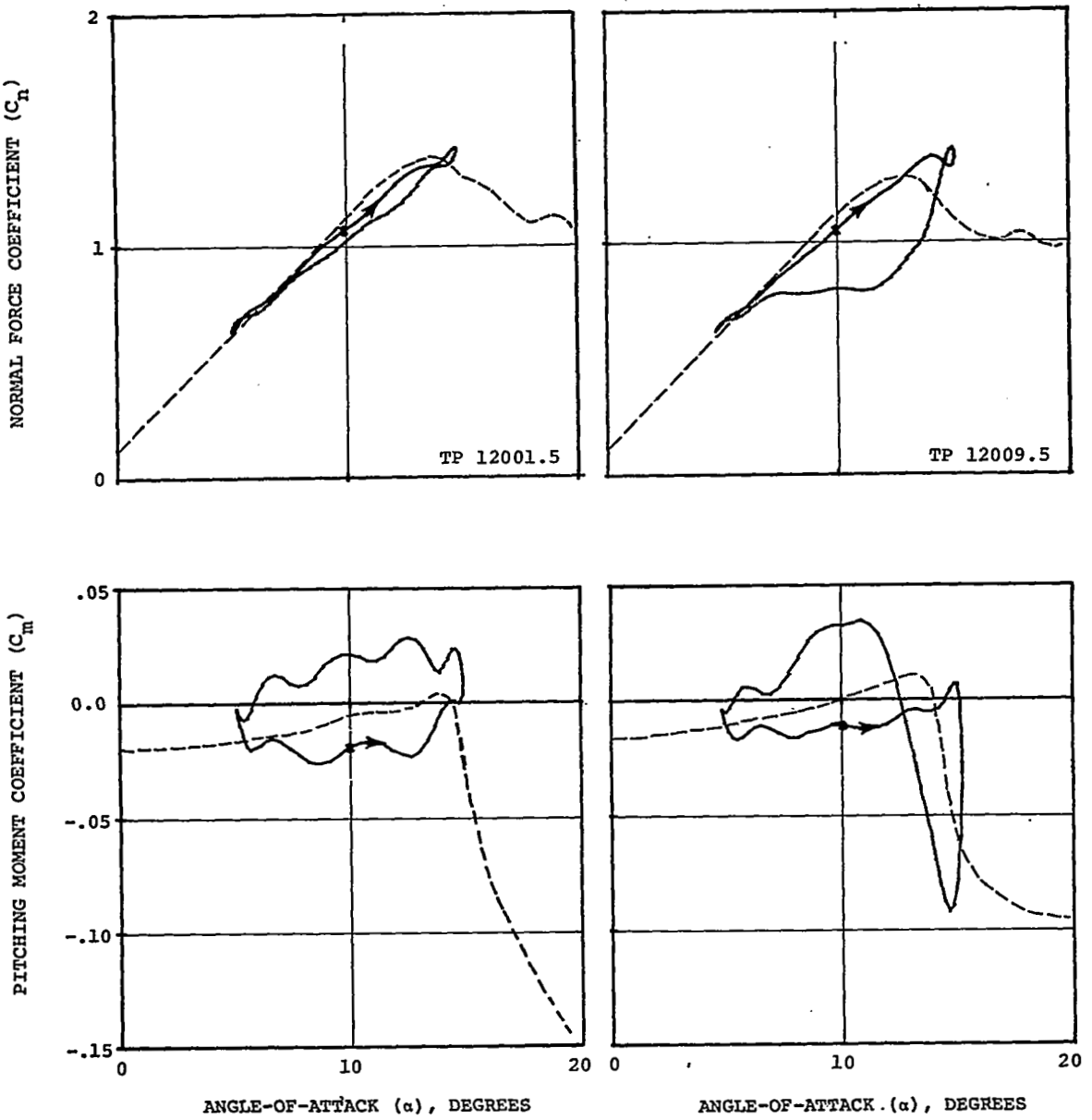

(a) M = 0.2 (b) M = 0.3

Figure 27. Effect of Mach number variation on the dynamic stall characteristics of the normal-force and pitching-moment coefficient of the NLR 7223-62 airfoil. Nominal conditions: f_D = 23.0 Hz, α_o = 10.0°, $\Delta\alpha$ = 5.0°.

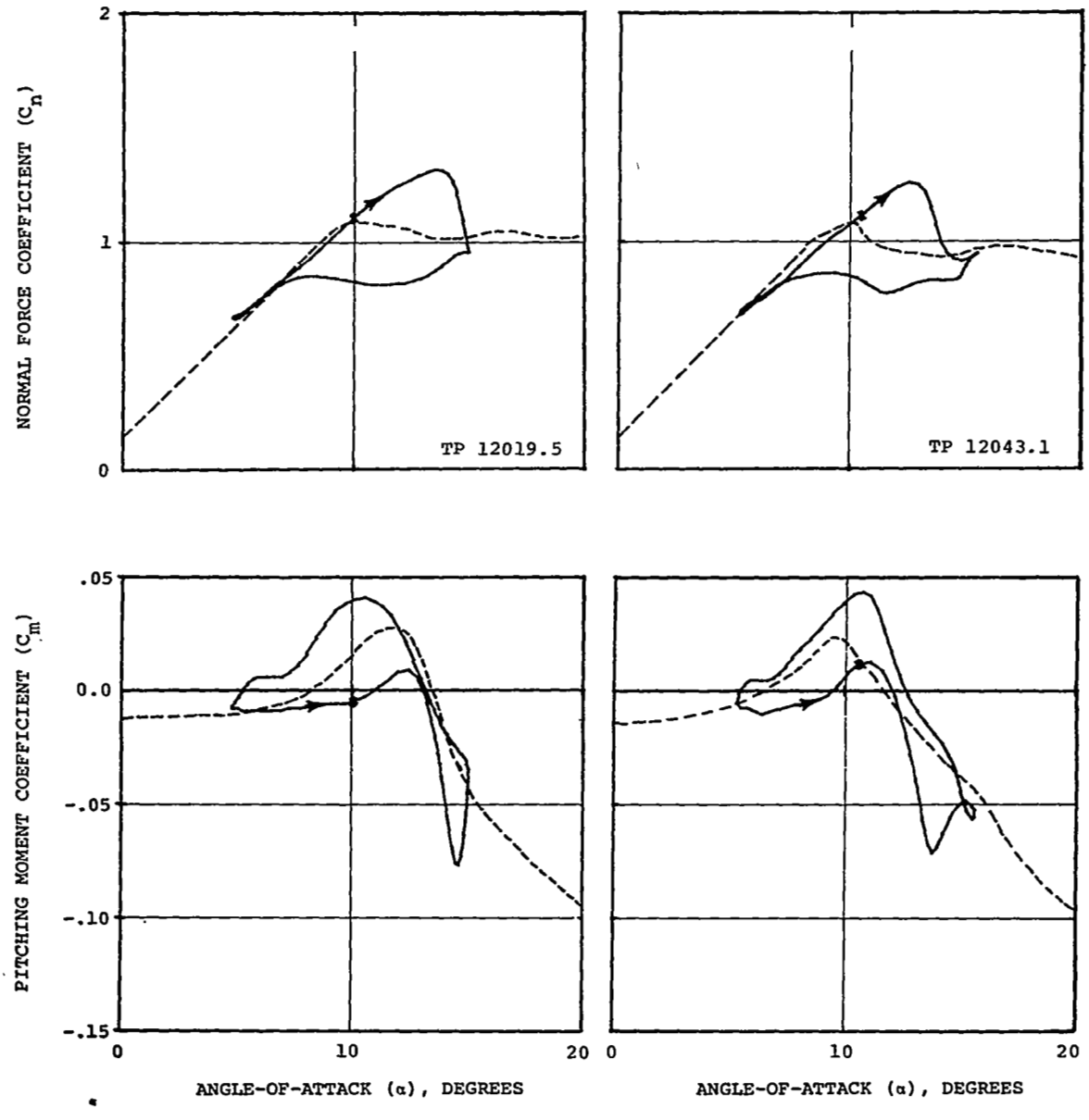

(c) M = 0.4 (d) M = 0.5

Figure 27. Continued

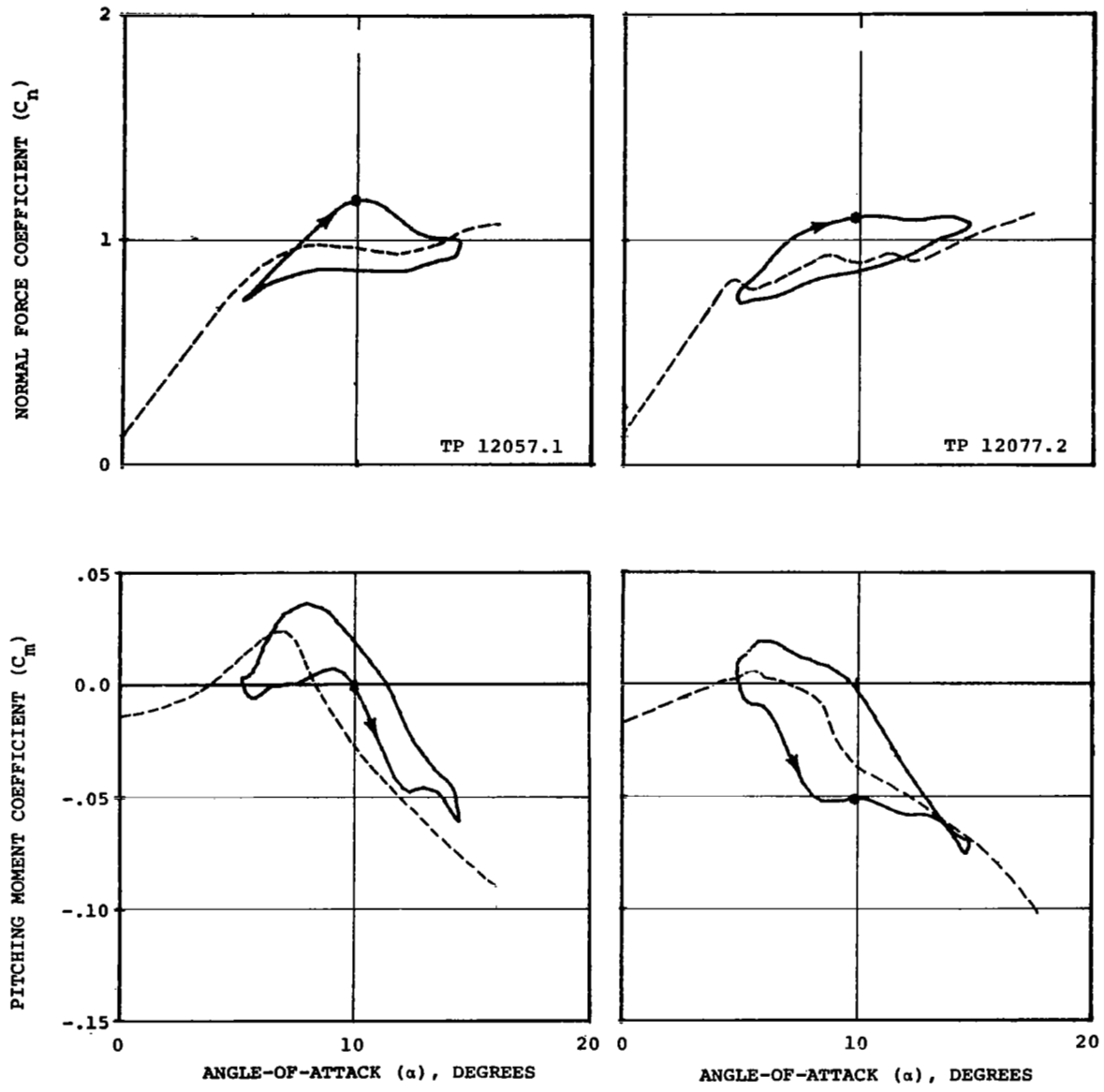

(e) M = 0.6

(f) M = 0.7

Figure 27. Concluded

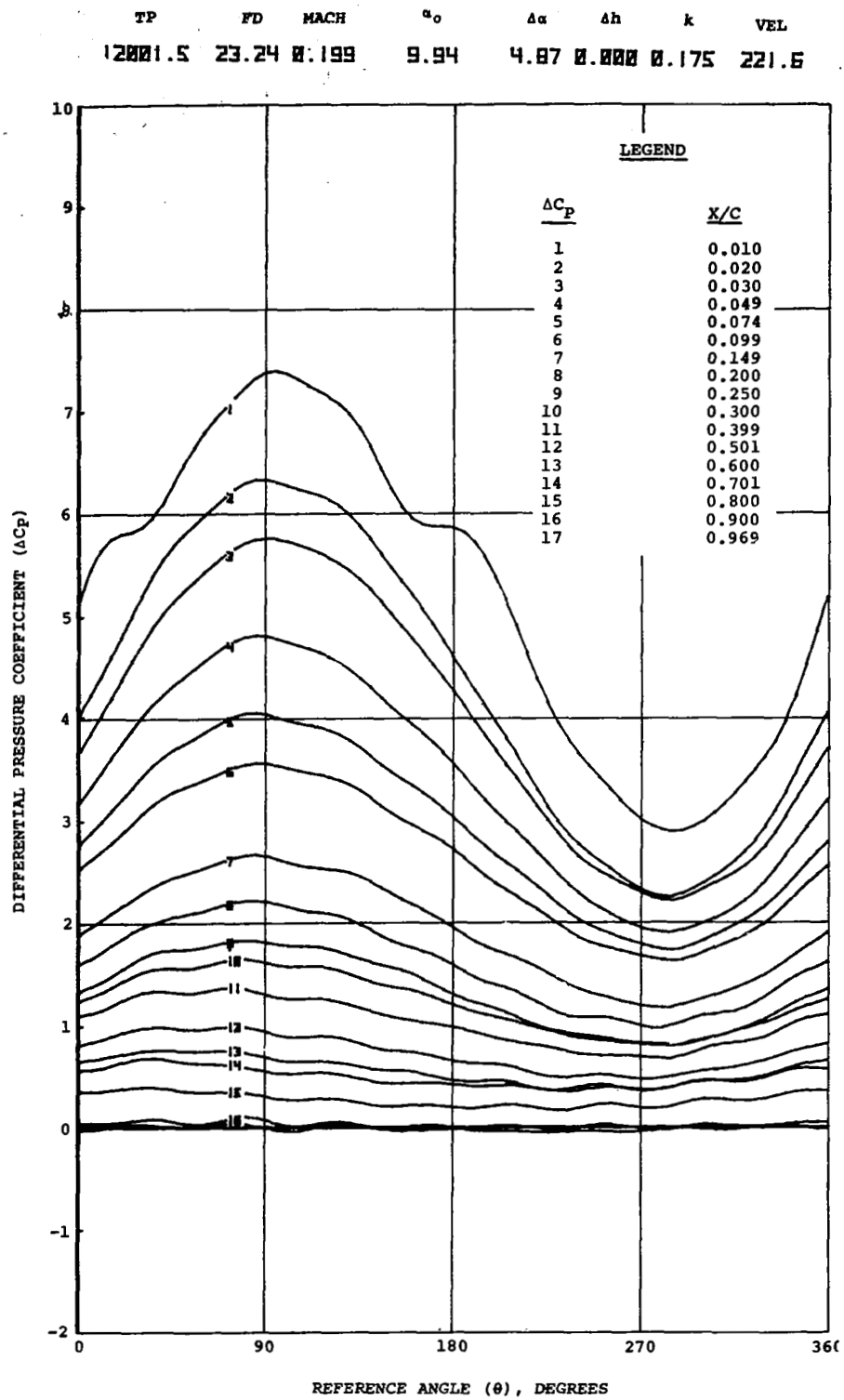

(a) M = 0.2

Figure 28. Effect of Mach number variation on the local differential pressures over the NLR 7223-62 airfoil. Nominal conditions: f_D = 23.0 Hz, α_o = 10.0°, $\Delta\alpha$ = 5.0°

TP	FD	MACH	α_o	$\Delta\alpha$	Δh	k	VEL
12009.5	23.26	0.300	9.99	5.12	0.000	0.117	331.9

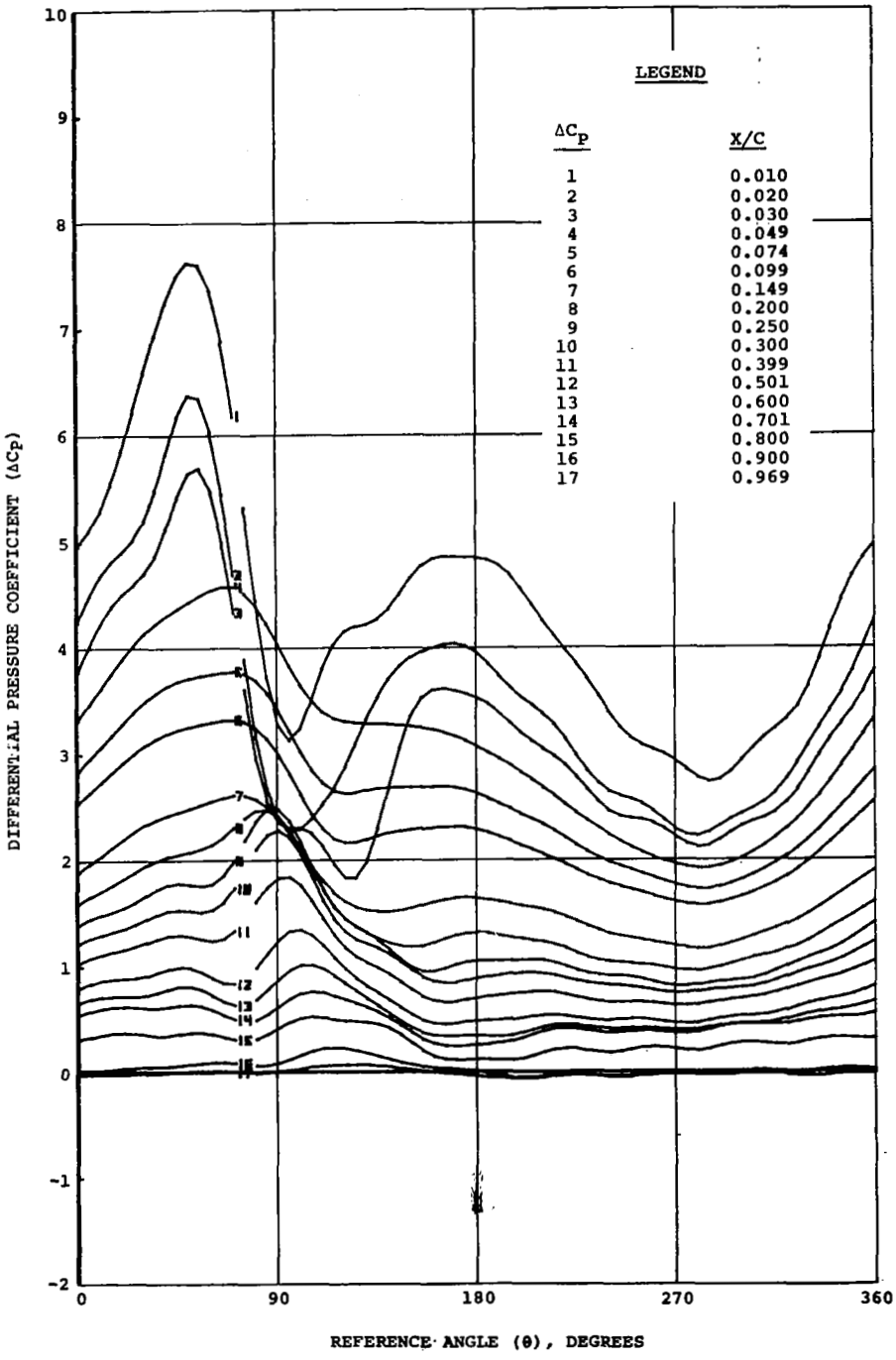

(b) M = 0.3

Figure 28. Continued

TP	FD	MACH	α_o	$\Delta\alpha$	Δh	k	VEL
12019.5	23.08	0.396	9.96	5.11	0.000	0.088	437.6

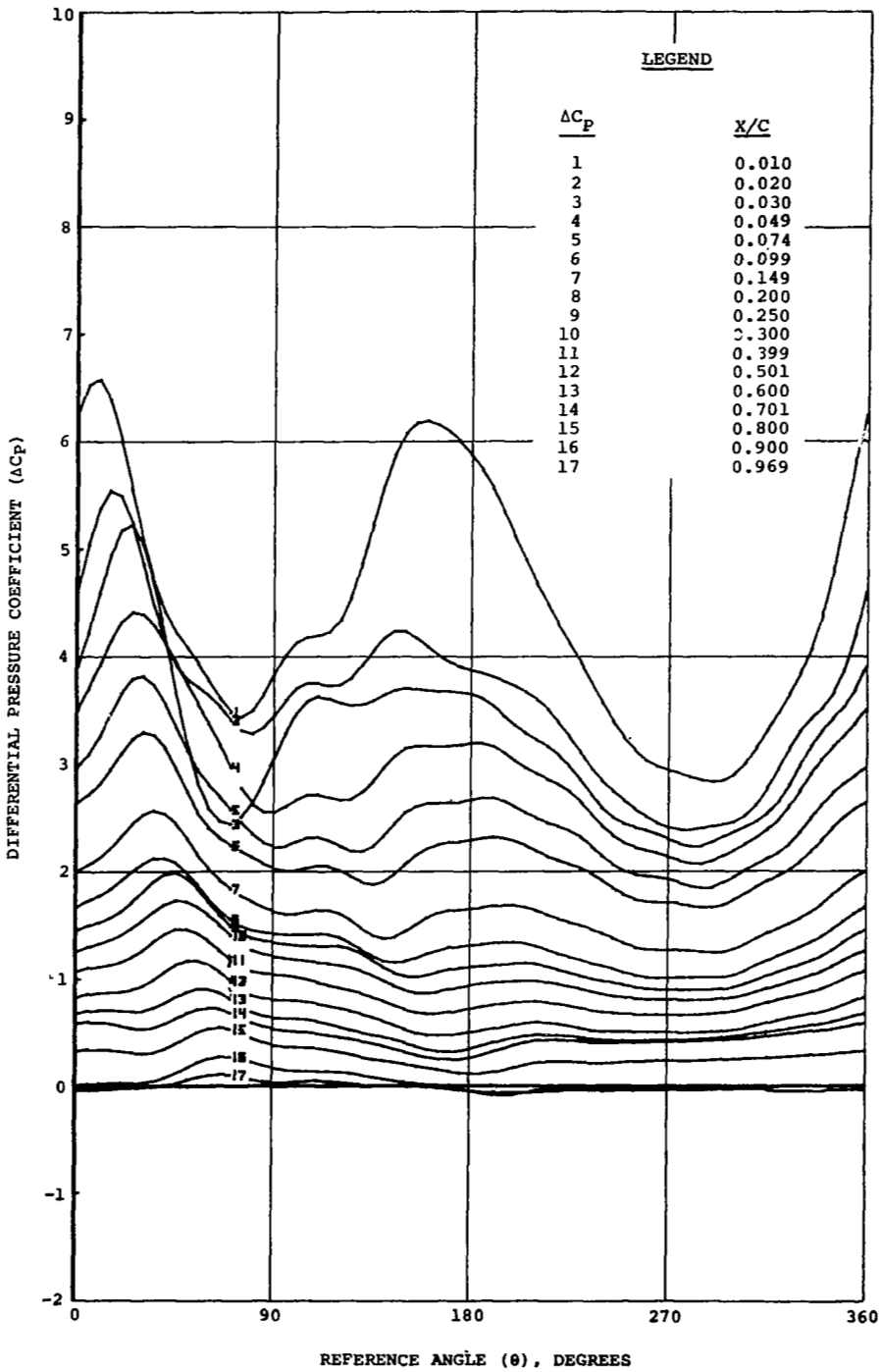

(c) M = 0.4

Figure 28. Continued

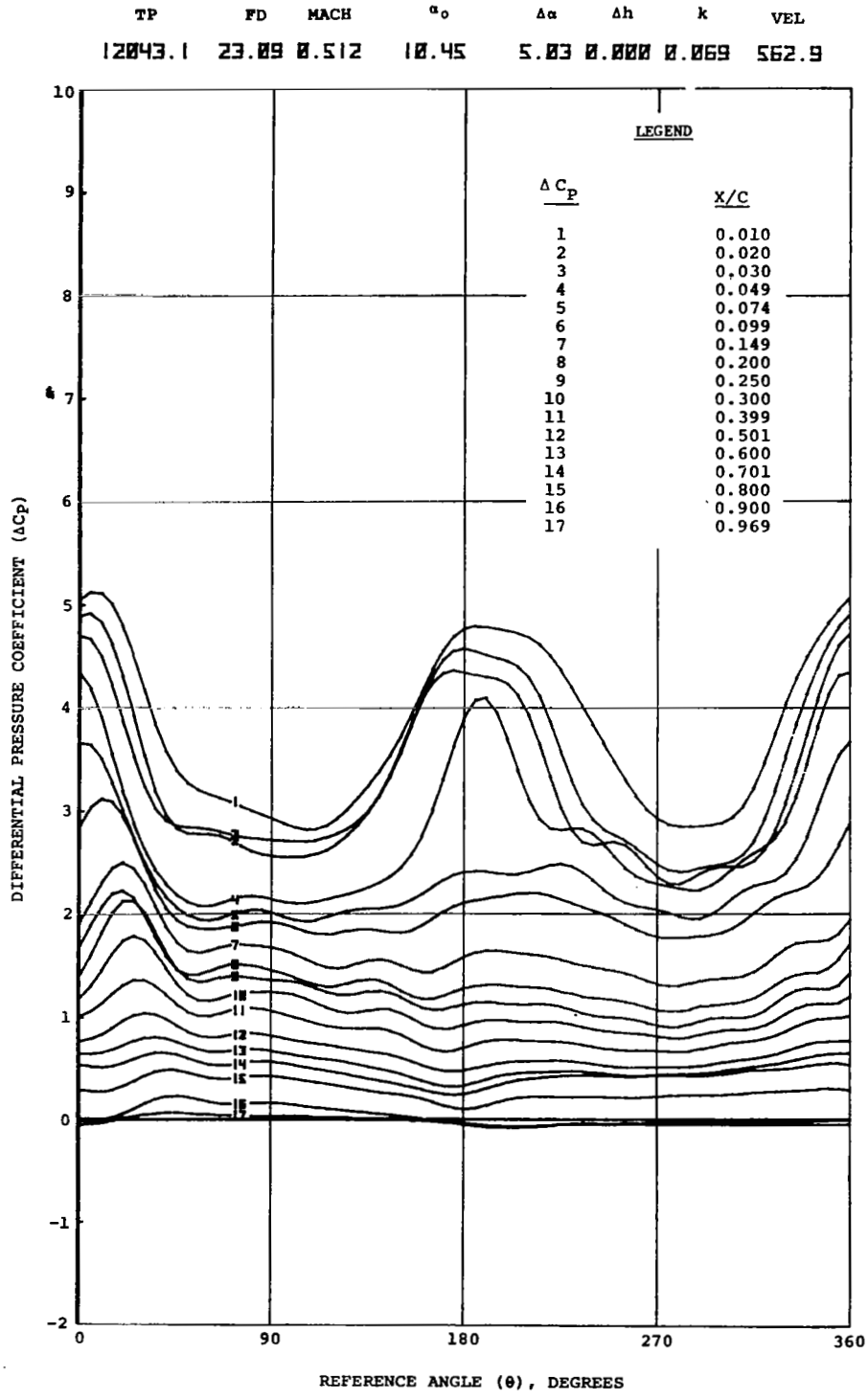

(d) M = 0.5

Figure 28. Continued

TP	FD	MACH	α_o	$\Delta\alpha$	Δh	k	VEL
12057.1	23.17	0.601	9.82	4.59	0.000	0.060	649.7

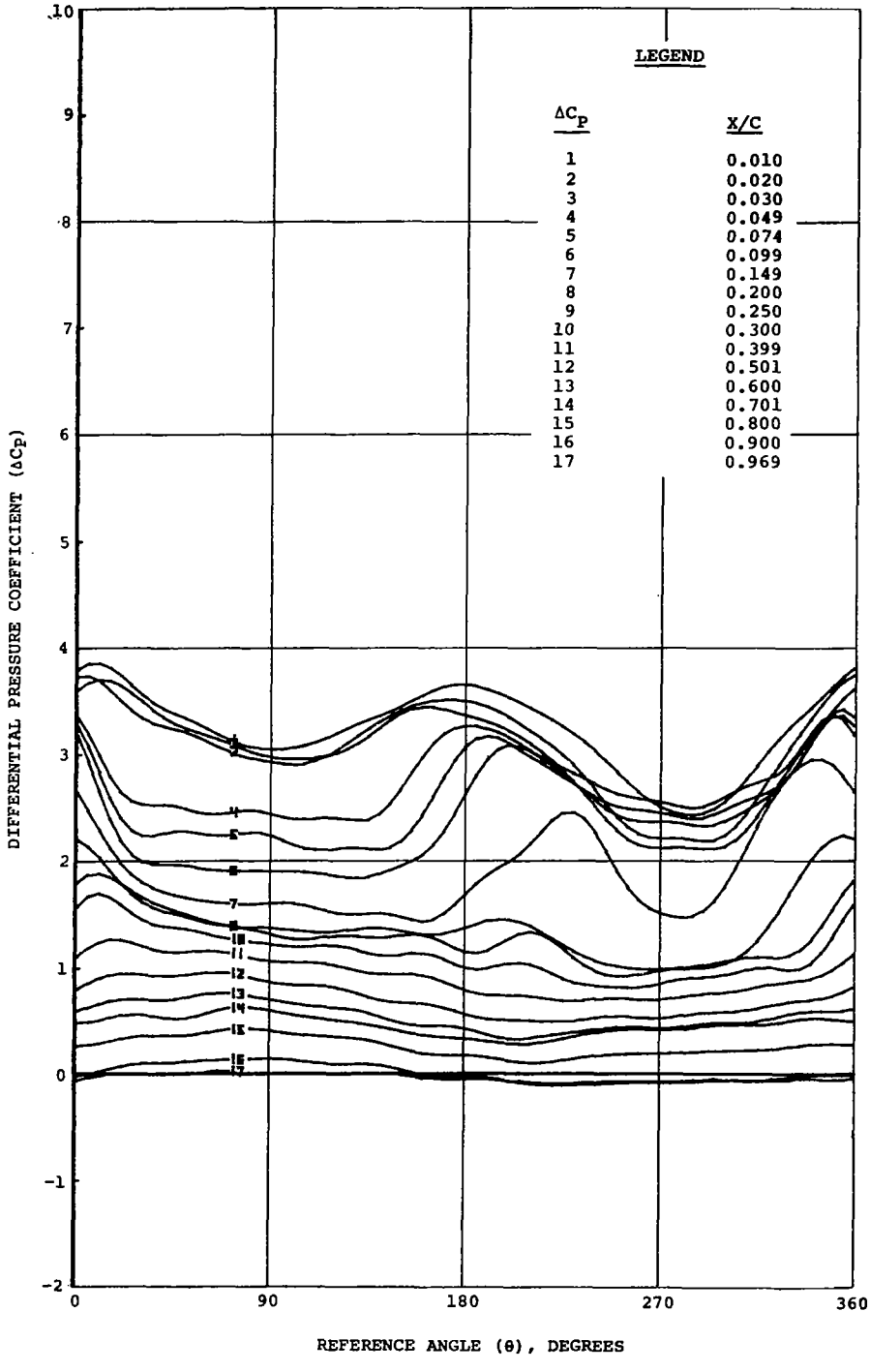

(e) M = 0.6

Figure 28. Continued

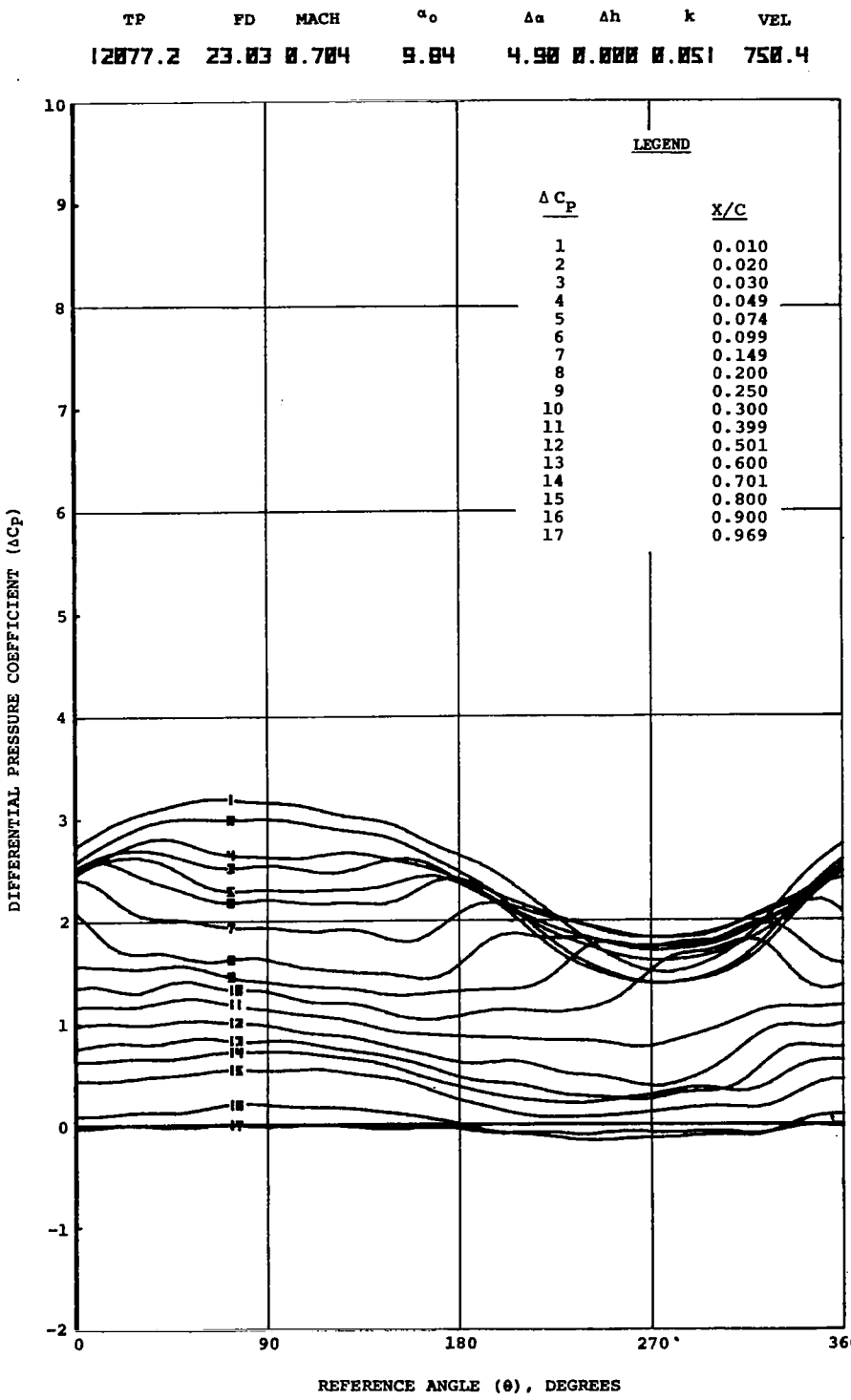

(f) M = 0.7

Figure 28. Concluded

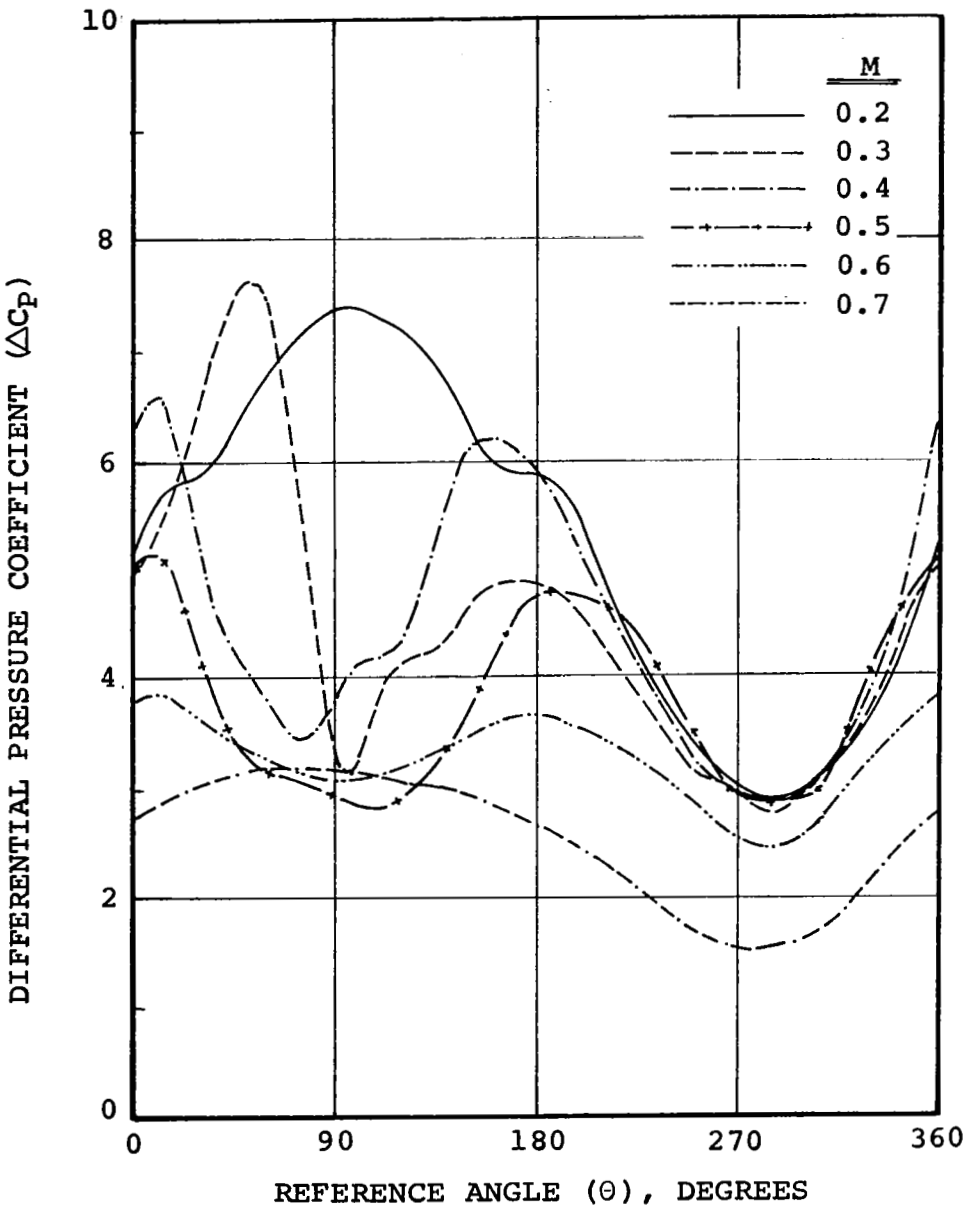

Figure 29. Effect of Mach number variation on the differential pressure at the 1% chord station of the NLR 7223-62 airfoil. Nominal conditions: α_o=10.0°, $\Delta\alpha$=5.0°, f_D=23.0 Hz, M=0.2 to 0.7.

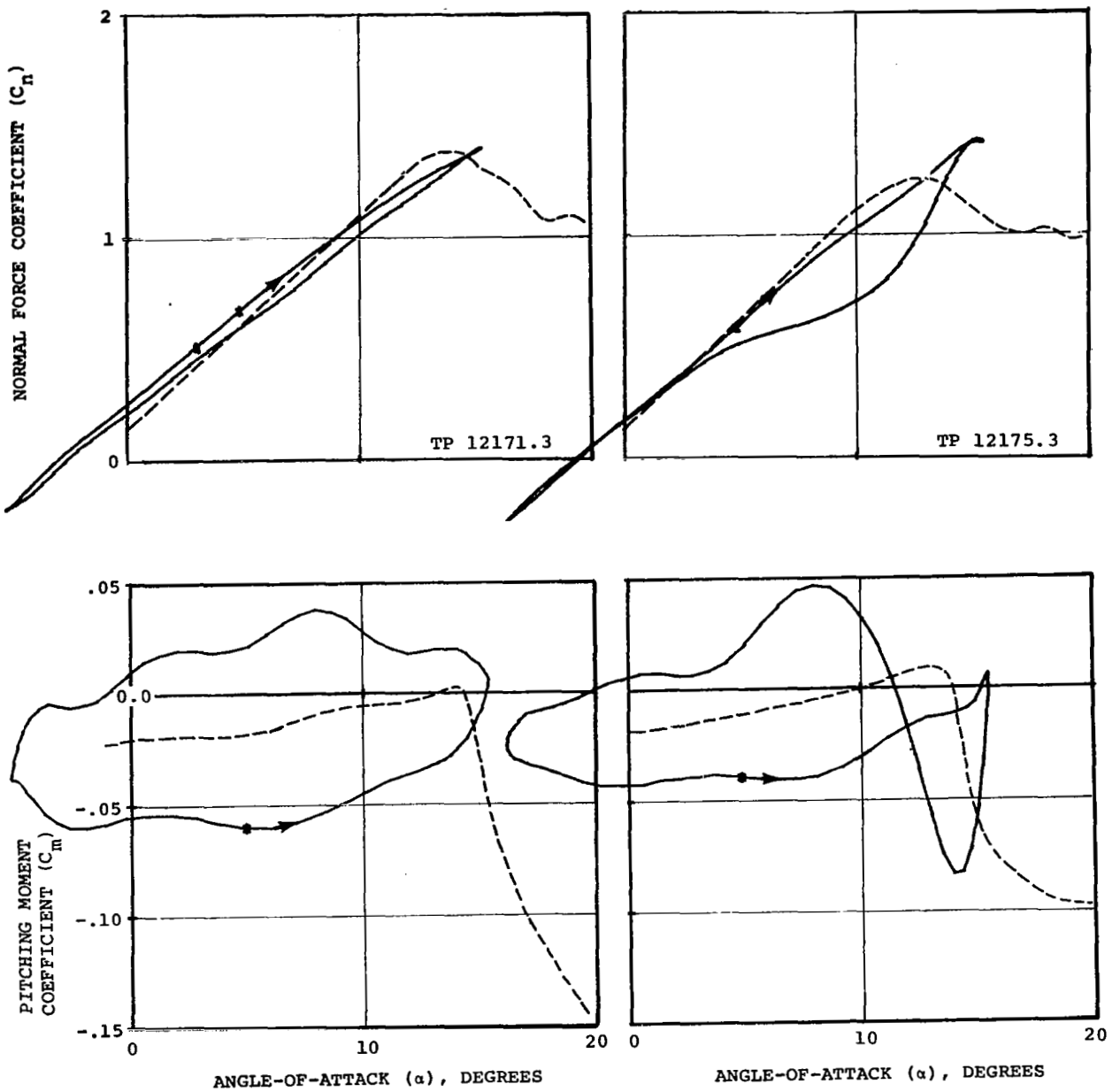

Figure 30. Effect of Mach number variation on the dynamic stall characteristics of the normal-force and pitching-moment coefficients of the NLR 7223-62 airfoil. Nominal conditions: f_D = 23.0 HZ, α_o = 5.0°, $\Delta\alpha$ = 10.0°

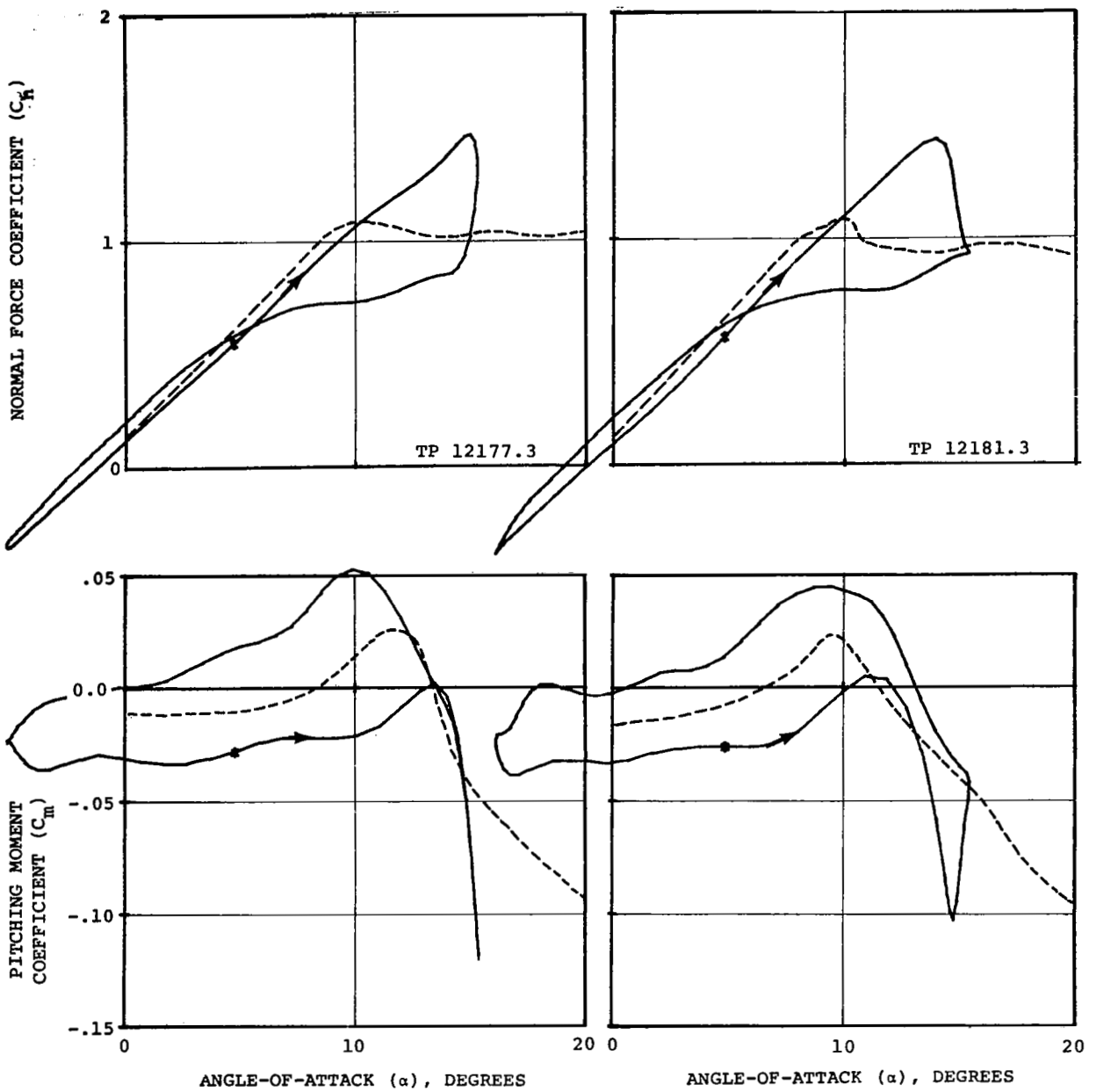

(c) M = 0.4

(d) M = 0.5

Figure 30. Continued

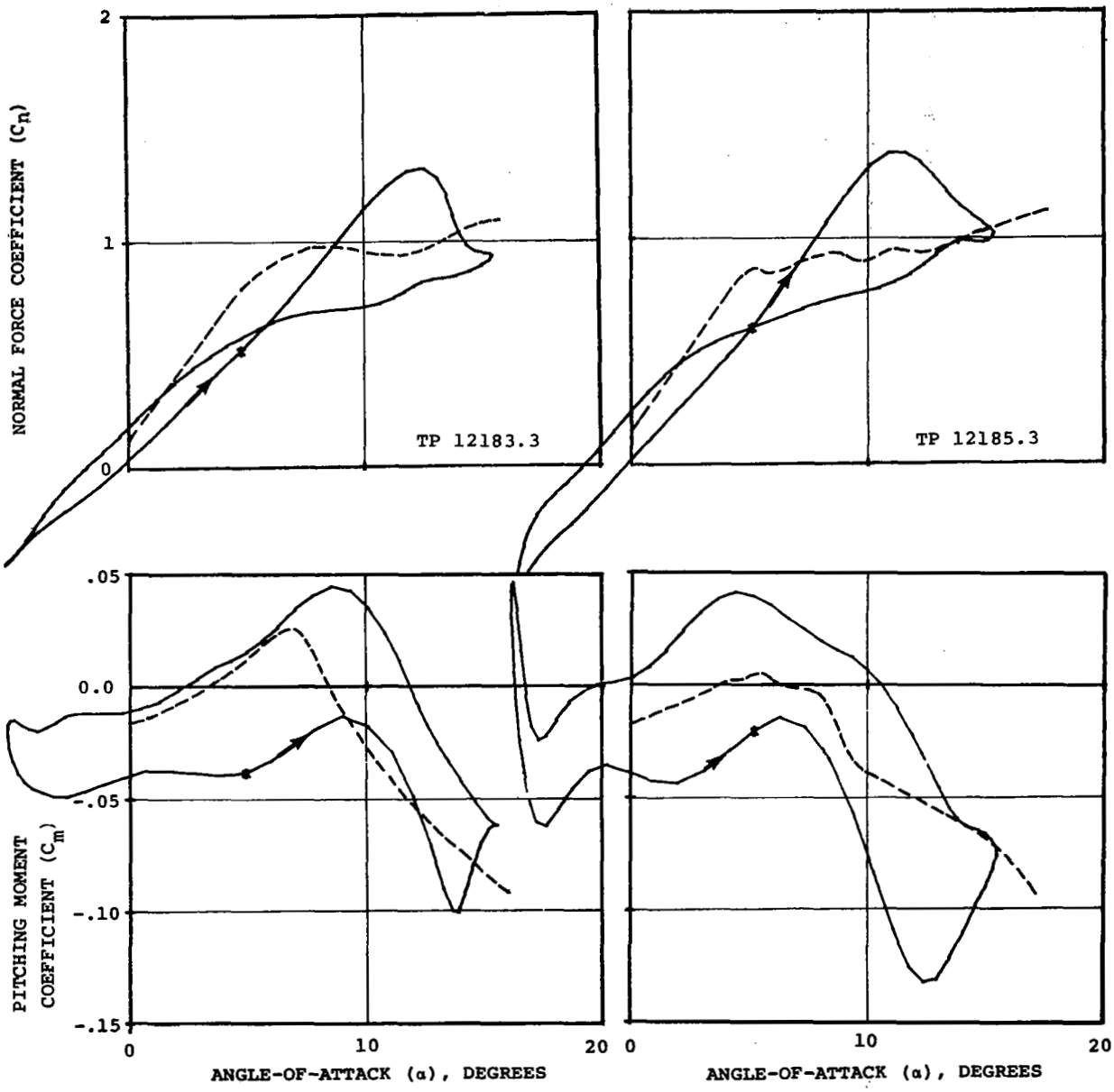

(e) M = 0.6 (f) M = 0.7

Figure 30. Concluded

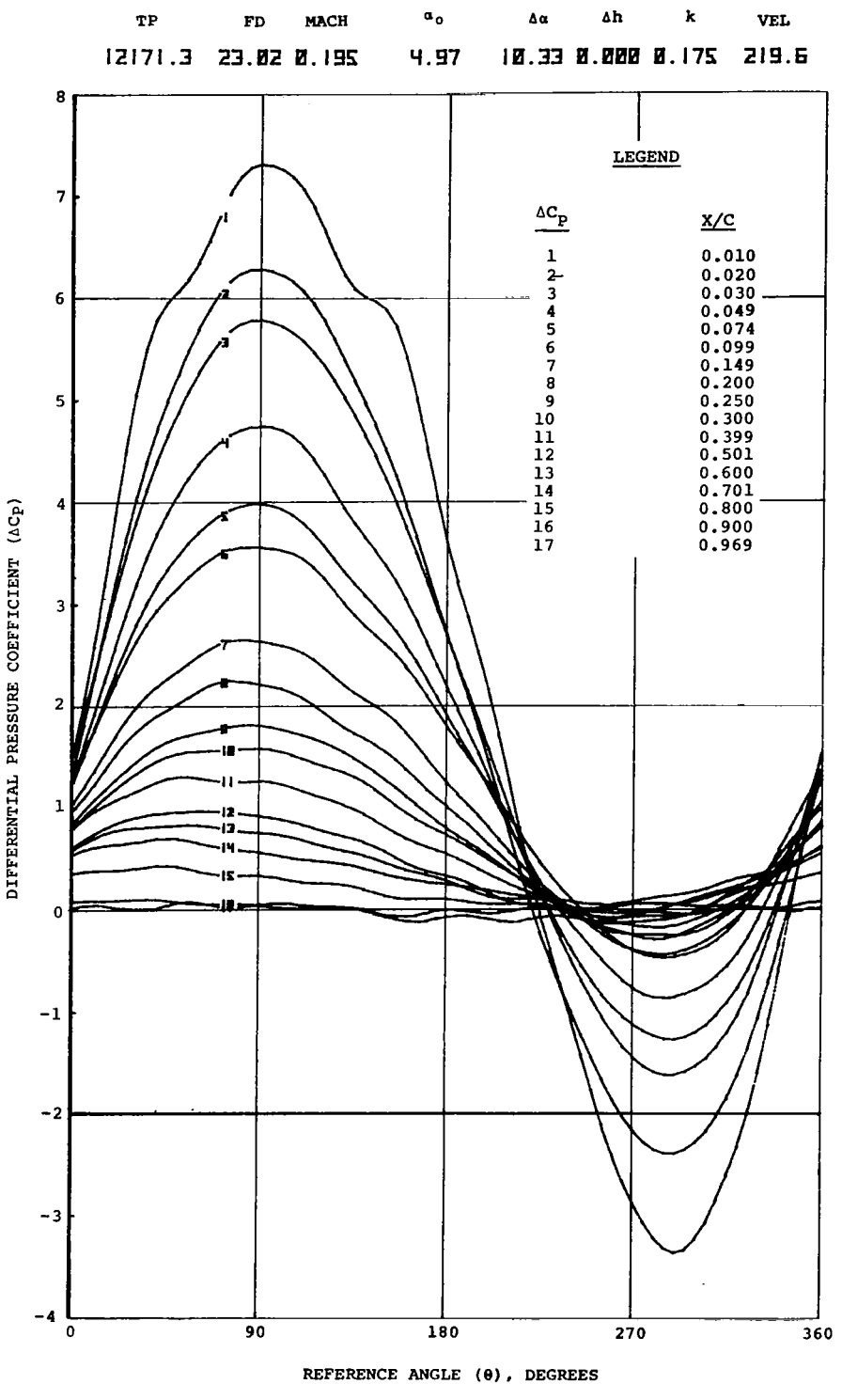

(a) M = 0.2

Figure 31. Effect of Mach number variation on the local differential pressures over the NLR 7223-62 airfoil. Nominal conditions: f_D = 23.0 Hz, α_o = 5.0°, $\Delta\alpha$ = 10.0°

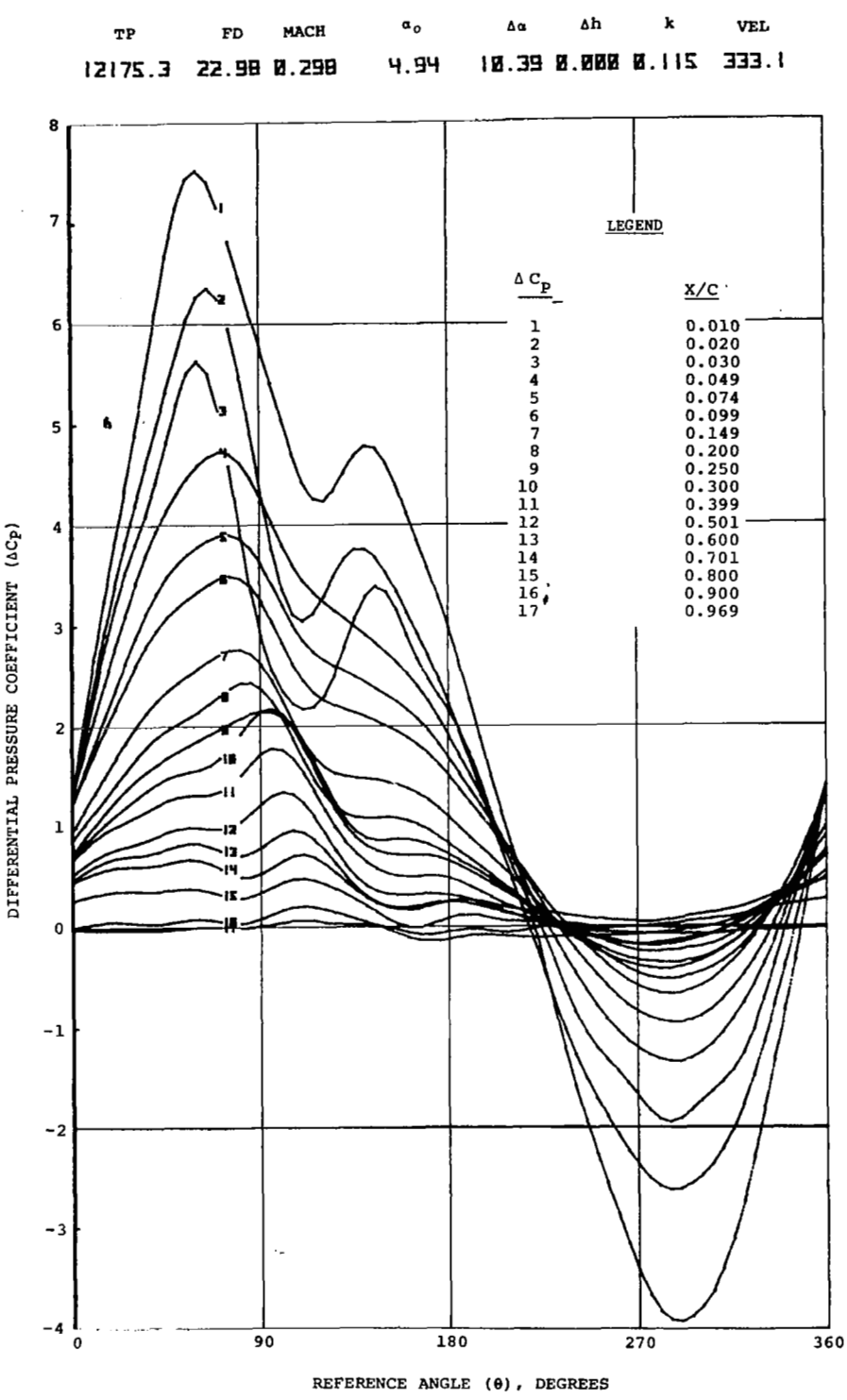

(b) M = 0.3

Figure 31. Continued

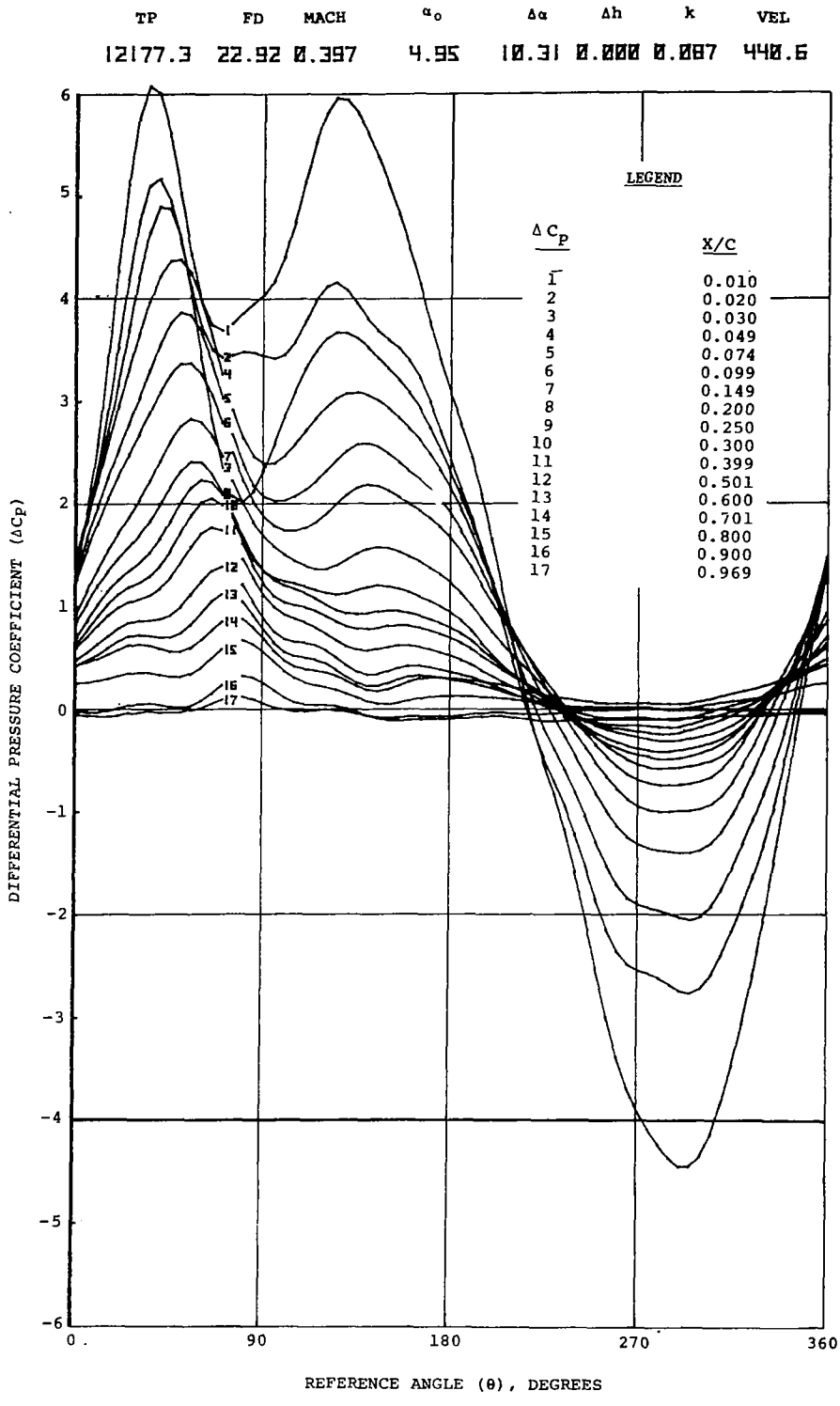

(c) M = 0.4

Figure 31. Continued

TP	FD	MACH	α_o	$\Delta\alpha$	Δh	k	VEL
12181.3	23.01	0.494	4.93	10.22	0.000	0.071	543.3

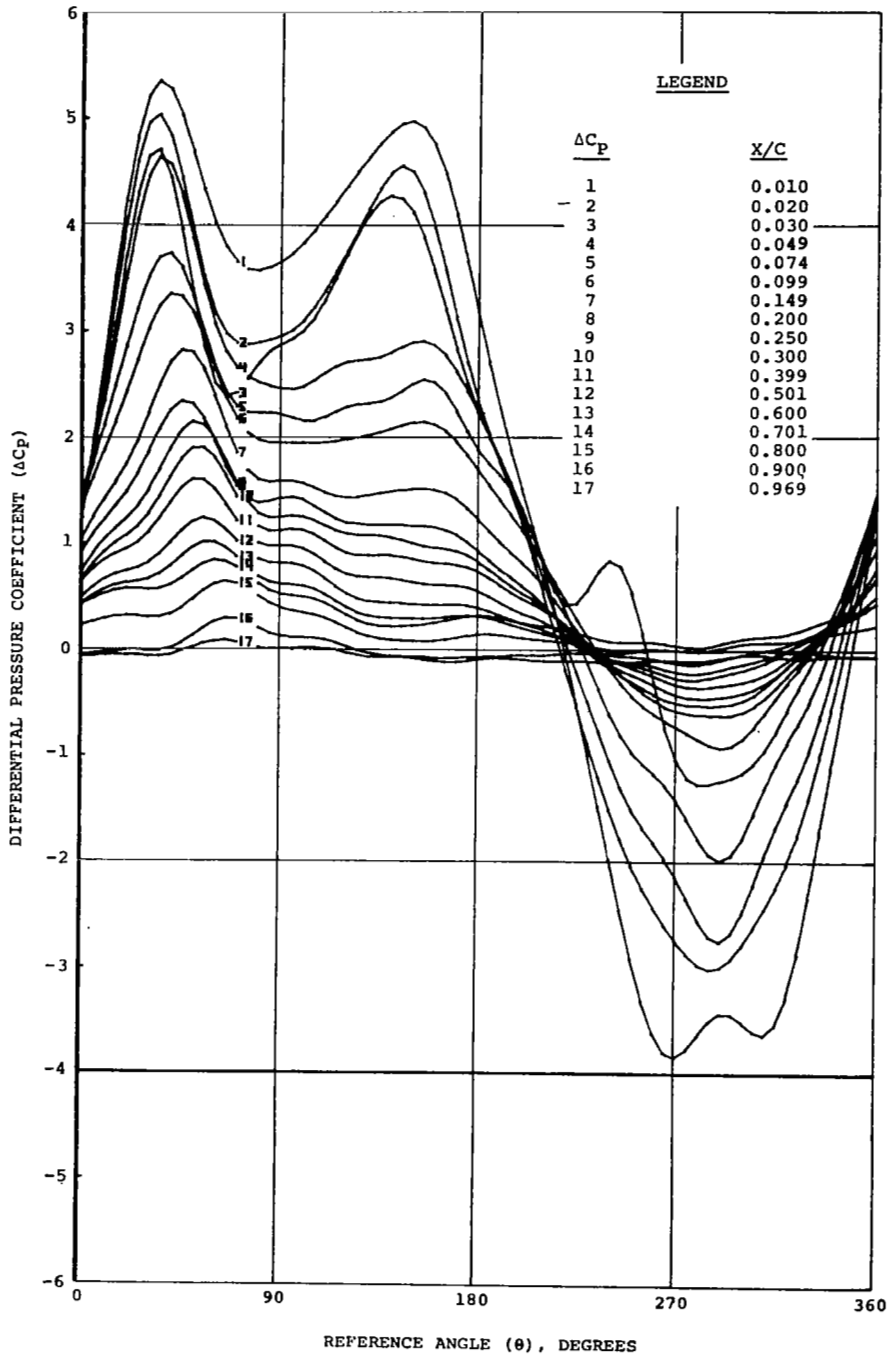

(d) M = 0.5

Figure 31. Continued

TP	FD	MACH	α_o	$\Delta\alpha$	Δh	k	VEL
12183.3	23.17	0.602	4.87	10.22	0.000	0.060	647.8

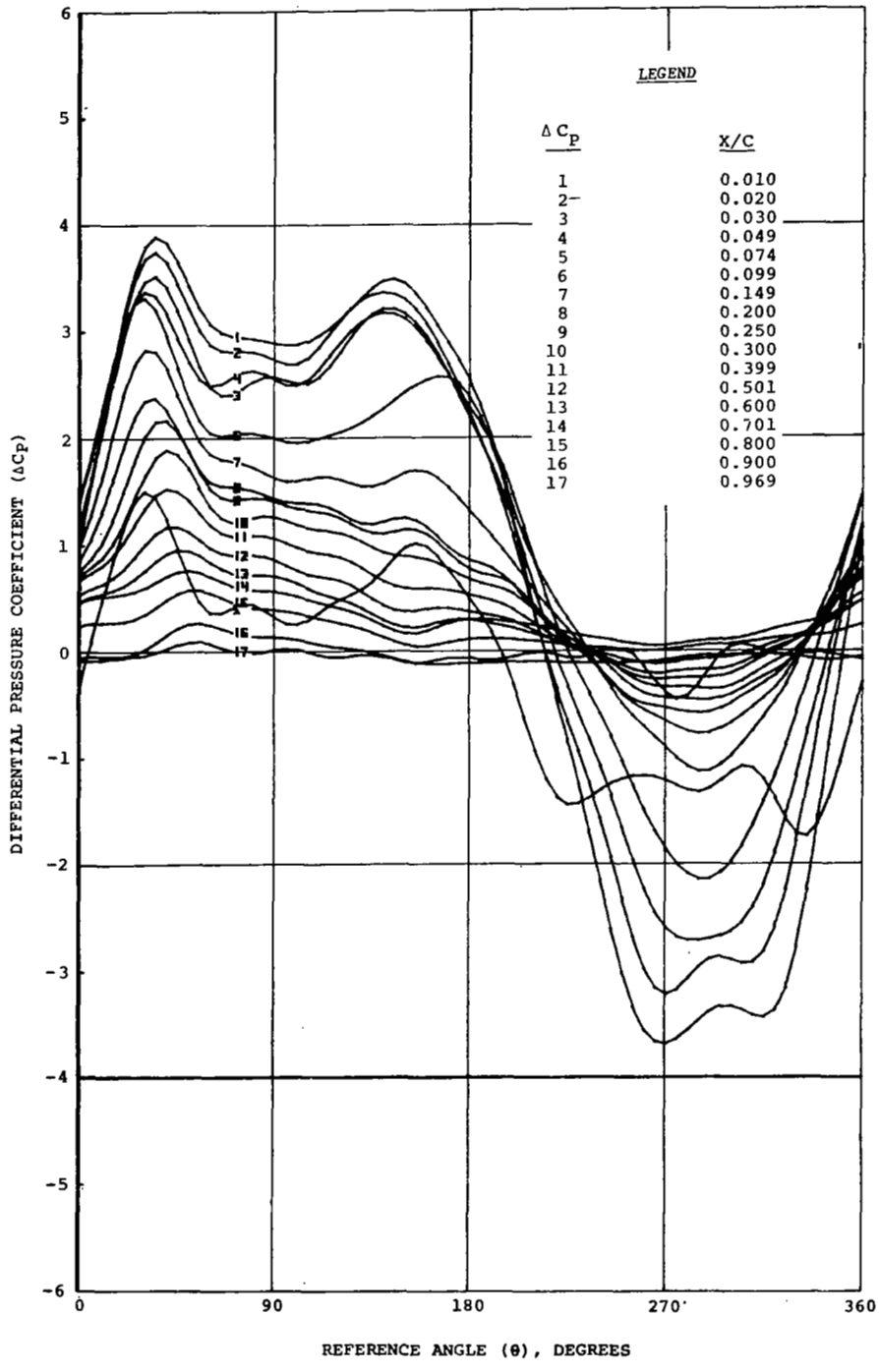

(e) M = 0.6

Figure 31. Continued

TP	FD	MACH	α_o	$\Delta\alpha$	Δh	k	VEL
12185.3	23.20	0.698	4.97	10.17	0.000	0.052	741.6

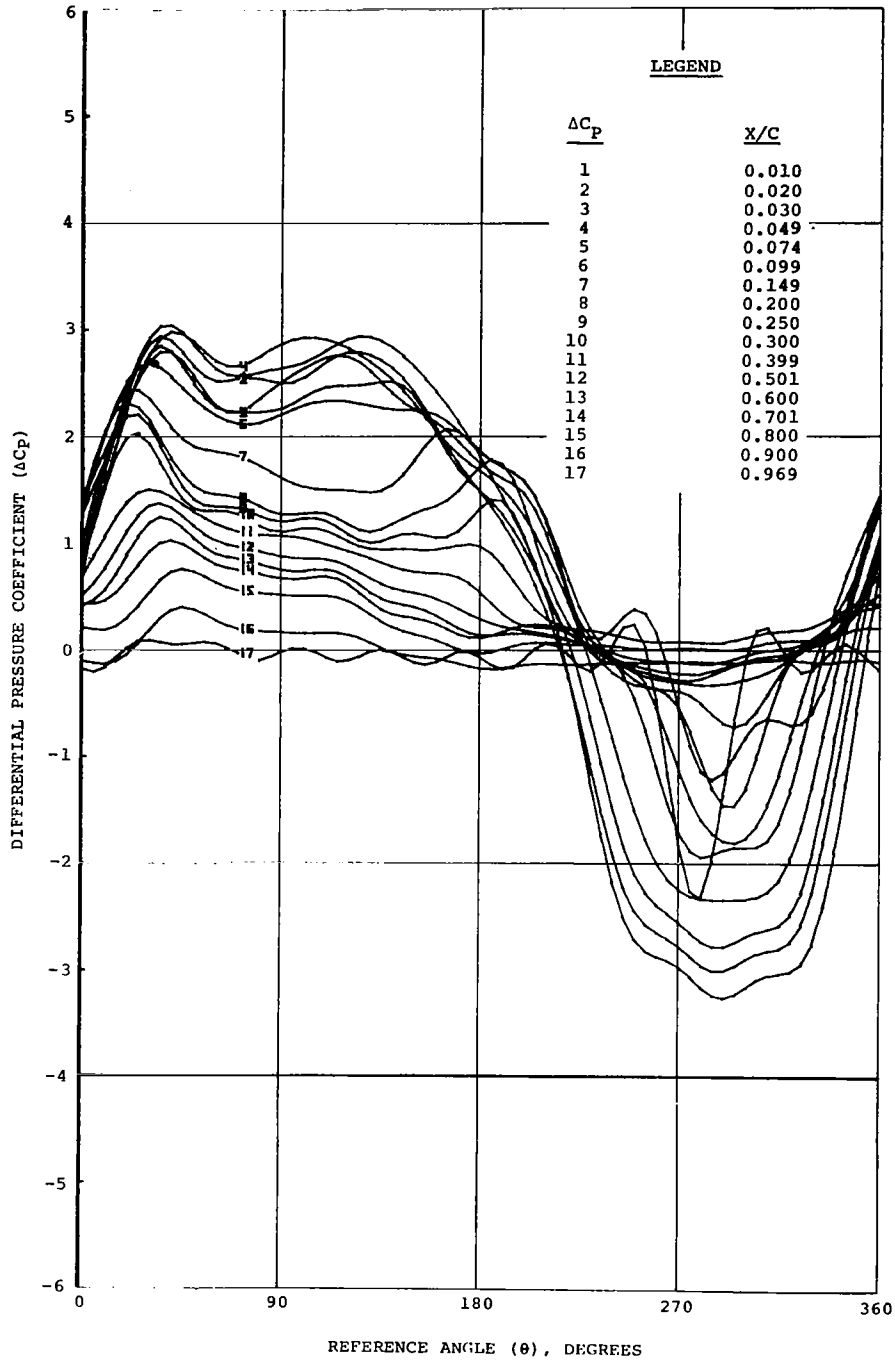

(f) M = 0.7

Figure 31. Concluded

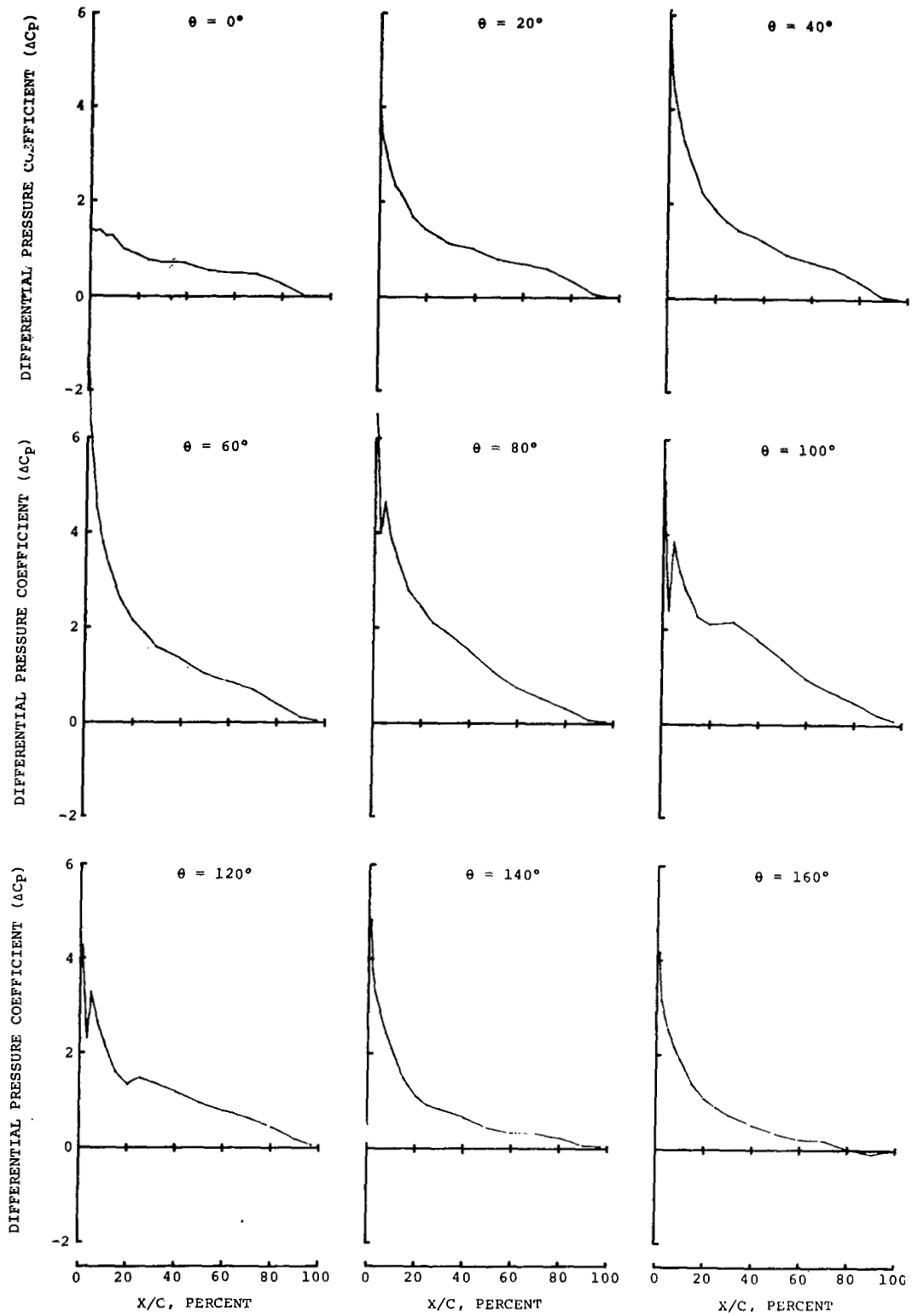

Figure 32. Differential pressure distributions over the NLR 7223-62 airfoil. Nominal conditions: M = 0.3, f_D = 23.0 Hz, α_o = 5.0°, $\Delta\alpha$ = 10.0° (T.P. 12175.3).

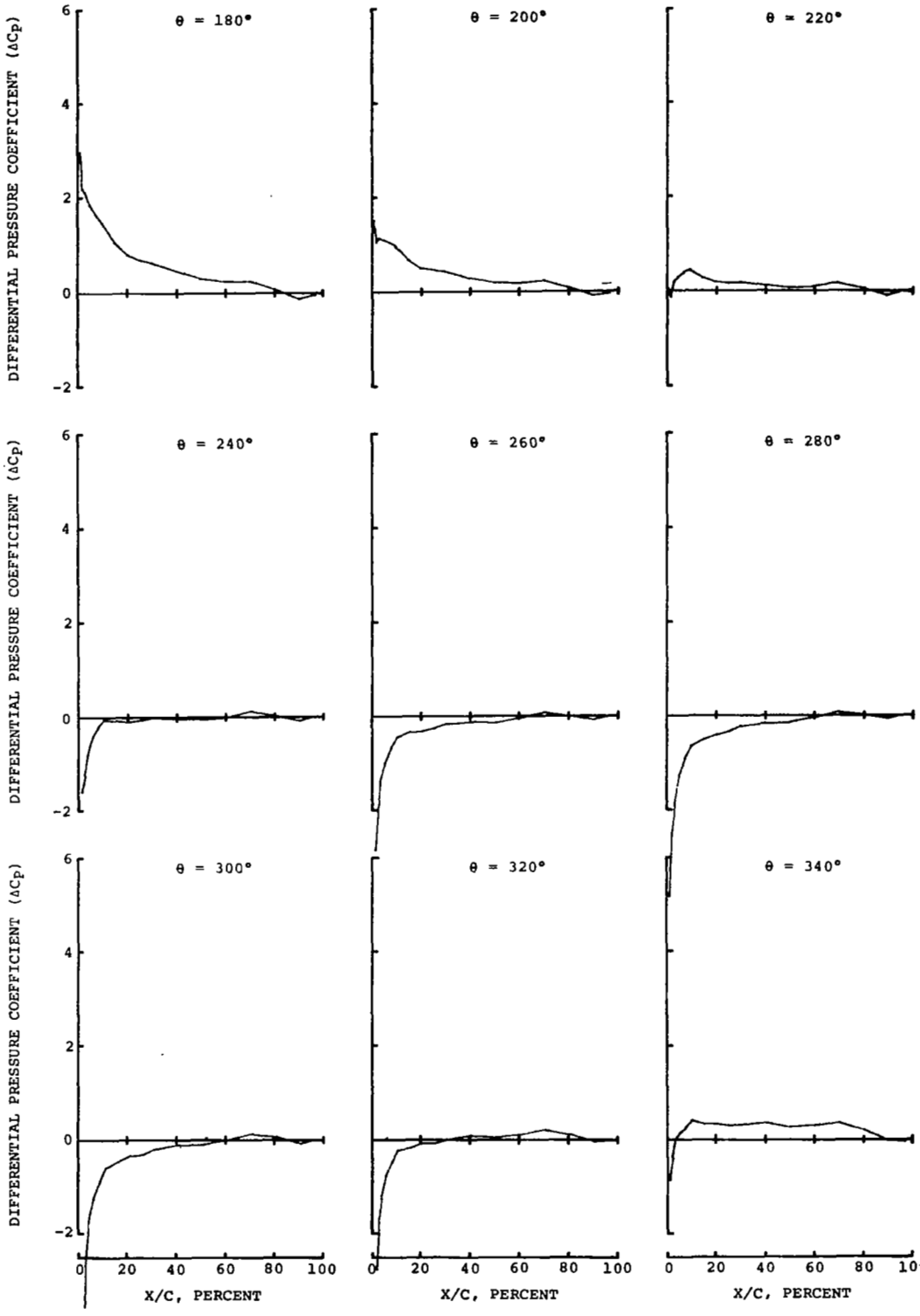

Figure 32. Concluded

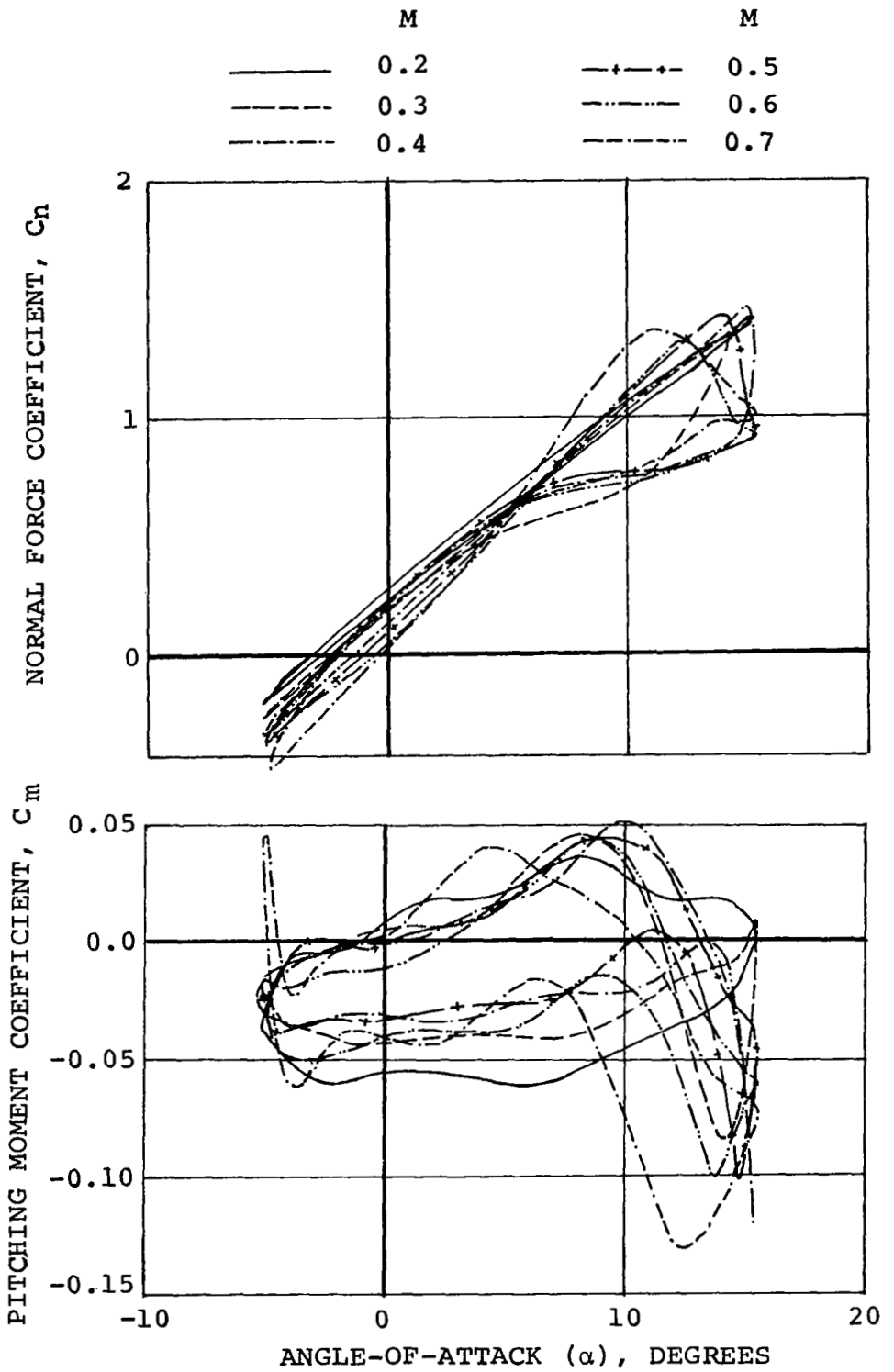

Figure 33. Overlay of normal-force and pitching-moment loops of the NLR 7223-62 airfoil to illustrate the effect of Mach number variation. Nominal conditions: α_o=5.0°, $\Delta\alpha$=10.0°, f_D=23 Hz.

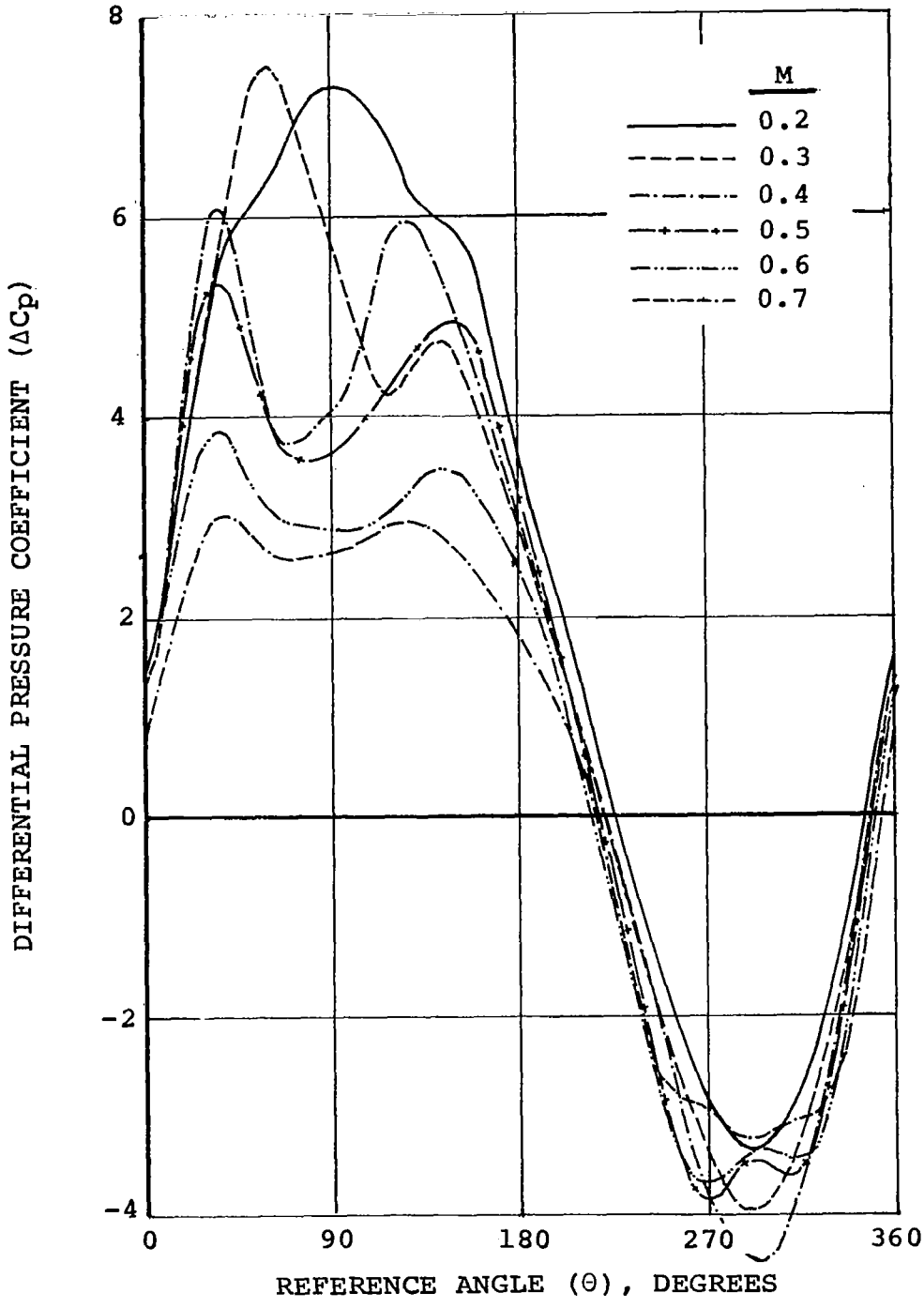

Figure 34. Effect of Mach number variation on the differential pressure at the 1% chord station of the NLR 7223-62 airfoil. Nominal conditions: α_o=5.0°, $\Delta\alpha$=10.0°, f_D=23 Hz.

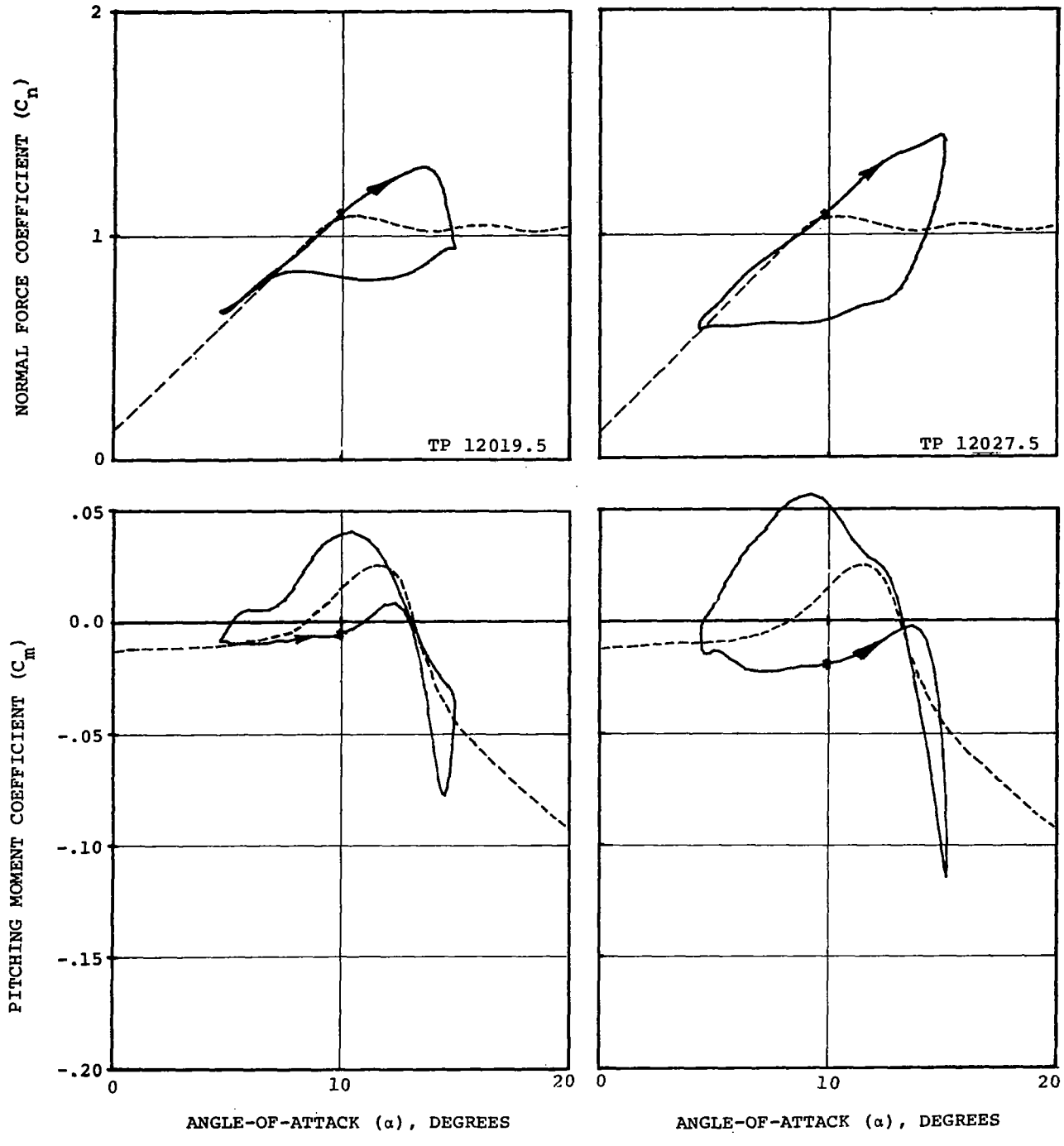

(a) f_D = 23.0 Hz (b) f_D = 46.0 Hz

Figure 35. Effect of drive frequency variation on the dynamic stall characteristics of the normal-force and pitching-moment coefficients of the NLR 7223-62 airfoil. Nominal conditions: M = 0.4, Rn = 6.4 x 10^6, α_o = 10.0°, $\Delta\alpha$ = 5.0°.

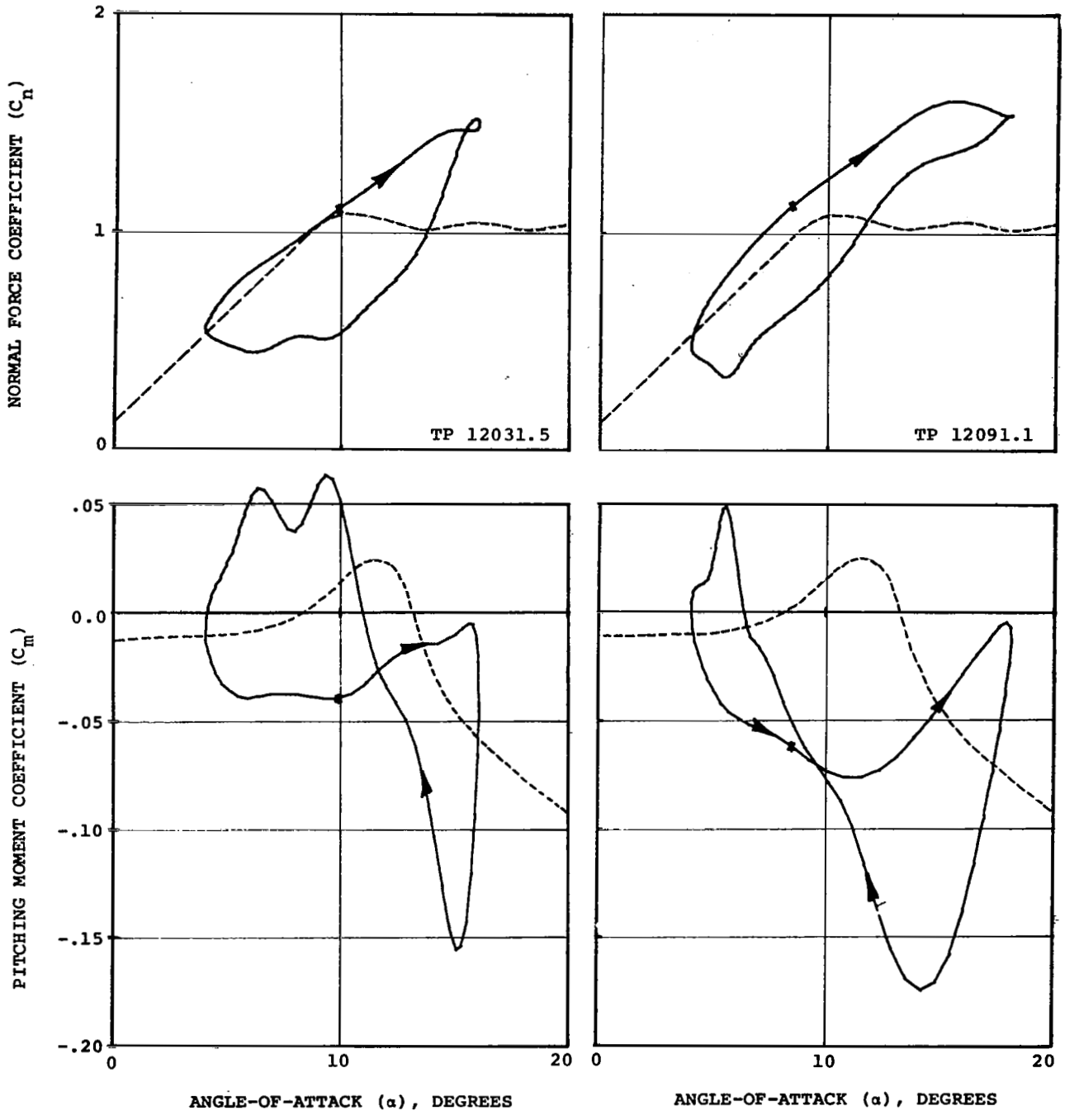

(c) f_D = 69.0 Hz

(d) f_D = 88.0 Hz

Figure 35. Concluded

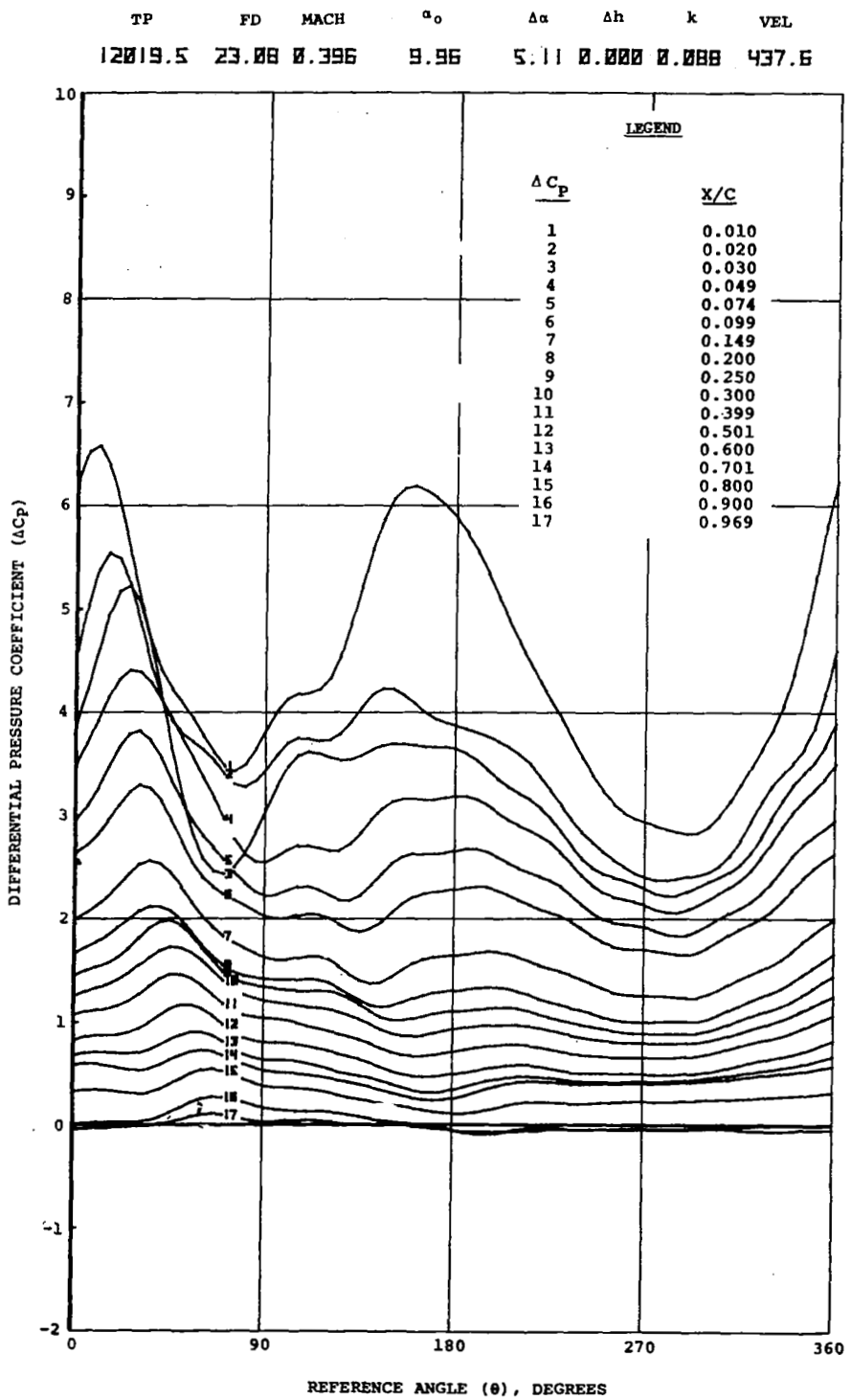

(a) f_D = 23.0 Hz

Figure 36. Effect of drive frequency variation on the local differential pressures over the NLR 7223-62 airfoil. Nominal conditions: M = 0.4, Rn = 6.4 x 10^6, α_o = 10.0°, $\Delta\alpha$ = 5.0°.

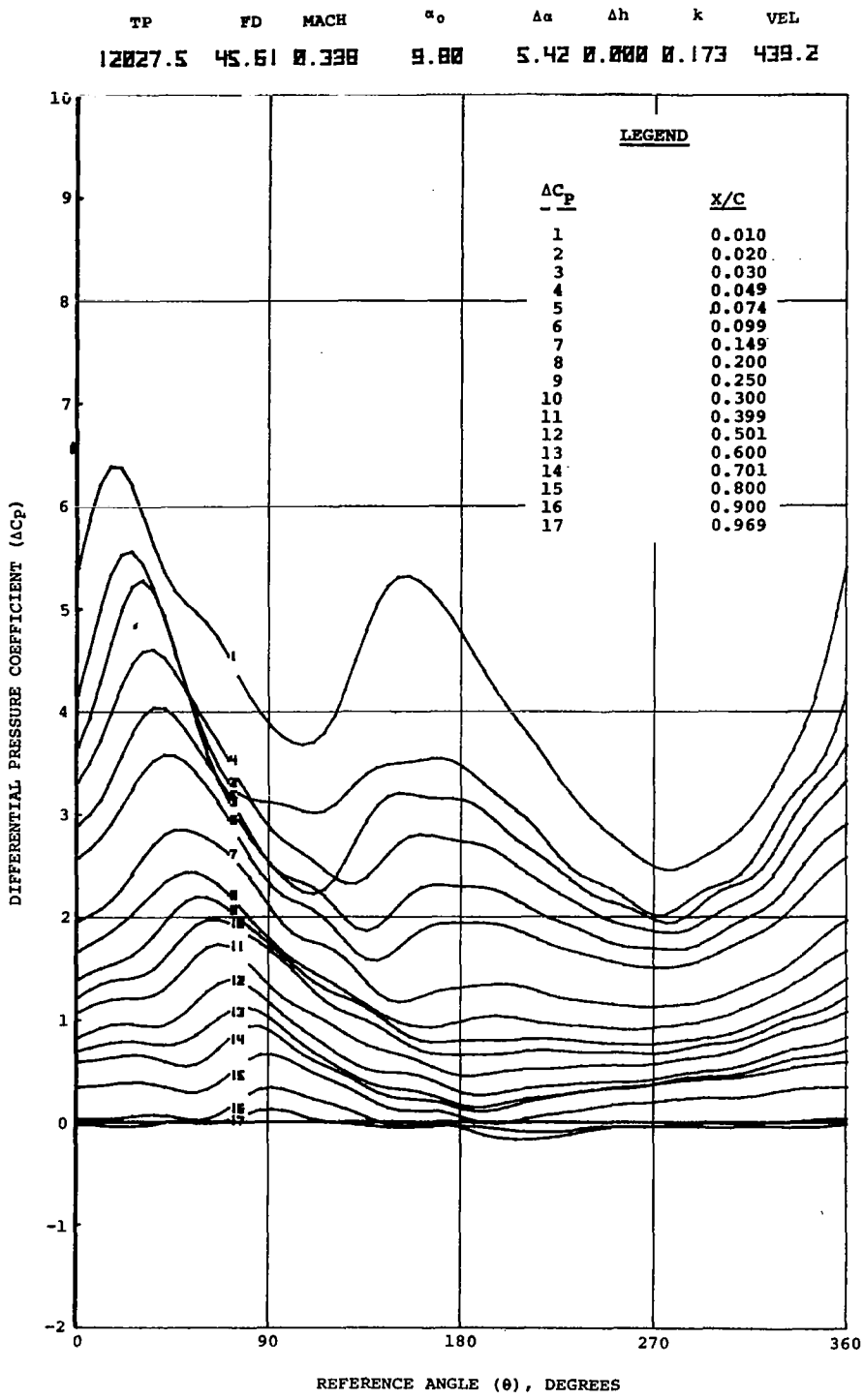

(b) f_D = 46.0 Hz

Figure 36. Continued

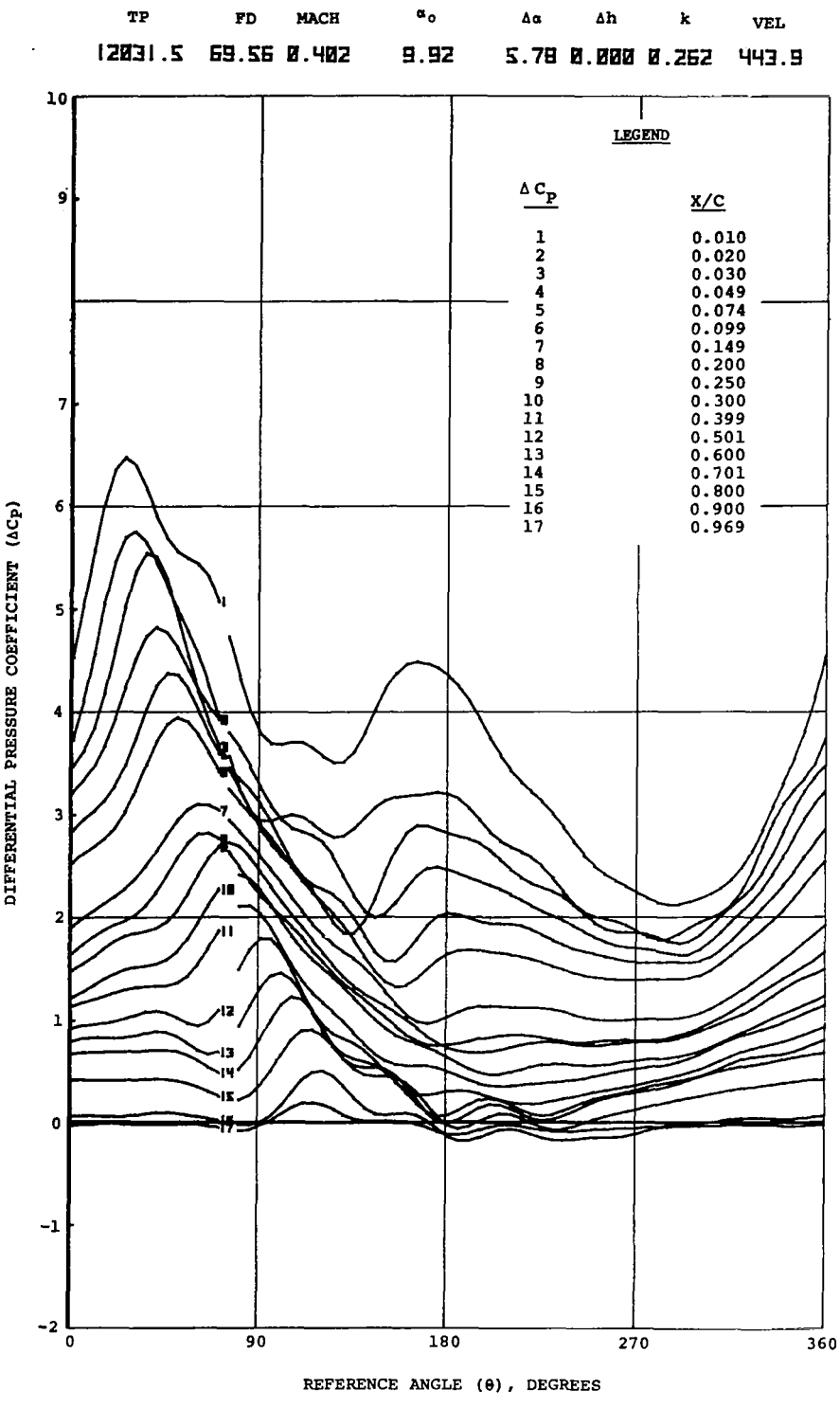

(c) f_D = 69.0 Hz

Figure 36. Continued

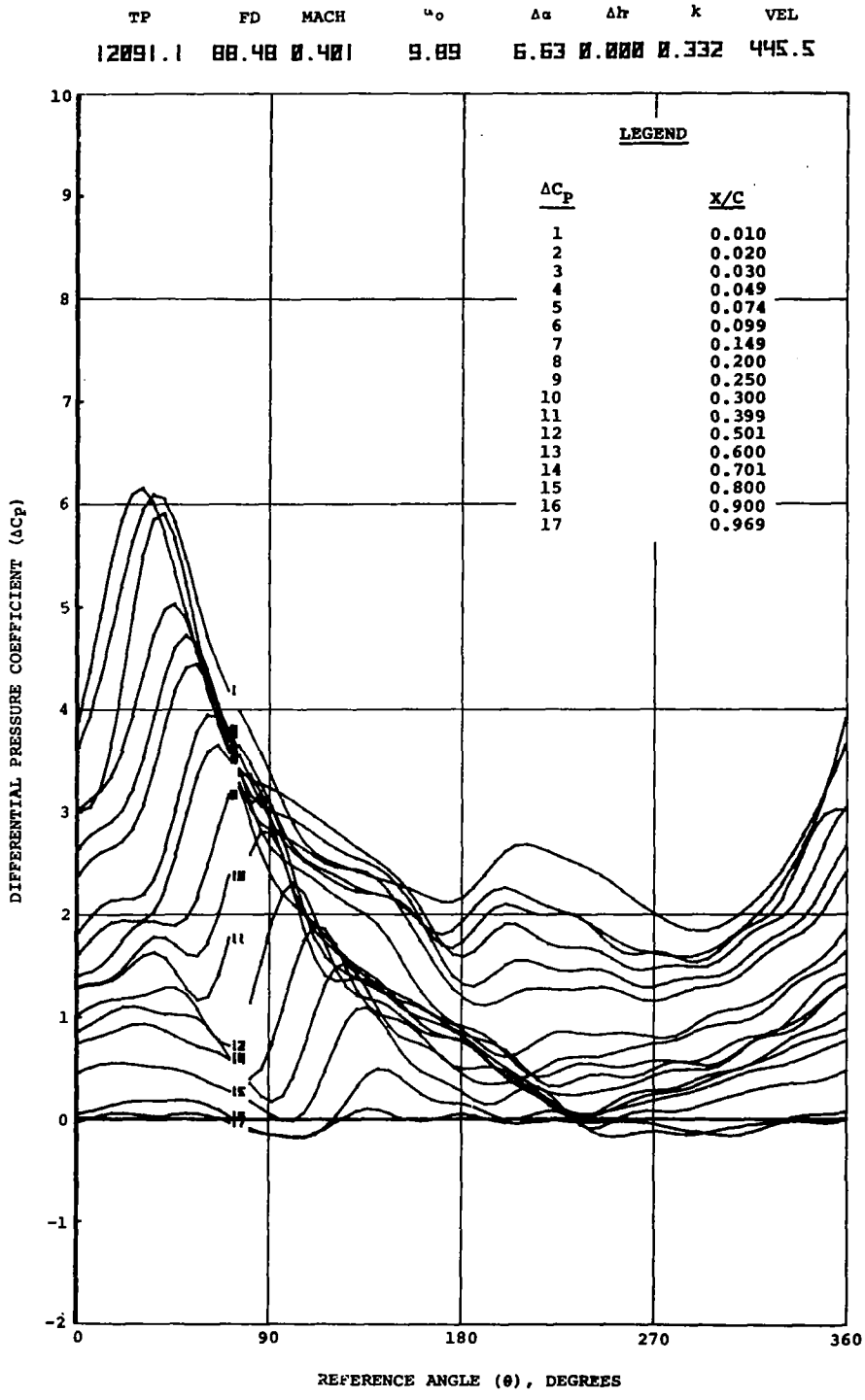

(d) f_D = 88.0 Hz

Figure 36. Continued

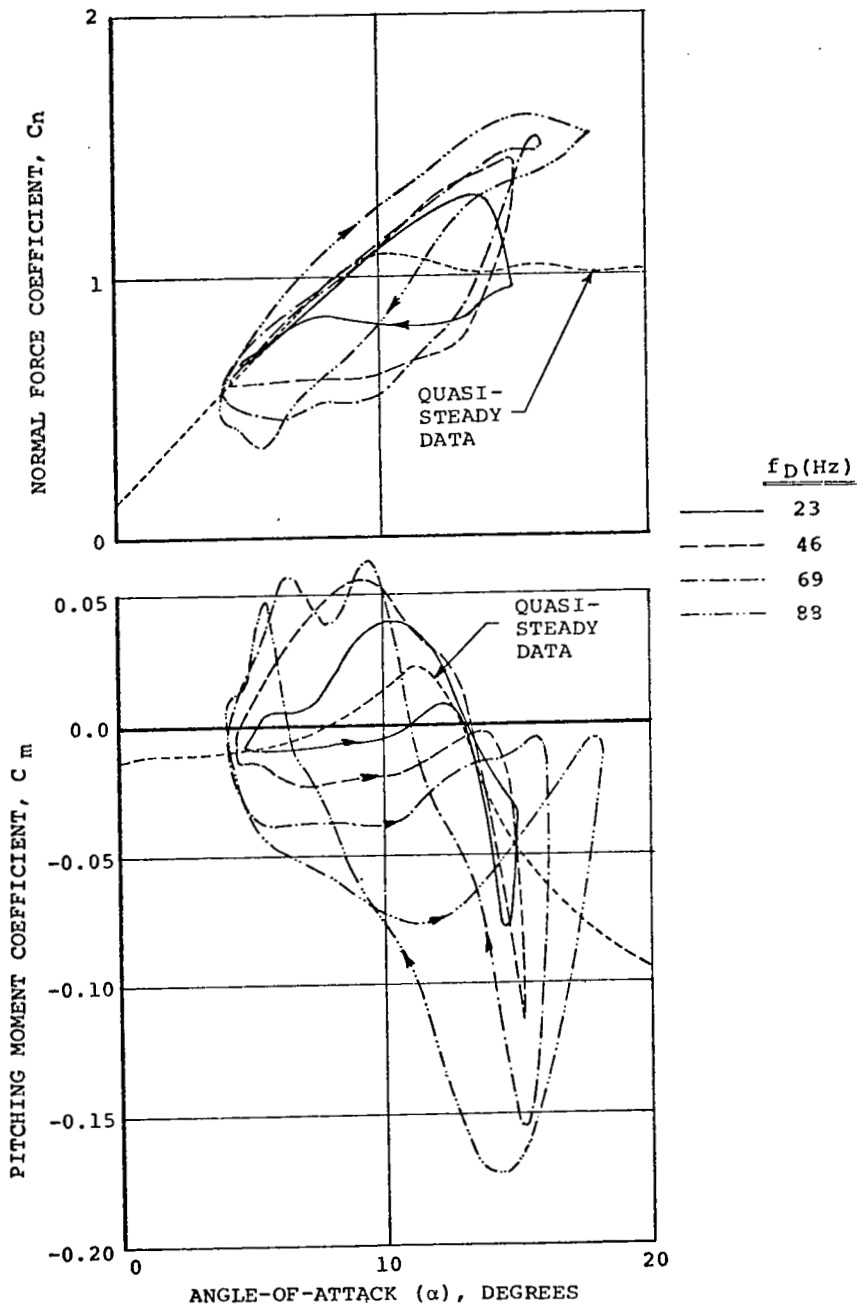

Figure 37. Overlay of normal-force and pitching-moment loops of the NLR 7223-62 airfoil to illustrate the effect of drive-frequency variation. Nominal conditions: M=0.4, α_o= 10.0°, $\Delta\alpha$=5.0°.

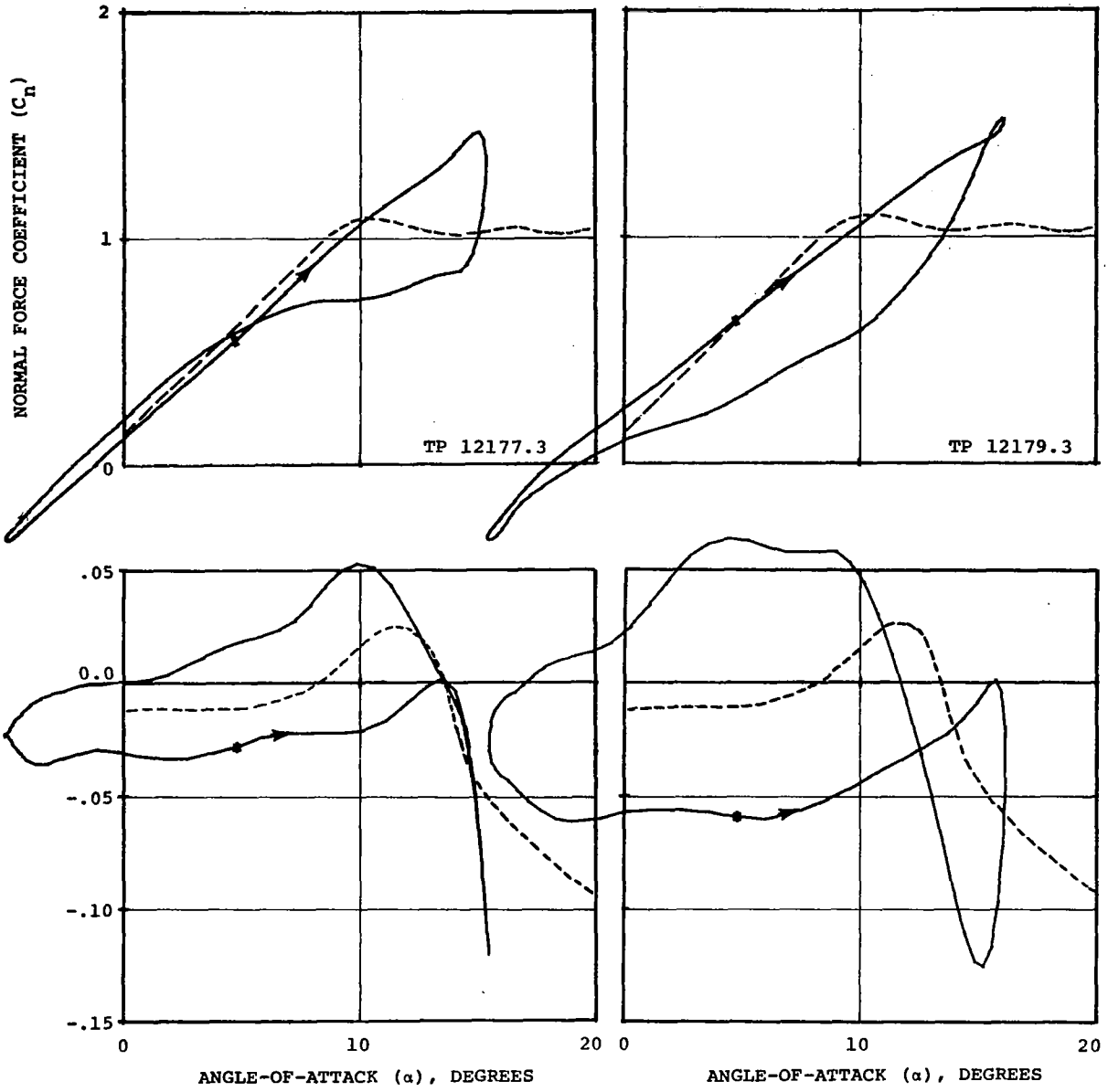

(a) f_D = 23.0 Hz (b) f_D = 46.0 Hz

Figure 38. Effect of drive-frequency variation on the dynamic stall characteristics of the normal-force and pitching-moment coefficients of the NLR 7223-62 airfoil. Nominal conditions: M = 0.4, Rn = 6.4 x 10^6, α_o = 5.0°, $\Delta\alpha$ = 10.0°.

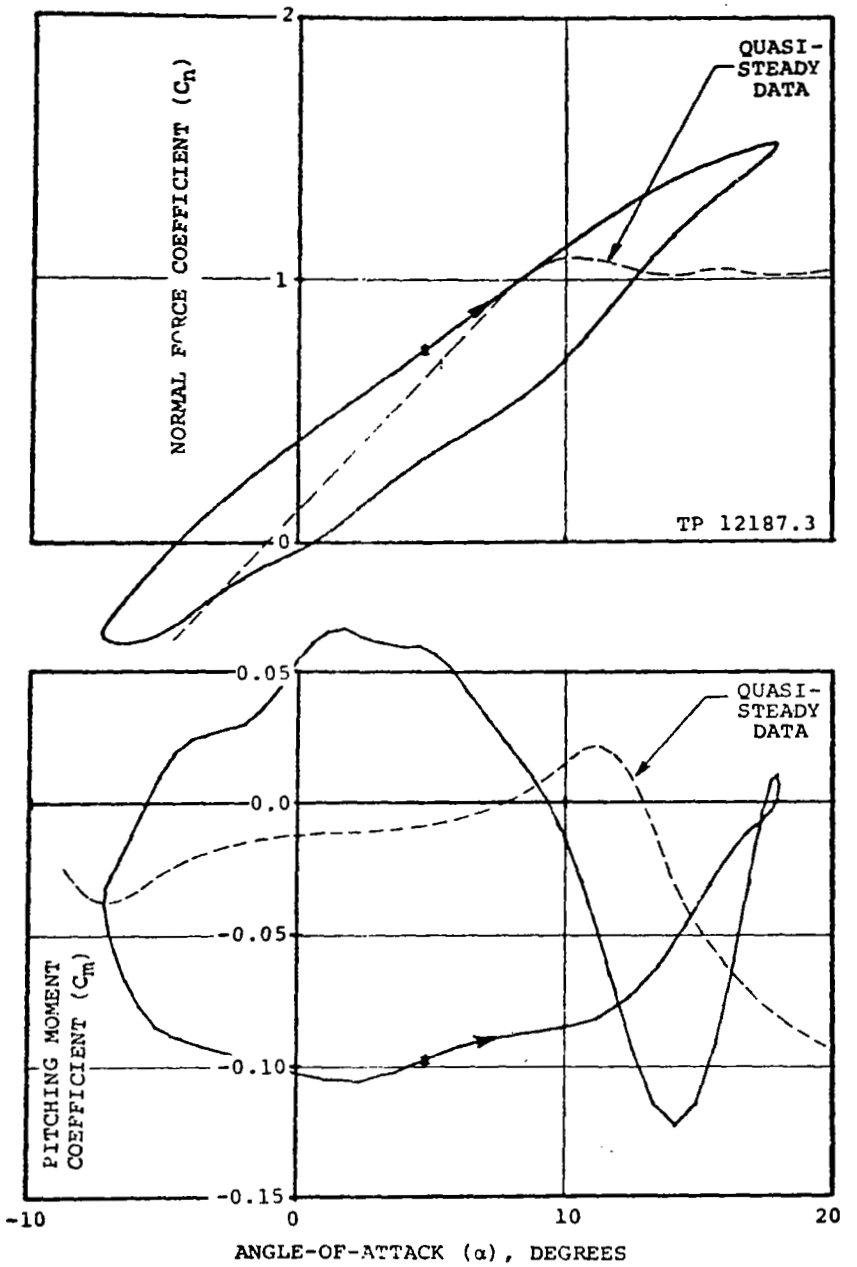

(c) f_D = 70.0 Hz

Figure 38. Continued

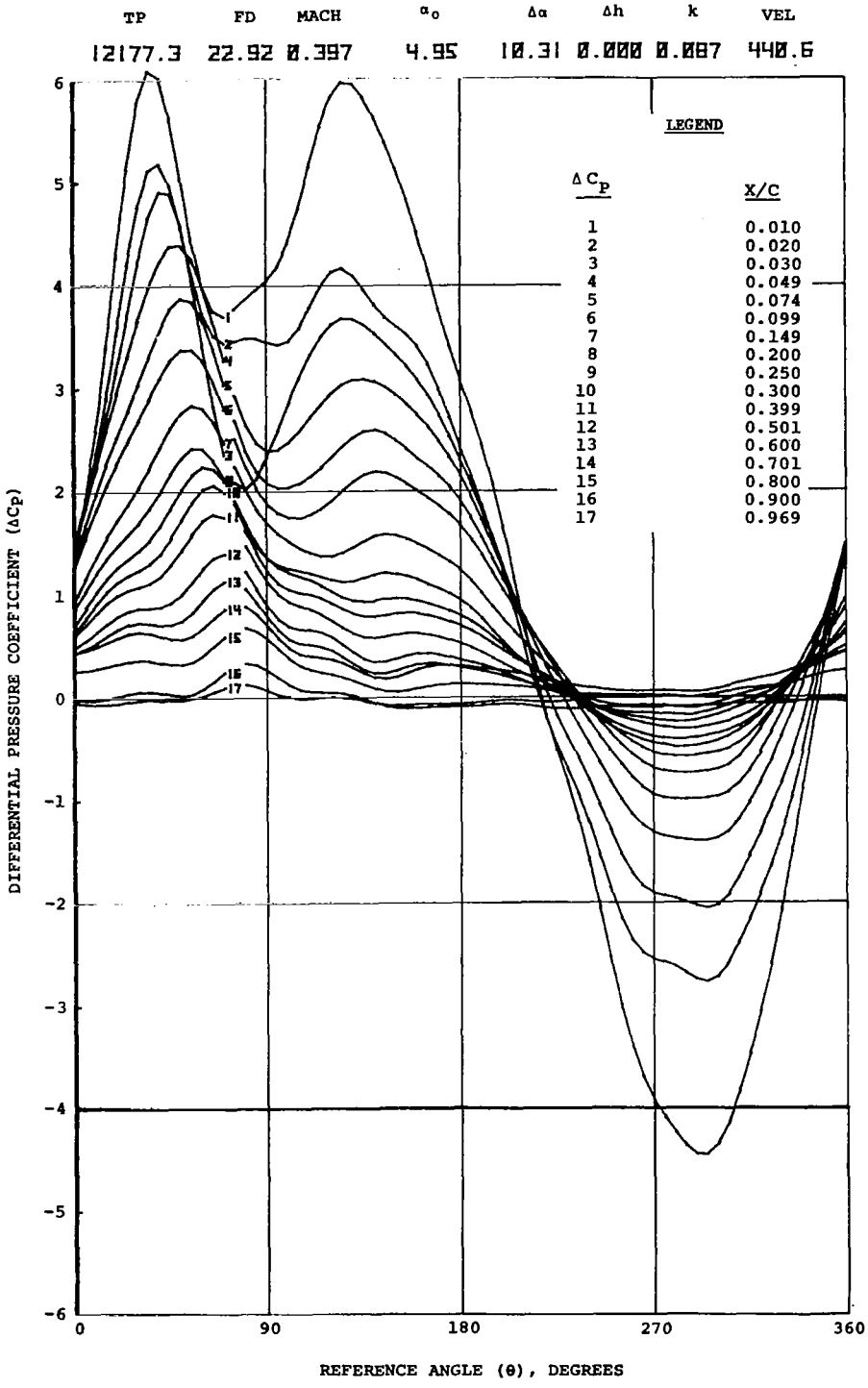

(a) f_D = 23.0 Hz

Figure 39. Effect of drive frequency variation on the local differential pressures over the NLR 7223-62 airfoil. Nominal conditions: M = 0.4, Rn = 6.4 x 10^6, α_o = 5.0°, $\Delta\alpha$ = 10.0°

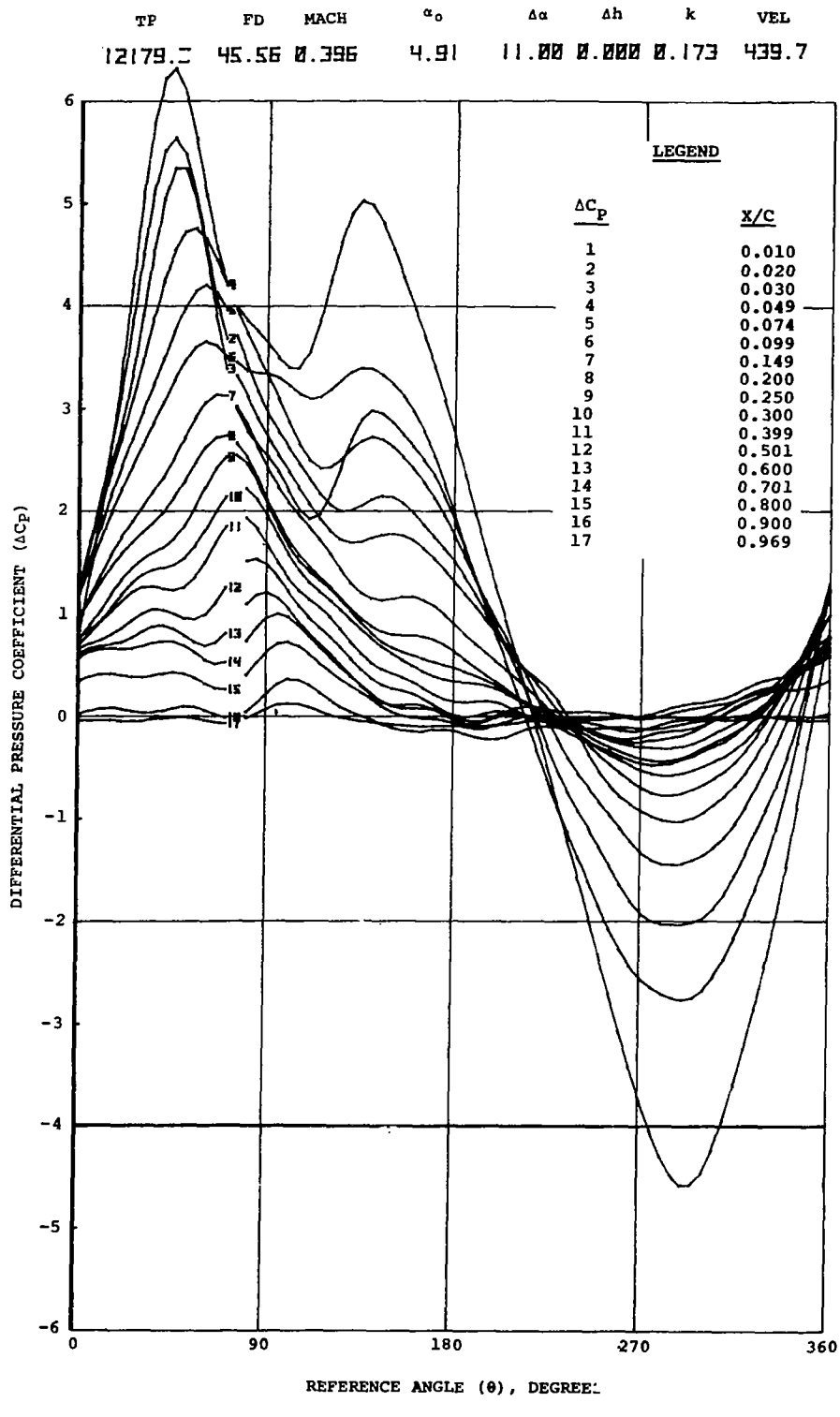

(b) f_D = 46.0 Hz

Figure 39. Continued

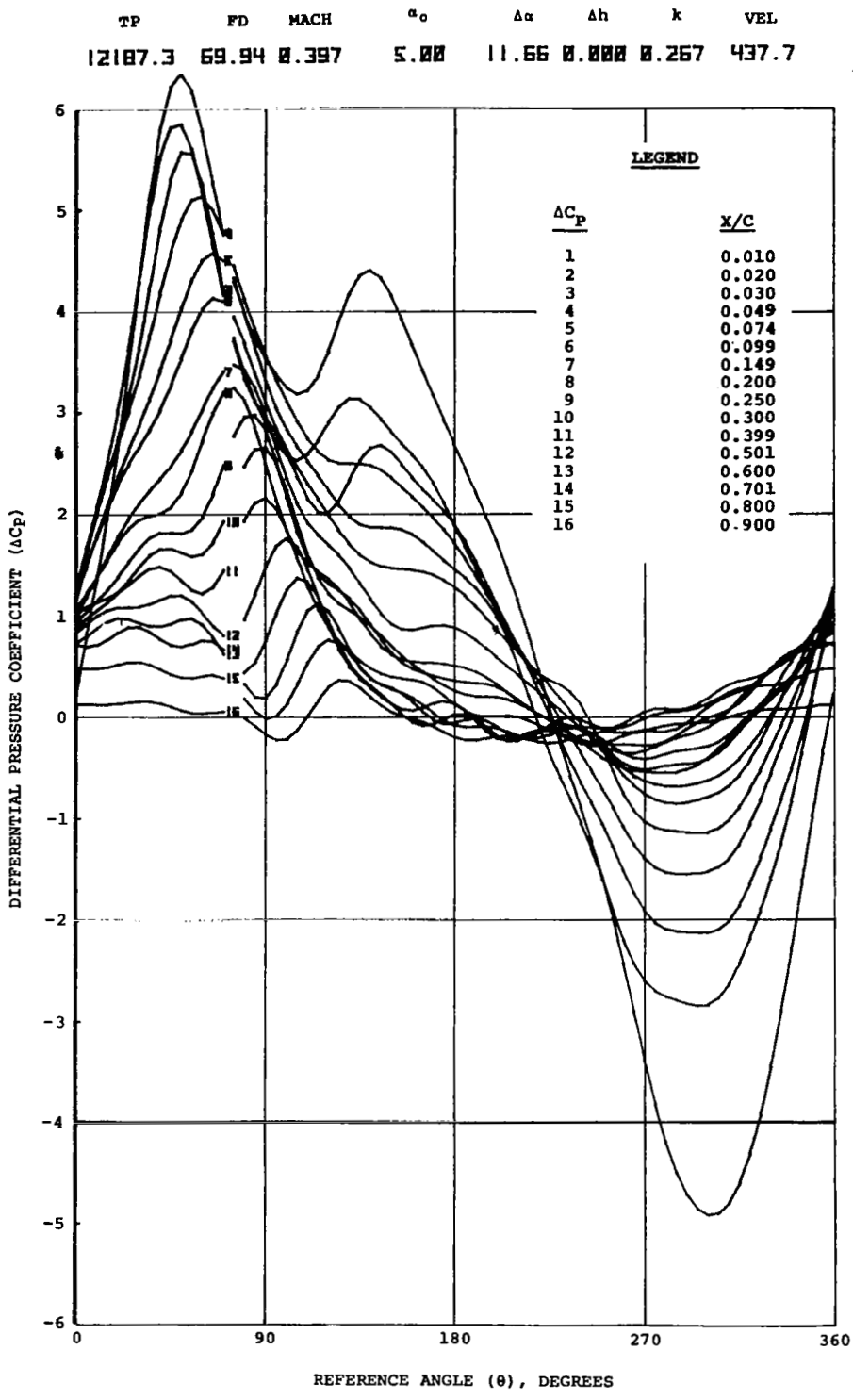

(c) f_D = 70.0 Hz

Figure 39. Concluded

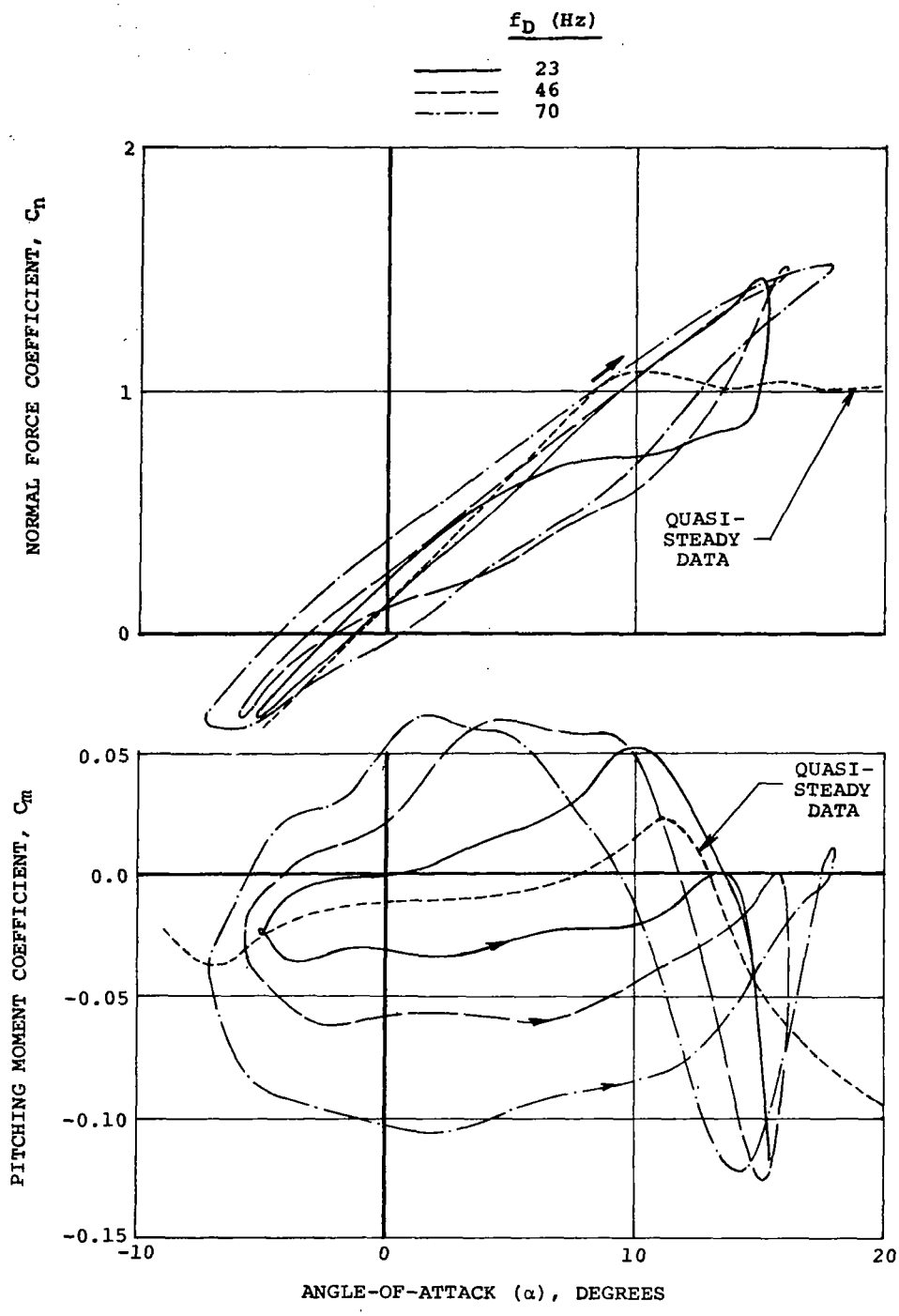

Figure 40. Overlay of normal-force and pitching-moment loops of the NLR 7223-62 airfoil to illustrate the effect of drive-frequency variation on dynamic stall inception. Nominal conditions: M=0.4, Rn=6.4x10^6, α_o=5.0°, $\Delta\alpha$=10.0°, f_D=23.0 Hz to 70.0 Hz.

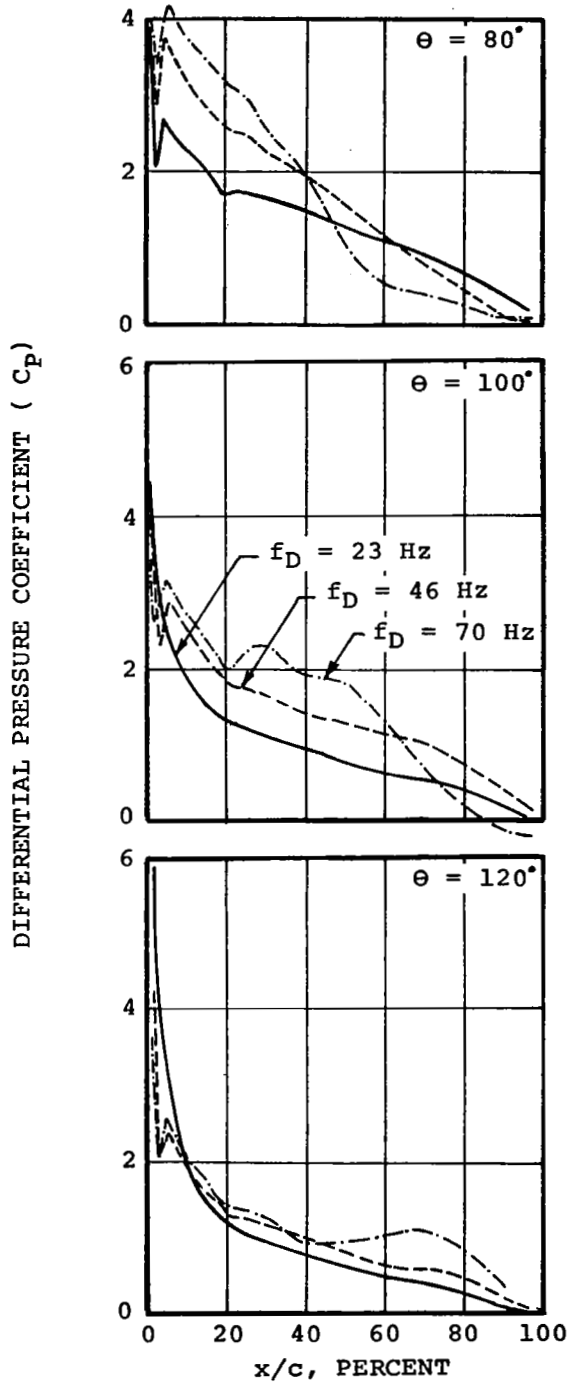

Figure 40. Continued

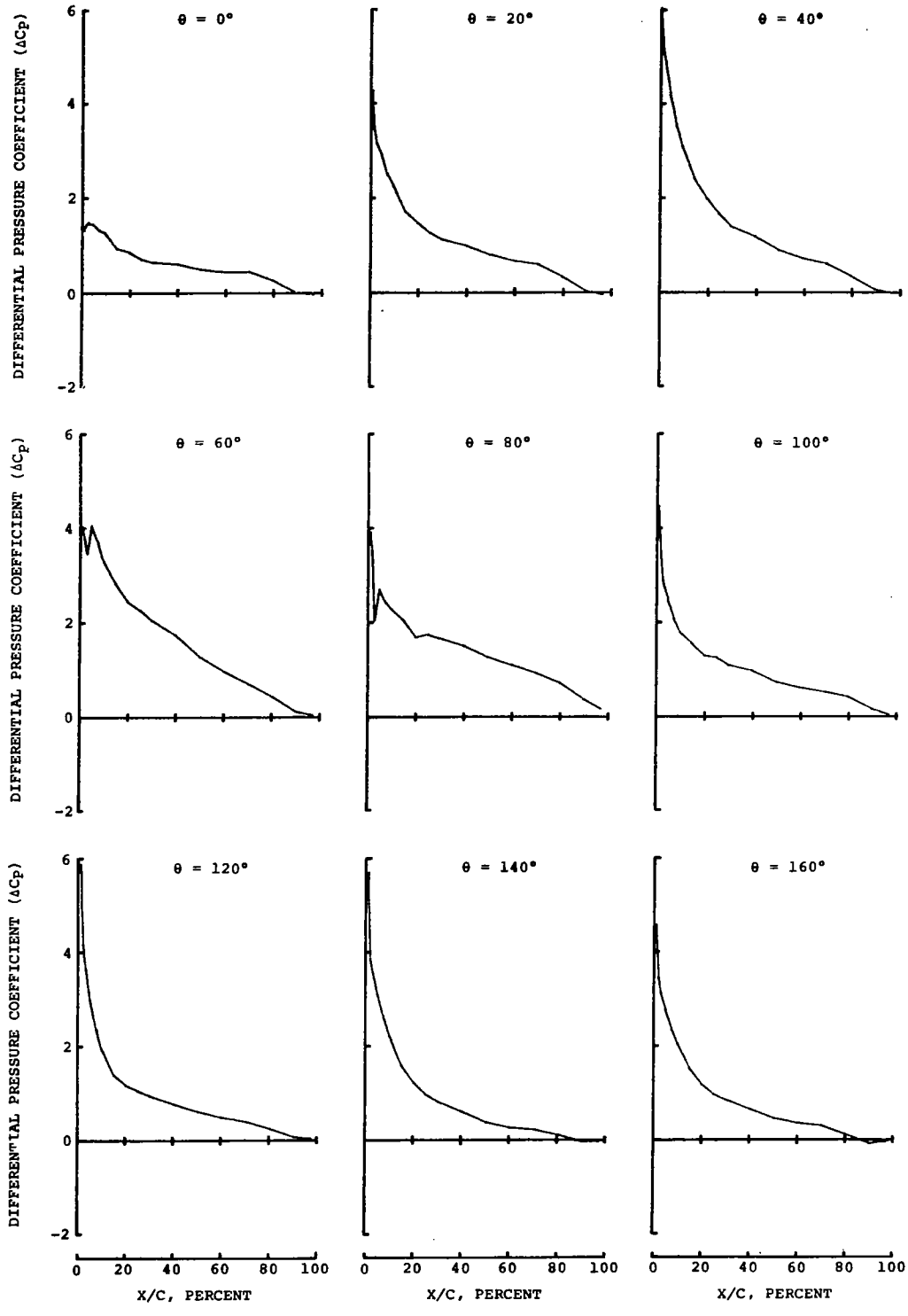

Figure 41. Differential pressure distributions over the NLR 7223-62 airfoil. Nominal conditions: M = 0.4, Rn = 6.4 x 10^6, α_o = 5.0°, $\Delta\alpha$ = 10.0°, f'_D = 23.0 Hz (T.P. 12177.3).

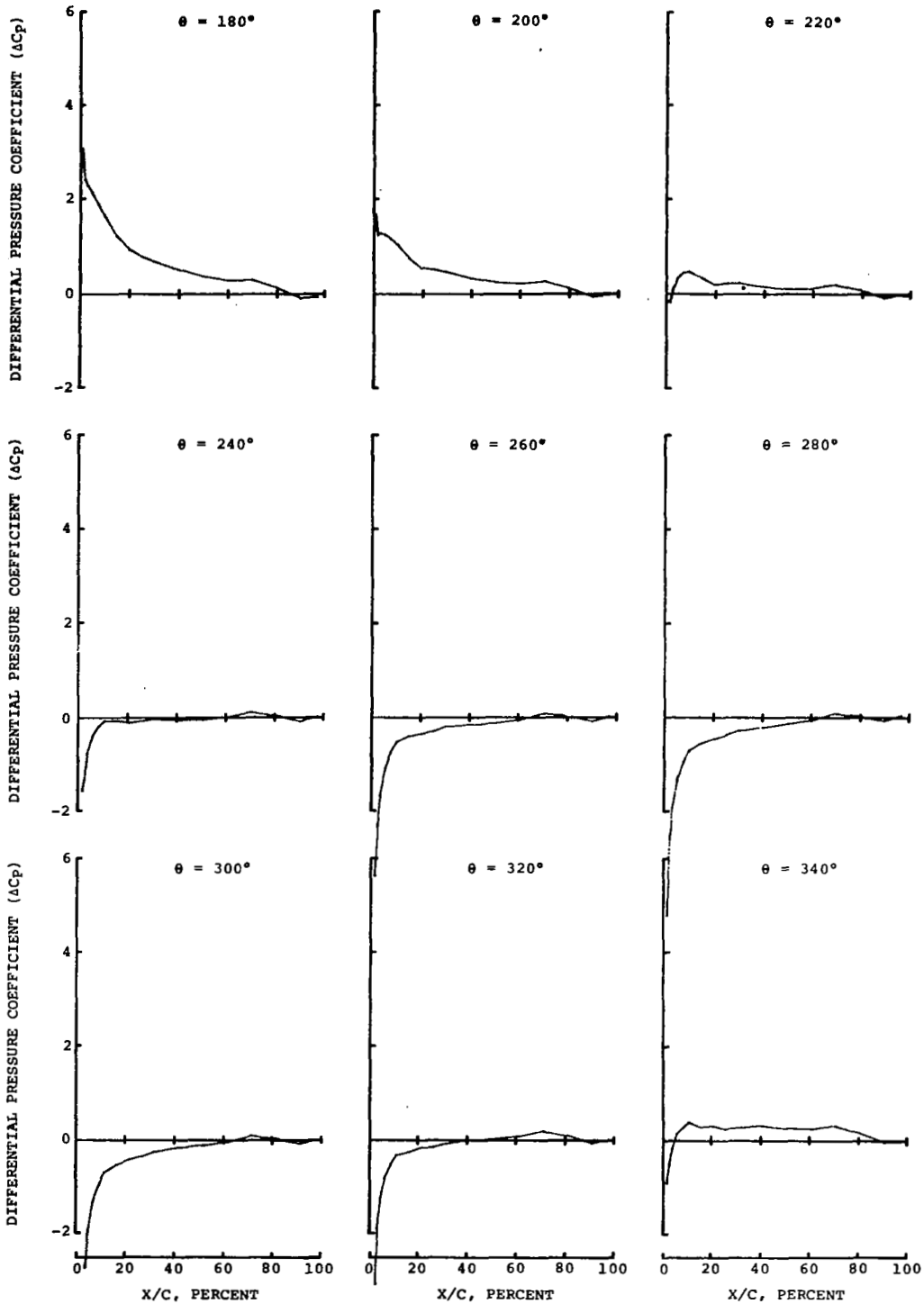

Figure 41. Concluded

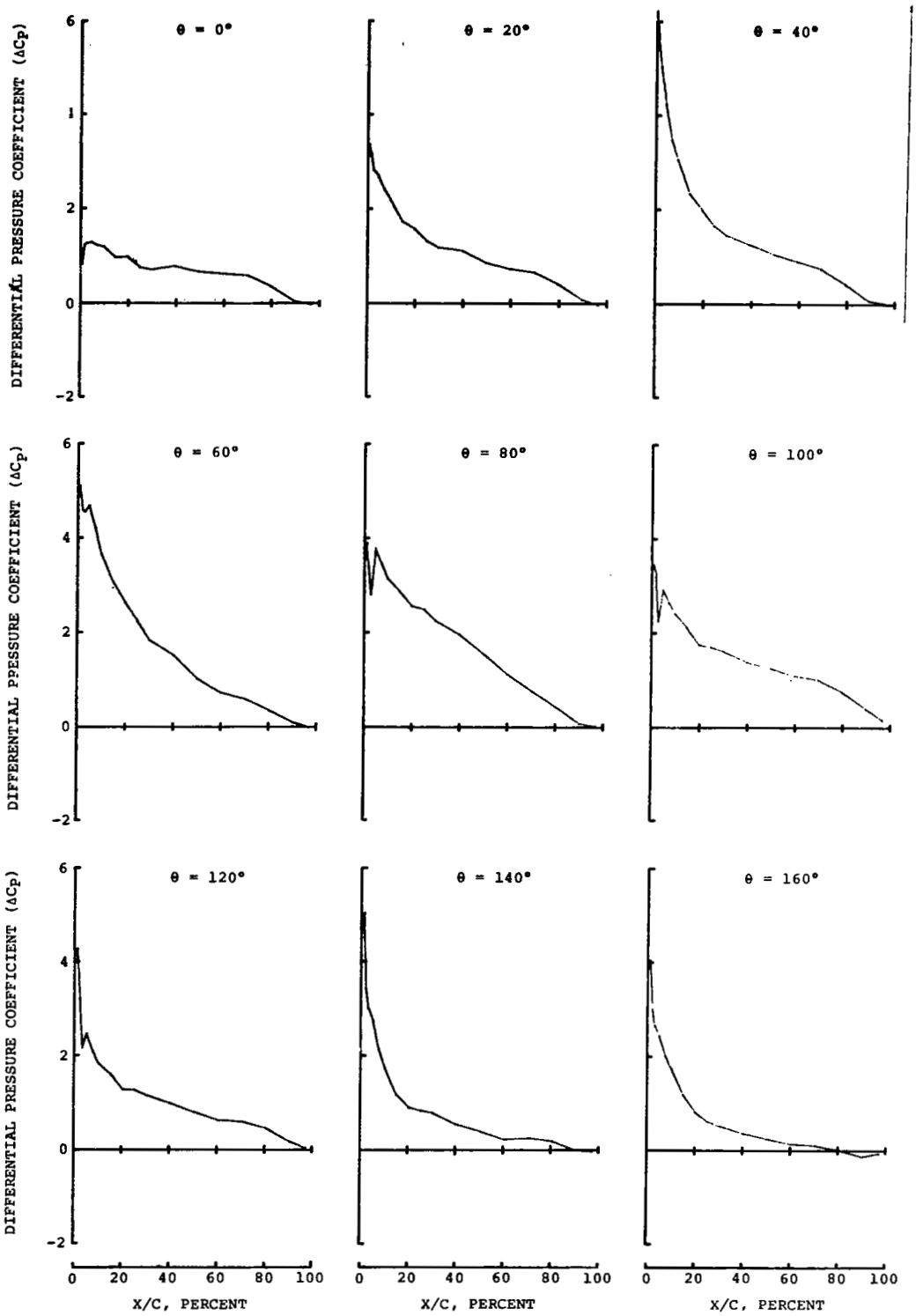

Figure 42. Differential pressure distribution over the NLR 7223-62 airfoil. Nominal conditions: M = 0.4, Rn = 6.4 x 10^6, α_o = 5.0°, $\Delta\alpha$ = 10.0°, f_D = 46.0 Hz (T.P. 12179.3).

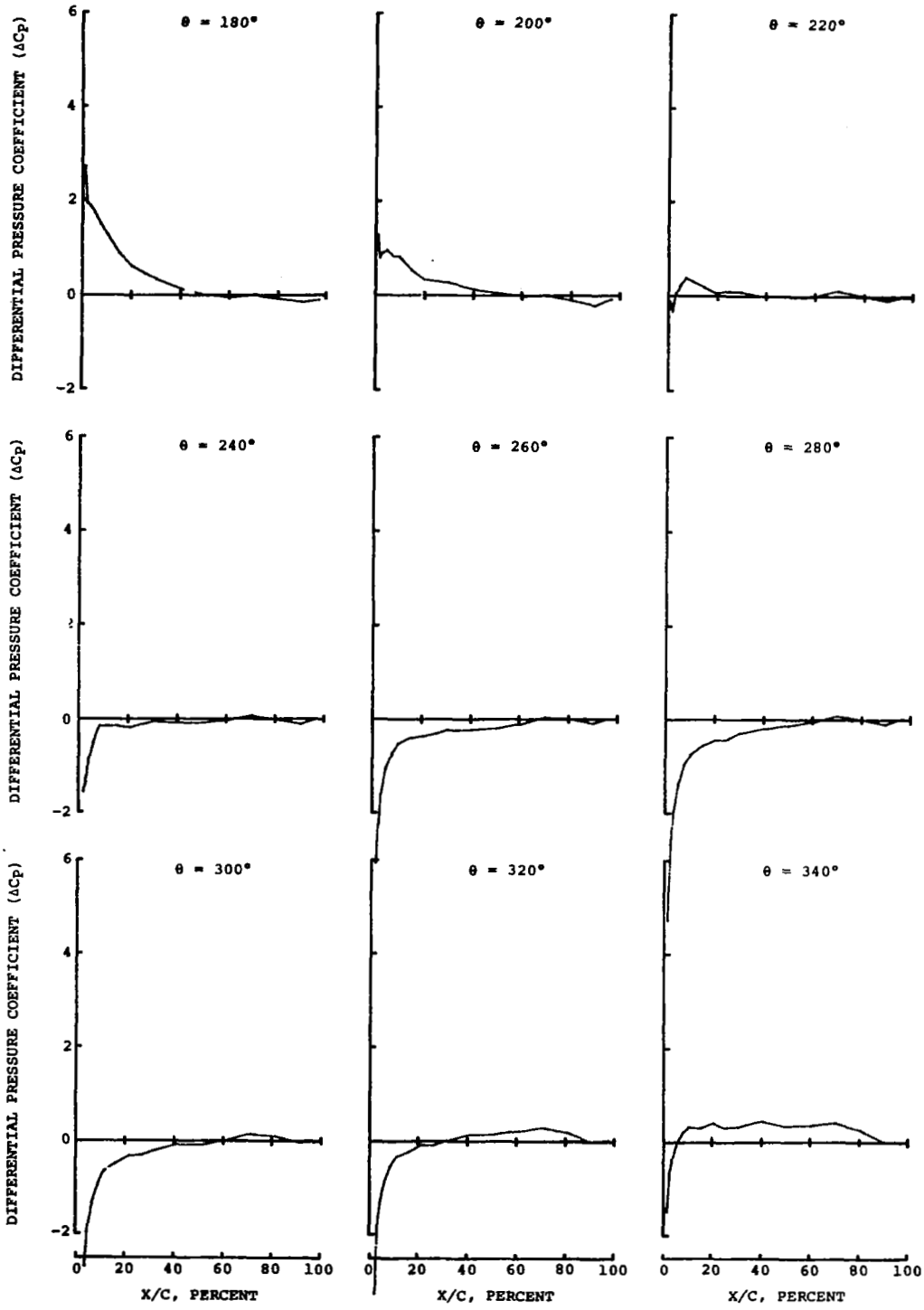

Figure 42. Concluded

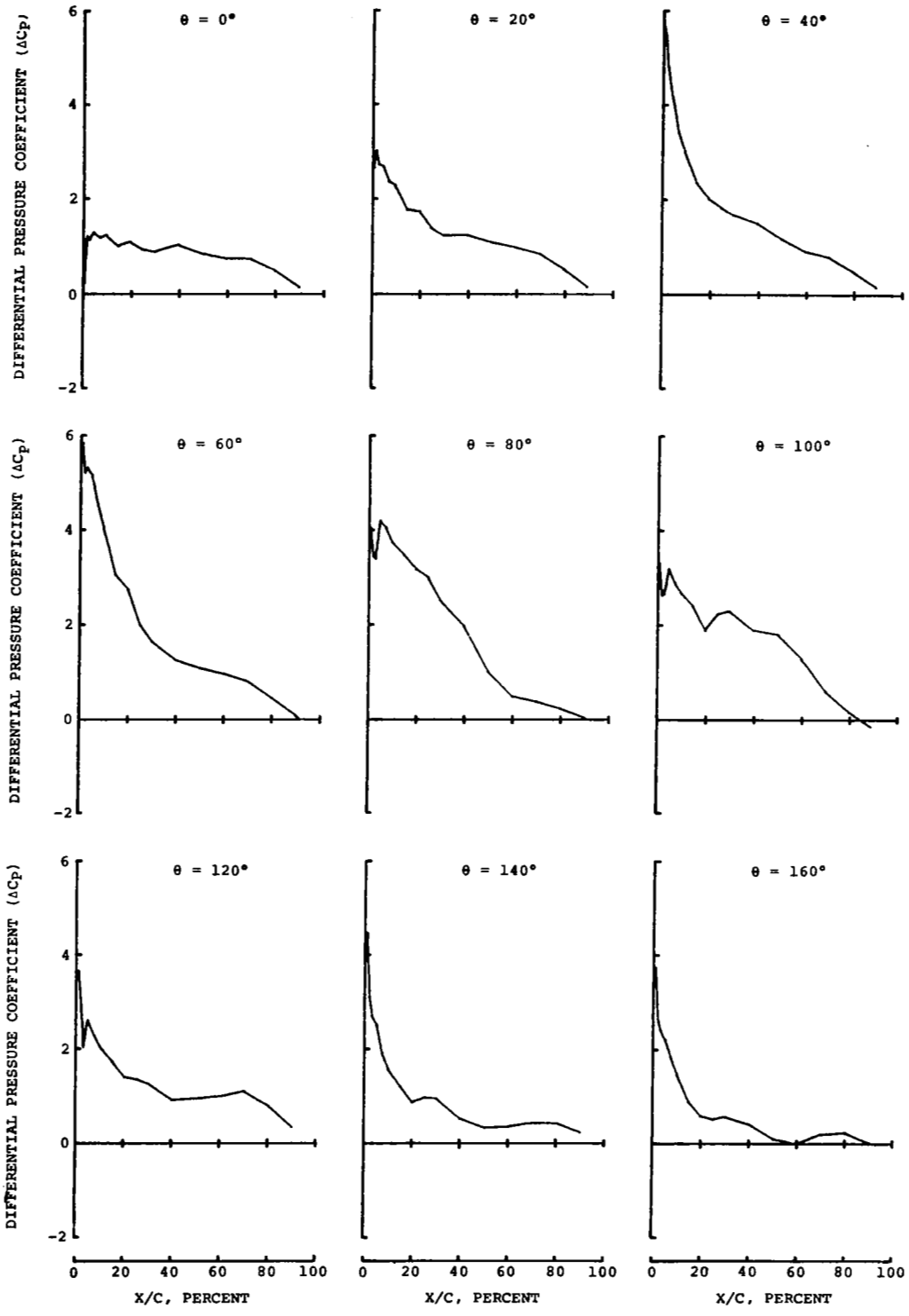

Figure 43. Differential pressure distribution over the NLR 7223-62 airfoil. Nominal conditions: $M = 0.4$, $Rn = 6.4 \times 10^6$, $\alpha_o = 5.0°$, $\Delta\alpha = 10.0°$, $f_D = 70.0$ Hz (T.P. 12187.3).

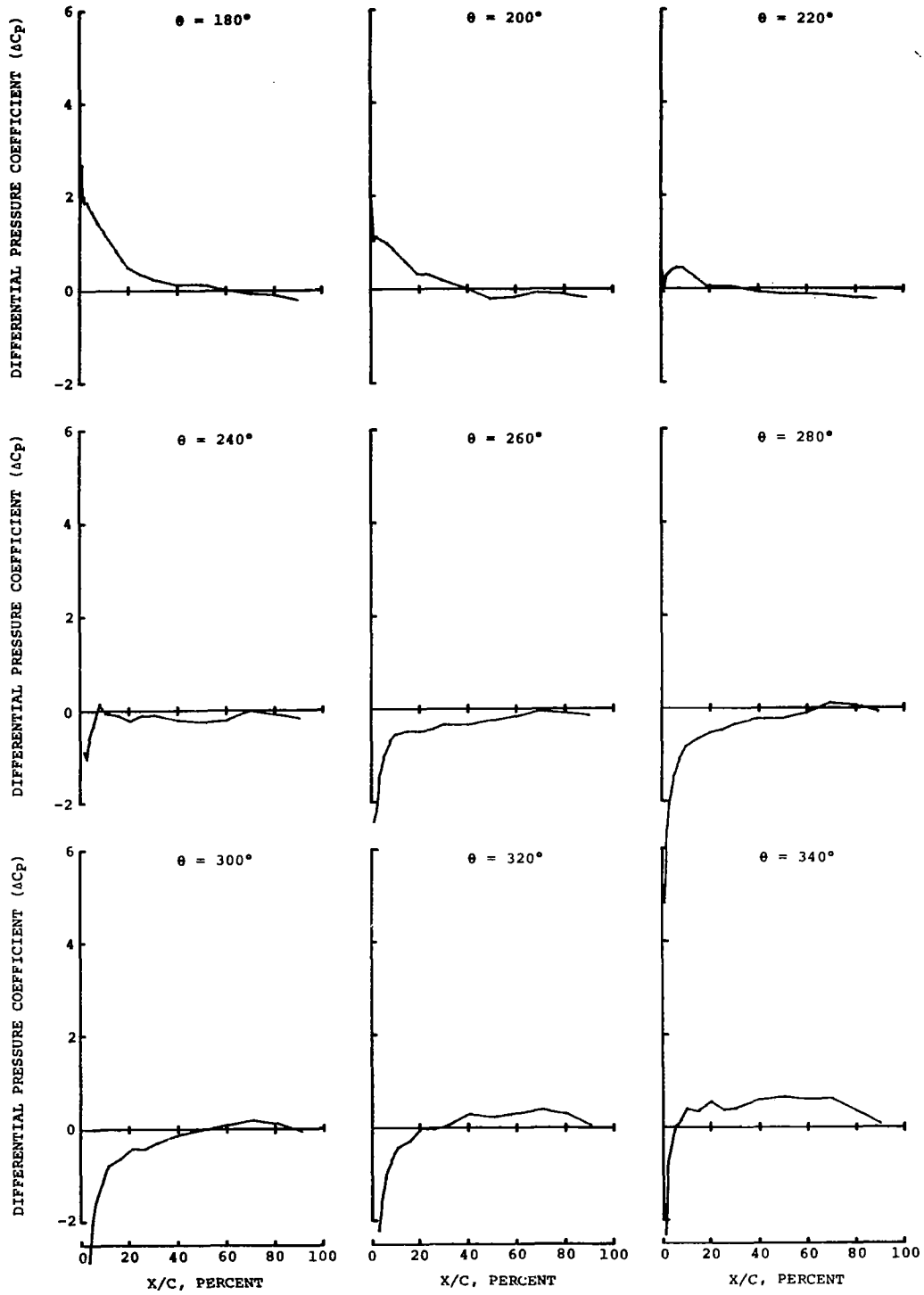

Figure 43. Concluded

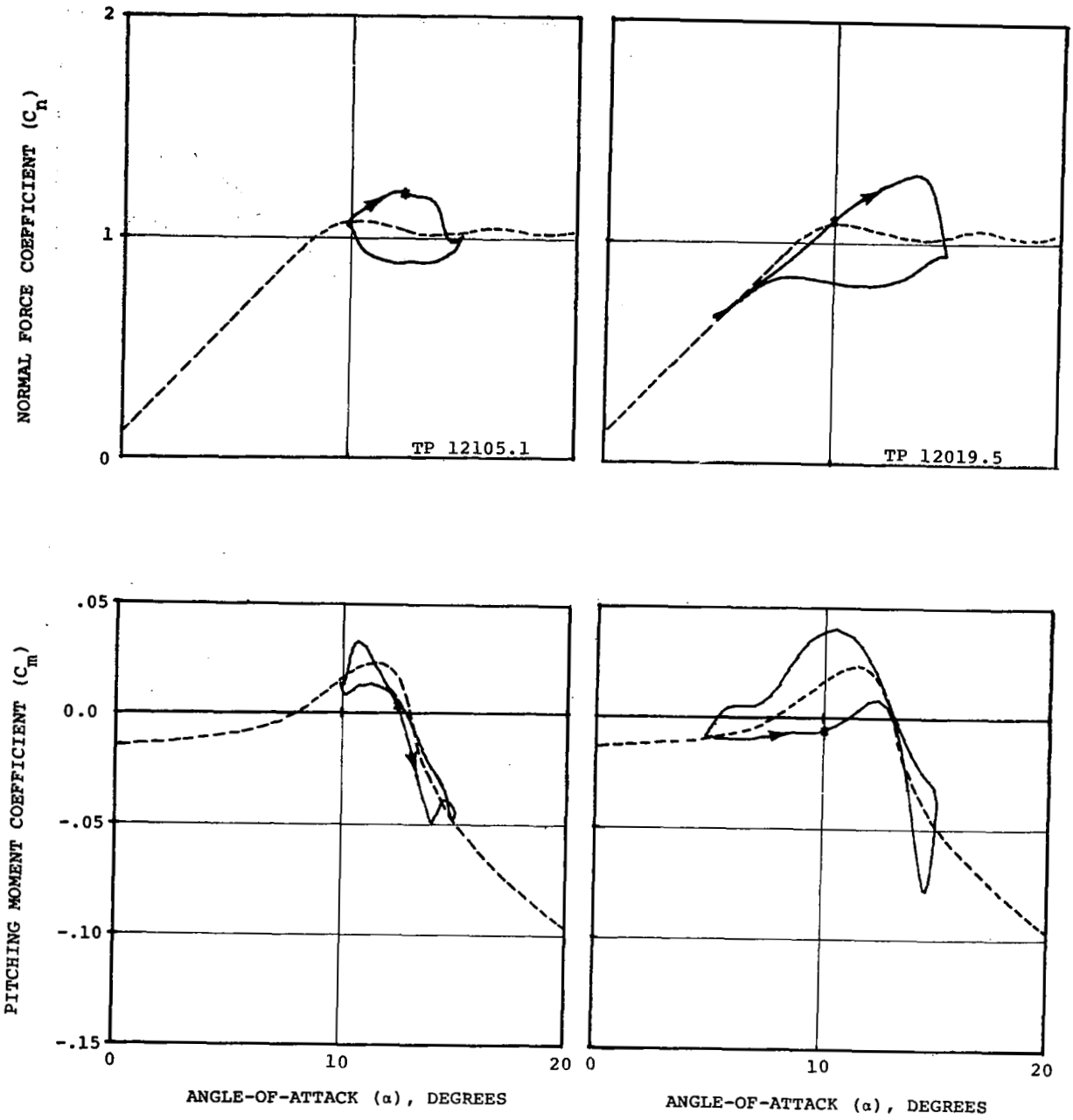

(a) $\Delta\alpha = 2.5°$ (b) $\Delta\alpha = 5.0°$

Figure 44. Effect of pitch oscillation amplitude on the dynamic stall characterisitcs of the normal-force and pitching-moment coefficients of the NLR 7223-62 airfoil. Nominal conditions: M = 0.4, Rn = 6.4 x 10^6, f_D = 23.0 Hz, α_{max} = 15.0°

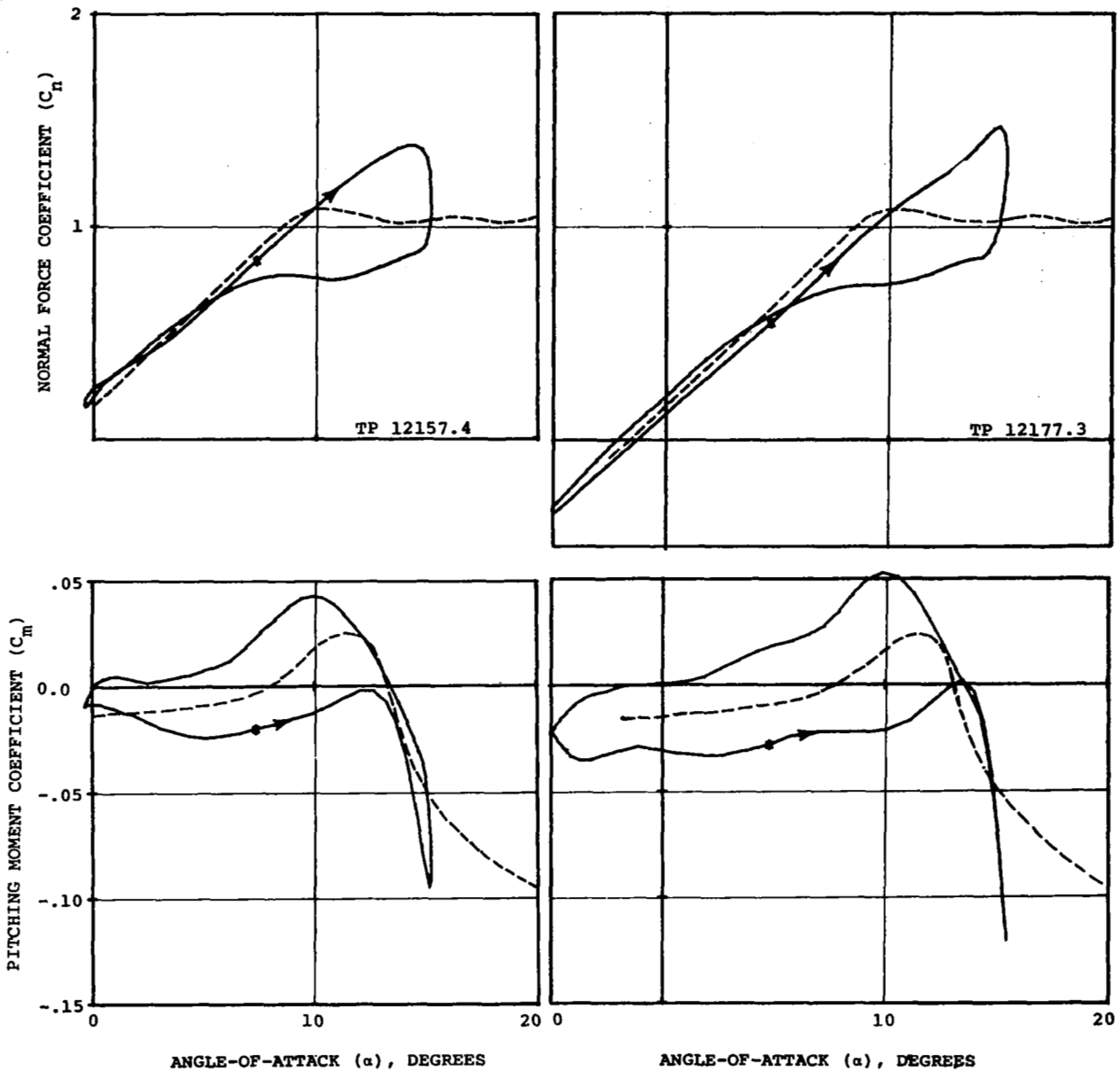

(c) $\Delta\alpha = 7.5°$ (d) $\Delta\alpha = 10.0°$

Figure 44. Concluded

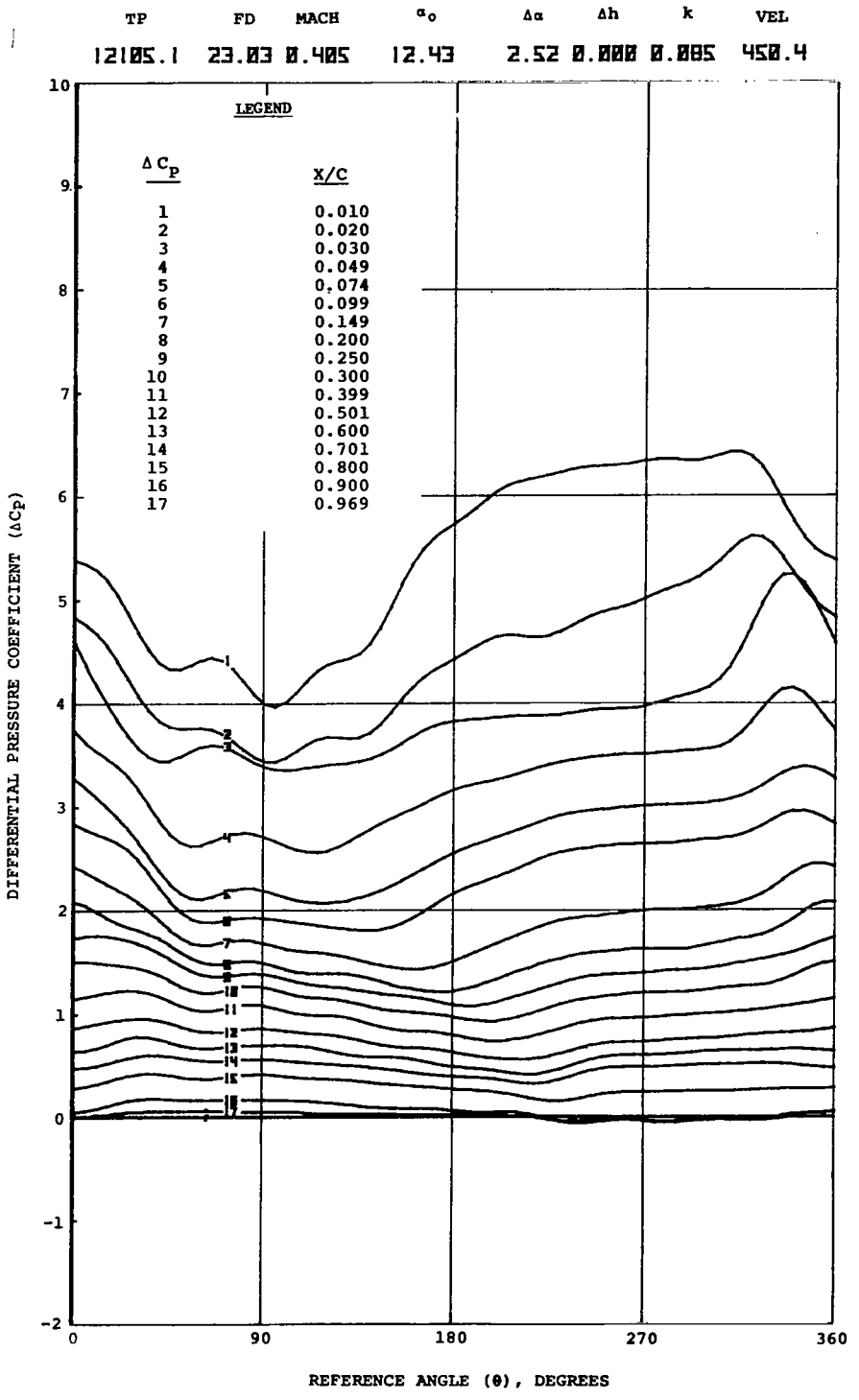

(a) $\Delta\alpha = 2.5°$

Figure 45. Effect of pitch oscillation amplitude on the local differential pressure over the NLR 7223-62 airfoil. Nominal conditions: M = 0.4, Rn = 6.4 x 10^6, f_D = 23.0 Hz, α_{max} = 15.0°.

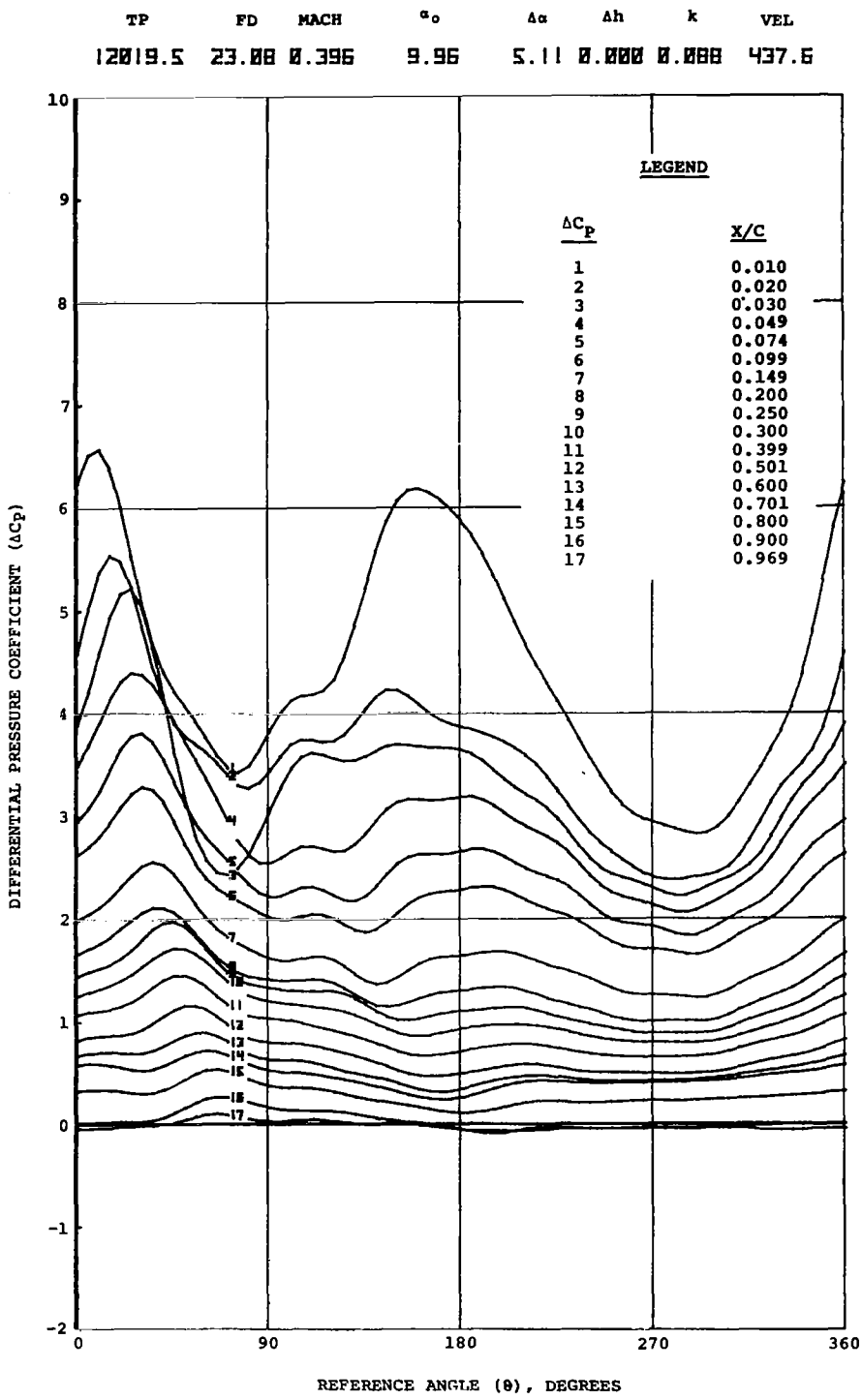

(b) $\Delta\alpha = 5.0°$

Figure 45. Continued

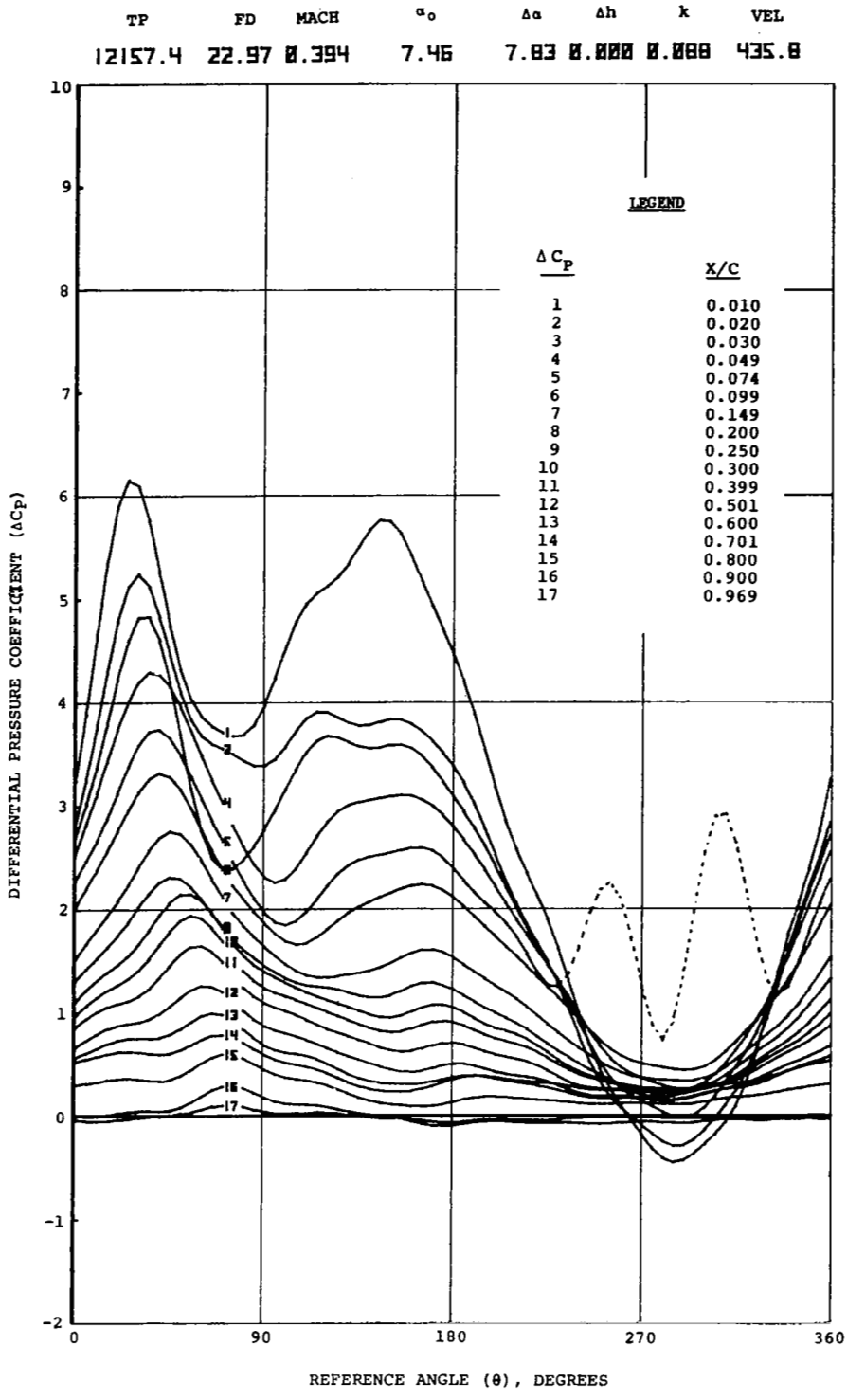

(c) $\Delta\alpha = 7.5°$

Figure 45. Continued

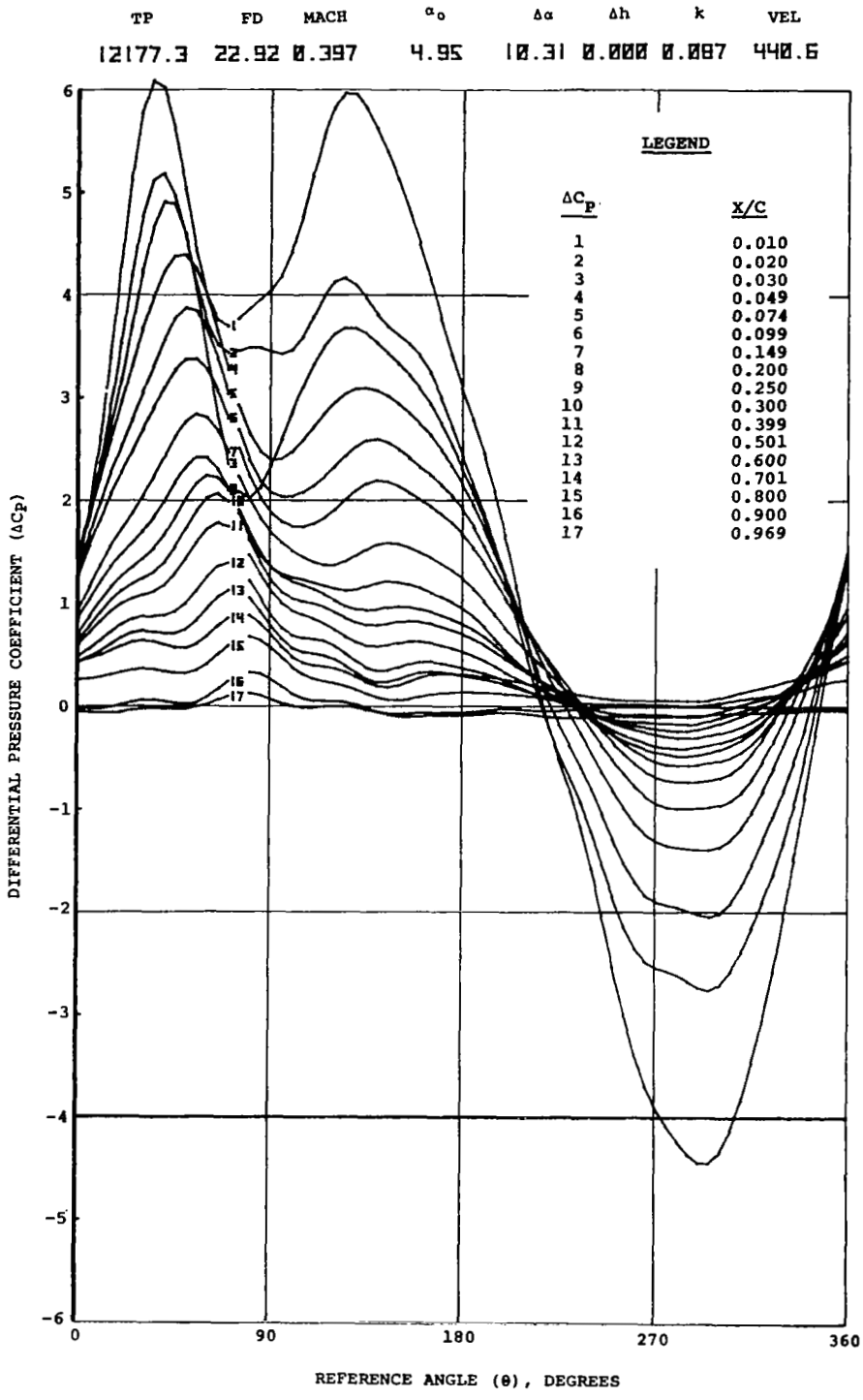

(d) $\Delta\alpha$ = 10.0°

Figure 45. Concluded

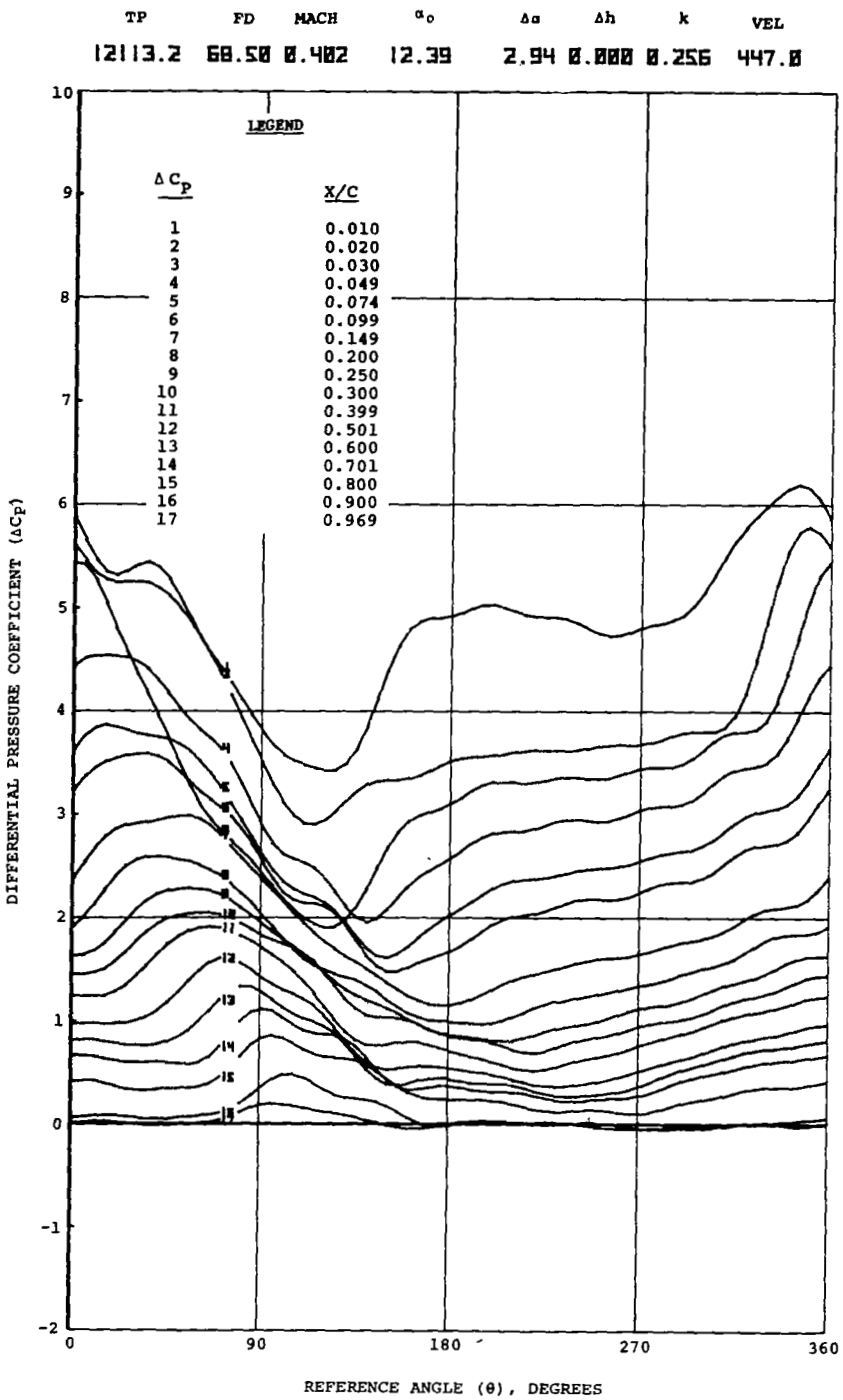

(a) $\Delta\alpha = 2.5°$

Figure 47. Effect of pitch oscillation amplitude on the local differential pressures over the NLR 7223-62 airfoil. Nominal conditions: M = 0.4, Rn = 6.4 x 10^6, f_D = 70.0 Hz, α_{max} = 15.0°.

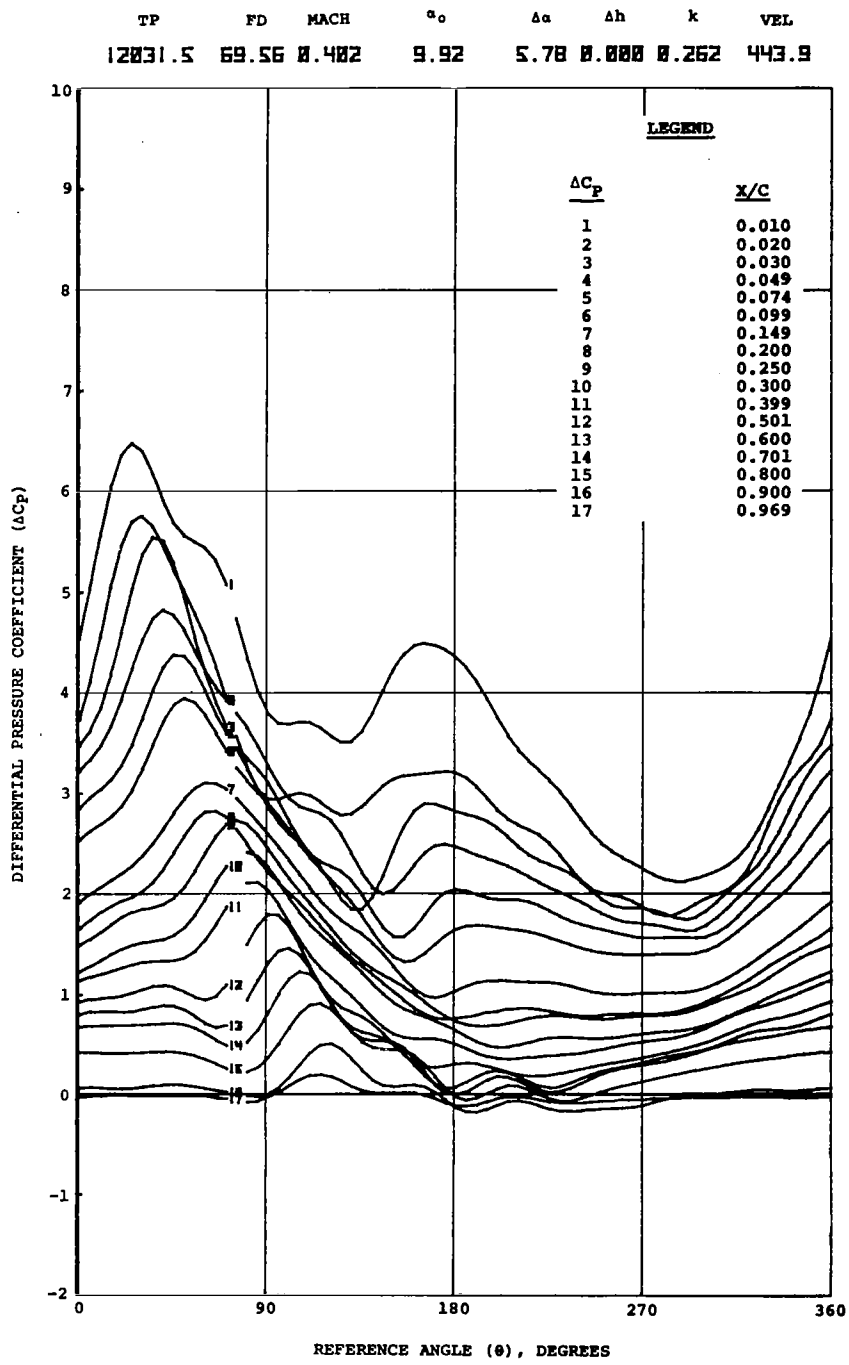

(b) $\Delta\alpha = 5.0°$

Figure 47. Continued

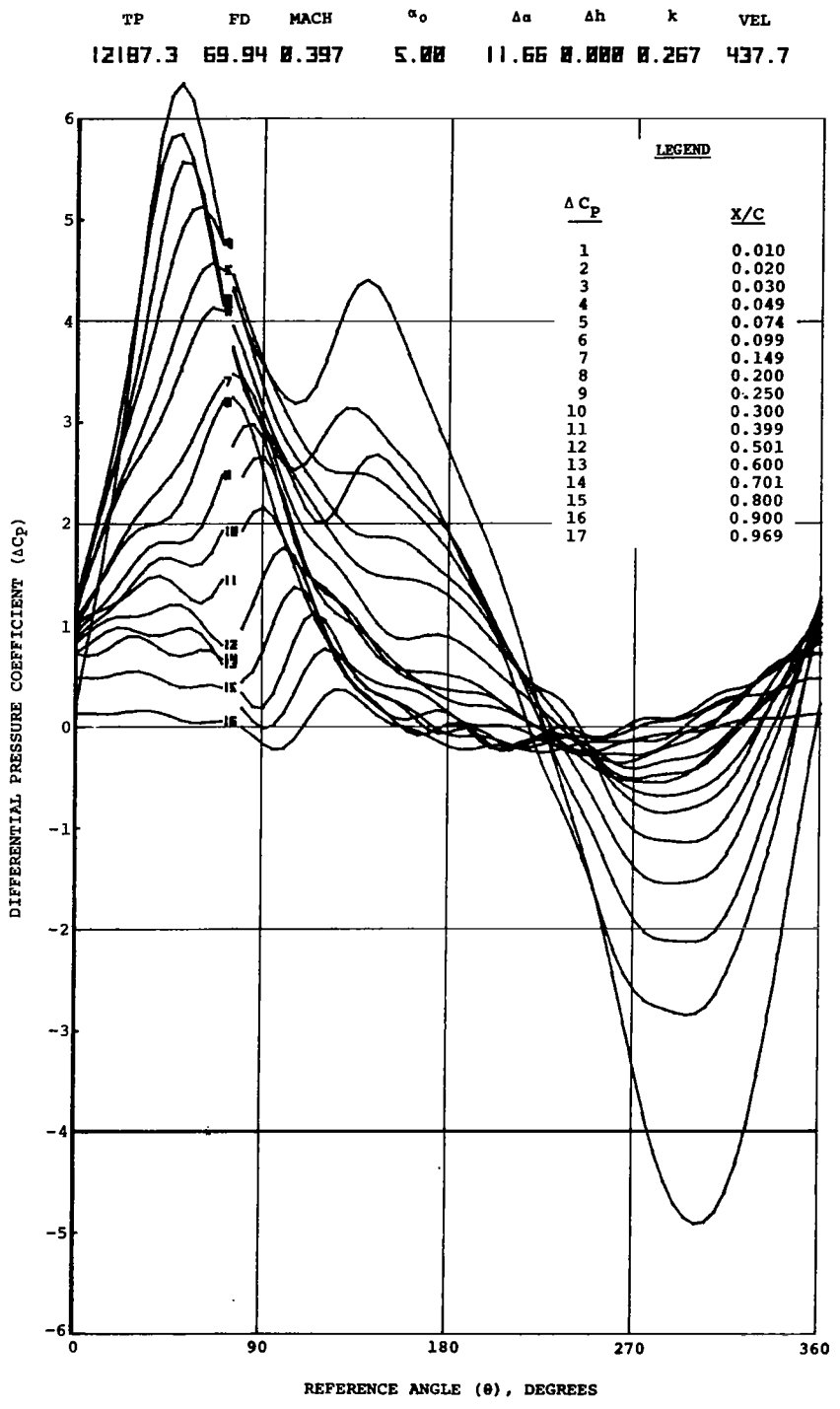

(c) $\Delta\alpha$ = 10.0°

Figure 47. Concluded

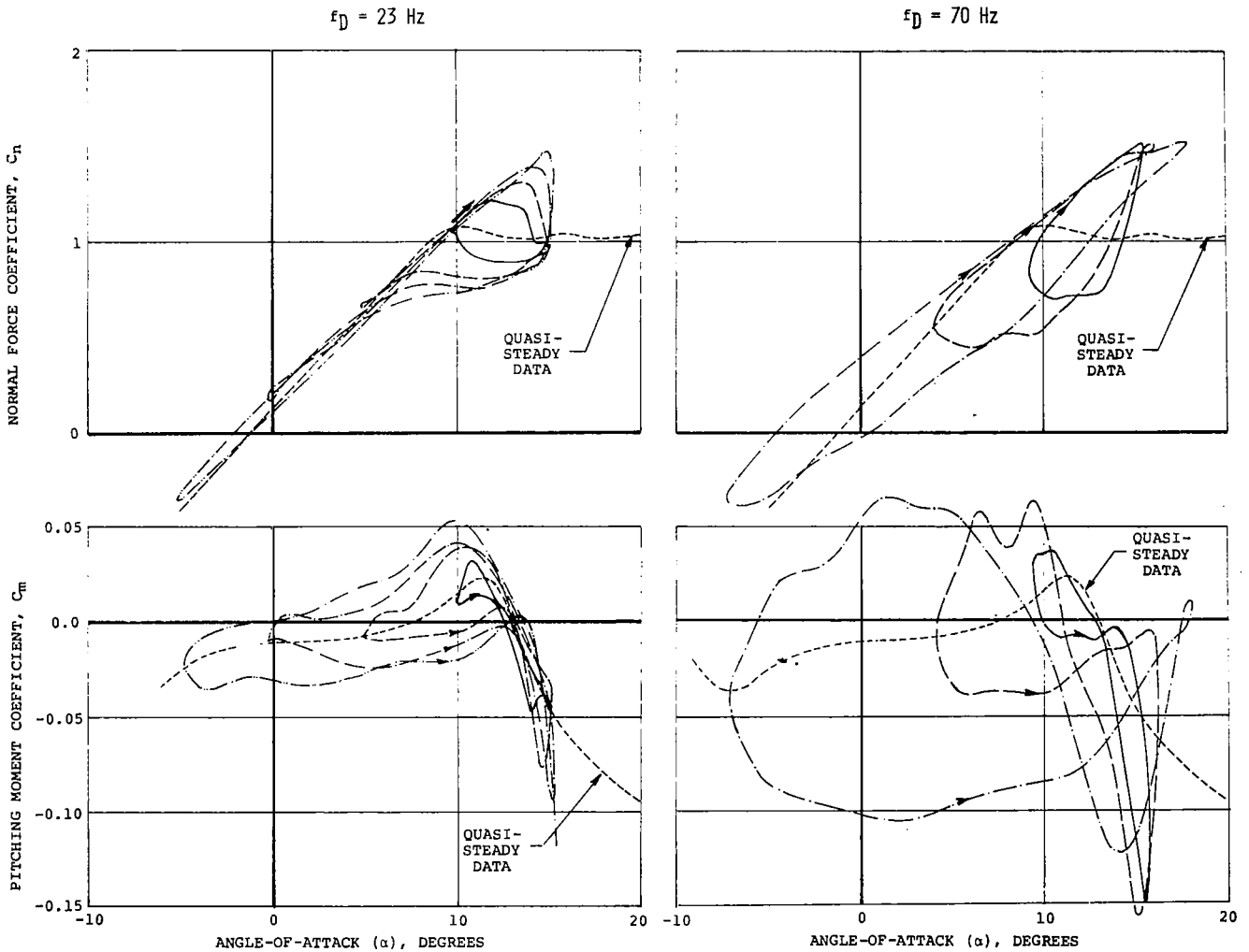

Figure 48. Overlay of normal-force and pitching-moment loops of the NLR 7223-62 airfoil to illustrate the effect of amplitude of oscillation on dynamic stall at two drive frequencies. Nominal conditions: M=0.4, Rn=6.4x10^6, $\alpha_{MAX} \simeq 15.0°$, $\Delta\alpha$=2.5° to 10.0°.

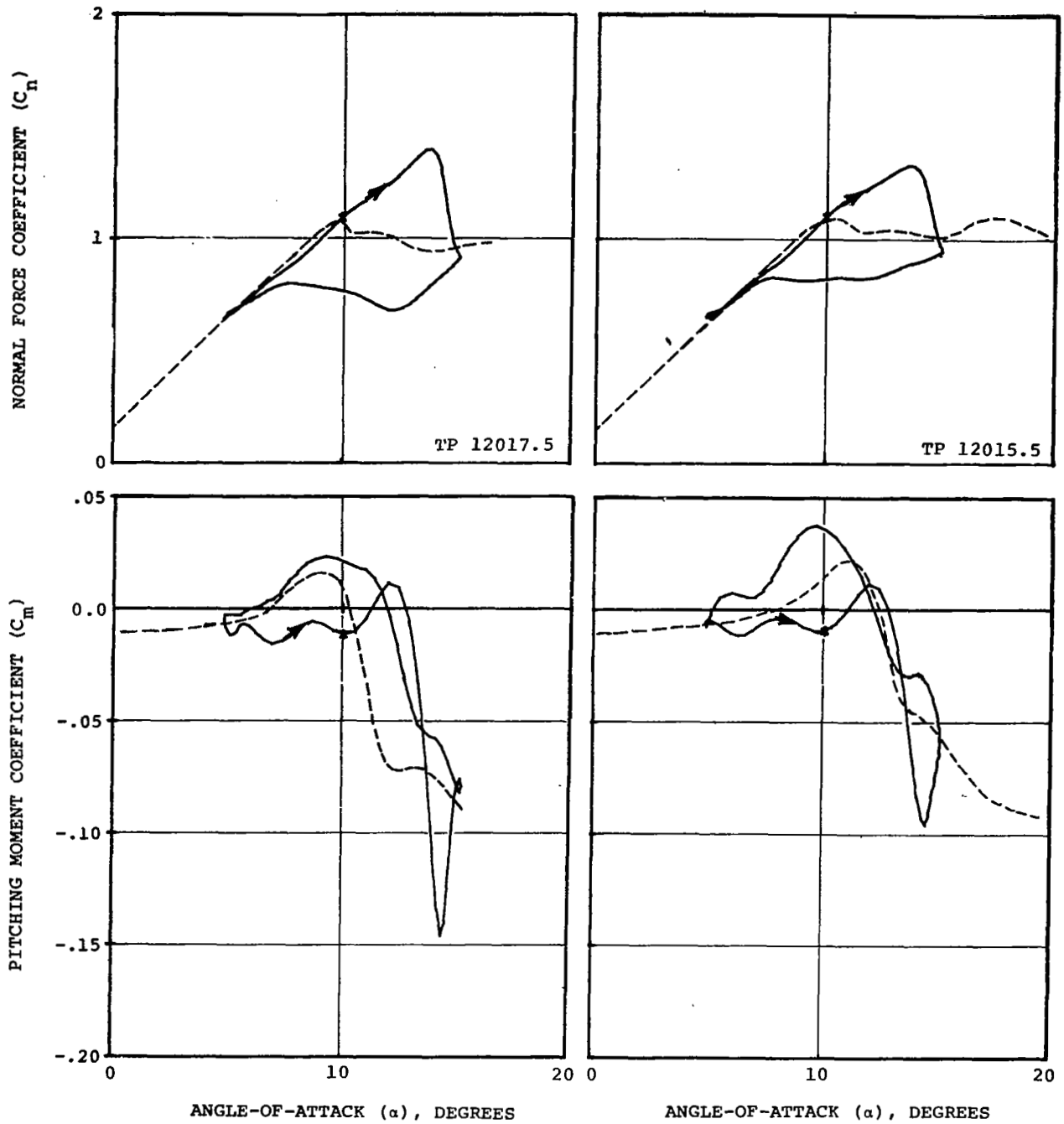

(a) Rn = 2.4 x 10^6 (b) Rn = 4.7 x 10^6

Figure 49. Effect of Reynolds number variation on the dynamic stall characteristics of the normal force and pitching moment coefficients of the NLR 7223-62 airfoil. Nominal conditions: M = 0.4, f_D = 23.0 Hz, α_o = 10.0°, $\Delta\alpha$ = 5.0°.

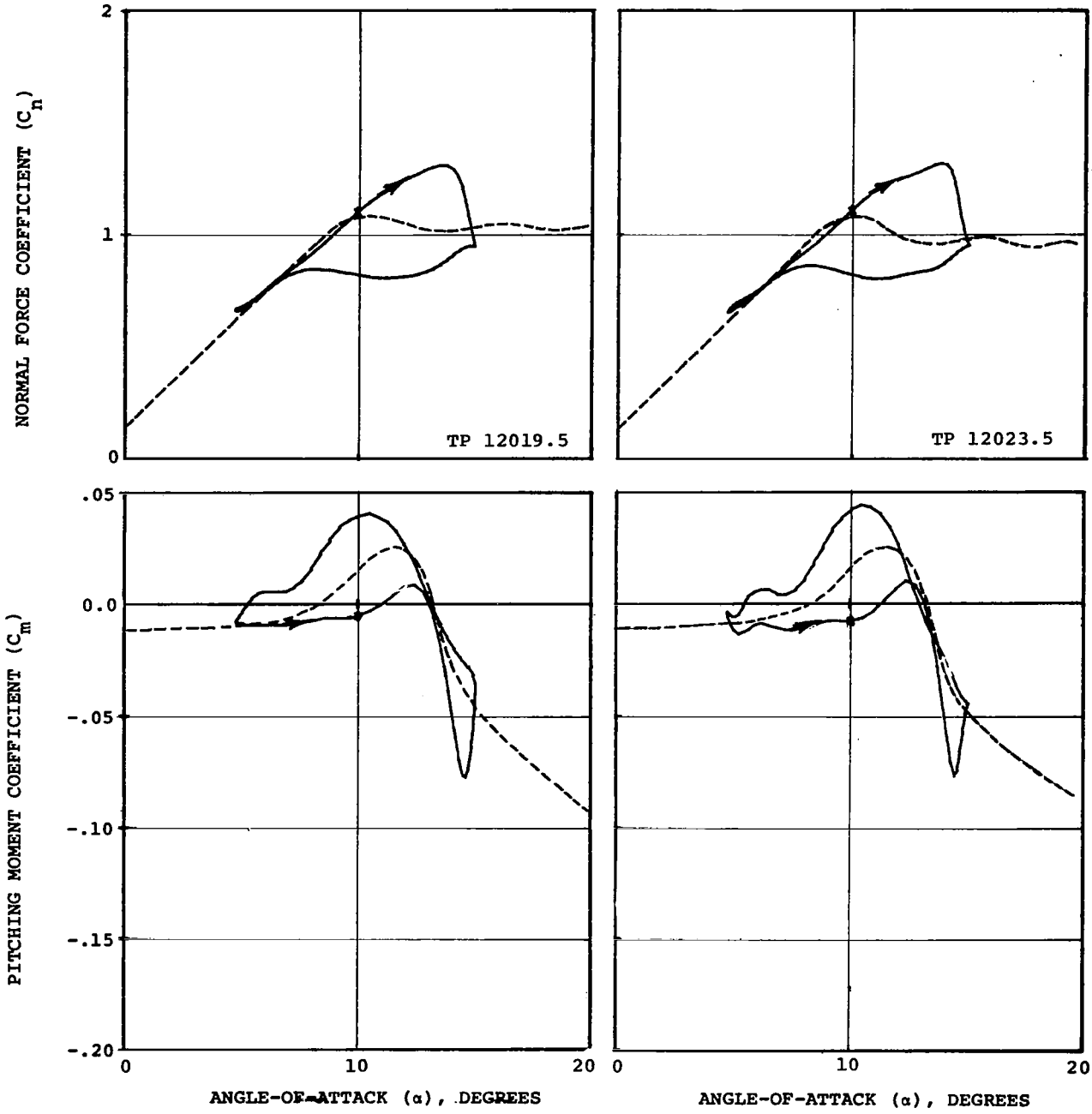

(c) Rn = 6.4 x 10^6

(d) Rn = 7.0 x 10^6

Figure 49. Concluded

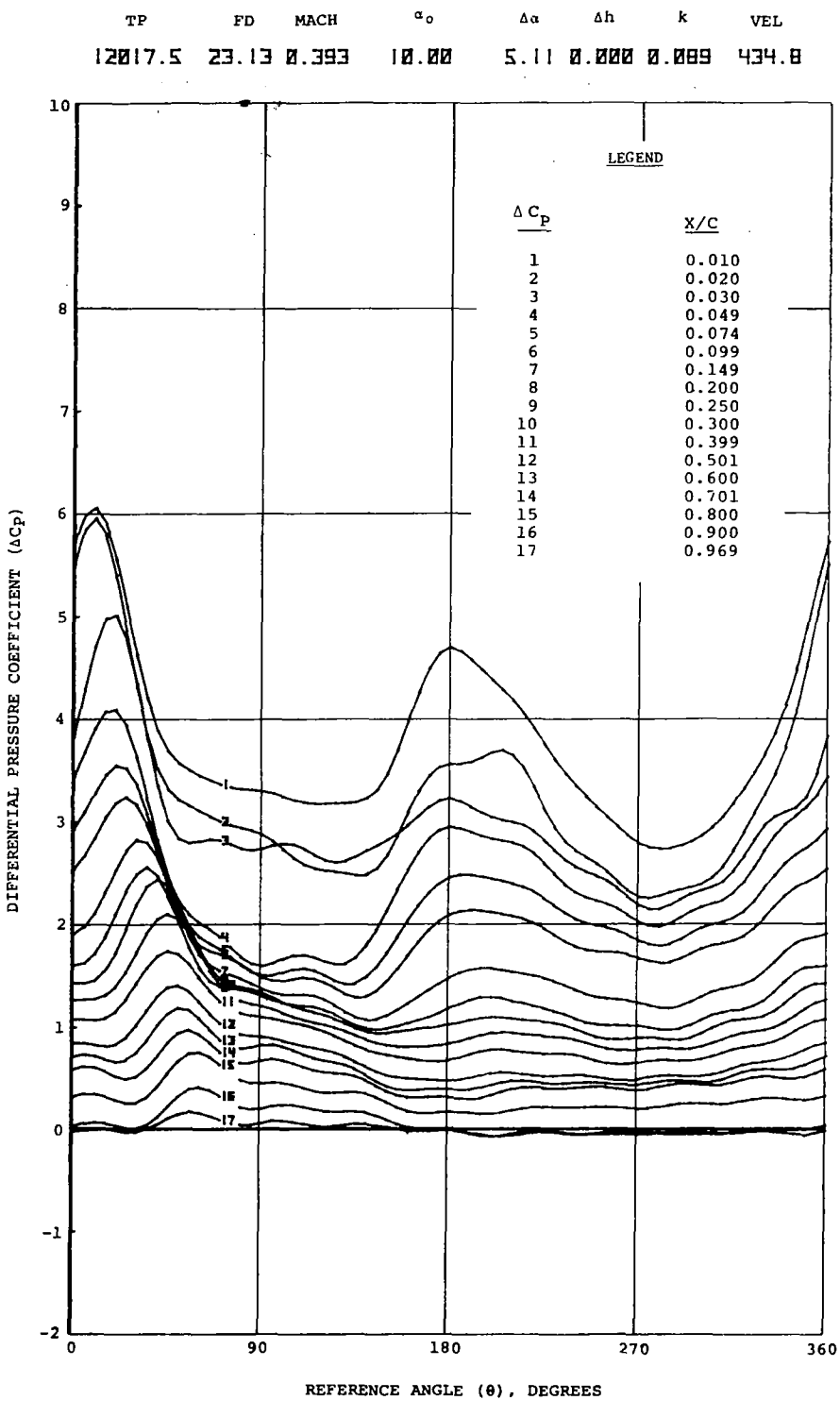

(a) Rn = 2.4 x 10^6

Figure 50. Effect of Reynolds-number variation on the local differential pressures over the NLR 7223-62 airfoil. Nominal conditions: M = 0.4, f_D = 23.0 Hz, α_o = 10.0°, $\Delta\alpha$ = 5.0°.

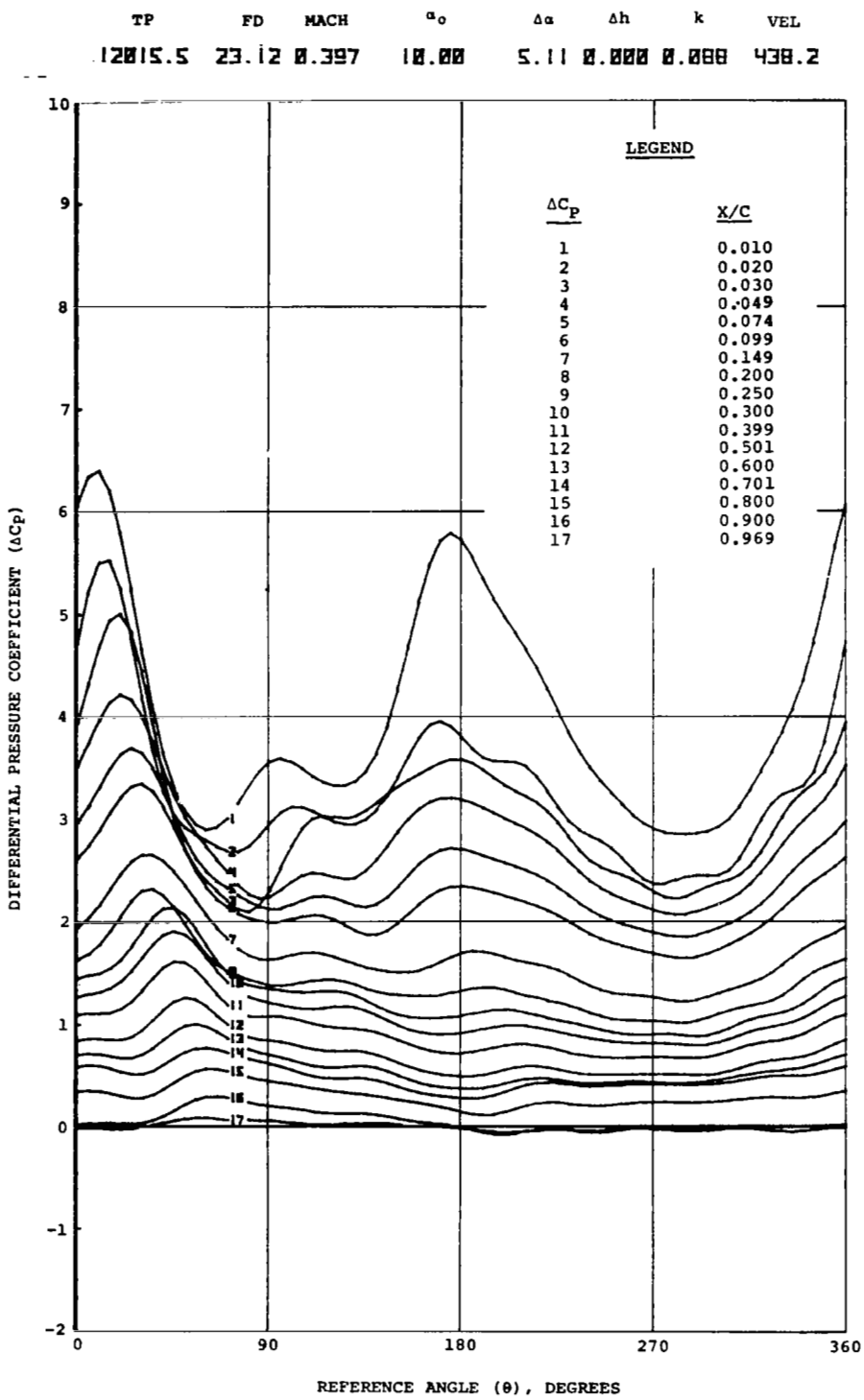

(b) Rn = 4.7 x 10^6

Figure 50. Continued

TP	FD	MACH	α_o	$\Delta\alpha$	Δh	k	VEL
12019.5	23.08	0.396	9.96	5.11	0.000	0.088	437.6

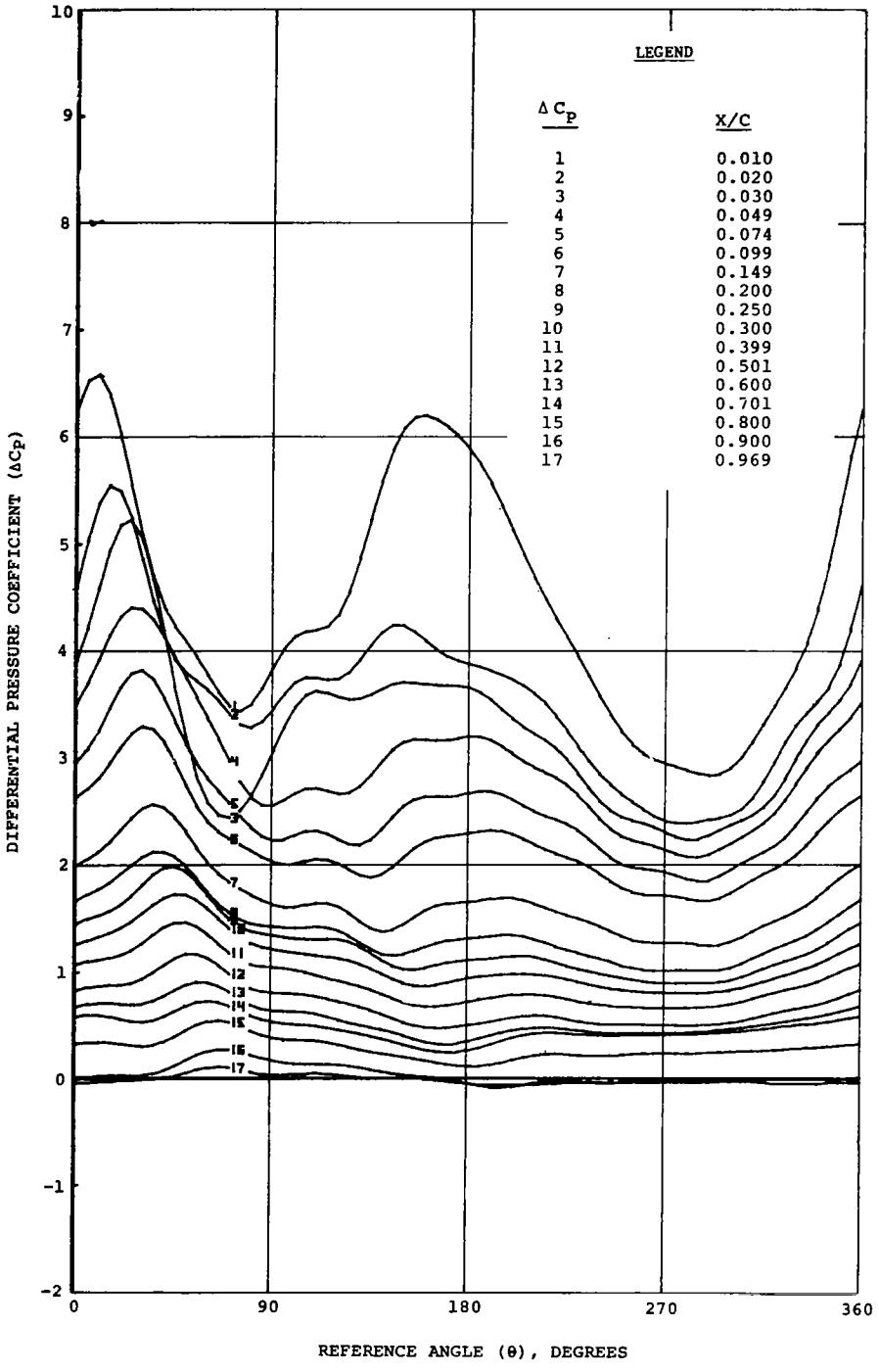

(c) $R_n = 6.4 \times 10^6$

Figure 50. Continued

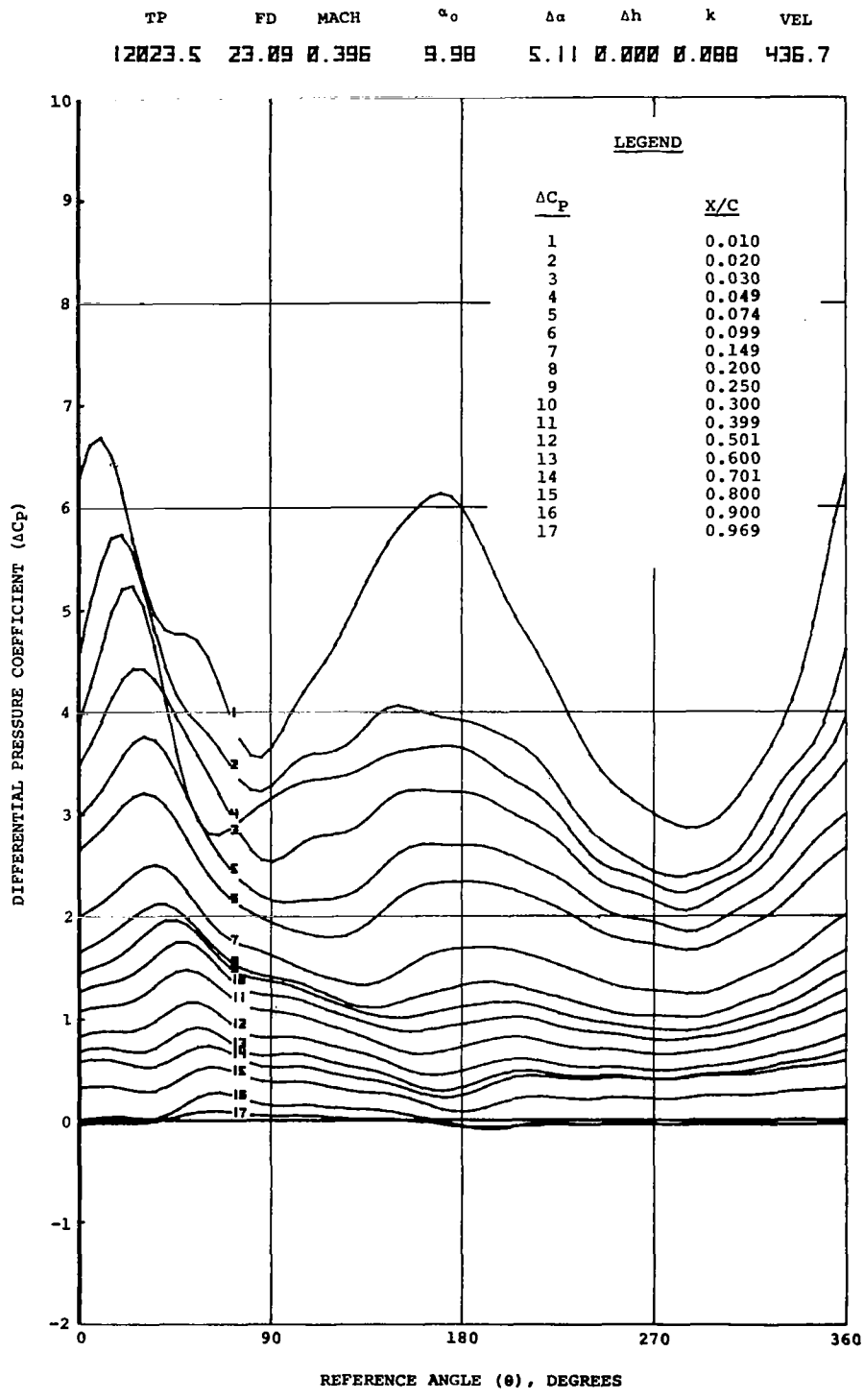

(d) Rn = 7.0 x 10^6

Figure 50. Concluded

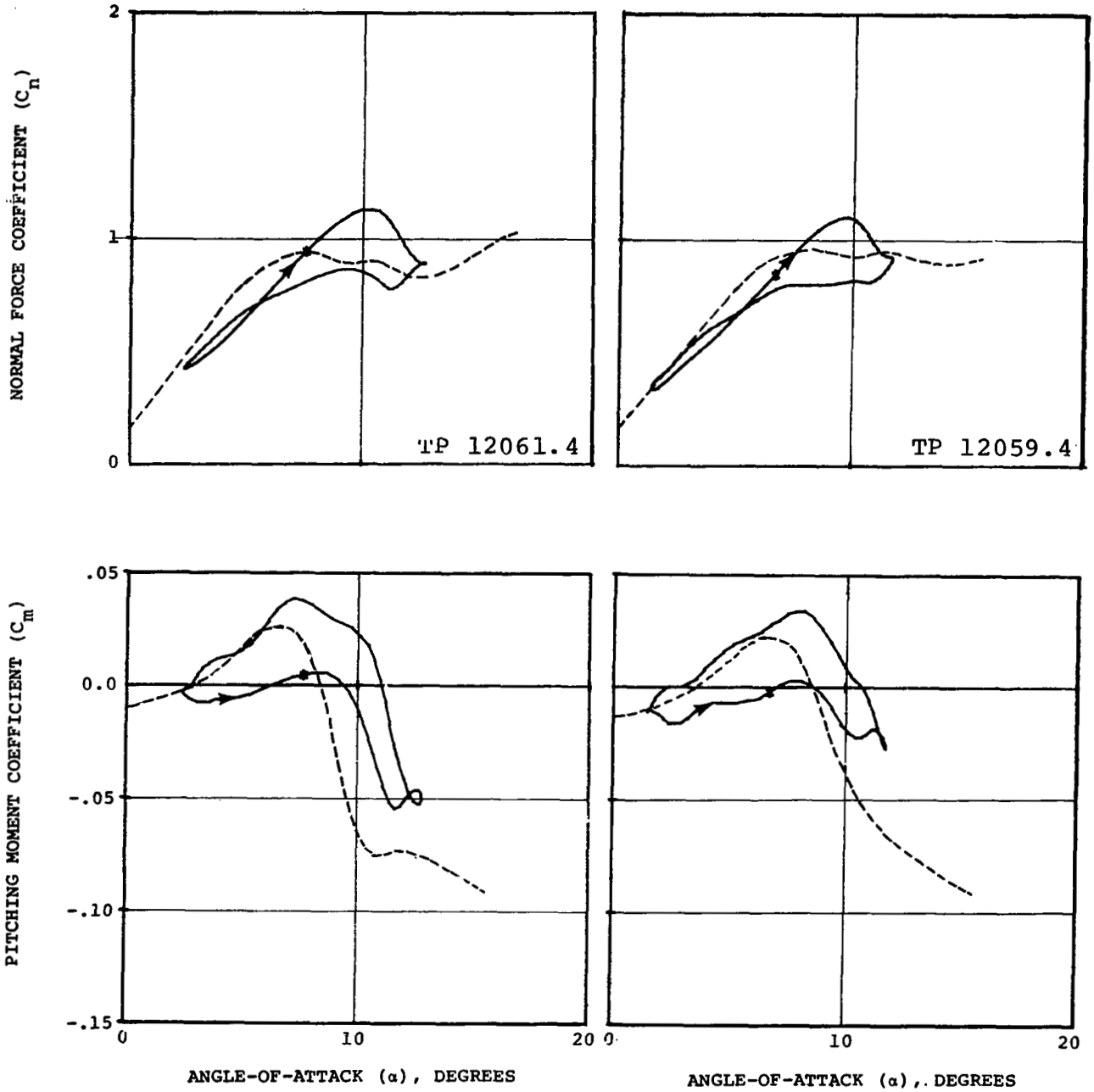

(a) Rn = 3.1 x 10^6
α_o = 7.5°

(b) Rn = 6.2 x 10^6
α_o = 6.6°

Figure 51. Effect of Reynolds-number variation on the dynamic-stall characteristics of the normal force and pitching-moment coefficient of the NLR 7223-62 airfoil. Nominal conditions: M = 0.6, f_D = 23.0 Hz, $\Delta\alpha$ = 5.0°.

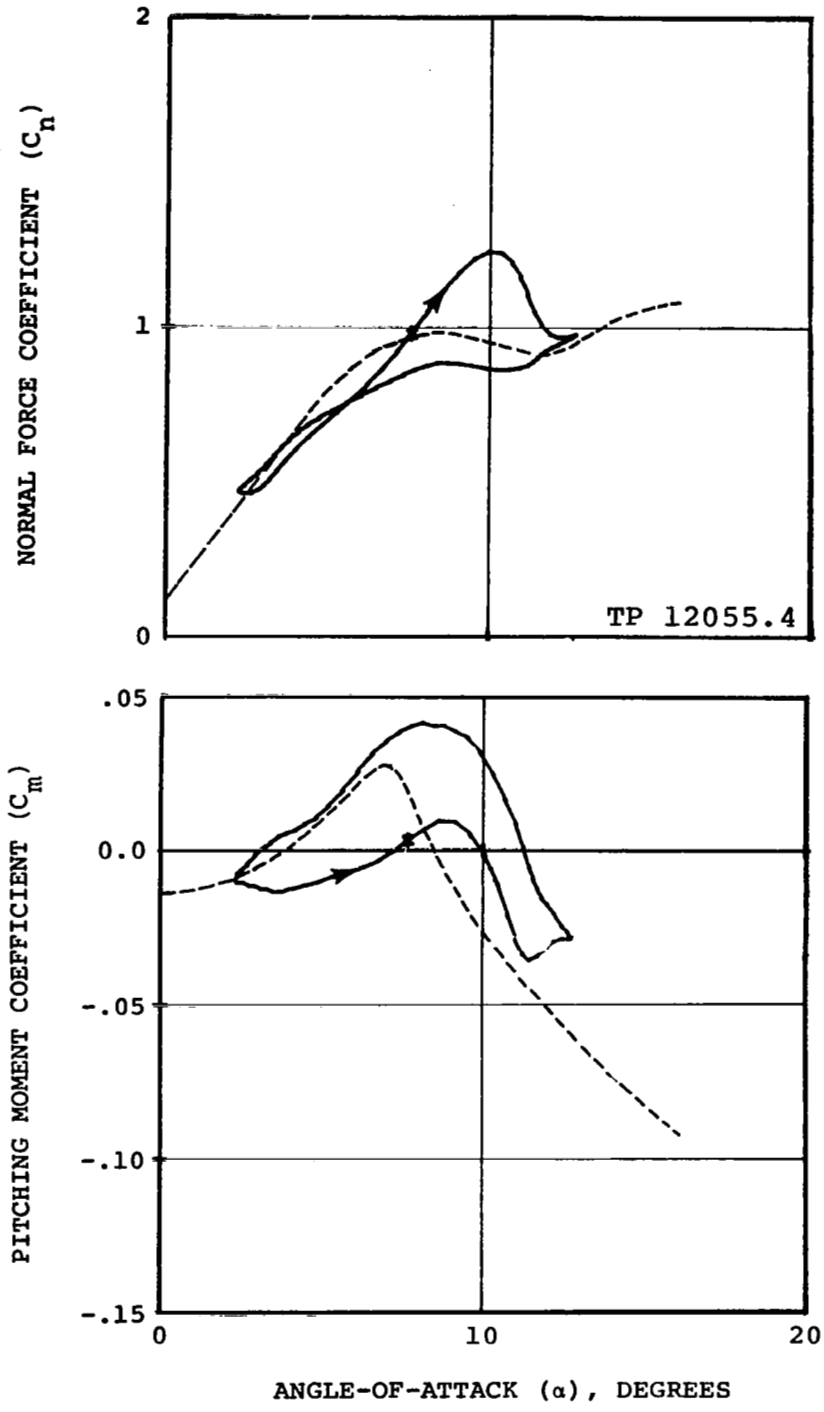

(c) Rn = 9.0 x 10^6
α_o = 7.5°

Figure 51. Concluded

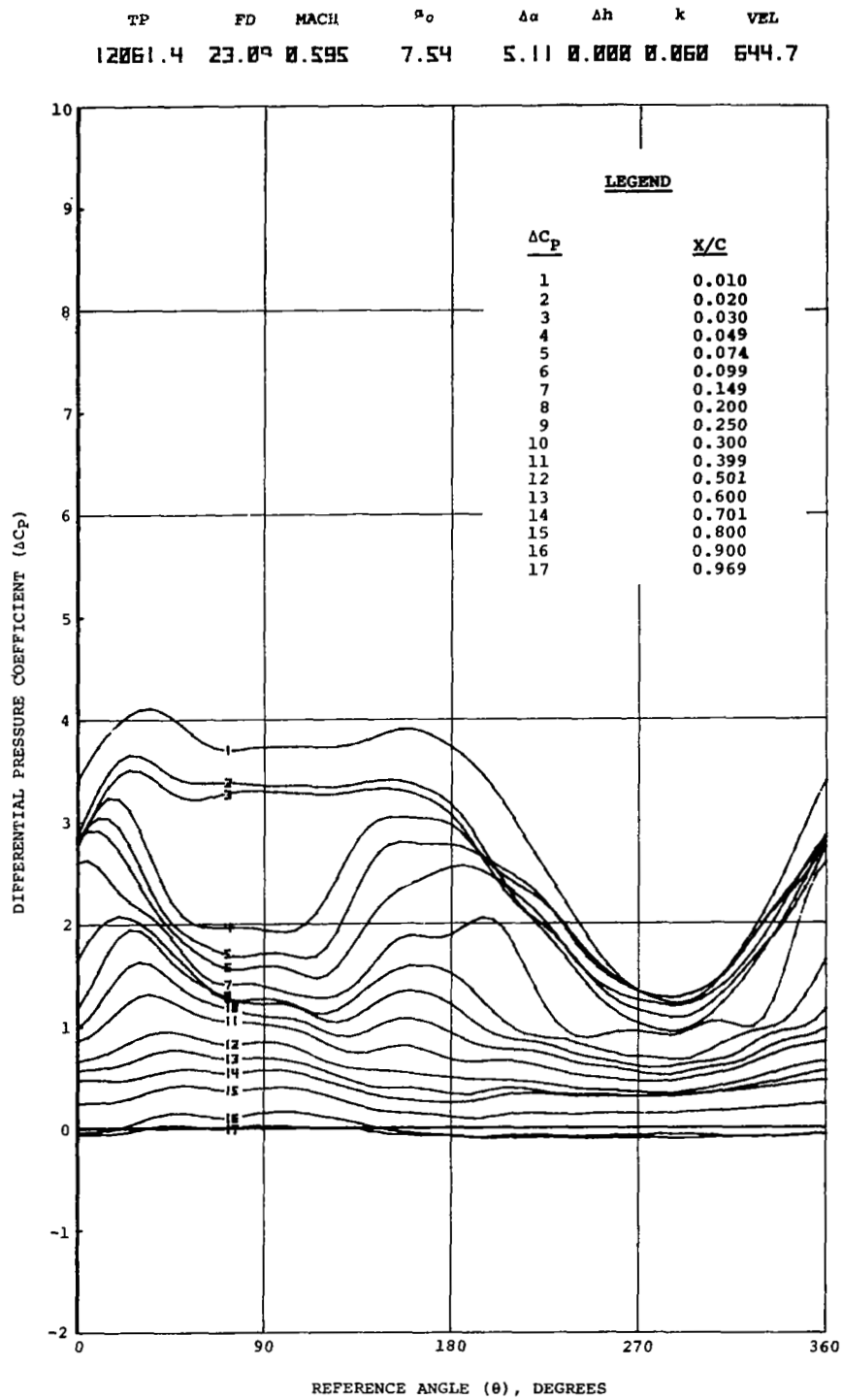

(a) Rn = 3.1 x 10^6
α_o = 7.5°

Figure 52. Effect of Reynolds number variation on the local differential pressures over the NLR 7223-62 airfoil. Nominal conditions: M = 0.6, f_D = 23.0 Hz, $\Delta\alpha$ = 5.0°

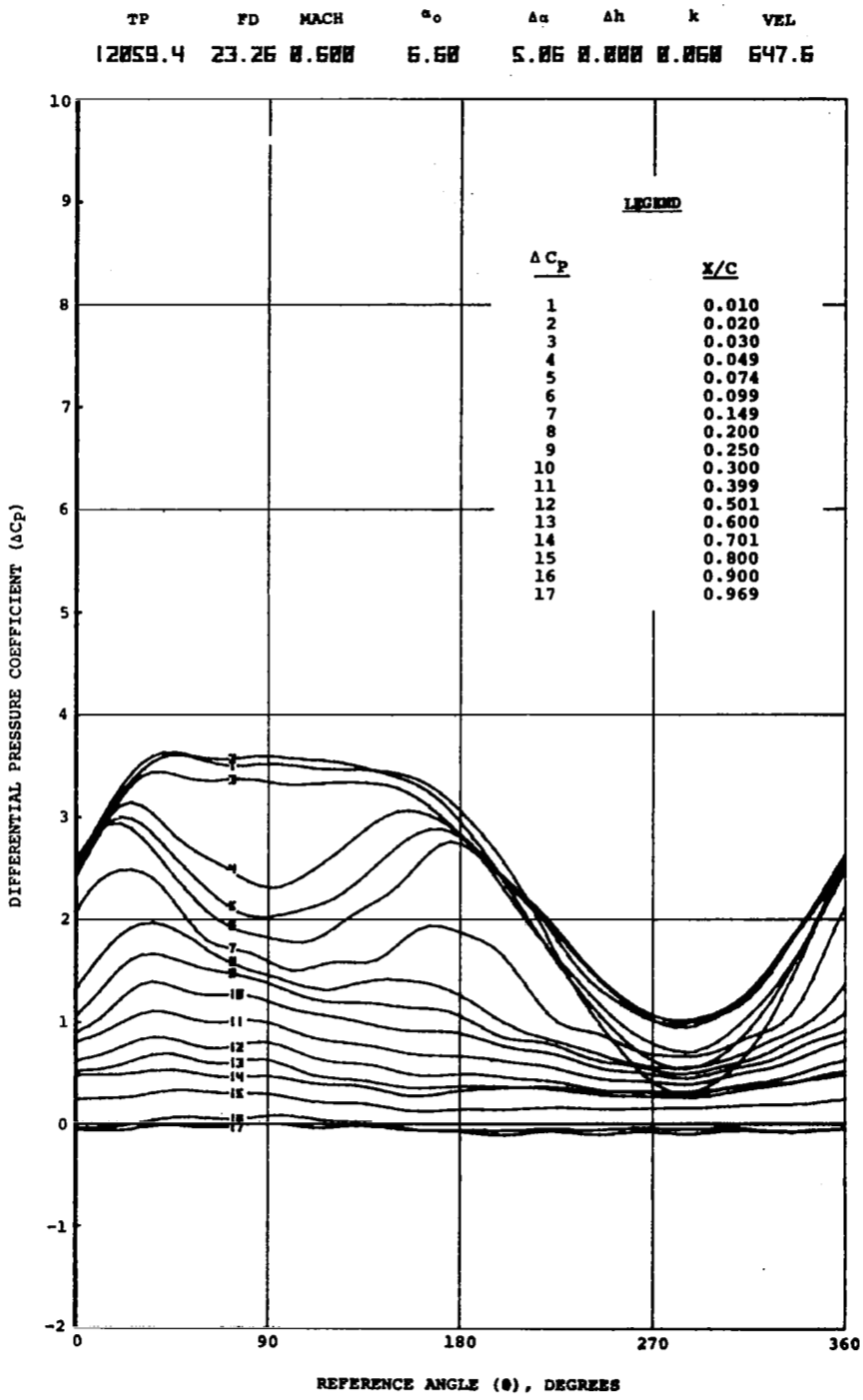

(b) Rn = 6.2 x 10^6
α_o = 6.6°

Figure 52. Continued

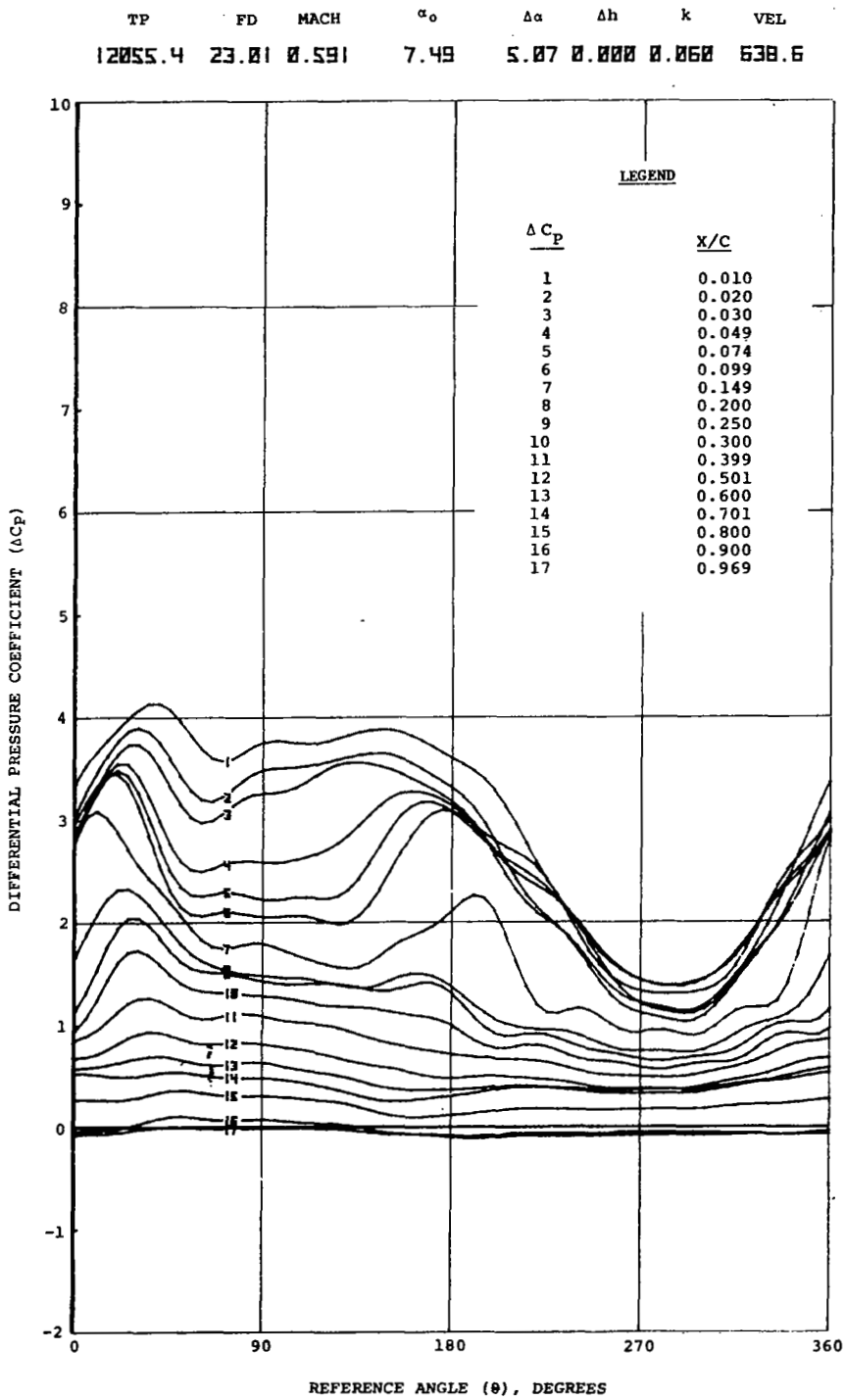

(c) Rn = 9.0 x 10^6
α_o = 7.5°

Figure 52. Concluded

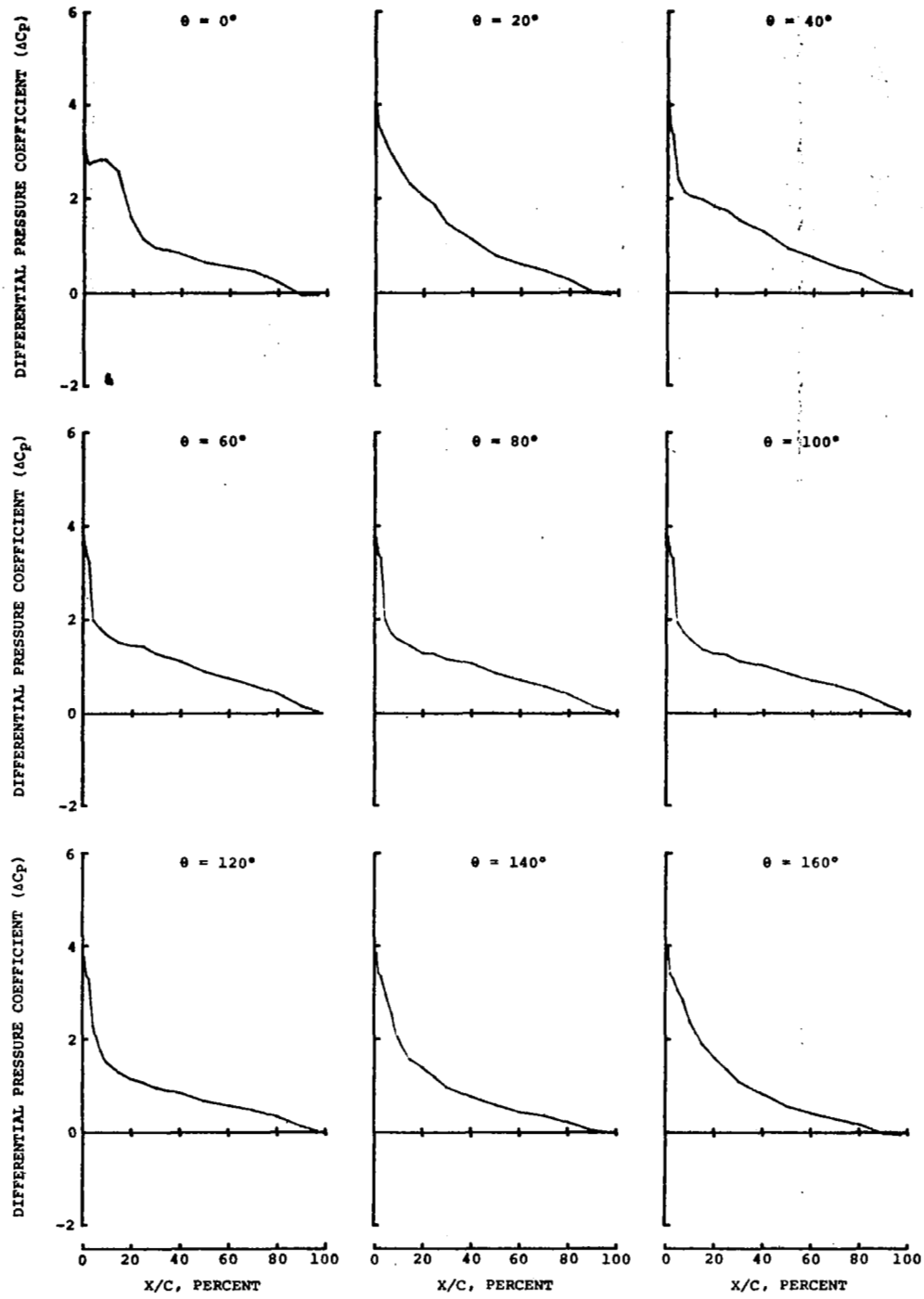

Figure 53. Differential pressure distribution over the NLR 7223-62 airfoil. Nominal conditions: M = 0.6, Rn = 3.1 x 10^6, α_o = 7.5°, $\Delta\alpha$ = 5.0°, f_D = 23 Hz, TP 12061.4.

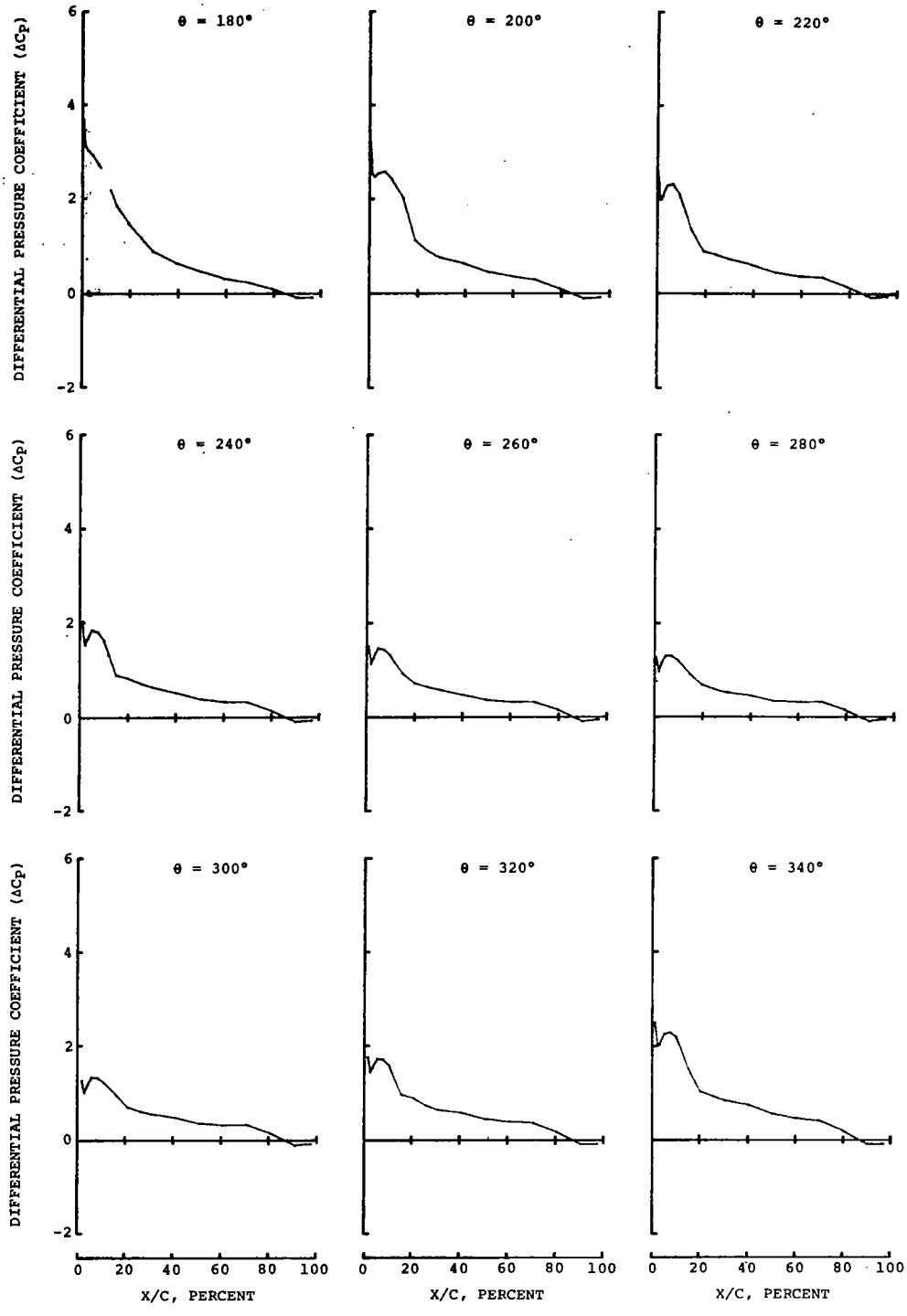

Figure 53. Concluded

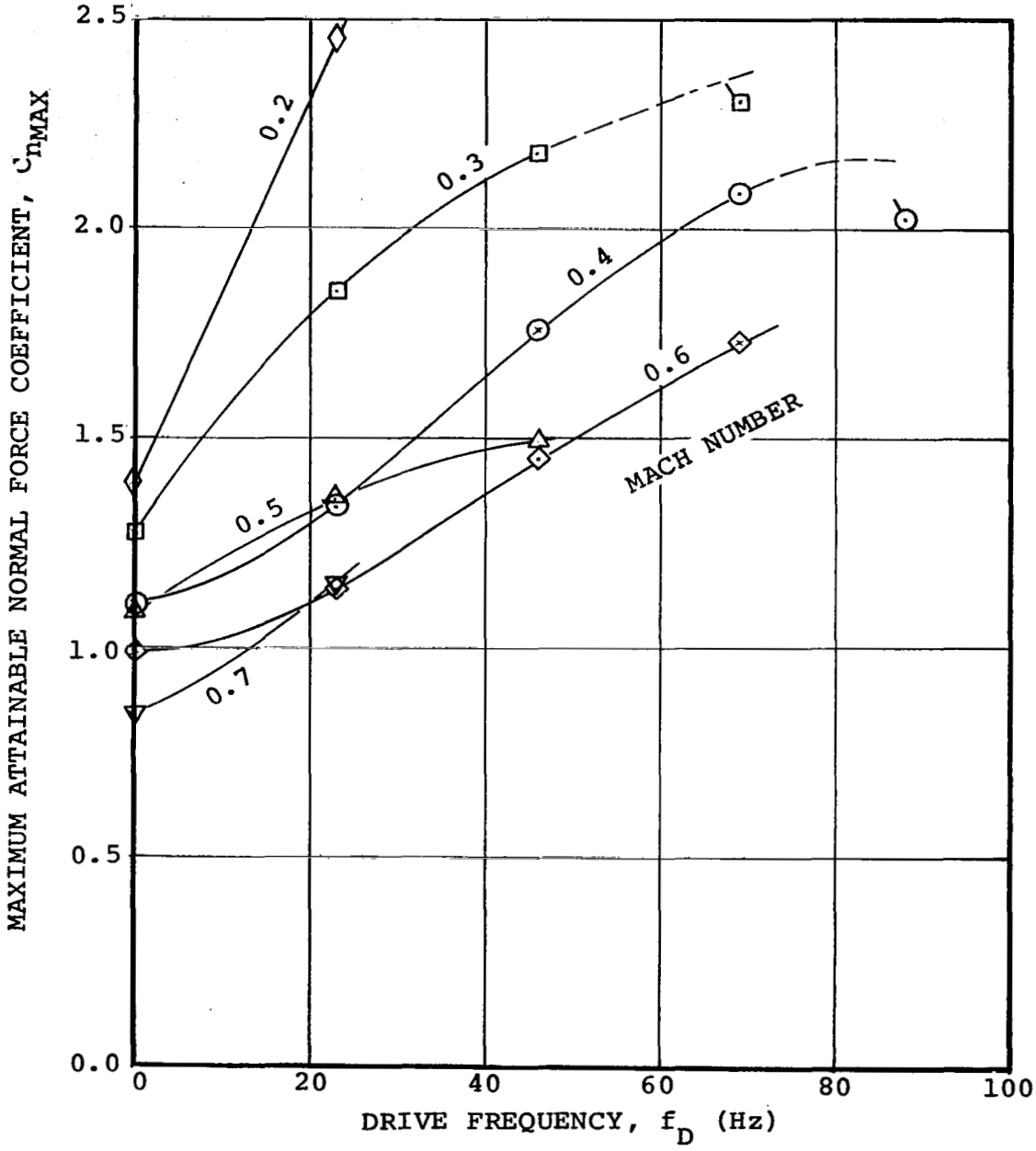

Figure 54. Maximum normal-force boundaries of the NLR 7223-62 airfoil in forced pitch oscillation with amplitude $\Delta\alpha = 5.0°$.

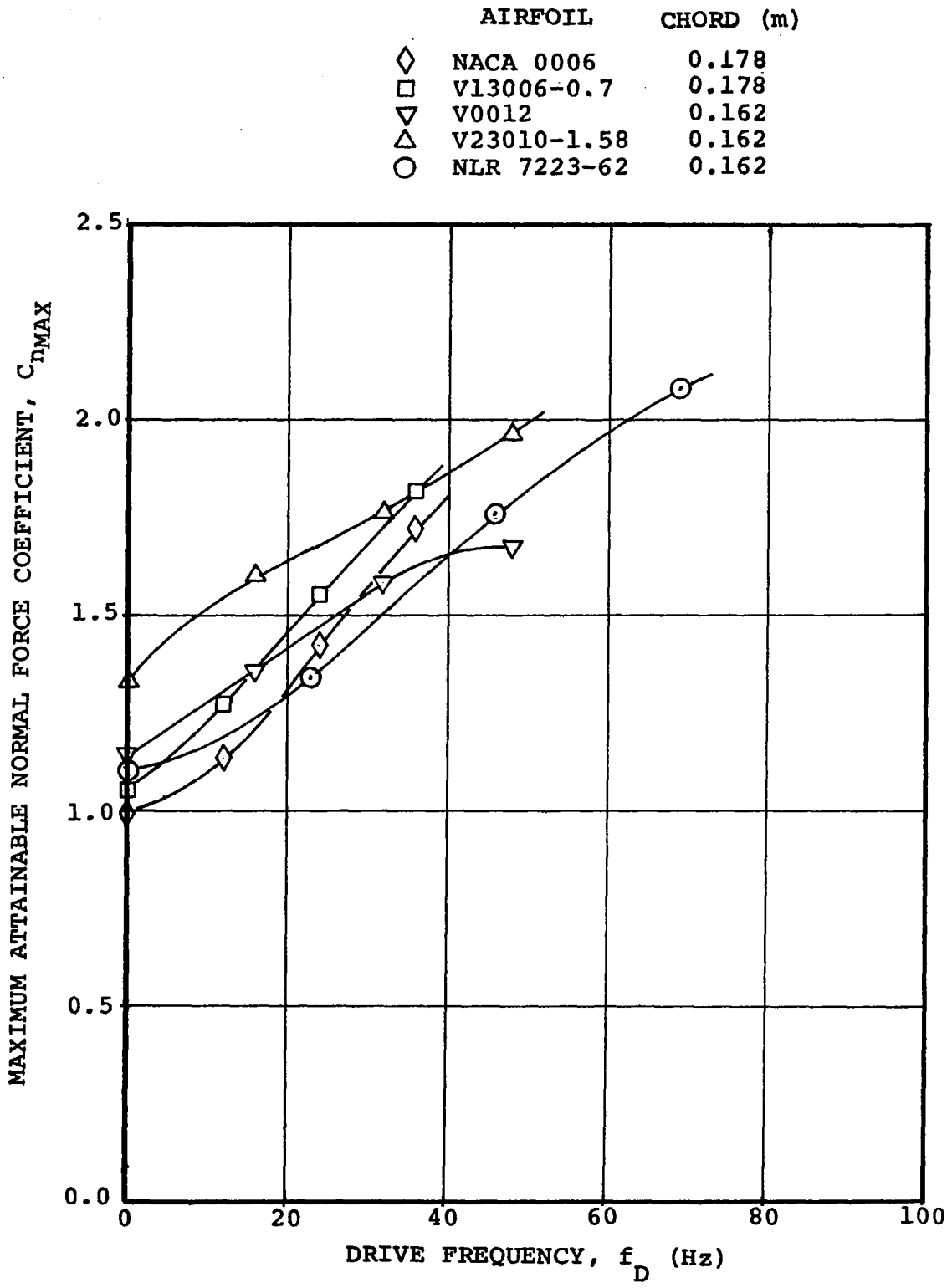

Figure 55. Comparison of the maximum normal-force boundaries of several helicopter rotor airfoils in forced pitch oscillation at M = 0.4, $\Delta\alpha$ = 5.0°.

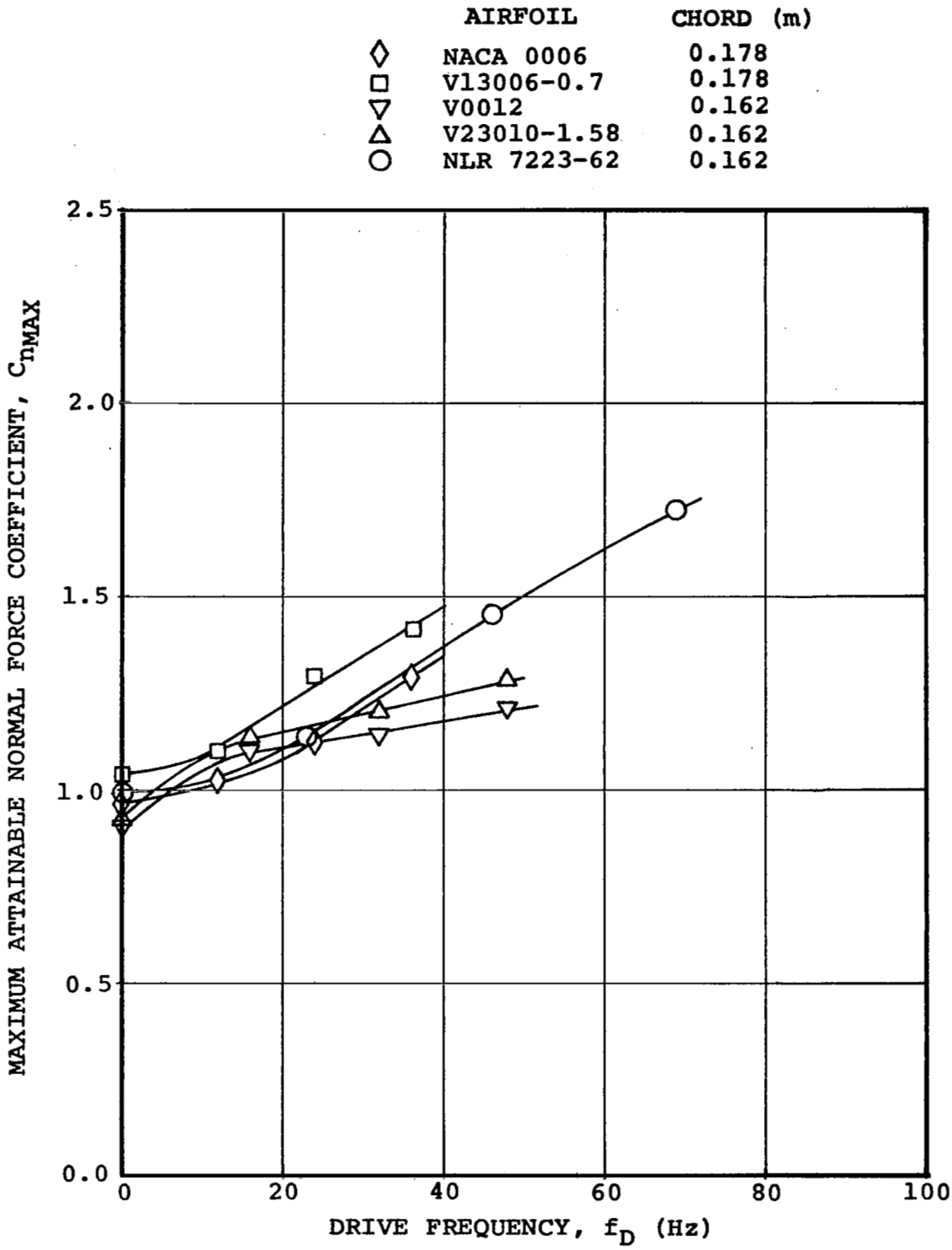

Figure 56. Comparison of the maximum normal-force boundaries of several helicopter rotor airfoils in forced-pitch oscillation at M = 0.6, $\Delta\alpha$ = 5.0°.

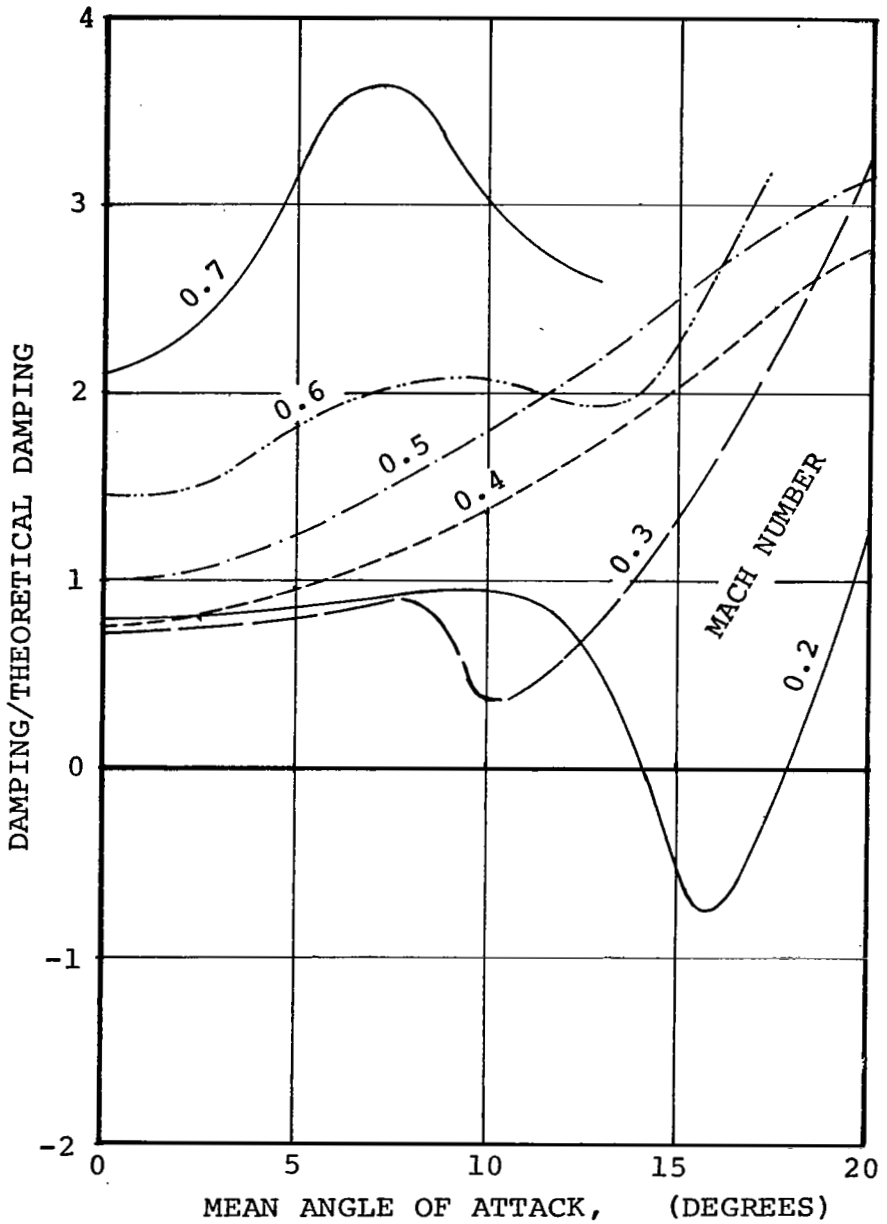

Figure 57. Effect of Mach number variation on the aerodynamic damping of the NLR 7223-62 airfoil in forced-pitch oscillation at f_D = 23.0 Hz, $\Delta\alpha$ = 5.0°.

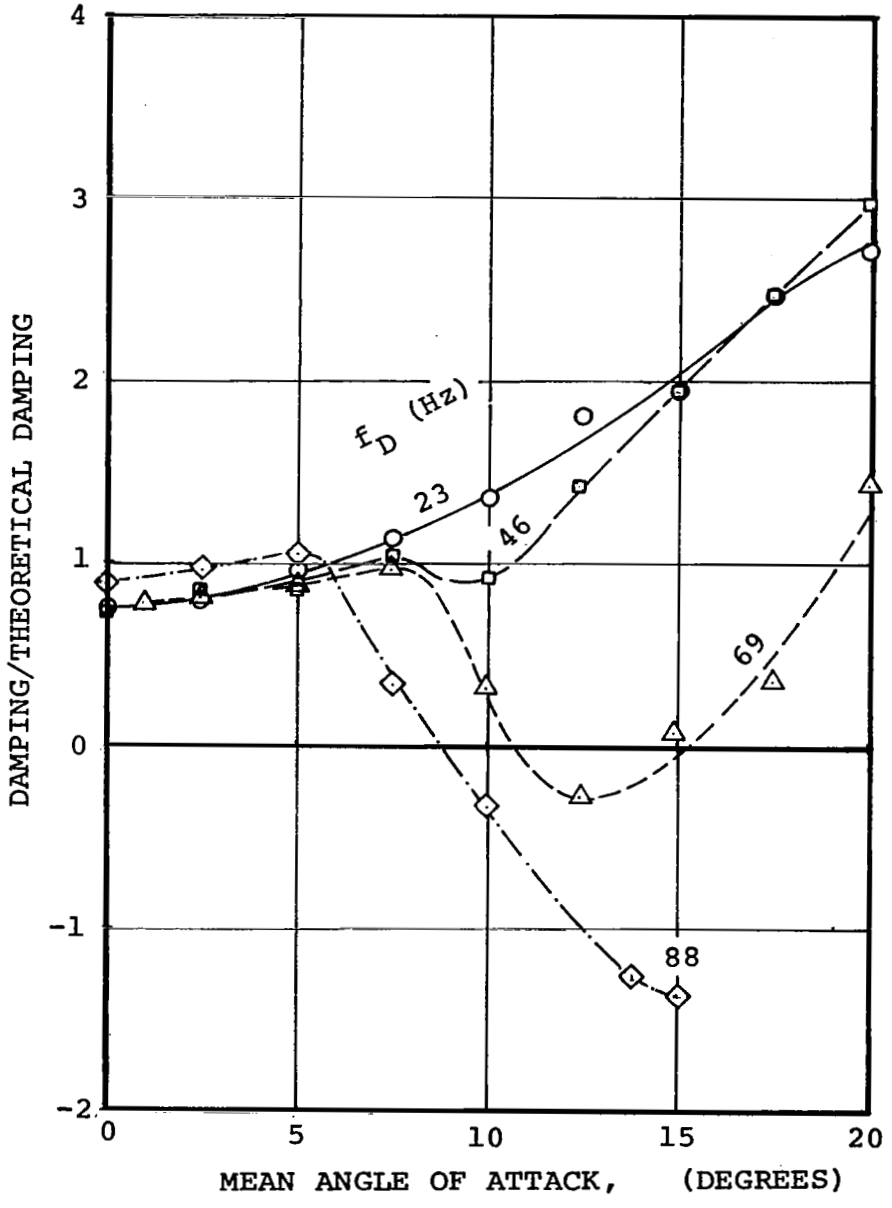

Figure 58. Effect of drive-frequency variation on the aerodynamic damping of the NLR 7223-62 airfoil in forced-pitch oscillation at M = 0.4, $\Delta\alpha$ = 5.0°.

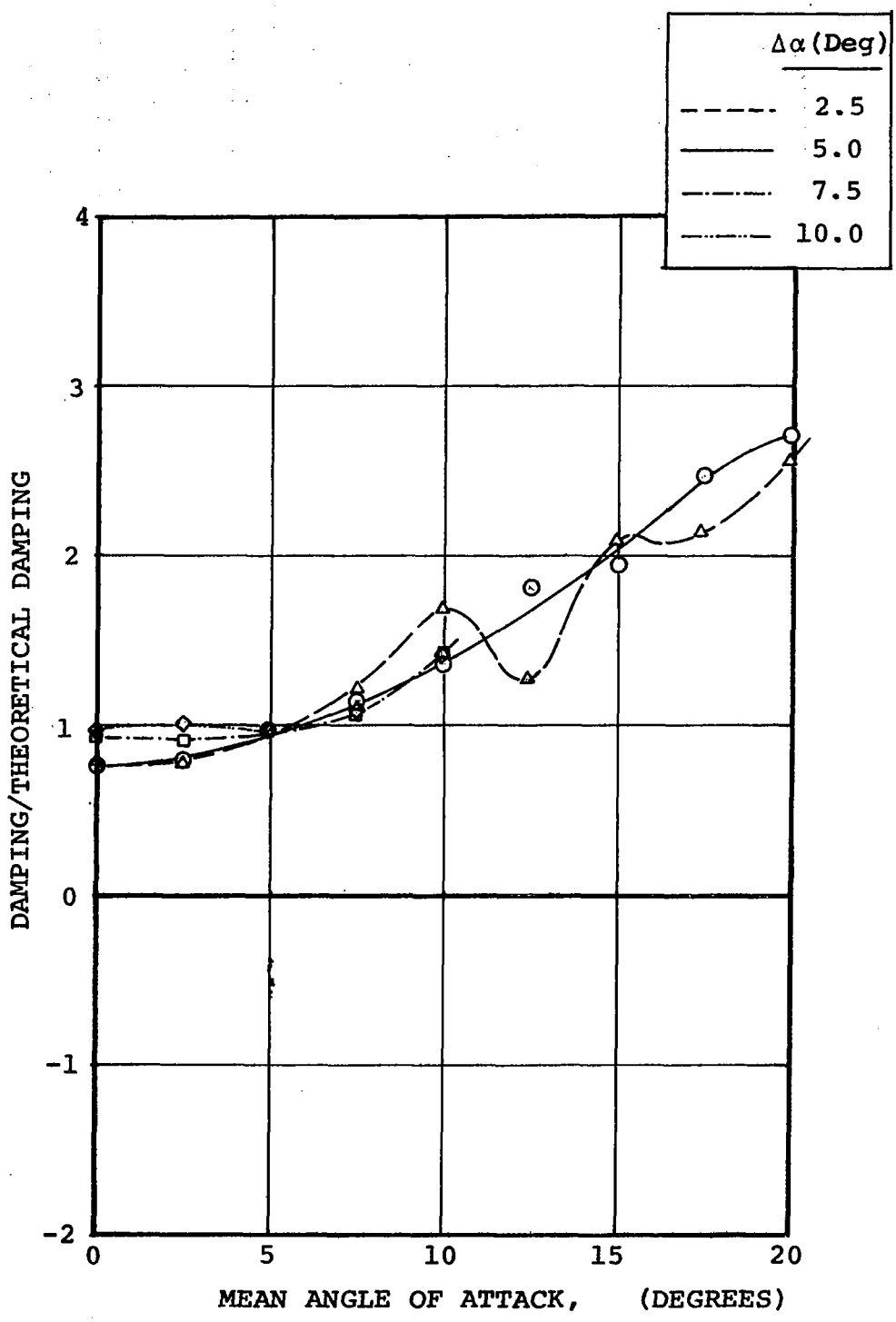

Figure 59. Effect of variations in oscillatory pitch amplitude on the aerodynamic damping of the NLR 7223-62 airfoil at M = 0.4, f_D = 23.0 Hz.

Note: for NLR 7223-62 airfoil k = 0.088
for all other sections k = 0.062

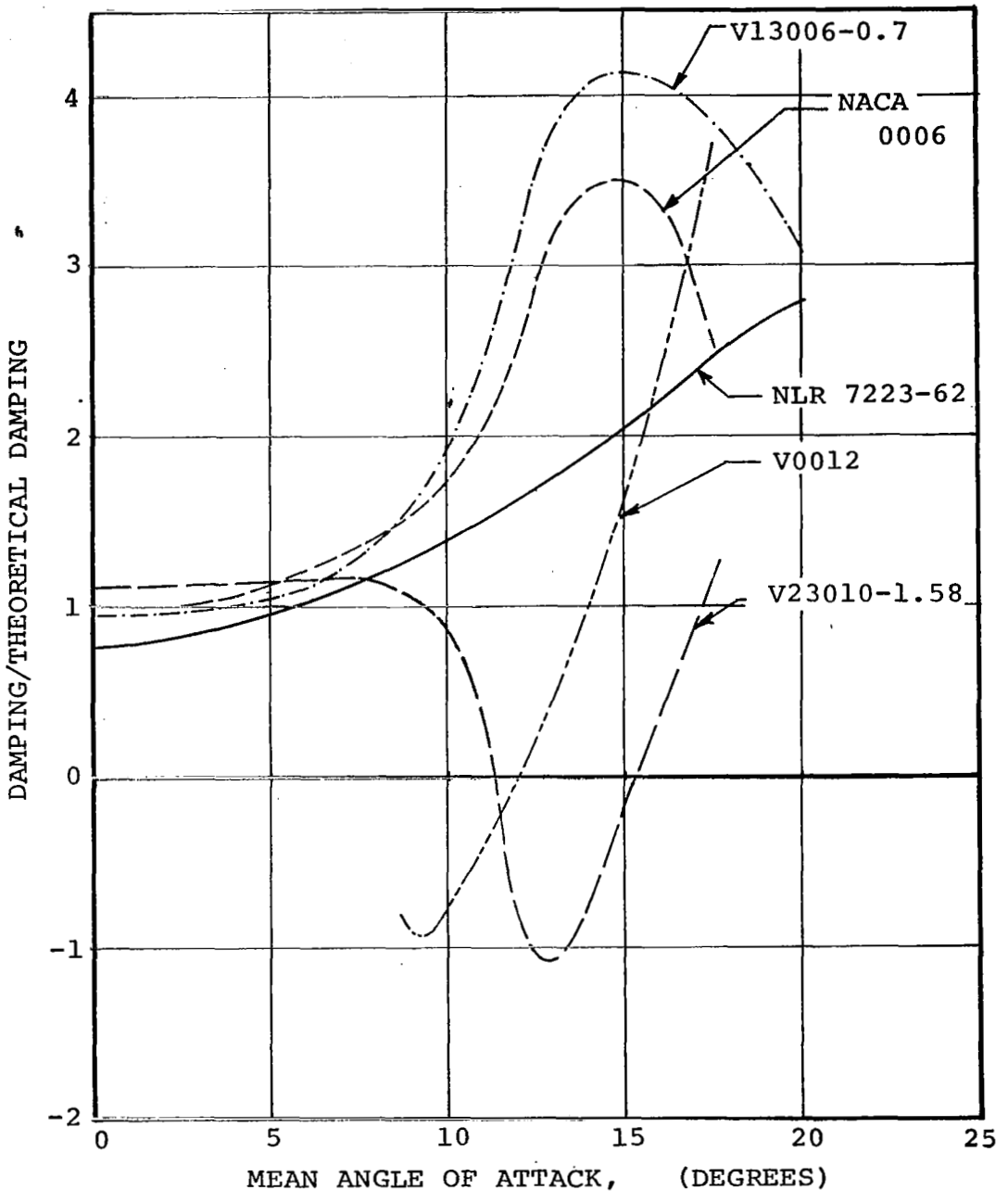

Figure 60. Comparison of the aerodynamic damping characteristics of several helicopter airfoils at the 1/rev frequency of oscillation for $M = 0.4$ and $\Delta\alpha = 5.0°$.

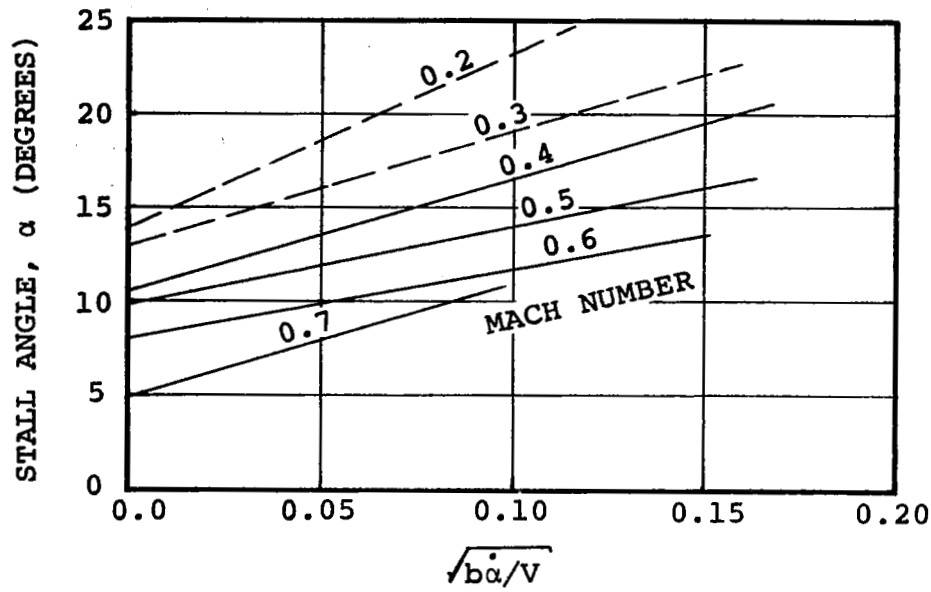

(a) NORMAL FORCE

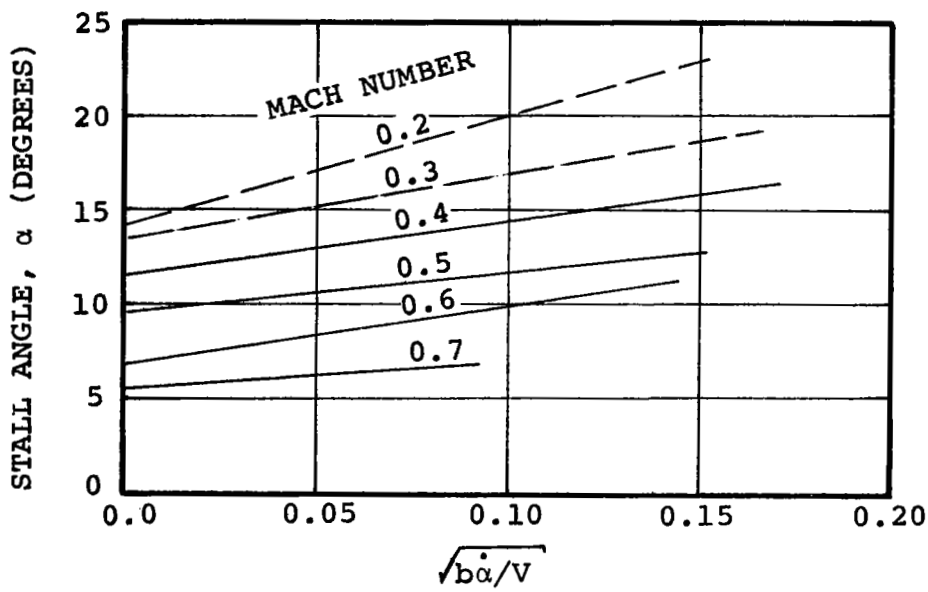

(b) PITCHING MOMENT

Figure 61. Dynamic stall delay characteristics of the NLR 7223-62 airfoil.

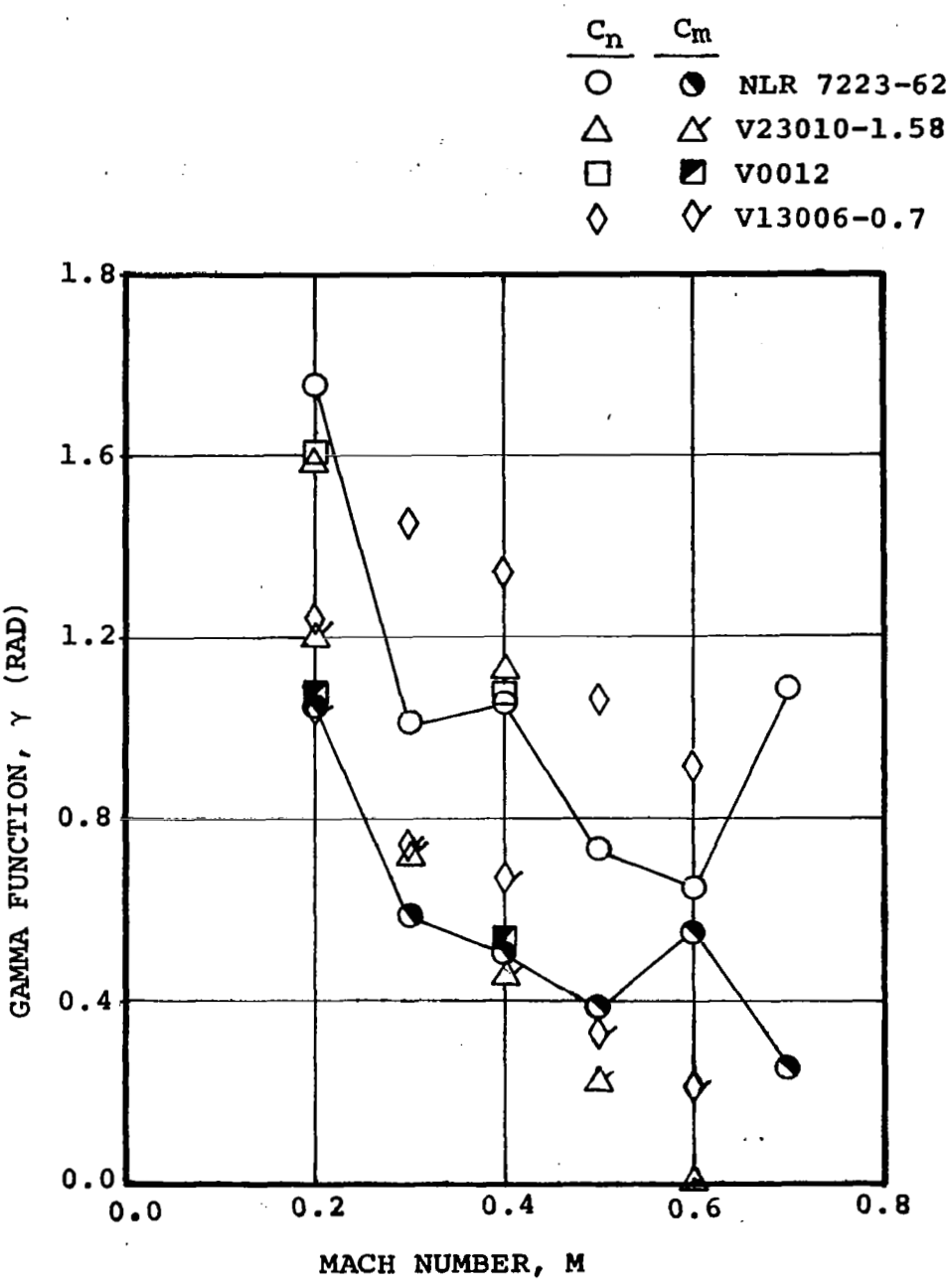

Figure 62. Comparison of the dynamic-stall delay parameters of several helicopter-rotor airfoils.

APPENDIX A

Data Acquisition and Reduction System

All model pressure transducers, together with other gages and transducers monitoring model incidence and flow conditions in the test section, were connected with the standard data reduction system for most of the quasi-steady test conditions, and with a separate data monitoring and recording system for some of the quasi-steady and all of the oscillatory test conditions. The separate data acquisition system employed during the oscillatory runs consisted of two 14-channel Honeywell 5600 tape recorders, with each channel input displayed through a Calico multi-channel oscilloscope system. The recorded signals were also picked up by the tape monitors and displayed on two Honeywell 1612 oscillographs. The two tape recorders were run simultaneously. On each tape, three channels were devoted to:

1) A binary time-code signal

2) A 1/rev signal from a magnetic pickup in the airfoil drive mechanism

3) The oscillatory component of the angle of attack, $\Delta\alpha$.

The remaining 22 channels contained:

1) The 17 pressure transducer signals

2) The mean angle of attack, α_o

3) The airfoil drive frequency, f_D

4) The tunnel flow conditions, P_T, $(P_T - P_S)$, T_T

Each run, whether static or oscillatory, was divided into the following data acquisition steps:

1) Initial wind-off-zero of all data channels

2) Reference zero volts (short) on all data channels

3) Reference 1 volt (from standard) on all channels

4) Reference zero volts (short)

5) Test data

6) Final wind-off-zero

A comparison of initial and final wind-off-zero from the oscillograph stripouts after each run showed whether or not the equipment drifted because of temperature problems. Generally, no temperature problems were encountered. In very few instances, a run had to be repeated to stabilize the temperature of the model, but this was necessary only after unusually large (more than 2 hours) intervals between runs when the scheduled cooling run was not sufficient.

Following the completion of the wind tunnel test, all data oscillograph stripouts were examined and a written record was made of the time intervals containing useful data.

Upon transfer of all tapes to the off-site data reduction facility the data was processed through the following steps:

1) Analog to digital conversion, during which all data in the tapes was converted into digital values, in engineering units, at the rate of 3200 samples/sec for the oscillating data, and 40 samples over 100 msec intervals for the static (quasi-steady) data. For the oscillatory data, the sampling rate resulted in the acquisition of the following samples/cycle:

Drive Frequency (Hz)	Approximate Samples/Cycle
23	139
40	80
46	70
50	64
52	62
53	60
54	59
69	46
92	35

2) Deletion of data outside of the time intervals identified for further processing.

3) Identification and storage of the required number of cycles of data (generally 20) for each oscillatory test condition.

4) Merging of the two data tapes into one tape.

5) Harmonic analysis up to the ninth harmonic of each cycle of data.

6) Averaging of the harmonic coefficients of all cycles for each channel of data.

7) Final data reduction. Calculation of flow conditions, calculation of integrated normal force and pitching moment coefficients from reconstituted pressure time histories, evaluation of aerodynamic damping. Printout of all data in the form of harmonic coefficients and tabulation of values reconstituted from the harmonics. Static data is processed in a similar manner.

8) Automatic plotting of selected data points. Oscillatory data for selected test conditions can be plotted in one or all of the following plotting options:

   a) Normal-force and pitching-moment hysteresis loops (C_n and C_m vs α).

   b) Normal-force and pitching-moment time histories (C_n, C_M, α, and $d\alpha/dt$ vs θ, where θ, the reference angle within a 360° cycle, is equivalent to time).

   c) Time histories of pressure coefficients, ΔC_p vs θ.

   d) Chordwise pressure distribution, ΔC_p vs x/c, at selected reference angles, θ.

The overall data acquisition and data reduction path is outlined in figure 4.

APPENDIX B

Key Terms

Net or instantaneous angle of attack. Ignoring higher order terms (which are included in the reconstitution of data from harmonics), the angle of attack during pitch oscillation is

$$\alpha = \alpha_o + \Delta\alpha \sin wt$$

where $\theta = wt$ is the reference angle within a cycle. The stall events of interest generally start while $d\alpha/dt > 0$.

Angle of attack for stall. Such angle is generally chosen for

$$dC_n/d\alpha = 0.0$$

and

$$dC_m/d\alpha = 0.0$$

although at Mach numbers above M = 0.6 or for pitch oscillations at high angles of attack with little flow reattachment, this does not always apply.

Maximum attainable normal force, $C_{n_{max}}$. When an airfoil undergoes pitch oscillations at fixed Mach number, drive frequency, and amplitude for increasing mean angle of attack, dynamic stall delay will cause a loss in maximum normal force at levels beyond the quasi-steady level. The highest normal force achieved while an airfoil undergoes oscillations, over a range of conditions from fully attached flow to deep stall, has been used as a measure of its stall delay potential. Such maximum attainable normal force is a function of reduced frequency and Mach number, and it has not been successfully predicted yet by theoretical or empirical means.

Maximum pitching moment after stall. Dynamic stall effects cause the quarter chord pitching moment coefficient to drop to large negative values after stall. The largest negative pitching moments reached are a function of both amplitude and frequency of oscillation and they can exceed the quasi-steady after-stall level by as much as a factor of 4.

Aerodynamic damping. The area enclosed by the C_m, α trace and the sense of motion around the loop have an important physical significance. The net work done by the airfoil on the surrounding air is proportional to the integral

$$w = \oint C_m d\alpha$$

1. Report No.	2. Government Accession No.	3. Recipient's Catalog No.
NASA CR-2914		

4. Title and Subtitle	5. Report Date
TWO-DIMENSIONAL WIND TUNNEL TEST OF AN OSCILLATING ROTOR AIRFOIL - Volume I	December 1977
	6. Performing Organization Code
7. Author(s)	8. Performing Organization Report No.
Dadone, L.U.	D210-11188-1
	10. Work Unit No.
9. Performing Organization Name and Address	11. Contract or Grant No.
Boeing Vertol Company Boeing Center, P.O. Box 16858 Philadelphia, Pa. 19142	NAS 1-13795
	13. Type of Report and Period Covered
12. Sponsoring Agency Name and Address	Final
NASA Langley Research Center Hampton, Va. 23665	14. Sponsoring Agency Code

15. Supplementary Notes

The contract research effort which has lead to the results in this report was financially supported by U.S. Army R&T Laboratories (AVRADCOM), Langley

Langley technical monitor: Charles E. K. Morris, Jr. Volume I of Final Report

16. Abstract

A two-dimensional wind tunnel test was conducted to obtain the quasi-steady and unsteady characteristics of the NLR 7223-62, an advanced airfoil designed for helicopter rotor applications. The test report is in two volumes. The first volume outlines and discusses the test results. The second volume presents the test data in a tabular form.

Differential pressures were measured at 17 locations along the chord of the airfoil model. The airfoil motions were sinusoidal forced-pitch oscillations about the quarter chord at amplitudes varying from 2.5° to 10.0° and at frequencies from 23 Hz to 90 Hz. The quasi-steady tests were conducted at Mach numbers from 0.2 to 0.9, and the oscillatory tests between M = 0.2 and M = 0.7. At quasi-steady conditions a limited number of drag measurements was made with a wake-traversing probe.

17. Key Words (Suggested by Author(s))	18. Distribution Statement
AIRFOILS UNSTEADY AERODYNAMICS ROTORS	Unlimited - Unclassified Subject Category 02

19. Security Classif. (of this report)	20. Security Classif. (of this page)	21. No. of Pages	22. Price*
Unclassified	Unclassified	161	$6.75

* For sale by the National Technical Information Service, Springfield, Virginia 22161